

**EVALUATION OF ADHESIVE BONDING FOR HVAC&R
APPLICATIONS**

by

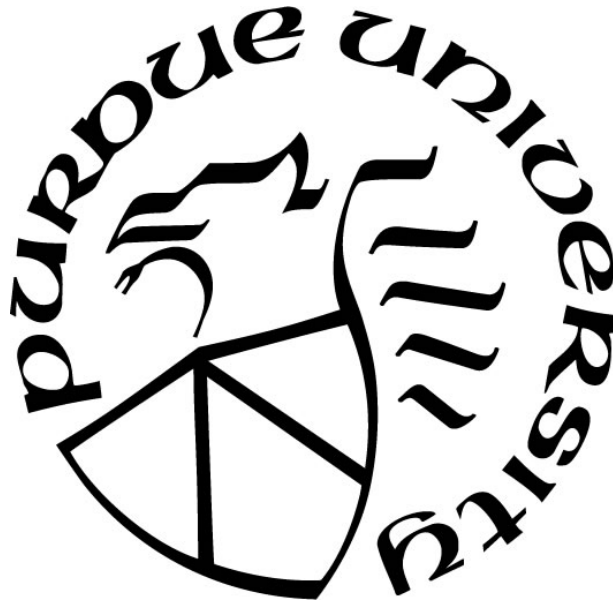
Haotian Liu

A Dissertation

Submitted to the Faculty of Purdue University

In Partial Fulfillment of the Requirements for the degree of

Doctor of Philosophy



School of Mechanical Engineering

West Lafayette, Indiana

August 2021

THE PURDUE UNIVERSITY GRADUATE SCHOOL
STATEMENT OF COMMITTEE APPROVAL

Dr. Eckhard A. Groll, Co-Chair

School of Mechanical Engineering

Dr. Justin A. Weibel, Co-Chair

School of Mechanical Engineering

Dr. Dr. Ganesh Subbarayan

School of Mechanical Engineering

Dr. Carol A. Handwerker

School of Materials Engineering

Approved by:

Dr. Nicole L. Key

To my family

ACKNOWLEDGMENTS

Accomplishing this PhD work has been a wonderful journey and I cannot do any of these with the influence, support and inspiration provided by people around me. My first thanks and appreciation to my co-advisor Prof. Eckhard A. Groll for the opportunity he provided to start my research work in thermal system and components. His continued contribution, guidance and support to my personal and profession growth during my time at Purdue made this journey memorable. I would also express my thanks to Prof. Justin A. Weibel as my co-advisor, who provided detailed and helpful instructions to help me complete and establish my research. As my advisors, they provided numerous opportunities to work on different projects and helps to improve my research skills. This is such a great experience, and I am looking forward to working with them as a Post-Doc researcher at Purdue and Ray W. Herrick Laboratories.

I would like to thank Prof. Ganesh Subbarayan and Prof. Carol A. Handwerker to serve as committee members in my examination committee. Their experts and experience on mechanical structural modeling, material engineering helped me significantly on developing the modeling and completing the PhD work. Their thorough reviews, remarks and suggestions on the thesis are also higher appreciated.

I would like to acknowledge Prof. Davide Ziviani for his support, knowledge and experience in research and academia helped me and we had great time together in work and life. His positive, hard-working attitude towards everything in life encourage and inspire me to overcome the challenges and difficulties lying in the road.

I would like to thank the Department of Energy and Oak Ridge National Laboratory for funding the research and Patrick Geoghegan as the principle investigator for starting this research and providing feedback and guidance all along.

I wish to also express my sincere appreciation to all the staff in the laboratories, particularly Orkan Kurtulus and Frank Lee. Their patience, vast knowledge and endless support made all the experimental work for my PhD work possible. I would also acknowledge Prof. Jeffrey Rhoads and his research group for allowing me to use their facility and helping me performing test.

During the PhD study, I enjoyed my life and work at Purdue with extraordinary people that truly encouraged and accompanied me to go through this journey. It is impossible to name and

thank everyone all in the acknowledgement, but I am deeply grateful to all the colleagues and friends of mine.

I would like to express my sincere appreciation to Xinye Zhang who helped me significantly since the start of my work in Herrick and we have been working together for the many years and left great memories. I vividly remember the time we spent in discussing the thermodynamics, compressors modeling, job carrier, future planning and so much more. He also helped me in writing and presenting my thesis.

I would like to thank my research colleagues in our research group at Ray W. Herrick Laboratories. They provided research ideas and support over the weekly meetings and helps me improve my research work: Akash Patil, Andreas Josef Hoess, Cai Rohleder, Jonathan Ore, Junyan Ren, Leon Brendel, Nick Salts, Parveen Dhillon, Riley Barta, Steven Liang, Tayler Shelly, Vatsal Shah, and many others.

I would like also to say thanks to all my friends that supported me to go through this journey: Clare, Chen Li, Eva Hsuan, Hongya, Heather and Laurent, Junlin Pan, Jie Ma and Yangfan, Li Cheng, Sheng Qian, Tamara and Erin, Tongyang, Xiaoxuan, Xiongfei, Yiyu, Jiakai, Yingying, Yutong and April, Yifan, Zhe Liu and many more. I had a great time at Purdue with all the colorful activities and exciting adventures together.

Finally, I have to say a huge thank you to my family: my parents, grandfather, and my girlfriend. Family is always my driving force to move forward with their constant support and love. My girlfriend Bailu, who provided endless support and always be there for me. She helped me in various ways, not only in daily life but also with her research talents and skills. Her understanding and support are undeserved but highly appreciated. For my parents and grandfather, it is impossible to list the invaluable support they have provided and sacrifices they have made for me to be able to pursue my academic career far away from home. It has been a great journey and I am looking forward to the exciting future adventures.

TABLE OF CONTENTS

- LIST OF TABLES 10
- LIST OF FIGURES 12
- NOMENCLATURE 16
- ABSTRACT..... 20
- 1. INTRODUCTION 24
 - 1.1 Background..... 24
 - 1.2 Current HVAC&R System Joints..... 26
 - 1.3 Emerging Challenges 29
 - 1.3.1 Energy Consumption 29
 - 1.3.2 Manufacturing Cost..... 29
 - 1.3.3 Aluminum Brazing..... 30
 - 1.3.4 Galvanic Corrosion..... 31
 - 1.4 Alternative Joining Technologies..... 32
 - 1.4.1 Compression Joints..... 33
 - 1.4.2 Press-Connect Joints..... 34
 - 1.4.3 Push-Connect Joints 36
 - 1.5 Adhesive Joints..... 37
 - 1.6 Objectives..... 40
- 2. LITERATURE REVIEW FOR ADHESIVE PROPERTIES AND FAILURE MECHANISM 43
 - 2.1 Adhesive Joint Failure..... 43
 - 2.1.1 Material-Strength-Based Models..... 43
 - 2.1.2 Plastic Yield Criteria 44
 - 2.1.3 Fracture Mechanics 46
 - 2.1.4 Fatigue Failure Modeling..... 47
 - 2.1.5 Summary of Failure Criteria..... 48
 - 2.2 Properties of Adhesives..... 48
 - 2.2.1 Density 48
 - 2.2.2 Viscosity..... 49

2.2.3	Stress-Strain Behavior	50
2.2.4	Fracture Energy.....	50
2.2.5	Cohesive Zone Model.....	51
2.3	Surface Preparation in Adhesive Bonding	54
2.3.1	Traditional Surface Preparation Methods.....	55
2.3.2	Surface Preparation Procedure	56
2.3.3	Surface Preparation Summary.....	57
3.	ADHESIVE BONDING OF COPPER PREPARED BY LASER-INTERFERENCE NEAR THE INTERFERENCE STRUCTURING LIMITS.....	58
3.1	Background.....	59
3.2	Materials, Surface Preparation, and Characterization.....	61
3.2.1	Laser Interference Technique and Target Surface Topology.....	61
3.2.2	Process Parameters for Laser Surface Preparation.....	62
3.2.3	Analysis of Surface Topology Periodicity Induced by Laser-Interference	65
3.2.4	SEM Characterization of Surface Topology for As-Received, Unprocessed Specimen	67
3.2.5	SEM Characterization of Surface Topology for Spot-by-Spot Technique.....	69
3.2.6	SEM Characterization of Surface Topology for Spot-by-Spot Specimens Without Interference	75
3.2.7	SEM Characterization of Surface Topology for Raster Technique.....	78
3.2.8	Surface Profile.....	80
3.3	Joint Strength Evaluation.....	82
3.3.1	Experimental Setup	83
3.3.2	Single-Lap Shear Strength Results	85
3.4	Conclusions and Discussions.....	90
4.	FATIGUE AND RELIABILITY ANALYSIS.....	92
4.1	Introduction	92
4.2	Literature Review.....	92
4.2.1	Mechanical Loads and Fatigue.....	93
4.2.2	Thermal Stress and Fatigue.....	95
4.2.3	Fatigue Testing in HVAC&R Systems	95

4.3	Proposed Adhesive U-joints for Testing.....	97
4.4	Pressure and Temperature Cyclic Testing for Thermal Fatigue.....	99
4.4.1	Test Stand Design.....	99
4.4.2	Test Sections and Conditions	103
4.4.3	Cycling Procedure and Instrumentation.....	105
4.4.4	PTC Test Stand Performance	107
4.4.5	PTC Test Conclusion.....	110
4.5	Vibration Testing for Vibrating Fatigue.....	111
4.5.1	Experimental Setup	111
4.5.2	Testing Procedure.....	115
4.5.3	Results and Discussion	115
4.6	Summary and Discussion.....	116
5.	ANALYTICAL MODEL OF STRESS AND STRAIN IN ADHESIVE TUBE-TO-TUBE JOINTS.....	117
5.1	Introduction	117
5.2	Literature Review.....	118
5.2.1	Analytical Analysis	118
5.2.2	Finite Element Analysis.....	121
5.2.3	Summary and Discussions	122
5.3	Model Formulation.....	123
5.3.1	Geometry, Material, and Boundary Condition.....	123
5.3.2	Governing Equations.....	125
5.3.3	Boundary Conditions.....	132
5.4	Solution Method.....	134
5.5	Results and Discussion.....	139
5.5.1	Model Validation.....	139
5.5.2	Parametric Studies Setup	141
5.5.3	Influence of Geometric Sizes	143
5.5.4	Influence of Thermal Expansion	148
5.5.5	Discussion on Thermal Stress	153
5.6	Summary and Conclusions	154

6. PROOF OF CONCEPT TEST.....	156
6.1 Experimental Design.....	156
6.2 Heat Pump Dryer System Modeling.....	158
6.3 Adhesive Joining Procedure.....	159
6.4 Testing Procedure	160
6.5 Results and Discussion.....	161
6.6 Summary	164
7. SUMMARY AND RECOMMENDATIONS.....	165
7.1 Overall Conclusion.....	165
7.2 Recommendations for Future Research.....	166
7.2.1 Extended Reliability Testing.....	166
7.2.2 Improvements to the Analytical Structural Model.....	167
7.2.3 Other Possible Research	167
APPENDIX. WOLFRAM MATHEMATICA PRINTOUT	170
REFERENCES.....	189
VITA.....	211
PUBLICATIONS.....	212

LIST OF TABLES

Table 1.1. Estimated annual HFC leakage rates for common HVAC&R categories	25
Table 1.2. Summarized comparison among main types of joints in HVAC&R joints.....	40
Table 3.1. Laser processing parameters using for the <i>spot-by-spot</i> method (average power 3.5 W).	64
Table 3.2. Laser processing parameters for the <i>laser raster</i> method (average power 3.5 W).....	64
Table 3.3. Survey of surface topology features for single pulse laser-interference processing of pure Al and Cu.....	67
Table 3.4. Topology variation for spot-by-spot laser processing with 4 mm spot size.....	71
Table 3.5. Topology variation for spot-by-spot laser-interference processing with 5 mm spot size.	73
Table 3.6. Topology variation for one-beam laser processed Cu specimens with 5 mm spot size.	78
Table 3.7. Topology variation for the raster laser processing with 5 mm spot size.....	80
Table 3.8. Geometry, maximum loading, maximum shear stress, and displacement at maximum loading for the laser-structured (raster method) and baseline specimens (A: Baseline; B: 6 mm/s; C: 12 mm/s; D: 2 mm/s;).....	88
Table 3.9. Statistics and percentage increase in the maximum shear stress and maximum displacement for the laser-structured specimens with respect to the baseline.....	89
Table 4.1. Simulation results for the typical operating conditions of the Hot Gas Bypass Test stand with selected compressor.....	105
Table 4.2. On/off status of solenoid valves under different test conditions	107
Table 4.3. Sensor specification for the hot-gas bypass test stand.....	107
Table 4.4. Vibration test parameters for joints from ISO Standard 14903.....	111
Table 4.5. Technical specification for amplifier A 3 08 3 057.....	113
Table 5.1. Geometric size of the validation case in the literature (Dragoni and Goglio, 2013).	140
Table 5.2. Material properties and loading condition of the validation case in the literature (Dragoni and Goglio, 2013).....	140
Table 5.3. Comparison of the numerical values of the initial conditions at $z = 0$ of the reported data in the literature with the solved model in this study.....	140
Table 5.4. Geometric size of the tested adhesive joints in this study.....	142

Table 5.5. Material properties and loading conditions of the tube and adhesive used in this study	142
Table 5.6. Geometric size of the tested adhesive joints in this study.....	153
Table 6.1. Components and material applied in the heat pump dryer system	156

LIST OF FIGURES

Figure 1.1. Projected GWP-Weighted HFC consumption for HVAC&R applications under business-as-usual scenario	25
Figure 1.2. Schematic illustration of a brazed joint (Brazing Handbook, 2007)	27
Figure 1.3. Flare joint during the assembly (left) and completed flared joint (right) (Copper Tube Handbook, 2016).....	34
Figure 1.4. Press-connect joints: cutting view elastomeric gasket (left) and completed joints with insertion mark visible (Copper Tube Handbook, 2016)	35
Figure 1.5. Removable copper push-connect fitting (left) and permanent copper push-connect fitting (right) (Copper Tube Handbook, 2016)	37
Figure 2.1 Schematic figure of a typical CZM traction separation law	52
Figure 2.2 Different shapes of the cohesive traction separation law: (a) exponential (Barenblatt, 1962), (b) polynomial (Needleman, 1987), (c) constant (Dugdale, 1960), (d) tri-linear (Tvergaard & Hutchinson, 1992), (e) linear (Camacho & Ortiz, 1996) and (f) bi-linear (Geubelle & Baylor, 1998).	53
Figure 3.1. Schematic diagram of the laser interference system. An angle between the beams of $\alpha = 12^\circ$ is used in this study.....	62
Figure 3.2. Photographs of the laser-processed area on copper using the spot-by-spot method with laser spot sizes of: (a) 4 mm and (b) 5 mm. The photos were taken immediately after processing. The label numbers correspond to conditions shown in Table 3.1.....	65
Figure 3.3. SEM micrographs of the as-received unprocessed copper surface at different magnifications: (a) 300 \times , (b) 500 \times , (c) 1000 \times , (d) 2000 \times , (e) 5000 \times	68
Figure 3.4. SEM micrographs (2000 \times) of the laser-interference-processed area using the spot-by-spot method with a 4 mm spot size on copper. Each frame shows a different number of pulses per spot: (a) 2, (b) 4, (c) 6, (d) 8, (e) 10, (f) 12.....	70
Figure 3.5. SEM micrographs (2000 \times) of the laser-interference-processed area using the spot-by-spot method with a 5 mm spot size on copper. Each frame shows a different number of pulses per spot: (a) 2, (b) 4, (c) 6, (d) 8, (e) 10, (f) 12.....	72
Figure 3.6. SEM micrographs of the laser interference processed Cu surface (spot-by-spot method) with a 4 mm spot size and 2 pulses per spot at different magnifications: (a) 300 \times , (b) 500 \times , (c) 1000 \times , (d) 2000 \times , (e) 5000 \times	74
Figure 3.7. SEM micrographs for one-beam laser processed Cu specimens using the spot-by-spot method with a 5 mm spot size for number of pulses per spot of: (a) 2, (b) 4, and (c) 6.....	76
Figure 3.8. SEM micrographs for one-beam laser processed Cu specimens using the spot-by-spot method with a 5 mm spot size for number of pulses per spot of: (a) 8, (b) 10, and (c) 12.....	77

Figure 3.9. SEM images (2000× magnification) of the laser-interference-processed area using the laser raster method with a 5 mm spot size on copper. Each frame shows a different raster speed (mm/s): (a) 2, (b) 4, (c) 6, (d) 8, (e) 10, (f) 12.....	79
Figure 3.10. 3D surface profile at 50× magnification for: (a) as-received, unprocessed specimen and (b, c, d) laser interference processed Cu with 4 mm spot size: (b) spot-by-spot, 2 pulses, (c) raster, 2 mm/s and (d) raster, 4 mm/s.....	81
Figure 3.11. Schematic figure for the single lap shear joints.....	84
Figure 3.12. Photographs showing the single lap shear joint bonding process and fixture: (a) specimens place on one side of the fixture; (b) adhesive applied on the bonding area; (c) specimens placed on the other side of the fixture; (d) tightened bolts press the two specimens firmly onto each other.....	85
Figure 3.13. Selected photographs of the overlapping bonding area after single lap shear testing. Each top and bottom pair of images correspond to the same bonded specimen: (a) A2 baseline specimen; mixed failure, (b) C3 (12 mm/s) adhesive failure; and (c) C4 (12 mm/s) adhesive failure).....	86
Figure 3.14. Load versus displacement variation during single-lap shear testing for (a): baseline specimen A3 and (b) laser-structured specimens B4 and C1 (6 and 12 mm/s raster speed, respectively).....	87
Figure 3.15. Shear strength (left) and displacement at maximum loading (right) for the laser-structured specimens and baseline (A: Baseline; B: 6 mm/s; C: 12 mm/s).....	89
Figure 4.1. Pressure and temperature cycling (PTC) test example adapted from ISO 14903 (2017).	96
Figure 4.2. Vibration test facility from Wilson and Bowers (2014).....	97
Figure 4.3. Copper and aluminum U-joints used in the tube-and-fin heat exchangers	98
Figure 4.4. Geometric size of the U-joint for testing.....	98
Figure 4.5. Schematic diagram of the developed pressure and temperature cycling test stand with hot-gas bypass control under (a) non-testing, (b) heating, and (c) cooling modes.....	101
Figure 4.6. 3D model for the fixture plate with adhesively bonded U-joints.....	104
Figure 4.7. Temperature of the compressor inlet and outlet as well as the temperature of the inlet and outlet of the test section for one complete cycle.....	108
Figure 4.8. Temperature and pressure of the compressor inlet and outlet as well as the temperature of the inlet and outlet of the test section.....	110
Figure 4.9 Pictures of the shaker test stand (left) and its base plate (right).....	112
Figure 4.10. Technical parameters for vibration exciter S 59935/*-440.....	112
Figure 4.11. Photographs of the U-shape joints with adhesive (left) and the fixtures containing a set of 8 samples each installed on the vibration shaker test stand.	114

Figure 4.12. 3D Drawing of the fixture assembly with U-shaped joints wrapped with black rubber sheet.	114
Figure 4.13. Photographs of the U-shape joints after the vibration test for adhesive joints(left) and vibration joints compared with brazed joints (right).	116
Figure 5.1 Schematic diagram of a typical tube-to-tube joint with adhesive bonding.....	123
Figure 5.2 Schematic figure of the tube-to-tube joint with the main geometric sizes and material properties labelled.	124
Figure 5.3 3D view of a section of the tube with forces and stresses.....	125
Figure 5.4 Elementary free body diagrams of the joint with forces and stresses.....	125
Figure 5.5 Solution algorithm using Laplace transform with boundary conditions.....	135
Figure 5.6. Comparison of the normalized stress field with the Lubkin-Reissner solution and Goglio-Paolino solution using the data given in Table 5.1 and Table 5.2. (Note that the lines are exactly overlapping and appearing as one).....	141
Figure 5.7. Axial force balance with pressure different across the tubes.....	143
Figure 5.8. Variation of stress distributions with the change of bonding length (2l) plotted against the dimensionless variable z: (a) normal stress; (b) shear stress.	144
Figure 5.9. Variation of the normal stress distributions with the change of bonding length (2l) plotted against the dimensionless variable z.....	145
Figure 5.10. Variation of stress distributions with the change of adhesive thickness (t) while keeping the axial force constant. The results are plotted against the dimensionless variable z: (a) normal stress; (b) shear stress.....	147
Figure 5.11. Variation of stress distributions with the change of temperature ($\Delta T = 10K \sim 100K$) plotted against the dimensionless variable z: (a) normal stress; (b) shear stress.	149
Figure 5.12. Variation of stress distributions with the small and negative change of temperature (ΔT) plotted against the dimensionless variable z: (a) normal stress; (b) shear stress.	150
Figure 5.13. Comparison of normal stress distributions with low and high axial loading force experience the same temperature change ($\Delta T = 50 K$) plotted against the dimensionless variable z: (a) low axial force $F = 152 N$; (b) high axial force $F = 5000 N$	151
Figure 5.14. Comparison of shear stress distributions with low and high axial loading force experience the same temperature change ($\Delta T = 50 K$) plotted against the dimensionless variable z: (a) low axial force $F = 152 N$; (b) high axial force $F = 5000 N$	152
Figure 6.1. Schematic drawing (left) and photograph (right) of the custom-instrumented heat pump dryer test stand with the locations of the pressure transducers (P) and thermocouple measurements (T) indicated. The adhesive joints are placed at the locations labelled “1” and “2”.	157

Figure 6.2. Photographs of the cut location “1” for the tube-to-tube joint after preparing bonding surface (left) and within the coupling in place over the cut after application of the adhesive (right).
..... 160

Figure 6.3. Schematic diagram of the heat pump system showing the pressure and temperature values measured or calculated at each state point. The baseline data are shown in blue and the data for the tests with the adhesive joints are shown in red. 162

Figure 6.4. T-s (top) and P-h (bottom) diagrams of heat pump system operation conditions at the baseline condition and for three selected tests over a 6-month period after installing the adhesive joints..... 163

NOMENCLATURE

Symbol	Units	Description
E	(Gpa)	elastic modules
b	(mm)	sample width
d	(μm)	undulations distance
F	(N)	force
G	(MPa)	shear modules
G	(J/cm^2)	fracture toughness
h	(kJ/kg)	specific enthalpy
l	(mm)	sample length
T	(N/m)	hoop force per unit length
M	(kgm^2/s^2)	moments
\dot{m}	(lbm/hr)	mass flow rate
r	(m)	radius
s	(kJ/kgK)	specific entropy
P	(Pa)	pressure
P	(N)	applied load on the sample
t	(m)	thickness
p	(Pa)	hydraulic pressure
T	($^{\circ}\text{C}/\text{K}$)	temperature
T	(N/m)	axial force per unit length
u	(m/m)	longitudinal strain
v	(m/m)	transverse strain
V	(N/m)	transverse force per unit length
\dot{W}	(W)	power consumption
z	-	dimensionless location
α	-	angel of the laser beam
α	(1/K)	thermal expansion coefficient
Δ	-	difference

ν	-	Poisson ratio
λ	(μm)	laser wave length
τ	(MPa)	shear stress
τ_o	(MPa)	pure shear stress
σ	(MPa)	normal stress
δ	(mm)	displacement
μ	-	pressure sensitivity

Subscripts

0	initial
$1, 2, 3$	first, second and third orthogonal direction, respectively
$1, 2$	adherent index
a	<i>adhesive</i>
c	critical valve
d	saturated discharged dew-point temperature
<i>capli</i>	capillary tube
<i>comp</i>	compressor
<i>cond</i>	condenser
<i>evap</i>	evaporator
f	failure
i	index
<i>in</i>	inlet / inside
j	index
<i>out</i>	outlet / outside
<i>max</i>	maximum valve
<i>min</i>	minimum valve
t	Tresca yield criterion
m	Von Mises yield criterion
n	normal direction
s	Laplace symbol

<i>s</i>	shear direction
<i>s</i>	saturated suction dew-point temperature
<i>S</i>	Matrix
sub	subcooling
<i>sup</i>	superheat
<i>x</i>	x axis
<i>y</i>	y axis
θ	θ axis

Abbreviations

Description

ASTM	American Society for Testing and Materials
AWS	American Welding Society
BV	ball valve
CFPC	carbon fiber polymer composite
CV	check valve
FEM	finite element method
FPL	Forest Products Laboratory
EPA	Environmental Protection Agency
EXV	thermal expansion valve
GWP	global warming potential
HFC	hydrofluorocarbon
HVAC&R	heating, ventilation, air conditioning, and refrigeration
IPA	isopropyl alcohol
MOPD	maximum operating pressure difference
ND:YAG	neodymium-doped yttrium aluminum garnet
NV	needle valve
MV	metering valve
PAA	phosphoric acid anodizing
PT	pressure transducer
SEM	scanning electron microscope
SG	sight glass

SV

solenoid valve

TC

thermocouple

ABSTRACT

In the heating, ventilation, air conditioning and refrigeration (HVAC&R) industry, bonding and joining play an important role in the manufacturing and assembly process, which is critical to the cost, safety, reliability, and design freedom of systems. The goal of this thesis is to understand and evaluate the usage of adhesive bonds in the manufacture of HVAC&R systems, specifically in regards to leakage/reliability characterization and stress analysis under loading.

The bonding performance under static loading is first studied using a commercial epoxy adhesive product. In addition to the traditional surface preparation methods of mechanical and chemical etching, a novel laser-interference surface structuring preparation technique was utilized to improve bonding performance. Laser interference structuring uses a ND:YAG laser beam that is split into two beams that are re-directed to overlap on the same area of a copper alloy. A structuring pattern near the interference structuring limits is achieved due to the phase shift between the beams that is imparted as they are re-directed. Two different laser structuring methods were tested: spot-by-spot and laser raster. Different structuring parameters were varied including the laser spot size and pulses per spot (2, 4, 6, 8, 10, 12 pulses/spot) for the spot-by-spot method, and raster speed (2, 4, 6, 8, 10, 12 mm/s) for laser raster method. The microstructure morphology and surface profile after processing were characterized using the scanning electron microscopy (SEM) and profilometry for all surfaces. It was found that the laser-interference structuring removed the surface contaminants efficiently and formed dot- or net-shaped structures on the surface. This indicates that melting, vaporization, and solidification of the metal happened differently. Due to the much higher speed of the laser raster method, considering practical industrial applications, it is selected for additional investigation for shear strength improvement. The shear strength is measured by a single lap shear test which pulls apart adhesively bonded single lap joint specimen under shear loading using a mechanical tester.

Based on the surface profiles, three different laser raster speeds of 2 mm/s, 6 mm/s and 12 mm/s were selected for the manufacture of single lap joint specimens for comparison with the traditional surface preparation methods. The shear lap strength and displacement at maximum load were obtained for the specimens. The laser raster at 6 mm/s increased these values by approximately 11.0% and 25.1%, respectively, while the 12 mm/s condition had an increase of 16.8% and 43.8%, compared with the baseline traditional surface preparation method. It is

concluded that laser structuring can enhance the single lap shear joint bonding performance. Within the tested laser processing parameters, a higher laser raster speed results in a larger enhancement.

In addition to the static loading test with epoxy adhesive, different adhesive formulations are investigated and developed by the collaborating adhesive manufacturer to determine their suitability for use under the temperature and pressure conditions in HVAC&R systems. Reliability, especially fatigue failure, is another major concern because the strength of the adhesive joints is sufficient for HVAC&R applications. Two primary types of fatigue may happen in practical applications: thermal fatigue and vibration fatigue. Two test facilities were designed and built to test the adhesive performance and understand the failure mechanisms. For the thermal fatigue testing, a novel pressure and temperature cyclic (PTC) test stand was designed to simulate the pressure and temperature changes that may occur in HVAC&R systems. The test stand was designed to switch between hot high-pressure gas and cold low-pressure gas by using a compressor with hot gas bypass setup. For the vibration testing, a standard industrial shaker was used to provide the required vibration at a given displacement and frequency with a specially designed fixture for the tested joints. In both tests, adhesive joints were tested in parallel with brazed joints, undergoing extreme thermal and vibration loading conditions. All the samples were leak-checked before and after the testing, which were found to be leak-free after the testing, indicating that they pass the required qualification test according to available standards. It is confirmed that adhesive joints can be a potential alternative when dealing with thermal and vibration fatigue in the common working conditions of HVAC&R systems.

The qualification testing is specific to the required loading conditions, such as pressure and temperature variations, and limited to certain tube sizes. An analytical model is developed to allow for design and evaluation across various operating conditions. The model aims to predict the adhesive stress and strain fields of in tube-to-tube joints based on the geometric parameters, material properties, and the loading conditions. In particular, the model uniquely considers the influence of thermal expansion and contraction in the joint, which is necessary for the periodically changing temperatures in HVAC&R systems. It is numerically solved using Mathematica and validated against the published data in the literature. The exact same solutions are achieved using the reported data in the literature, under simplified conditions without any temperature change involved. The validated model is then used in parametric studies to investigate the influence of

geometric sizes and temperature change. Several conclusions are made about the trend of stress changes as well as the maximum stress, which provide insight from a perspective of general design guidance. Adhesive bonding length should be selected such that the maximum stress is smaller than the allowed material strength for both normal and shear stress. Adhesive thickness has less impact in the parametric range considered and is nevertheless usually dictated by the manufacture recommendation in view of other practical considerations. In regard to the thermal stresses, it is found that in practical HVAC&R working environment, the temperature-induced thermal stress dominates the stress fields and leads to significant change in the stress distribution across the adhesive layer. If a temperature change is present, the combination of all possible loading and temperature change should be analyzed to find the most extreme loading condition. This work demonstrates the first stress and strain analysis of tube-to-tube adhesive joints considering the working conditions of HVAC&R applications involving temperature cycling. All of these results provide a detailed guidance for use of adhesive joints across different application or locations in HVAC&R systems. The model can be also used as a framework to evaluate and compare the performance of different adhesives, as long as the adhesive properties are available.

Lastly, it is also essential to demonstrate the application of these joints in real HVAC&R systems. A proof-of-concept test was done to demonstrate that the use of adhesive joints in a real system would cause no change in operation or leakage. A commercial heat pump dryer system was used to perform the testing at the Ray W. Herrick Laboratories. Two adhesive joints were installed to replace the brazing joints at the compressor inlet and outlet, where the most extreme temperature and pressure conditions are present. Results show that the system operates without any change in performance and experience no obvious leakage after more than 50 hours of testing over 6 months.

This work explores the feasibility and reliability of adhesive bonding of copper for HVAC&R applications. The bonding strength of adhesive was studied and tested with both traditional surface preparation and advanced laser-interference structuring technique. The results show that for the tested structural epoxy adhesive, the bonding strength is large enough considering the internal pressure in the tube and the laser structure technique can increase the shear strength.

The long-term reliability with respect to thermal, stress and vibration fatigue are then experimentally investigated and the adhesive joints pass the qualifications tests required by the standard. Further modeling work for predicting the stress distribution in adhesively bonded joints is developed to understand the influence on geometric parameters and temperature change. The

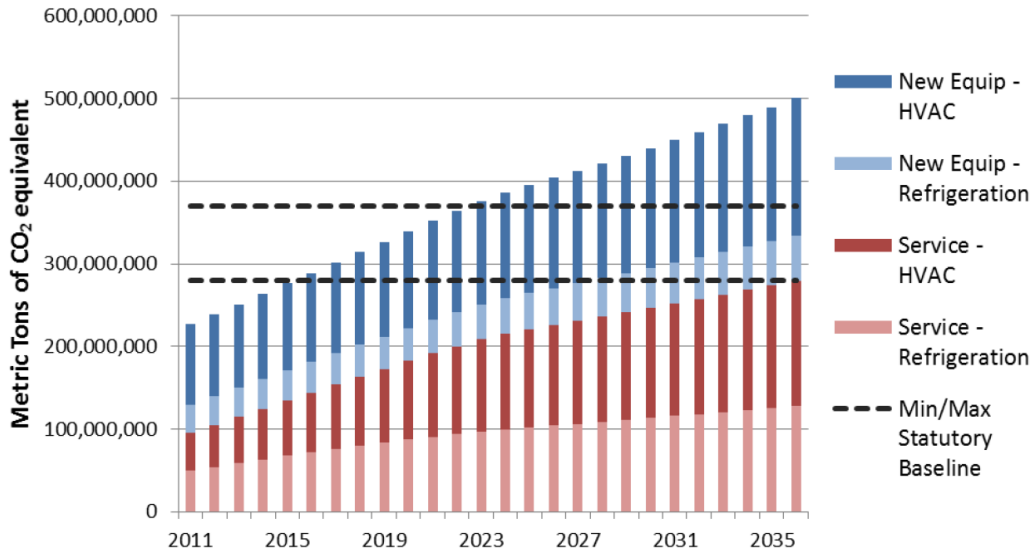
adhesive length can influence the stress distribution significantly and temperature-induced stress dominates the stress distribution under the HVAC&R loading conditions. Further material characterization is needed for crack propagation or detailed fatigue analysis, which is highly dependent on the adhesive formula, working environment and loading conditions, which can be performed with a more specific targeted application. The experimental and modeling work in this thesis provides a foundation for adhesives to be applied in HVAC&R applications and a framework to further develop, optimize, and utilize adhesive joining in HVAC&R applications.

1. INTRODUCTION

The background and motivation for the present research is described in this chapter. With rapid industrial development and rising environmental issues, the existing joining technology in HVAC&R has ever more challenges. There are growing demands for alternative novel joining technologies. The environmental issues, current and other alternative joining technologies, as well as the objectives of the study are presented in this chapter.

1.1 Background

With over a century of developments in the HVAC&R industry, thermal systems are widely used in almost every area in our daily life and industry. However, the massive usage of these systems also results in some concerning issues including energy consumption, ozone depletion, greenhouse effect, etc. HVAC&R systems contribute to the greenhouse gas emissions both directly through the massive usage of refrigerants and indirectly through fossil fuel and electrical consumption in their manufacture and operation. In an amendment to the U.S.'s proposed submission to the Montreal Protocol, the U.S. Environmental Protection Agency (EPA) targets global warming potential (GWP) weighted hydrofluorocarbon HFC consumption reductions of 85% during the period of 2016–2035. Greenhouse gas emissions by HVAC&R systems are generated through the initial product manufacturing and installation as well as maintenance services to charge the lost refrigerant through leakage. According to the EPA Navigant refrigerant consumption model, HVAC&R equipment will account for over 55% of HFC consumption in the US by 2035 including servicing the existing and new systems. Figure 1.1 (EPA, 2013) provides the projected GWP-weighted HFC consumption attributed to new equipment and equipment servicing as usual scenario. As can be seen, the service refrigerant accounts for a significant percentage of the total amount.



Source: Navigant HFC consumption model (EPA, 2015)

Figure 1.1. Projected GWP-Weighted HFC consumption for HVAC&R applications under business-as-usual scenario

According to EPA report (EPA 2015), many HVAC&R equipment types have leakage rates of 10% per year due to limitation in joining techniques, system design, operations and maintenance practices, etc. Table 1.1 (EPA, 2015) summarizes estimated annual HFC leakage rates for common HVAC&R categories.

Table 1.1. Estimated annual HFC leakage rates for common HVAC&R categories

Equipment Category	Estimated Annual HFC Leakage Rates (%)
Supermarkets and Other Retail	1-25
Mobile Air Conditioners	2-18
Cold Storage	15
Residential Unitary AC	12
Industrial Process Refrigerant	4-12
Centrifugal Chillers	2-11
Commercial Unitary AC	8-9
Packaged Terminal AC / Heat Pump	4
Refrigerated Appliances	1

Refrigerant leakage causes not only greenhouse gas emissions but also a series of negative influences including losing cooling capacity, decreasing energy efficiency and lowering equipment lifetime, which also brings indirect emissions. In order to address this issue, one of the critical task is to investigate and evaluate new joining technology to reduce the leakage of refrigerants from HVAC&R equipment. Before discussion of new and alternative technologies in detail, a brief review of the joining technology development is given.

1.2 Current HVAC&R System Joints

A typical HVAC&R system consists of various individual components connected together by tubes and joints to form a complex piping system for energy generation or distribution. These major components usually include compressors, heat exchangers, different type of valves and some other accessories such as filters, pumps, etc. Among these components, there are subassemblies that are joined together by more essential parts, e.g., tube and fin type heat exchangers are manufactured by joining individual tubes and metal sheets together with U-shape bends. At every point where two individual parts meet, joining technologies produce a mechanically adequate bond between the surfaces without any damage to the original part. These must meet the structural requirements for the initial weight and operational pressure of the system and allow the refrigerant flow through their path as designed. A strong and reliable joint can provide a stable, efficient and leak-free system assembly. The failure of joining will cause leakage and a series of negative consequences including danger to the system, wasted energy, and pollution to the environment.

Traditionally, brazing is the most common joining technology in the HVAC&R industry. It is a well-established commercial process capable of producing strong joints, which is widely used in industry due to the ability of joining most metallic and ceramic materials. The process of brazing can be performed using both manual technique as well as automated production modes. As defined by the American Welding Society (AWS), the term brazing encompasses a group of joining processes that produce the coalescence of materials by heating them to the brazing temperature in the presence a filler metal having a melting point above 450 °C (840 °F) and below the solidus of the base metal. The brazing filler metal is distributed between the closely fitted surfaces of the joints by capillary action. The term brazing temperature refers to the temperature to which a material is heated to enable the brazing filler metal to spread and adhere to, or wet, the base metal

and form a brazed joint. From the definition, it distinguishes brazing from other common joining technologies of soldering and welding. Brazing and soldering have very similar features, but the term brazing is used to refer to the joining processes performed above 450 °C (840 °F) while soldering refers to the joining process performed under this temperature. With respect the difference with welding, brazing is intended to melt the brazing filler metal, not the base material while in welding both the brazing filler and base metals are melted to affect the coalescence of materials.

In brazing, the assembly is heated to the point at which the brazing filler metal becomes molten and fills the joint clearance between the two surfaces that are being joined. The assembly is then cooled and the molten filler is solidified. The filler metal is held in the joints by capillary action, anchoring the surfaces together by metallurgical reaction and atomic bonding. This process is shown in Figure 1.2.

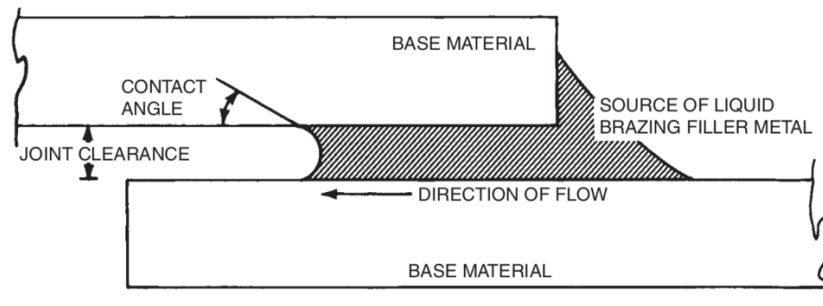


Figure 1.2. Schematic illustration of a brazed joint (Brazing Handbook, 2007)

The properties of the brazed joints are determined mainly by these significant factors: joint design and clearance, brazing filler materials, surface preparation, proper temperature distribution and alignment. The joining procedure is similar for all joints design and materials. The surfaces for joining will be prepared first to clean the contamination attached on the surface, such as dirt and oil. After preparation, flux is applied when necessary, depending on the metals characterization, to remove the oxide layer. Then the two parts are assembled together with proper fixture and support. Heating is applied to the assembly afterwards. The filler material is applied when reaching the designed temperature. When the molten filler fills the clearance of the two surfaces, heating is stopped and the assembly is allowed to cool down. In some situations, post-brazed cleaning is needed to finish the brazing procedure (Brazing Handbook, 2007).

Traditionally in the HVAC&R industry, the most common geometry for brazed joints are tube-to-tube joints. As for the materials, traditionally copper is the most widely used metal in HVAC&R systems due to its flexibility and good heat transfer performance. Recently, there is an emerging trend to use aluminum heat exchangers to replace the copper ones (Q.Y. Zhang and H.S. Zhuang, 2008), which will be discussed in detail later.

For most of the tube-to-tube joints, a coupling with a slightly larger diameter than the tubes will be applied so that both tubes have an overlap area within the coupling for the filler material to flow in and establish the bonding. Alternatively, the two components can be connected directly without an overlapping coupling to form a butt joint. Strong, uniform, leak-proof joints can be made rapidly and inexpensively with brazing, especially for joints that are inaccessible and parts that may not be joinable by many other methods.

The most common heating methods in the HVAC&R industry are furnace brazing and flame brazing. Furnace brazing is usually seen in massive manufacturing processes, where components or parts enter a continuous or batch furnace with filler material in place and ready to braze. The heat generated by the furnace can melt the filler materials uniformly and form the desired brazed joints simultaneously for all the components and parts. Most large-scale coil manufactures are using furnace brazing. Flame brazing can be used in both factory manufacture and field installation: a handheld oxyacetylene torch will be used to melt the filler material and create the brazing joint. There are also some other brazing methods available: induction, resistance, dip, diffusion, infrared and laser. (Brazing Handbook, 2007)

Compared to other common metal-joining techniques, such as welding, the major advantages of brazing joints in HVAC&R systems are:

1. Brazing does not melt the base material. It gives a tighter control over the tolerances and produces a clean joint without secondary finishing, which can save time and cost in manufacture and installation process. It can keep the inner surface of the joints clean and neat without creating extra deformation and roughness, which may increase the pressure drop.
2. In general, brazing produces less thermal distortion because it usually has a uniform heating, especially when a brazing furnace is used. The joints in the HVAC&R systems will go through multiple temperature and pressure cycles; a high thermal distortion and residual stress create a higher opportunity to cause failures or cracks.

3. Complex and multi-part assemblies can be brazed cost-effectively and easily adapted to mass production with automation manufacture since the individual process parameters are less sensitive to variation. This is very important for HVAC&R industry, considering the massive number of joints are needed in both manufacture and field installation.

1.3 Emerging Challenges

Brazing has been used in the HVAC&R industry for decades and proved successful due to the previously discussed reasons. However, new challenges have been identified where the current brazing technology needs improve.

1.3.1 Energy Consumption

Energy consumption and greenhouse gas emissions associated with the high-temperature, controlled-atmosphere brazing furnaces is a concern for massive production, especially for tube-and-fin type heat exchangers. Although there are many optimizations that have been done to increase the energy efficiency, and control strategies implemented to reduce the energy consumption of brazing furnaces, very high temperature furnaces inevitably consume a significant amount of energy. Besides, when using brazing furnaces, since the whole component need to be put together into the furnace, the heat is not localized on the joints but applied to all the parts of the assembled components like tubes, fins, and sheets in the system. The heat used on the extra parts is wasted. The consumed energy contributes the green gas emissions indirectly.

1.3.2 Manufacturing Cost

A more cost-effective manufacturing method is desired. A complete HVAC&R system usually has a very large number of joints. For example, for a common tube-and-fin air-to-refrigerant heat exchanger used in domestic heat pump applications, there can be up to hundreds of brazed U-shape joints. Considering the huge number of the manufactured units, a cheaper joining method will be very beneficial. Building and maintaining brazing furnaces is a large investment while flaming brazing is very time consuming and requires large labor cost.

1.3.3 Aluminum Brazing

Another significant issue is aluminum brazing (aluminum-to-aluminum and aluminum-to-copper). Traditional brazed joining methods have limitations in working with aluminum alloys. Over the last 30 years, the traditional copper/brass heat exchangers have been almost completely replaced by brazed aluminum units in automobiles and trucks. Cost savings and light weight are the major motivation for this change. A similar trend can be seen for the HVAC&R industry, as most of the manufacturers are switching to aluminum coils or aluminum alternatives for the same reasons. Experimental studies show that micro-channel systems with aluminum alloys achieve better thermal performance and lower refrigerant charge than ones with copper tube condensers. Continuous developments of aluminum alloys have improved the extrudability, brazability, corrosion resistance, and mechanical strength of materials at both room and elevated temperatures. However, aluminum brazing is harder and more complicated compared to copper brazing because aluminum has very similar melting temperature to the common filler material. After the heat exchanger is assembled, the aluminum heat exchangers are introduced into the hot zone of a brazing furnace following several pre-braze steps, e.g. cleaning, degreasing, fluxing, and finally drying off and proper control of every step is necessary for the brazing quality (Swidersky H W, 2001). Different filler materials like Si-Al series alloys will be required for aluminum brazing. They are quite suitable for aluminum brazing and classified as the BA1Si series of filler alloys by the American Welding Society. The solidus temperature of the filler is at least 40 °C lower than that of the base metal to avoid melting of the base metal during the heating process (Brazing Handbook, 2007; Q.Y. Zhang and H.S. Zhuang, 2008). Studies have provided detailed analyses of the structure and composition of intermetallics and the distribution of the Si particles (Dehmas et al., 2006; Lacaze et al., 2005; Gray et al., 2006).

In aluminum brazing, besides for the filler material itself, there are some other differences compared to copper/brass brazing such as brazing sheet and flux processing, which make the brazing process more complicated and costly. Also, in order to improve joint strength, many studies have been done on aluminum brazing processes, including investigation of the effects of the initial clad thickness, Si concentration, heating conditions, oxide layer, flux material, etc. Modeling and experiments show that a thick initial clad layer causes the residue to increase (Zhao and Sekulic, 2006; Sontgerath et al., 1996; Gray et al., 1999). As for the flux, the aluminum

surfaces are covered by a tenacious oxide, which can re-form in a very short time after removal if exposed to water or air (Jordan and Milner, 1956–7; Hatch, 1984; Shapiro, 2010). This oxide layer will be an issue for aluminum brazing that restricts the liquid flowing freely while the sample was heated above solidus melting temperature, which is contrary to the requirements of a good brazing process. The free flow of the molten filler and good wetting of the base surfaces are required to braze two surfaces together. In practice, the oxide layer is usually removed by deposition a flux on the aluminum surfaces. Over the decades, different flux materials have been proposed and studied for oxide layer removal. Traditionally, chloride fluxes are used to remove the oxide layer. The principle of the oxide layer removal is when the flux is heated and molten, it will penetrate along the oxide/substrate interface through cracks/defects in the oxide film (e.g. due to heating), eventually leading to the detachment of the oxide from the metal surface (Jordan and Milner, 1956–7; Terrill et al., 1971). However, when these fluxes are used, the post-brazed part must be thoroughly cleaned to remove the hygroscopic, corrosive flux residue under strict environmental and safety procedures. There are many studies on new flux technologies to have a better oxide layer removal and wettability, including the current state-of-art flux: a non-hygroscopic, potassium fluoroaluminate flux, which removes the oxide layer and can stay on the surface after the brazing to provide some protection against corrosion. (Timsit and Janeway, 1993; Gray et al., 1999; Yoon et al., 2007; Garcia et al., 2010)

1.3.4 Galvanic Corrosion

Galvanic corrosion, also called dissimilar-metal corrosion or bimetallic corrosion, is electrochemical process in which one metal corrodes preferentially, when in electrical contact with a different type of metal or if both metals immersed in an electrolyte such as water. When electrical contact is made between two different metals, ions travel from one metal or “anode” to the receiving metal or “cathode”. When this occurs, the anode metal corrodes and the cathode metal is protected from corrosion as the anode metal is corroded (Cottis et al., 2010). It is always a threat in any type of bimetallic system or structures (Wong et al., 1979; Tadjamoli et al., 1984; M. Slámová et al., 2002).

Although more and more aluminum is being used in HVAC&R systems, not all the components can be made with aluminum. Accessories such as valves, bends, pump bodies and volutes are almost never made of aluminum, because they cannot be manufactured as easily in

aluminum as in copper. Hence, when heat exchangers and some of the tubes are made in aluminum, if it circulates in a closed loop, there will be direct or indirect contact between aluminum and copper. As a specific example, in many of the systems, a common combination is aluminum heat exchanger with copper tubes. The outlet tube from the heat exchanger is made of aluminum but the connection tube between the components is made of copper. If the aluminum tube and copper tube are brazed together, the filler metal becomes the connection and keeps the electrical continuity between the metals. Due to the nature of the HVAC&R systems, they usually work in humid environment with possible moisture absorption and water condensation. Some outdoor units may be exposed to direct rain water directly. The water on the surface works as an electrolyte to ensure ionic conduction.

With all these conditions satisfied, galvanic corrosion can happen at the location of the connections. Based on the electronegativity of Cu and Al, the process will corrode the copper material but leave no appreciable galvanic corrosion of aluminum under atmospheric conditions. However, the corrosion product of copper, verdigris, attacks aluminum and may be reduced under the formation of small copper particles. It has been reported that pits can be initiated in aluminum when copper ions are available (Blackwood and Chong, 1998; Bakos and Szabó, 2008; Khedr and Lashien, 1992). Both the corroded copper and damage to the aluminum need to be avoided for the normal operation of HVAC&R systems, especially when using more and more aluminum parts are becoming the trend in industry.

1.4 Alternative Joining Technologies

With so many emerging challenges associated with traditional brazing, a larger effort has been devoted to the development and improvement of joining technology in the HVAC&R industry. Different principles have been explored and applied in order to produce cheaper and better joints. Some of the common alternative joining technologies are described below. Note that the majority of brazing joints are used for tube-to-tube connections and the material is copper. The following joining technologies are designed for copper, if not otherwise specified.

1.4.1 Compression Joints

Compression joints are a very common alternative for brazing joints when using an open flame is either not desired or impractical. Compression joints belong to the category of mechanical joints. The compression joint usually is composed of an outer compression nut and an inner compression ring or ferrule that is typically made of brass or copper. Ferrules can have different shapes and materials but most commonly are in the shape of a ring with beveled edges. The longest sloping face of the ferrule needs to face away from the nut for the joints to work properly. In the joining process, the nut is being tightened and the ferrule is compressed between the nut and the receiving fitting. It will seal the gap between the tube and nut, producing a tight joint by clamping the end of the ferrule around the tube and bowing away the middle of the ferrule.

There are two different types of compression joints, flare joints (British type-B/manipulative) and standard compression joints (British type-A/non-manipulative). Standard joints require no modification on the tube while the flare joints require flaring of the tubing. The standard joints are typically used for water and air connectors and can be installed using an ordinary wrench to tighten the surrounding nut. Flare joints are used more for gas and high pressure lines and need a special tool for flaring before assembly. The tube flaring tool consists a die that grips the tube with a mandrel forced into the end of the tube. Tube flaring is considered a type of forging operation and is usually a cold working procedure. It is important to use the flare tool properly to avoid stress concentration, which will cause early failure of the joints. (Hirschberg et al., 2017; Lorkring, 2019).

Before flaring, it is necessary to anneal the end of the tube and make sure the tube is cut square by the proper tube cutter. After cutting, the tube must be reamed to the full inside diameter leaving no inside burr and the tube should be sized to round for later process. Surface cleaning, for example using an abrasive cloth, should be used to clean dirt, debris, and foreign substances from the tube end. Once the preparation work is done, a flare nut is placed over the tube end and the flaring bars of the tool are inserted in the proper opening for the tube size. After flaring, the final flared tube end should have a smooth, even, round flare of sufficient length to fully engage the mating surface of the flare nut without protruding into the threads (Copper Tube Handbook, 2016). As shown in Figure 1.3, are the completed flare tube end and completed flared joint.

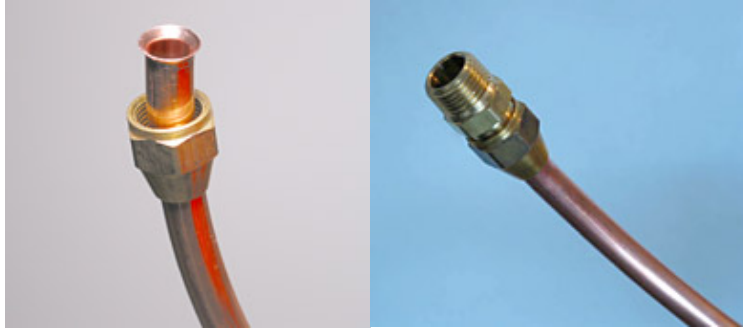


Figure 1.3. Flare joint during the assembly (left) and completed flared joint (right) (Copper Tube Handbook, 2016)

Compared with brazing joints, the advantages and disadvantages of compression (as well as flare) joints are summarized:

Advantages:

- No need for open flame or heating which makes it quick and safe
- Works at high pressure and with toxic gases
- Some of the joints are able to occasionally be disassembled, allowing the joints to be disconnected and reconnected without compromising the integrity of the joints

Disadvantages:

- Restriction on the joint geometry (only applied to tube-to-tube joints)
- Not as robust and reliable as brazed joints and not tolerant to flexing, bending and pressure shock, and therefore leakage is more like to happen in long-term use
- Bulkier size that takes more space and looks less aesthetically pleasing

1.4.2 Press-Connect Joints

Similar to compression joints, press-connect joints are mechanical joints and require no heat or open flame. The press-connect joining method was patented in Europe in the late 1950s and continues to be used successfully. The method and associated fittings and tools were introduced in the United States in the late 1990s. (Copper Tube Handbook, 2016)

The idea of press connect joints is based on copper's excellent malleability. The joints rely on the sealing ability of special gasket or seal, usually O-ring shape in tube joining, as shown in Figure 1.4. Special pressing tools and jaws are necessary for a leak proof connection. There are

several manufactures that offer full-product lines of press-connect fittings, valves, and specialty items.

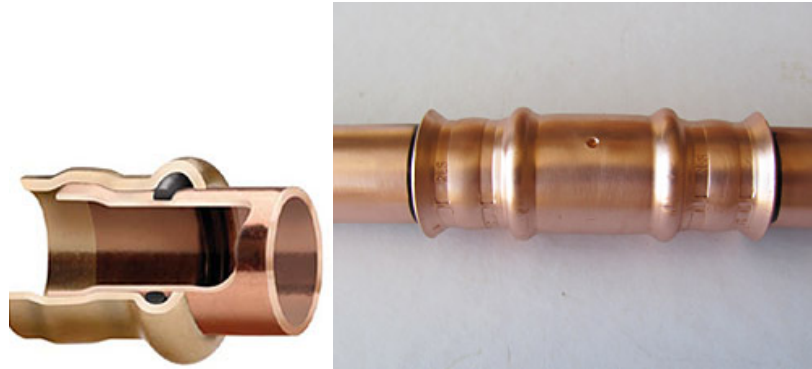


Figure 1.4. Press-connect joints: cutting view elastomeric gasket (left) and completed joints with insertion mark visible (Copper Tube Handbook, 2016)

For press-connect joints, the tube must be free of dents, deep scratches, oils, dirt, or other surface contamination. Mechanical cleaning is needed as well as the rounding tool before joints assembly. A very detailed and mature joining procedure has been proposed for joint assembly. With a specially designed measurement tool, the cutting location and tube insertion length is marked. After cutting the tube properly, burrs must be removed from the inner and outer diameter of the tube end. The tube must be inserted to the proper depth based on the mark and pressed into the joint using a tool. Most of the products in the current market use an electric-drive pressing tool to ensure the appropriate pressure. As the last step, addition verification step is required to check the press completion by verifying the final dimensions of the joints.

Compared with brazing joints, the advantages and disadvantages of press-connect joint are summarized (Arment et al., 2012; Wilson and Bowers, 2014; Elbel et al., 2016):

Advantages:

- No need for open flame or heating which makes it quick and safe
- Work at high pressure and with toxic gases
- Reliable operation if following the assemble and verification procedure

Disadvantages:

- Restriction on the joint geometry (only applied to tube-to-tube joints)

- Special tools and fittings are needed, which increases the cost and weight significantly.
- Pressing tool requires a large installation space
- Due to the thermal expansion of the copper, it performs worse when working under high temperature
- Complicated procedure for automated manufacture

1.4.3 Push-Connect Joints

A push-connect joint is another very common mechanical joint, which requires no heat and no additional tools. The joint can be easily made by hand. It has a similar design principle as press-connect joints that use a special fitting for connection. On the inner diameter of the fitting, an integral elastomeric gasket or seal and stainless-steel gripping ring help to produce a strong, leak free joint. Once pushed on, the gripping ring and the gasket together provide a positive and strong seal on the outer diameter of the insertion tube. The usage of a gripping ring avoids the need for electrical pressing tool in the press-connect joint.

As shown in Figure 1.5, there are two common types of push-connect fittings. One allows easy removal and re-connection after installation while the second one cannot be easily removed once the fitting is installed. The removable fitting is widely used in refrigerant charging, testing and fault detections, which requires frequent connection and disconnection.



Figure 1.5. Removable copper push-connect fitting (left) and permanent copper push-connect fitting (right) (Copper Tube Handbook, 2016)

The same procedure as for press-connect joints is needed to prepare clean, round, and burr-free tube ends for push-connect joints. Lubrication may be needed depending on the manufacture recommendation. After all preparation work is done, the insertion tube is pushed into the fitting until the joint is locked securely in the designed location.

Compared with brazing joints, the advantages and disadvantages of press-connect joint are summarized:

Advantages:

- No need for open flame, heating or special tools, which makes it quick and safe
- Work at high pressure and with toxic gases
- Removable type fitting can be disconnected without breaking the joint and tube

Disadvantages:

- Restriction on the joint geometry (only applied to tube-to-tube joints)
- Leakage is more like to happen in long-term use
- Special fittings are needed, which increases the cost and weight significantly
- Complicated procedure for automated manufacture

1.5 Adhesive Joints

As previously shown, several methods have been investigated and applied to serve as joints in HVAC&R systems. However, there are certain limitations for every single existing joining technology. Most alternative joining methods have not proven that they can replace brazing with reliable performance and low cost. Further work needs to be conducted to introduce new technology into the HVAC&R industry to develop viable alternatives to brazing.

Adhesive joining is the process of uniting materials with the aid of an adhesive, a substance capable of holding materials together by surface attachment (ASTM D 907, 2015). It is a widely used industrial joining process including automotive, electronics, etc. and is proven to be reliable. There are many types of adhesives. Some of them need unheated or heated curing while some do not. Adhesives for structural bonding are usually cured to have the adequate strength to transfer the loads through the joints. Depending on the components, there are one-part adhesives that need to heat up before applying and two-part adhesive that need to mix evenly before applying. Based on the applications, there is freedom to design and develop adhesives with certain characteristics such as curing temperature/time, assembly time, drying temperature/time, etc., which is very beneficial when developing adhesives for a specific application.

From the literature review and market survey, adhesive tube-to-tube joints are not a mature product for HVAC&R systems due to the lack of investment and research on the product development and qualification. Most of the existing products are focusing on quick repair, instead of initial manufacture. The most common type of adhesive in current HVAC&R joints is two-part epoxy with heat curing. Epoxies are widely used as high-performance structural adhesive because of their ability to cure without producing volatile byproducts, resistance to chemicals, and low shrinkage during curing (Tai and Szklarskasmialowska, 1993; Kahraman and Al-Harhi, 2005). When using, the epoxy resin is mixed with hardener at a certain mass ratio to form a homogeneous mixture. The mixture needs to be applied to the prepared surface in its working time. The strength of the adhesive joint largely depends on several factors, such as the design of the joints, the thickness of the adhesive, the bonding area, and modifications to the bonding area. There are not many studies that have been done to evaluate the usage of adhesives in HVAC&R systems.

The general advantages of adhesive bonding include:

1. Adhesive can be used on different joint geometries, not limited to tube-to-tube joints
2. Adhesive bonding provides a more uniform stress distribution than mechanical joints by eliminating the individual stress concentration peaks by avoiding mechanical force
3. No need for special designed fittings and tools, which usually results in lighter system and sometimes cheaper as well
4. Room temperature curing avoids using heat torch or furnace, which save energy and cost

5. The ability to join dissimilar materials with electrical insulation prevents galvanic corrosion of metal adherents
6. Cured adhesive can provide a strong and leak-proof seal between the bonding surfaces, which can hold high-pressure gas or liquid

However, there are also disadvantages of adhesive bonding including:

1. Adhesive joining is much more sensitive to surface preparation than mechanical joints and even brazing joints. Proper surface preparation is essential to make a strong and reliable joint. It can be extremely hard to conduct proper surface preparation in field assembly.
2. There are no reliable nondestructive tests for determining the strength of a formed adhesive joint and the bonding performance is highly dependent on the assembly procedure.
3. Adhesive materials are perishable, unlike filler metals or mechanical fittings. They must be stored either refrigerated (one part) or separated (two parts). Once ready to use (mixed or heated), they must be assembled and cured within a specific time interval.
4. The curing process may consume a longer time for than brazing and mechanical joints, especially at room temperature.
5. Long-term reliability is not clearly studied, especially for HVAC&R systems. Adhesives are susceptible to degradation when absorbing moisture, undergoing thermal cycling, or by chemicals.

The comparison of brazing joints, compression joints, press-connect joints, push-connect joints and adhesive joints are summarized in Table 1.2. Compared with previously discussed joining technologies, adhesive joints provide some unique features that are key to overcoming certain challenges facing the HVAC&R industry. Using adhesive joints can decrease system weight, reduce manufacturing energy and cost, and avoid galvanic corrosion. In addition, unlike all the mechanical joints that needs mechanical force, the adhesive joints manufacturing process is similar to brazing in nature.

Although detailed procedures for use of adhesives in HVAC&R systems have not yet been introduced to this industry, there is a huge potential to use adhesive joining in massive production with assembly line processing. Being aware of all adhesive joint disadvantages, this study aims to

evaluate and improve adhesive joining performance in HVAC&R systems and to propose an appropriately designed adhesive joint, including adhesive formula, joint geometry, manufacture processes, that could potentially outperform traditional brazing and mechanical joining technologies.

Table 1.2. Summarized comparison among main types of joints in HVAC&R joints

	Various geometry	No open flame	Permeant fittings	No clamping tools	No Extra components	Easy joining for dissimilar metals
Brazing joints	✓	✗	✓	✓	✓	✗
Compression joints	✗	✓	✗	✗	✗	✓
Press-connect joints	✗	✓	✓	✓	✗	✓
Push-connect joints	✗	✓	✗	✓	✗	✓
Adhesive joints	✓	✓	✓	✓	✓	✓

1.6 Objectives

The objective of this study is to evaluate and develop a better understanding of adhesive joints for HVAC&R applications, so that their unique features can be leveraged to overcome the challenges facing this industry without risk of joint failure. This will involve a comprehensive analysis of adhesive joints strength and fatigue, as well as rigorous thermal performance and mechanical reliability tests with consideration of manufacturing processes. To achieve this, the following tasks will be undertaken:

1. Perform a detailed review of the literature and available standards to understand the joints strength definition and requirements for HVAC&R applications and to identify the critical factors that influence the joints strength such as surface preparation, properties of the adhesive and adherents, adhesive thickness etc.
2. As an important factor of the joints strength, surface preparations of the adhesive joints will be studied in detailed. Traditional surface preparation methods are well described in the literature and will be used as the baseline technology. New

alternative technology: laser interference structuring will be tested and compared to the traditional methods.

3. The failure mechanism of the adhesive under static loading will need to be investigated for strength analysis and modeling. Experiments will be performed to aid in the validation of models and to provide feedback for adhesive formula development.
4. Long-term reliability of the adhesive joints will be analyzed and tested. The adhesive joints in a system under real operation conditions will experience pressure/temperature change and vibration. Two accelerated fatigue test stands focus on pressure and temperature cycling and vibration will be designed and built, respectively.
5. Tube-to-tube adhesive joint model for stress distribution across the adhesive layer will be developed. The model will be exercised to perform parametric studies and optimize the geometry. In particular, the thermal effect on the stresses will be investigated.
6. Proof-of-concept prototypes will be constructed to demonstrate the application of adhesive joints in commercial HVAC&R systems.

The documentation is organized as follows.

- Chapter 1: Introduces the current joining technologies and challenges in HVAC&R applications to provide the background and motivation for this study.
- Chapter 2: A detailed literature review of adhesive properties, failure mechanism and other critical factors that influence the joint strength.
- Chapter 3: This chapter investigates the surface preparation methods. Traditional surface preparation with mechanical and chemical etching is compared with an innovative laser structuring method. The surface profile and bonding performance under static loading are evaluated for both methods.
- Chapter 4: An extensive analysis of adhesive joint fatigue failure and long-term reliability under vibration and thermal fatigue. The details of the proposed thermal and vibration fatigue test stands are presented, focusing on the failure under dynamic loading condition.

- Chapter 5: An analytical model for stress distributions in adhesively bonded tube-to-tube joints is developed and solved. The model is validated to carry out parametric studies and understand the determining factors of adhesive joint performance.
- Chapter 6: Proof-of-concept tests of adhesive joints are presented with detailed design of a commercial heat pump dryer test stand.
- Chapter 7: The final chapter summarize the main contributions and discusses potential future work

2. LITERATURE REVIEW FOR ADHESIVE PROPERTIES AND FAILURE MECHANISM

There are many advantages of using adhesives in structural joints. Sophisticated designs of structures can be often seen in aerospace, aircraft, automotive, electronics, and HVAC&R applications. Despite great advances in adhesive development and applications, some issues have so far limited their wider application. In this chapter, adhesive joint strength and failure mechanisms are reviewed.

2.1 Adhesive Joint Failure

Massive efforts have been made in finding an appropriate criterion that will define a critical level of stress or strain or energy that causes failure. A number of approaches listed below have been developed or adopted by various researchers for predicting the failure load under static loading conditions for adhesives and adhesively bonded structures.

2.1.1 Material-Strength-Based Models

In predicting failure of common brittle materials like metals, the strength definition for materials is clear and useful. A known strength can be used as a simple and accurate failure criterion. For example, when the material is under tensile loading, the failure happens when the largest normal principal stress reaches the uniaxial tensile strength the material. (Dieter, 1976; Dowling, 1993; ASTM E8/EBM-09, 2009). Similarly, a number of strength-of-materials-based models have been developed to predict the failure load for adhesive joints including:

Average stress method: In this theory, the adhesive joint strength is estimated by the average shear or normal stress in the adhesive layer at the maximum load. For example, in a single lap joint specimen, failure occurring at an applied load P with joint width b and joint length l will have an average shear stress (Adams, 1986):

$$\tau = \frac{P}{bl} \quad (2.1)$$

This method is very simplistic and assumes rigid adherents so that the adhesive only deforms in shear. For single-lap joint tests, failure results from deformation with peel, shear, and strain concentration presents at the ends of adhesive joints.

Maximum stress method: This method compares the maximum stress presented in the adhesive layer with the strength of the adhesive. Failure initiates when the stress value exceeds the strength.

However, there are several complications for this method. First, the yield strength of the material is not defined for an adhesive. For homogeneous metallic materials, such as copper and aluminum, yield strength is a mechanical property of that material and measured by standard test. For adhesive joints, the same tensile test only determines the tensile strength of the joint, not the adhesive. Obviously, the properties of the adhesive and adherent contribute to the overall strength of the joint. It is well established that any change the geometry of the joint will change the strength test result and the stress strain field in the bonding layer (Broughton and Hinopoulos, 1999; Taib et al., 2006). Secondly, not all the adhesive joints have a brittle behavior. If relatively large plastic deformation prior to failure is present, the prediction will be inaccurate. Consequently, although the joint strength can be measured by standard testing, it is not a universal criterion to apply to all adhesive joints.

Maximum strain method: Instead of using stress as criterion, Hart-smith (1973) proposed a maximum strain criterion that argues the joint failure is mainly dependent on the strain. This criterion is widely used in the aerospace industry for determining the strength of metallic and composite joints. It also accounts for the non-linear deformation in the adhesive. However, when used in adhesive joints, this method has similar issues to the aforementioned methods.

2.1.2 Plastic Yield Criteria

The models described in the previous section assume that the adhesive behaves as a linear elastic solid, which is only true for brittle adhesives. However, this is not valid for adhesives that can go through large plastic deformation before failure. In order to simulate the failure status for these adhesives, several models considering the multi-component stress states are proposed, including Tresca yield, von Mises yield, and Drucker-Prager plasticity model (Ward, 1971; Bowden and Dukes, 1972; Young, 1981; Wang and Chalkley, 2000; Dean and Crocker, 2000).

Tresca yield criterion: Tresca proposed the maximum shear stress, τ_{max} , as the yield criterion. Based on different stress states in the joints, the maximum shear stress is calculated and compared it with the critical value. If the principal stress components in the 1-, 2- and 3- orthogonal direction satisfies $\sigma_1 > \sigma_2 > \sigma_3$, the maximum shear stress can be written as (Ward 1971, Young 1981):

$$\tau_{max} = \frac{1}{2}(\sigma_1 - \sigma_3) \quad (2.2)$$

This was initially applied in metal yielding but cannot accurately predict the yield behavior of adhesives under tensile, compressive or shear loads, as yielding in these materials is sensitive to hydrostatic stress. The validity in the case of structural adhesives is questioned (Haward, 1973), because it does not account for the effect of normal stresses. The criterion is then modified for reflect the effect of hydrostatic stress p , which adds hydrostatic pressure (multiplied by a pressure sensitivity μ_t) to the pure shear τ_o .

$$\tau_{max} = \tau_o + \mu_t p \quad (2.3)$$

$$\text{where } p = -\frac{1}{3}(\sigma_1 + \sigma_2 + \sigma_3) \quad (2.4)$$

Von Mises yield criterion: This criterion also considers that failure starts to initiate when the shear strain energy exceeds a critical value, which is restricted by the following symmetric relationship (Young 1981):

$$(\sigma_1 - \sigma_2)^2 + (\sigma_2 - \sigma_3)^2 + (\sigma_3 - \sigma_1)^2 = const \quad (2.5)$$

where *const* is some constant value.

Similar to the Tresca yield criterion, the original equation cannot be used directly in adhesive failure analysis since it does not account the effect of hydrostatic pressure. Modification has been made to account for the hydrostatic pressure:

$$\tau_{max, vonMises} = \tau_m^o + \mu_m p \quad (2.6)$$

where τ_m^o is the yield stress in pure shear and μ_m is pressure sensitivity that can be calculated by two different stress states. $\tau_{max, vonMises}$ is the von Mises yield stress and which is defined by:

$$(\sigma_1 - \sigma_2)^2 + (\sigma_2 - \sigma_3)^2 + (\sigma_3 - \sigma_1)^2 = 6\tau_m^2 \quad (2.7)$$

As reported by Wang and Chalkley (2000), when investigating the yield behavior of metals, the von Mises criterion is used more often than the Tresca criterion because it is found to offer a better agreement with experimental results. However, both the modified Tresca and the modified von Mises criteria can only correlate data with positive hydrostatic stress and tend to be un-conservative when hydrostatic is compressive, according to comparison against the experimental data.

2.1.3 Fracture Mechanics

Theories from fracture mechanics have been applied in adhesive failure prediction. The concept of fracture in materials deals with two general questions: the separation of a material from itself (cohesive fracture) and the separation of a material from a dissimilar material at the bonding surface between the two materials (adhesive fracture). Williams (1966) firstly elucidated the similarity of adhesive and cohesive fracture from a continuum mechanics viewpoint, in particular the energy concept of fracture.

Griffith (1921) first used an energy balance between strain energy released and the increase in surface energy with crack growth in predicting the fracture initiation for a central finite length crack in an infinite elastic sheet subjected to tension. Griffith's work was largely ignored by the engineering community until the early 1950s since it is only valid for brittle materials like glass. Irwin (1957) and Orowan (1949) modified Griffith's calculation to apply the energy balance to materials that undergo plastic deformation before fracture by including plastic work. An important concept of stress intensity factor was then proposed to describe the stress status of a sharp-tipped crack. The stress intensity was a function of the distance from the crack tip. Sih (1973) applied this to a wide range of crack configurations and it is convenient for mathematical analysis of the stress field. The stress intensity factor is equivalent to the early Griffith's energy balance concept but calculates the stress distribution. A more direct development of Griffith's idea became another important approach in fracture mechanics: the energy release rate approach. The applied energy release rate is the amount of the energy per unit crack area available to growing a crack by the applied loading conditions. The energy release approach can be shown to be equivalent to the stress intensity factor (Broek, 1978).

Lots of effort has been put into applying fracture mechanics to predict crack growth and failure of adhesive joints. Research has been done on the stress distribution and fracture prediction

of adhesively bonded joints using fracture mechanics. (Groth, 1985, 1999; Fernlund and Spelt, 1991, 1994) Ashcroft, Gilmore and Shaw (1996) explored the cyclic fatigue of adhesively bonded joints and found good correlation of energy release rate with the joints failure.

2.1.4 Fatigue Failure Modeling

Fatigue is an important loading condition for adhesives that can cause failure to happen at a small percentage of the static strength. For any structural joints under fatigue loading, failure prediction is required for safety. However, accurate modeling of fatigue failure is very challenging, especially when loading and unloading exists.

Early fatigue research on adhesive followed the stress-life approach, which is widely used in metal fatigue analysis and is an experimental-based approach. A series of tests under various loading conditions are performed to achieve the data for stress and the number of cycles to failure, which is known as S-N curve or Wohler's curve (Abdel Wahab, 2012). In the ideal case, there will be a fatigue threshold under which the joints will have an infinite lifetime. However, various research has shown this is not the case for adhesive joints and the threshold is effected by different factors (Zhang, 2008; Tenchev and Falzon, 2008; He 2011, Abdel Wahab, 2012; Jen, 2012). Because performing exhaustive experimentation on every different possible joint is very time consuming, finite element analysis (FEA) came into play for fatigue failure prediction. The fatigue modeling of adhesive joints still needs a significant research effort to understand the failure mechanism and all the influencing factors.

In the past research, most modeling work makes modifications to the FEA adhesive joint models based on static loading. The first approach is to utilize FEA to obtain the stress states of the joints and correlate the stress with the fatigue life data. A significant amount of research has been done to understand the determining factor of the stress and fatigue: Jen and Ko (2010) studied the effect of the bonding dimension on the fatigue strength; Bernasconi (2010) used different overlap length, shape, and material to investigate the peak elastic stress and fatigue life with 2D FEA. Similar approaches have been used quite often by others as well (Bachir Bouiadjra et al. 2007, Wang et al., 2005, Datla, 2010). Another popular approach in modeling is damage mechanics using FEA and the cohesive zone model (CZM) and considering the energy (He, 2011; Shenoy et al., 2010; Wahab 2010; Fessel et al., 2009; Ishii et al., 2007).

2.1.5 Summary of Failure Criteria

Among the three major failure criteria reviewed in this section, fracture mechanics is selected for further investigation due to the inevitable issues associated with the other two approaches. For material-strength-based models, adhesive joint strength is not material property as it is for metallic materials because the adhesive, adherent, and geometry collectively determine the adhesive joints strength. For plastic yield criteria, they lack accuracy when compressive hydrostatic pressure exists and show invalidity when compared against experimental data. In the recent studies for adhesive failure modeling using fracture mechanics, good correlations are observed between strain energy release rate (fracture energy) and joint fracture. The adhesive properties, especially fracture energy, will be introduced in the next section.

2.2 Properties of Adhesives

A number of physically relevant and important properties determine the curing of the adhesive and the bonding performance. For a typical adhesive material, physical properties including viscosity, density, fracture energy, stress-strain curve are often considered as intrinsic properties of the material. Methods of characterizing these properties are described in this section, along with interpretation and implications for adhesive joining system.

2.2.1 Density

Density is a common and important physical property of interest, which is defined as mass divided by the volume. Specific density is the reciprocal of the density and relative density is the ratio of the density of the material to that of a reference material. Density typically decreases with increasing temperature and increases with pressure.

There are several methods of measuring the density. The most common is direct measurement: the mass of a regular shaped object is measured and the volume is calculated from the geometry of the object. It can be applied to most of the liquid adhesive by determining the mass of a liquid use to fill a known-volume container. For those solid-state adhesives, indirect method of volume displacement technology by immersion of an object of interest into a known fluid is commonly used. The volume can be measured by the rise of the liquid in a regular shape container or the effluent from a container filled to the brim.

Although unlikely to be the determining factor in adhesive selection, density is an important indicator of the nature of a polymer, including chemical family, morphology, and filler or void content. In this study, when comparing the adhesive joints with brazed joints in HVAC&R systems, the mass/density of the joining material is important since lighter products are usually desired for most of the residential and commercial applications. The densities of the evaluated adhesives are provided by the adhesive manufacture.

2.2.2 Viscosity

Viscosity is a very important property of adhesives, especially in the manufacturing process for liquid uncured adhesives. The mixing, pumping, and dispensing processes are highly influenced by the adhesive viscosity, especially for the automated dispensing system with complicated flow paths. It is also a very basic property of the adhesive that provides insights into the chemical components, time, and temperature dependence. Changes in viscosity can be reflective of formulation, processing, and aging of the adhesive. Note that viscosity is not defined by for solid-state materials.

Newton observed the resistance to deformation of a fluid is proportional to the rate of change of deformation (Macosko, 1994). Viscosity is a measure of the internal resistance to flow or deformation for a fluid, which is defined as the ratio between the shear stress and the shear strain rate. There are two types of fluid that are commonly encountered in adhesives: Newtonian fluid and non-Newtonian fluid. A Newtonian fluid is a fluid in which the viscous stresses arising from flow, at every point, are linearly proportional to the local strain rate (Panton 2013). A non-Newtonian fluid will not follow the linear relationship. For formulated adhesives, many of them are non-Newtonian fluids and have more complex behavior since they often have high solids content, contain fillers and flow controllers, or contain high molecular weight metals. Non-Newtonian fluid viscosity is usually shear-rate-dependent, which can be important in the mixing and applying process. Viscosity is usually physically measured in a number of ways using viscometers or rheometers. In this study, the viscosity measured and reported by the manufacture is used.

2.2.3 Stress-Strain Behavior

Properties such as the viscosity are important for liquid-state adhesives that usually are uncured or partially cured. For cured solid-state adhesive, one of the most important properties is the stress-strain behavior. Tests need to be conducted to understand and characterize materials with very large Deborah numbers, where the time scale of the test is short compared to any relaxation times within the material (Da Silva & Ochsner, 2011).

The stress-strain behavior for adhesives can provide important information such as the force at different displacements and range of applicability. Some applications may desire a certain displacement under loading, such as sealants. The modulus must be sufficiently low and the strain capabilities sufficiently high under the mechanical or thermal deformation so that the adhesive can provide enough flexibility. In other applications, very stiff with high modulus may be required such as bearings and structural parts. Due to ease, the screw-driven test frame with constant crosshead displacement rate was historically the most common approach for stress-strain measurement. For adhesives, care is needed to consider the rate and temperature effect on the testing result.

As previously discussed in Section 2.1, the stress-strain curve is also influenced by the specimen configurations, which depends on the properties desired, the nature of the material, and the available equipment. The simplest and most common loading condition is uniaxial tension. Shear and peel loading conditions are also very important, depending on the applications. Based on the stress-strain behavior, a number of metrics can be assessed (Dowling 2007), such as modulus, yield stress, yield strain, ultimate strength, and strain at break. Note that for adhesives, these are not material properties because multiple factors such as the specimen geometry, curing procedure, and test conditions can change the values.

In this study, a single-lap joint specimen configuration will be used and the details will be introduced in the experimental setup in section 2.4.3.

2.2.4 Fracture Energy

In material science, fracture energy, also known as critical strain energy release rate, is a property that describes the ability of a material to resist fracture. It is one of the most important properties of any material for determining the application and safety range of operation. As a

material property, it is considered independent of the applied loads and the geometry of the body. As previously introduced in Section 2.1.3, fracture energy is a concept based on the energy criteria of failure, which is a well-established approach in fracture mechanics. Adhesive fracture energy is defined as the amount of energy per unit of new surface created on separation of dissimilar materials (Bennett et al., 1974). When the energy release rate of the adhesive is over the critical energy release rate (fracture energy), the crack will propagate.

The application of fracture mechanics to adhesive joints traces back to the 1960s, when Ripling and co-workers (Ripling et al., 1964; Mostovoy et al., 1967) developed a mode I test method to measure the toughness of structural bonds for metals. Their work then resulted in the publication of an ASTM standard in 1975 (ASTM, 1975). Since then, many efforts and developments from various researchers advanced the measurement technique and understanding of the adhesive fracture mechanics. Different sample geometries and specific tests with different procedures were proposed to measure the fracture toughness value for different loading modes. For mode I fracture energy characterization, extensive studies have been done by several researchers with good results (ESIS, 1997; Nairn, 2000; Ducept, 2000). However, for mode II loading conditions, the test procedure and geometry are still not well addressed (Blackman, 2005; Schuecker and Davidson, 2000; Leffer et al., 2007). As one of the most important properties, adhesive fracture energy is critical from failure prediction and modeling perspectives. Usually for modeling purposes, the value of the fracture energy will be provided by the manufacture or fitted from the experimental results.

2.2.5 Cohesive Zone Model

The cohesive zone model (CZM) is one of the tools to model the material failure, especially considering plastic zone and stress distribution ahead of the crack tip. Barenblatt (1959) proposed the idea of using a cohesive zone ahead of the crack tip to remove the stress singularity. Dugdale (1960) further assumed that there existed a yield-strength-dependent process zone at the crack tip. The cohesive zone model describes fracture as a material separation process along the interface. Originally, it was used to model concrete composites and interface fracture. With the development of the application of polymer-based composites and adhesive joints, it is widely used to model the adhesive failure.

The basic principle of the cohesive zone model is to describe material separation by using a traction-separation law at the process zone. A schematic figure of a typical CZM traction separation law is shown in Figure 2.1. Five important model parameters define the traction separation behavior: maximum stress σ_{max} and initial displacement δ_0 , failure displacement δ_f , fracture toughness G and penalty stiffness k . When a material follows the traction separation law under a loading condition, stress and strain will increase following the path OA with a slope of k . The crack initiation starts at point A when the stress reaching σ_{max} . The material then goes through a softening process along path AB. Note that the traction separation law may have different shapes: (1) exponential (Barenblatt, 1962), as shown in Figure 2.2(a); (2) polynomial (Needleman, 1987), as shown in Figure 2.2 (b); (3) constant (Dugdale, 1960), as shown in Figure 2.2 (c); (4) tri-linear (Tvergaard & Hutchinson, 1992) as shown in Figure 2.2 (d); (5) linear (Camacho & Ortiz, 1996), as shown in Figure 2.2 (e); and (6) bi-linear (Geubelle & Baylor, 1998), as shown in Figure 2.2 (f).

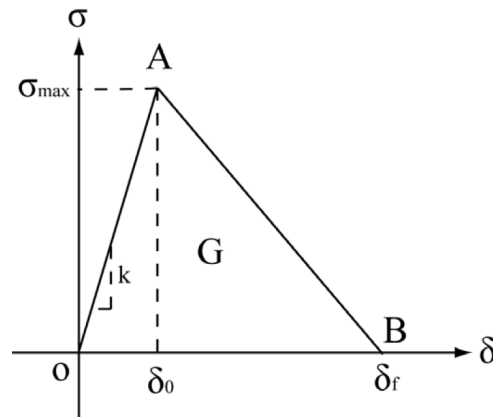


Figure 2.1 Schematic figure of a typical CZM traction separation law

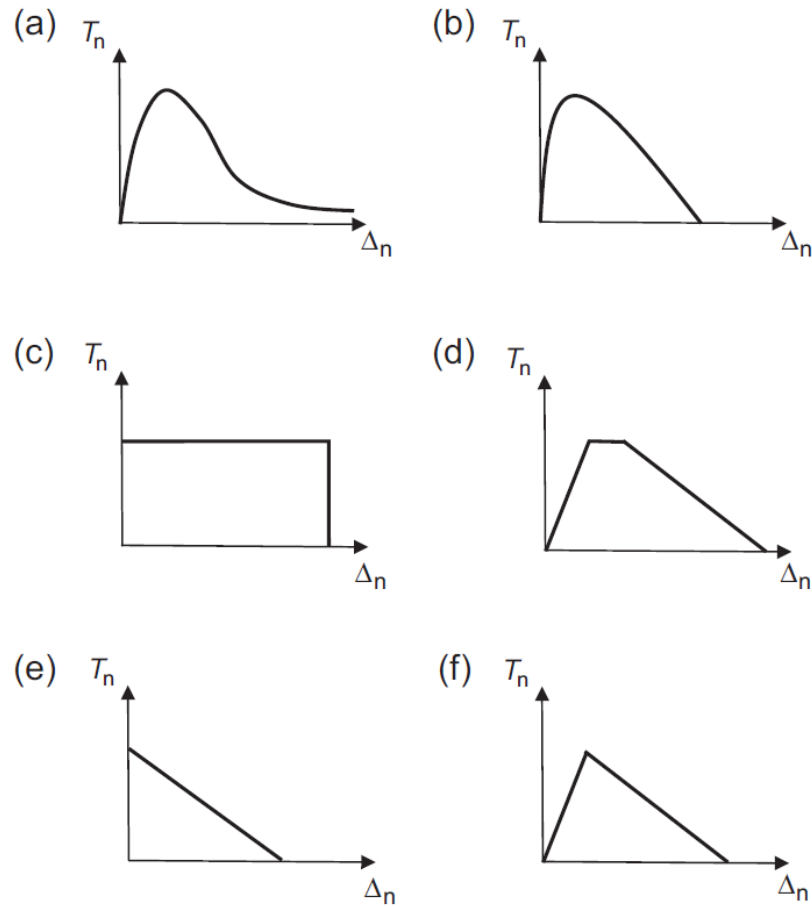


Figure 2.2 Different shapes of the cohesive traction separation law: (a) exponential (Barenblatt, 1962), (b) polynomial (Needleman, 1987), (c) constant (Dugdale, 1960), (d) tri-linear (Tvergaard & Hutchinson, 1992), (e) linear (Camacho & Ortiz, 1996) and (f) bi-linear (Geubelle & Baylor, 1998).

Applying the traction separation law removes the stress singularity at the process zone. An important development was made by Needleman (1987, 1990a, 1990b) and Xu and Needleman (1994) and they proposed that CZM can be used as cohesive elements and forming new surfaces without defining an initial crack. They related the traction and the material separation between the new surfaces. Since then, lots of effort has been put into understanding the physical process of crack growth applying the principle of local constitutive cohesion to predict fracture, failure, and crack growth. The development of numerical analyses also plays an important role in cohesive zone modeling since it is easily embedded with finite element method. A special element called cohesive zone element is introduced in FEM to form the interface between the continuum elements, which represents the adhesive. With this implementation, the cohesive surface connecting the top

and bottom surfaces of the adjoining material can be used to describe the cracks, interaction between the material, and surface separation. The process of failure initiation and propagation is characterized by the cohesive zone model defined by the constitutive law. Generally, the connection is defined by an interface constraint or sharing common nodes for both elements. During simulation, the adhesive material as cohesive element will hold the surfaces together with the force increasing as described by the surface separation law. Once critical value is reached, the crack will initiate and follow the curve until complete failure.

As a powerful tool to simulate and model the failure and crack along the interface, much research has been performed. One early and key issue is how to determine the cohesive zone parameters. At early stages, researchers assumed that the parameters can be determined based on which values give the best results compared with the experimental results. It requires a good estimation and large amount of experience to propose the correct value to fit into the model initially. With a massive number of experiments and data, later researchers proposed some certain tests that could determine these parameters such as double cantilever beam (DCB) or end-notched-flexure (ENF) testing, but needed to verify the results with tests of bulk materials (Yang, Thouless et al. 2001). Other researchers then applied a similar approach and achieved good results (Andersen and Stigh 2004). Liljedahl and Crocombe et al. (2006) determined the initial traction stress using the load displacement curve of the mixed-mode flexure (MMF) specimens and calculated the fracture energy used in the cohesive zone model under the criteria that the predicted failure load should match the experimental data. Blackman, Dear et al. (2003) used the cohesive zone model to simulate the fracture of adhesively bonded joints and compared with the analytical solutions to explore the implementation of maximum stress. There is also evidence showing that the detailed shape of the traction separation curve is less important than the values of fracture energy and maximum stress for accurate simulation. (Williams and Hadavinia, 2002)

2.3 Surface Preparation in Adhesive Bonding

Obtaining a strong adhesive bond requires various considerations. Wegman and Levi (1985) described several key steps of adhesive bonding that are summarized here: receiving materials, knowledge of the fabrication process for the parts, mating the parts to be bonded, and surface preparation. Among all these steps, surface preparation is usually the most critical, complex, and frequently neglected in the bonding sequence. Surface preparation can remove the intermediate

surface, paint, rust, or oxide layers. Different materials including adherents, adhesives, and chemicals require different surface preparation techniques, but in general, the surface preparation needs to consider the cleanliness, roughness, and functionality of the surface.

2.3.1 Traditional Surface Preparation Methods

Numerous different surfaces preparation techniques have been proposed and used in industry. Based on the mechanism of the techniques, they can be divided to two types: mechanical surface preparation and chemical surface preparation.

Mechanical surface preparations are generally for cleaning purposes. Physical contact with the surface is used to clean the prepared surfaces of grease, oil, dirt, rust, paint and other contaminants. The main techniques include wire brushing, sanding, and abrasive blasting. There are standards for surface preparation before application of coatings using mechanical techniques - refer to the standards: SSPC-SP2/3/11/15, ISO 8501 and ASTM D7803 (Ebnesajjad 2011; ASTM 2019).

Some typical mechanical preparation methods are summarized as follows:

Wire brushing: A wire brush tool consists of bristles most often made of steel wire. The steel used is generally a medium- to high-carbon variety and very hard and springy. Wire brushing can be performed using a hand tool with a handle or can be formed into a wheel or some other tool

Sanding: Sanding is usually used on non-porous surfaces to thoroughly abrade the surface. It can be done by hand or by power tools. For different applications, the sanding particle sizes and roughness can be different.

Abrasive blasting: Abrasive blasting is a more effective way to clean the surface with high-pressure sand, grit, or liquids. The blasting can remove the solid surface dust but also soluble corrosion products. One example is vapor honing. Vapor honing is satisfactory when minimum reduction is desired in metal thickness. In this method, powered abrasive material is propelled by high velocity water or are steam against the surface.

Chemical surface preparations are very widely used prior to adhesive bonding. The chemical preparations not only clean the surface but also provide some desired functional surface conditions (such as to ensure wetting of the surface by the adhesive). Chemical surface preparations usually have more complicated processes compared to mechanical preparation and careful handling of the chemicals is required. The main techniques include plasma treatment and chemical etching.

Some typical chemical preparation methods are summarized as following.

Plasma surface treatment: The most popular plasma treatment is air plasma, also known as Corona treatment. It is a surface modification technique that uses a low temperature corona discharge plasma to impart changes in the properties of a surface. Another more effective alternative way of plasma surface treatment is atmospheric pressure (air) plasma (APP). APP has a much greater plasma density and it is one of the most effective surface treatment process for cleaning, activating or coating (Gilbertson, 2001). APP also increases surface energy levels achieving complete wettability.

Chemical Etching: Chemical etching is traditionally the process of using strong acid or mordant to cut into the unprotected parts of a metal surface. Etching as a surface treatment immerses a metal substrate in an aqueous acid solution. The purpose of etching is to clean the surface, especially the loose layer of oxide. The material, the type of oxide, and adhesive needs to be carefully considered to choose the proper acid.

2.3.2 Surface Preparation Procedure

Aluminum and Aluminum Alloy Surfaces:

The standard industry practice of surface preparation for adhesive bonding used to be the Forest Products Laboratory etching, commonly referred to as FPL etch (Eickner and Schowalter, 1950). However, this method uses chromates and dichromates that are no longer allowed in many countries (Chen et al., 1977). There are many other methods modified from the FPL etch, such as the optimized FPL etch, the phosphoric acid anodizing (PAA) process, the P and P2 etchants, and the chromic acid anodize procedures (ASTM, 2651; ASTM, D3933; Wegman and Twisk, 2013). Different materials, chemicals, and equipment are used in these methods, but the general processes and purposes are quite similar. A summary of the main steps of these methods is degreasing, alkaline cleaning, etching (deoxidation), rinsing and drying.

Copper and Copper Alloy Surfaces:

Copper, brass (alloy with zinc) and bronze (alloy with tin) are very common materials in heat exchangers and they can be used for high performance adhesive bonding. Copper has a tendency of forming brittle amine components with curing agents from some adhesive systems. The most common and successful surface treatment is black oxide, which is especially recommend when the adhesive is corrosive to copper. Note that this method is mainly for relatively pure copper

alloys containing more than 95% copper (Wegman and Levi, 1985). The procedure is given as following degrease, immerse in etching solution, rinse and immerse in to stabilization bath, rinse again and air dry.

Other methods for copper bonding including nitric acid etching, etc. (Ebnesajjad, 2011). For brass, sandblasting or other mechanical means can be used; the flowing procedure is one example that combines both mechanical and chemical methods (Rogers, 1966); other methods are also available (Ebnesajjad, 2011). Note that the methods given above are also viable for bronze.

1. Mechanical blast (particle size is not especially critical).
2. Rinse with deionized water
3. Treat with a 5% solution of sodium dichromate in deionized water
4. Rinse in deionized water and dry

2.3.3 Surface Preparation Summary

Traditional surface preparation methods using mechanical and chemical etching have been well studied and used for copper, aluminum and their alloys for decades. Many different procedures have been proposed and succeed in providing a clean surface for bonding. However, these procedures are not only relatively complicated involving both mechanical and chemical process, but also dangerous with toxic or flammable chemical material involved. The cost for human labor, safety and environmental issues can be a major concern for manufacturers.

3. ADHESIVE BONDING OF COPPER PREPARED BY LASER-INTERFERENCE NEAR THE INTERFERENCE STRUCTURING LIMITS

In this chapter, a detailed investigation was carried out on a novel alternative surface preparation technology, small-periodicity laser interference structuring, with an experimental study including surface and joint strength characterization. Adhesive bonding requires adequate surface preparation for ensuring an appropriate joint quality. The interest in adhesive joining has recently expanded to thermal systems having a large number of joints employed for manufacturing and assembly. This study presents surface topology of copper 110 produced by a laser-interference setup that would theoretically yield a periodicity of $1.7 \mu\text{m}$, which is near the $1.6\text{-}2 \mu\text{m}$ structuring limit that was estimated based on thermal diffusion length scale for an 8 ns laser pulse. The results show that although the expected periodic interference structuring was not attained, the melt-induced texturing was affected by the laser-interference profile. Single-lap shear tests are performed with specimen surfaces prepared by traditional abrasion and laser interference structuring methods. Several laser processing parameters, such as the laser spot size, density, number of pulses, and raster speed were studied. Scanning electron microscope and profilometry measurements were used to characterize the processed surface microstructures. Web-like structures, which indicate widespread melting, were shown to be formed at different processing conditions. Based on the surface topologies investigated, two laser raster speeds were selected to make single-lap-joint specimens. Baseline joints were prepared by abrading joining specimens. The shear-lap strength and displacement at maximum load were shown to be higher by 16.8% and 43.8% for the laser-structured specimens than those of the baseline specimens, respectively. Moreover, the load-displacement curves indicate that the laser-structured joints are more ductile than those without laser-structuring. The increase ductility for the laser-structured joints was found to yield an increase in the energy absorbed during shear-lap testing of approximately of 80-90% over those measured for baseline joints. It is another indicator that laser-interference structuring enhanced the bonding performance of single-lap shear joints.

3.1 Background

Adhesive joining is an attractive technology that has been widely adopted in automotive and aerospace industries. Recently, there is an increasing need for alternative joining technology for component and system manufacturing in the HVAC&R (heating, ventilation, air conditioning and refrigeration) industry. For HVAC&R industry, adhesive joining has potential energy and cost savings benefits, especially if the mechanical properties of the adhesive joints would be similar or better than those of traditional brazed joints (Ebnesajjad and Landrock, 2015). For the components and tubes in HVAC&R systems, copper and its alloys are the most common materials. However, Cu reacts with the atmospheric oxygen and form an oxide surface layer. The oxide layer, together with oils and other contaminants on the surface, reduces the surface energy and bonding strength (Ebnesajjad and Landrock, 2015; Wong et al. 1997). Thus, especially for Cu, surface preparation for joining is necessary and critical to ensure the bond quality and performance. The most common surface preparation techniques employed in industry include chemical and mechanical methods. Chemical methods (Ebnesajjad and Landrock, 2015; Ebnesajjad 2011) usually involve chemical etching or cleaning with solvents, which are toxic or flammable, such as strong acids, acetone, or isopropyl alcohol (IPA). Mechanical methods usually involve sanding, blasting, or brushing. These traditional methods are labor intensive and costly to ensure quality control, environmental protection, and management of the hazardous materials (Ebnesajjad, 2011).

In recent decades, with the development of laser technologies, new surface preparation techniques using high-energy lasers have attracted research interest. Compared with traditional methods, laser processing is a single-step and non-contact method. Laser processing has been shown to achieve surface cleaning and structuring. Previous research has studied the laser surface preparation of various materials with different laser types, energy levels, and optical setups. Neddersen et al. (1993) showed that for the activity of surface-enhanced Raman scattering colloids, laser ablation was comparable or superior to that of chemical preparation. The surface morphologies produced by laser processing have been studied for different materials, such as Cu alloys, Al alloys, Ti alloys, carbon fiber polymer composites (CFPC) using different laser processing methods and parameters (Baburaj et al., 2007; Pinto et al., 2003; Watkins, McMahon and Steven, 1997; Chérif et al., 2016; Benard et al., 2009).

The bonding performance enhancement by laser surface preparation has also been studied for Al alloys, Ti alloys, and polymers, and it was shown that laser structuring could increase the

bonding performance (Wong et al., 1997, Chérif et al., 2016; Benard et al., 2009). Baburaj et al. (2007) studied a laser ablation process that generates micro-columnar arrays and increases the adhesive bonding strength between plates by several mechanisms. Three reasons that were found for bond strength improvement: increase in bonding surface area, mechanical locking of adhesive between micro-columns, and modifications in surface chemistry of the adherent that improved the surface wettability. Romoli et al. (2017) studied the influence of surface laser texturing on adhesive strength using cylindrical specimens of aluminum alloys and showed an improvement of nearly 30% with respect to those of non-treated specimens. Hernandez et al. (2016) analyzed the effect of pulsed laser ablation on copper substrates for adhesive bonding by using scanning electron microscopy (SEM), X-ray photoelectron spectroscopy (XPS), and finite element simulations. Results indicated that the laser ablation modifies surface morphology and chemistry, enabling enhanced mechanical interlocking.

This paper explores use of the laser-interference structuring technique (Lasagni et al., 2007; Daniel et al., 2003; D'Alessandria et al., 2008) of copper for joining of HVAC components. Sabau and Greer et al. (2016) and Sabau and Chen et al. (2016) characterized the surface morphology and structures produce by different laser fluence using Al alloy, CFPC and conducted single-lap shear testing. It was concluded the laser interference technique yielded periodic structuring on the surfaces with a significant increase in the bonding strength. A similar bonding enhancement effect was also noted for laser-interference structuring of AlMg3 and Ti6Al4V with woven hybrid yarn composites of glass fiber/polypropylene (Schiefer et al., 2015). Compared to simple one-single beam laser ablation, the laser-interference technique creates periodic arrays on metallic surfaces in a size range from sub-micrometer to micrometers (Lasagni et al., 2007; Daniel et al., 2003; D'Alessandria et al., 2008). Laser-interference techniques split the main laser beam into two (or more) beams, and then guide the separate laser beams back to the targeted area using optical components. When the laser beam hits the metal surface, the dominating free-electron cloud on the surface will quickly transfer the electromagnetic wave into phonons. The subsequent photothermal effect creates a surface heat treatment with a designed spatial power distribution, with hot and cold spots along the surface according to the wave interference. Based on the designed interference, different patterns can be achieved such as dot-, line- and ring-shaped microstructures. The first laser-interference structures were reported by Birnbaum in 1965, who used ruby lasers to produce regular patterns on semi-conductors. While initial studies were focused on the proof-of-

principle of laser-interference structuring employing a spot-by-spot technique, i.e., firing several laser pulses while the laser beams were held focused on the same spot, more recent studies employed a raster technique, in which the laser spot moves at a constant speed as the laser is on.

After the description of the experimental setup and procedures for laser interference surface preparation of copper, the surface profile using SEM and profilometry is presented. Adhesive joining is then presented. Single-lap shear tests were performed. The bonding performance of laser-structured surfaces was tested, analyzed, and compared to an abrasion-based surface preparation method, which is considered as a baseline for the current state-of-the-art.

3.2 Materials, Surface Preparation, and Characterization

Copper 110 was selected as it is commonly used in the HVAC industry. All of the specimens were cut from the same batch of material, without any additional surface preparation or cleaning prior to the laser processing step. The specimens were cut in equal sizes of 101.6 mm (4 in.) by 25.4 mm (1 in.), as required for the single-lap shear testing.

3.2.1 Laser Interference Technique and Target Surface Topology

A 10-Hz Q-switched Nd:YAG laser (Quanta-Ray PRO230; Spectra Physics) was used as the laser source (Meyer and Sabau, 2007; Lasagni et al., 2007). The laser pulse duration is very short (8-10 ns), and at an average power of 3.5 W, yields a peak power of 350 MW, resulting in very high heating and cooling rates. The laser pulse fluence (pulse energy per unit area) was increased by using two identical focal lenses in each path of the beams to focus them to either 4 mm or 5 mm spot size from its original beam size of 8 mm (Sabau et al., 2016; Lasagni et al., 2007). The emission wavelength of 1064 nm was transformed to 355 nm using non-linear crystals, decreasing the pulse duration to 8 ns. The number of pulses were selected using a mechanical shutter. The laser interference power profile was created by splitting the beam and guiding those split beams to the sample surface by overlapping them with pre-defined angles with respect to each other (Figure 3.1). The coherent beams create an interference pattern instead of just adding their intensity. This allows a microscopic modulation and creates a light pattern without loss of energy during the interference process. The periodicity between power peaks, and laser-interference-induced undulations, is defined by the wavelength, λ , and the angle, α , between the two beams, as $d = \lambda/2(\sin$

$\alpha/2$). A short review on physical phenomena that yield laser-interference structuring is provided in the next paragraph to better understand the surface preparation considered in this study.

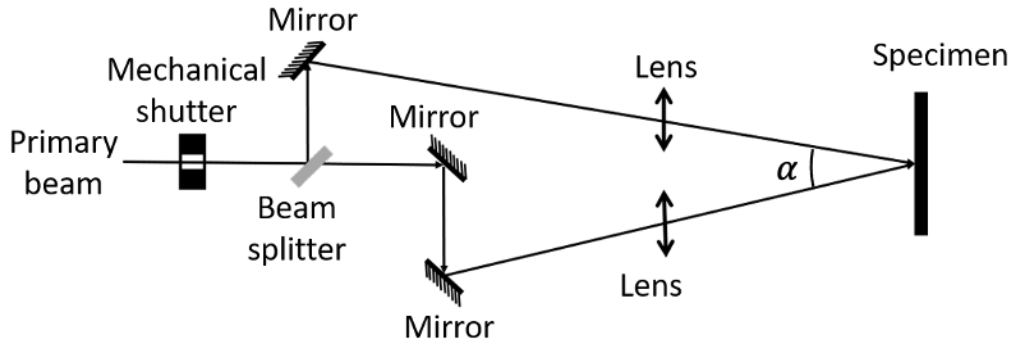


Figure 3.1. Schematic diagram of the laser interference system. An angle between the beams of $\alpha = 12^\circ$ is used in this study.

When the laser reaches the rough surface of the metal, multiple reflections due to the roughness increases the absorption coefficient. Absorbed photons are instantaneously transformed into heat, which causes a temperature rise in the metal. If the temperature of the metal exceeds its melting point or saturation temperature at environmental pressure, the metal will melt or evaporate, respectively, and induce surface structuring (Sabau et al., 2016). Lasagni et al., (2007) studied laser interference structuring of metals using steel, Cu, and Al by both simulation and experiment. Numerical simulations were conducted considering the energy required for melting and vaporization. Three critical parameters were identified that govern the type of surface morphology based on the power interference distribution on the metal surface: (1) the thermal diffusion length; (2) the thermal gradient from maximum to minimum power distribution; and (3) the surface flow of the molten metal. It was concluded that thermal gradient between the maxima and minima interference induced the surface tension gradient and flow in the molten metal. The surface structure was produced by the molten metal flow (Daniel et al., 2003)

3.2.2 Process Parameters for Laser Surface Preparation

In order to study the effects of laser interference structuring on copper 110, several different processing methods and parameters were controlled. There were two different processing methods explored: spot-by-spot and laser raster. The spot-by-spot method uses the mechanical shutter along

with a moving platform. The shutter opens and closes to control the number of pulses fired that hit on the same location of the surface. After one spot is finished, the platform that holds the specimen moves to the next spot and repeats the laser structure, eventually processing the whole area. For the same spot, a higher number of pulses results in a higher input energy and may cause a different surface profile. The spot-by-spot method provides a precise control over the number of laser pulses for each spot. For the laser raster method, the mechanical shutter stays open the entire time while the specimen is moved by the platform. There is no separately processed spot, but rather a continuously processed region. The raster speed determines the energy applied on the surface. A slower raster speed results in a higher input energy per area. Comparing the two methods, the main difference is whether the laser is moving on the surface. The spot-by-spot method therefore has an inherently slower processing speed compared to the raster method.

In this work, two laser fluences of $F_I = 1.782$ and 2.785 J/cm^2 per pulse were used by varying the laser spot size ($d_b = 5$ and 4 mm , respectively) while keeping the same average power of 3.5 W . In the experiments, 2, 4, 6, 8, 10, and 12 pulses per spot were used for the spot-by-spot method and 2, 4, 6, 8, 10, and 12 mm/s raster speeds were used for the laser raster method. Another crucial parameter is the laser spot size, which determines the energy density of each pulse on the surface. Based on the melting point of the copper and the absorbance of the surface, 4 mm and 5 mm spot sizes were selected for the spot-by-spot method (Meyer and Sabau, 2019). For the laser raster method, only a 5 mm spot size was used, based on the results acquired for the spot-by-spot processing method. The beam angle was 12° , for an optical theoretical periodicity of the structuring of $\sim 1.7 \mu\text{m}$.

To understand the effect of the rastering speed, U , of the laser beam on the energy deposited on the specimen surface, two process variables were introduced: (a) the number of equivalent pulses, N_P , and (b) the accumulated fluence on specimen surface, F_A . N_P represents the number of pulses that a local area is exposed, $N_{EP}(U) = \frac{d_b f_I}{U}$. F_A represents the total incident laser energy that a local area would be exposed from the total N_P pulses striking it as the laser beam is scanned over it, as $F_A = N_P F_I$, where the fluence of each shot is F_I . The specimen labels, number of equivalent pulses, N_{EP} , and the accumulated fluence on specimen surface, F_A , are given in Table 3.1 and Table 3.2 for all of the laser structuring conditions considered in this study. As the raster speed is increased, the surface is exposed to a smaller number of shots and smaller accumulated fluences.

Among all of these various processing methods and parameters, there were 18 different processing conditions. For each condition, two different specimens were processed resulting a total of 36 processed specimens. The detailed process parameters with specimen labels are shown in Table 3.1 and Table 3.2 for the spot-by-spot and raster methods, respectively.

Table 3.1. Laser processing parameters using for the *spot-by-spot* method (average power 3.5 W).

Case No.	Spot size (mm)	Number of pulses per spot, N_P	F_A [J/cm ²]	Figure
1	4	2	5.570	5 (a)
2	4	4	11.14	5 (b)
3	4	6	16.71	5 (c)
4	4	8	22.28	5 (d)
5	4	10	27.85	5 (e)
6	4	12	33.42	5 (f)
7	5	2	3.56	6 (a)
8	5	4	7.13	6 (b)
9	5	6	10.69	6 (c)
10	5	8	14.25	6 (d)
11	5	10	17.82	6 (e)
12	5	12	21.38	6 (f)

* $F_A = N_P \cdot F_I$ for spot-by-spot

Table 3.2. Laser processing parameters for the *laser raster* method (average power 3.5 W).

Case No.	Spot size (mm)	Raster speed (mm/s)	N_{EP}	F_A [J/cm ²]	Figure
13	5	2	26	44.55	7 (a)
14	5	4	13	22.28	7 (b)
15	5	6	8	14.85	7 (c)
16	5	8	6	11.14	7 (d)
17	5	10	5	8.91	7 (e)
18	5	12	4	7.42	7 (f)

As shown from the images of the processed samples in Figure 3.2, the processed area has a visibly different reflective color and roughness compared to the original surface. The edge of each spot can be clearly identified. Note that the edges of the spots overlap by design in order to eliminate unprocessed areas between the spots. Compared to the 5 mm spots, which blend together in color over the processed area, the 4 mm spot edges had changed to a dark color, even for the lowest two pulses per spot. This indicates that the energy per pulse is sufficiently high that the Cu reacted with the oxygen in the air while processing. This became more obvious with higher number of pulses per spot. This indicates that the energy density for the 4 mm spot size was too high, and subsequent surface structuring using the laser raster method only considered 5 mm spot sizes.

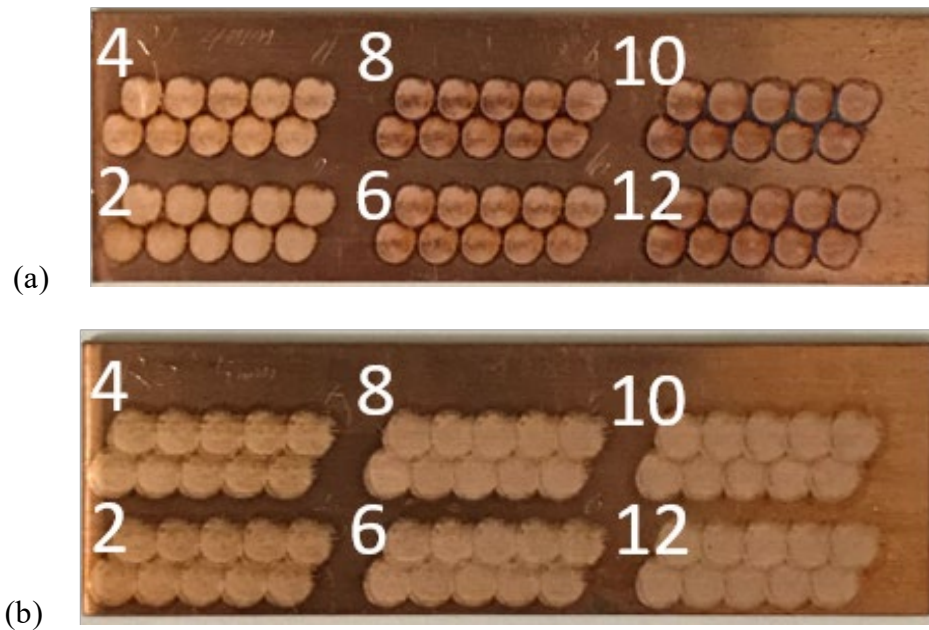


Figure 3.2. Photographs of the laser-processed area on copper using the spot-by-spot method with laser spot sizes of: (a) 4 mm and (b) 5 mm. The photos were taken immediately after processing. The label numbers correspond to conditions shown in Table 3.1.

3.2.3 Analysis of Surface Topology Periodicity Induced by Laser-Interference

The theoretical optical periodicity value of $1.7 \mu\text{m}$ is slightly lower than that of $\sim 2 \mu\text{m}$, which was estimated for Cu by Lasagni et al., (2007) for a 10 ns laser pulse based on thermal diffusion length considerations. The minimum periodicity of the structuring, p_{min} , can be crudely estimated to be $p_{min} \sim 2 L_{th}$, where the thermal diffusion length, L_{th} , a measure of the heating

localization, can be estimated using the time-scale given by the pulse duration (τ_p) and thermal diffusivity (α), as $L_{th} = \sqrt{\alpha\tau_p}$. For an 8 ns pulse of energy and thermal diffusivities of $\alpha \sim 11.2, 10, 9,$ and $8 \times 10^{-5} \text{ m}^2/\text{s}$ that were measured for electrolytic Cu at 400, 600, 900, and 1222 K (Kobayasi, and Kumada, 1968), the p_{min} was estimated to be 1.9, 1.8, 1.7, and 1.6 μm , respectively. Thus, for the optics used, the periodicity selected in this study ($\sim 1.7 \mu\text{m}$) is very close to the estimated minimum value based on thermal diffusion length. In addition, smaller values of maximum attainable structuring depths, d_{max} , are expected for smaller periodicities.

Concerning the laser fluence effect on the laser-interference induced structuring, the following considerations can be made. Based on the data in Lasagni et al. (2007) for single pulse experiments on Cu at periodicities of 3.51 μm , the structuring would be evident, although at very small depths (d_{min}) for laser fluences of $F_{min} \sim 1.7 \text{ J}/\text{cm}^2$ per pulse compared to the full structure depths (d_{max}) that would be attained at $\sim 2.7 \text{ J}/\text{cm}^2$ per pulse. To quantify the structuring effectiveness, Sabau et al. (2020) introduced a threshold fluence, F_{th} , for which the structure depth would be approximately half that of the maximum, or $d \sim 0.5d_{max}$. For $F_1 \geq F_{th}$, ‘effective’ structuring characterized as $0.5d_{max} \leq d \leq d_{max}$ would be attained. At $p=3.51 \mu\text{m}$, the threshold F_{th} is $\sim 2.15 \text{ J}/\text{cm}^2$ as summarized in Table 3.3. We note that the Cu surfaces used by Lasagni et al. (2007) were ground and polished with diamond suspensions while the Cu surfaces used in this study were cold-rolled. For aluminum, D’Alessandria et al. (2008) found that the interference structuring was attained at lower fluences for relatively rougher surfaces and larger periodicities. Using the trends in data for Al from D’Alessandria et al., both the F_{min} and F_{th} may be considered to shift from 1.7 and 2.7 J/cm^2 for polished Cu surfaces to 1.3 and 1.72 J/cm^2 for rough Cu surfaces. This was explained by the intrinsic smaller reflectivity for rougher surfaces than that for the polished surfaces. In this work, two laser fluences of $F_l = 1.782$ and 2.785 J/cm^2 per pulse were used by varying the laser spot size ($d_b = 5$ and 4 mm, respectively) while keeping the same average power of 3.5 W. In summary, considering these threshold fluences for polished surfaces, roughness effect, and the small periodicity selected ($\sim 1.7 \mu\text{m}$), the use of the $F_l = 1.782$ and 2.785 J/cm^2 per pulse seem to cover two possible laser-interference structuring domains, namely, the former with minor structuring and the latter with effective structuring. However, the quality of the structuring is expected to be affected by the small periodicity selected.

Table 3.3. Survey of surface topology features for single pulse laser-interference processing of pure Al and Cu.

p_{exp} [μm]	d_{max} [μm]	F_{min} [J/cm^2]	F_{th} [J/cm^2]	Metal	Surface condition	Reference
2.2	0.7	0.9	1.2	Al	rough	
3.4	1.4	0.97	1.37	Al	rough	D'Alessandria et al., (2008)
3.4	1.45	1.42	1.75	Al	polished	
4.5	1.5	0.8	0.9	Al	rough	
4.7	1.3	1.5	1.68	Al	polished	Lasagni et al., (2007)
3.5	1.4	1.7	2.7	Cu	polished	Lasagni et al., (2007)

* F_{min} indicates the minimum fluence for which data is reported

3.2.4 SEM Characterization of Surface Topology for As-Received, Unprocessed Specimen

A HITACHI S-4800 scanning electron microscope featuring a maximum resolution of 1.0 nm and a variable acceleration voltage of 0.5 – 30 kV was used. All of the images shown in this study used a 20 kV acceleration voltage and five different magnifications were used (300 \times , 500 \times , 1000 \times , 2000 \times and 5000 \times). SEM micrographs for the as-received surface are shown at different magnifications in Figure 3.3. The as-received surface exhibits horizontal rolling marks, many micro-cracks throughout the surface, and other surface defects. Even at a very high magnification at 5000 \times , the surface appears quite flat.

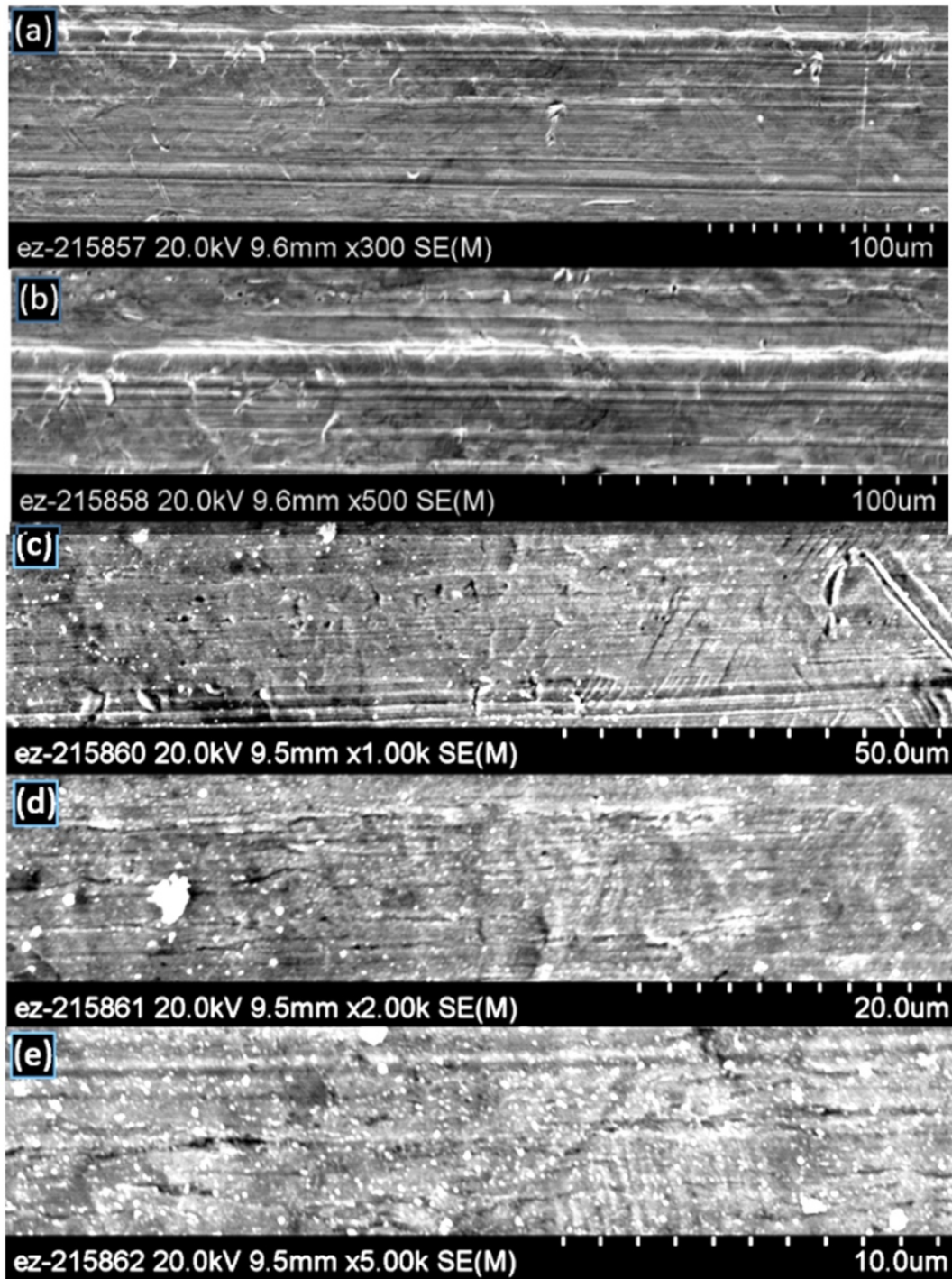


Figure 3.3. SEM micrographs of the as-received unprocessed copper surface at different magnifications: (a) 300 \times , (b) 500 \times , (c) 1000 \times , (d) 2000 \times , (e) 5000 \times .

3.2.5 SEM Characterization of Surface Topology for Spot-by-Spot Technique

Figure 3.4 and Figure 3.5 show the SEM images at 2000× magnification for the laser-interference-processed surface using the spot-by-spot method with 4 mm and 5 mm laser spot sizes, respectively. For the case of a 4 mm spot size, two pulses per spot already provided enough energy to form the finger-like protrusions, filament/network-like patterns that are evidence of widespread melting (Figure 3.4a). These types of filament/network-like topologies are a result of melting not only at the interference maxima but also at the interference minima. It is likely that the interference profile had a role to play in the formation of this type of fingering. In Table 3.4, an attempt was made to describe qualitatively the surface topology, by indicating the density of geometrical features (i.e., protrusions), their height, and their characteristic size. Further increasing the number of pulses seems to alter the type of the net-like geometrical features (Table 3.4). Larger surface areas are considered to be more beneficial for bonding. Large surface areas would result from taller features and higher density of features per unit surface area. The height and density of these melt-induced features appear to be maximized for 2 and 6 shots per spot. For these cases, the accumulated fluences on specimen surfaces were 3.56 J/cm² and 7.13 J/cm², respectively. The height and density of these melt-induced features seems to be minimized for specimens with 10 and 12 shots per spot.

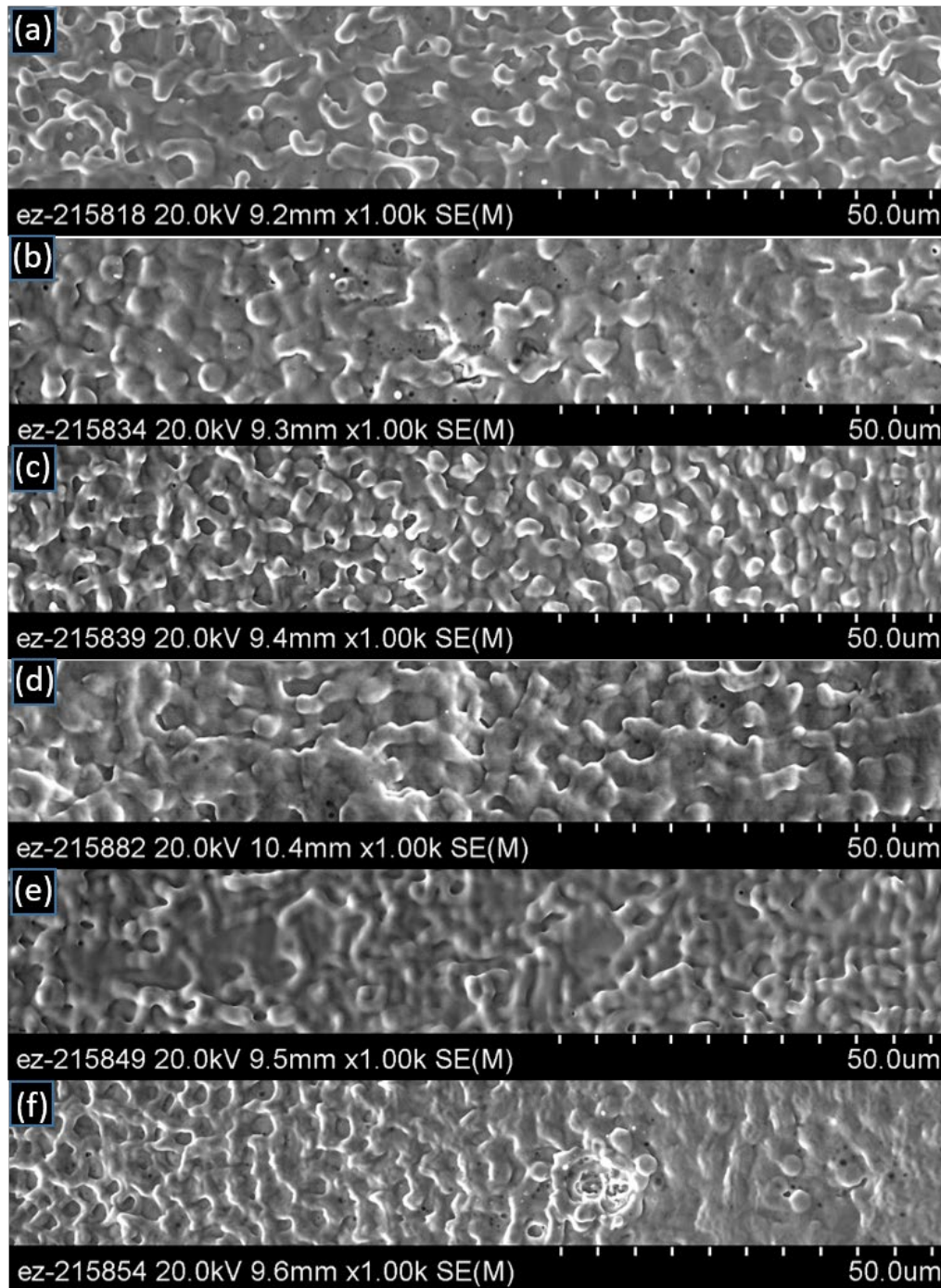


Figure 3.4. SEM micrographs (2000 \times) of the laser-interference-processed area using the spot-by-spot method with a 4 mm spot size on copper. Each frame shows a different number of pulses per spot: (a) 2, (b) 4, (c) 6, (d) 8, (e) 10, (f) 12.

Table 3.4. Topology variation for spot-by-spot laser processing with 4 mm spot size.

Case No.	N_P	Topology description	Protrusion size [μm]	Feature density	Feature height
1	2	Network protrusions	2	Medium	Medium
2	4	Flatter, thick network	3.5	Very low	Very small
3	6	Upward protrusions	2.5	Very high	Very high
4	8	Flatter, thick protrusions	3	Very low	Medium
5	10	Flat, thin protrusions	1.7	High	Very small
6	12	Flat protrusions	2.2-4.5	High to low	Very small

The surface topology is shown in Figure 3.5 for the 5 mm spot size cases. For 5 mm spot size and 2 pulses per spot (Figure 3.5a), surface topologies seem to be similar to those observed for the case with the 4 mm spot size and 2 pulses per shot (Figure 3.4a). When 4 pulses per spot are used (Figure 3.5b), melt rings and microcrater-like features appear. Further increasing the number of pulses does not appear to alter the characteristic size of geometrical features (Table 3.5), which in average was $\sim 1.6 \mu\text{m}$ for all conditions, while for the 4 mm spot size, larger features were observed, as large as $4.5 \mu\text{m}$. In general, fewer finger-like protrusions are evidenced for the 5 mm spot size than for the 4 mm beam size specimens (e.g., Figure 3.5a, 3.5d versus Figure 3.4a, 3.4c, and 3.4d) such that the net-like surface topology characterizes the 5 mm spot processing. Also, the density of geometrical features, e.g., protrusions, does not seem to vary with the number of pulses per spot, while a wider range of variation was observed for the 4 mm beam size specimens. For the 5 mm spot size, the surface is flatter for 10 and 12 pulses per spot than for all the other conditions.

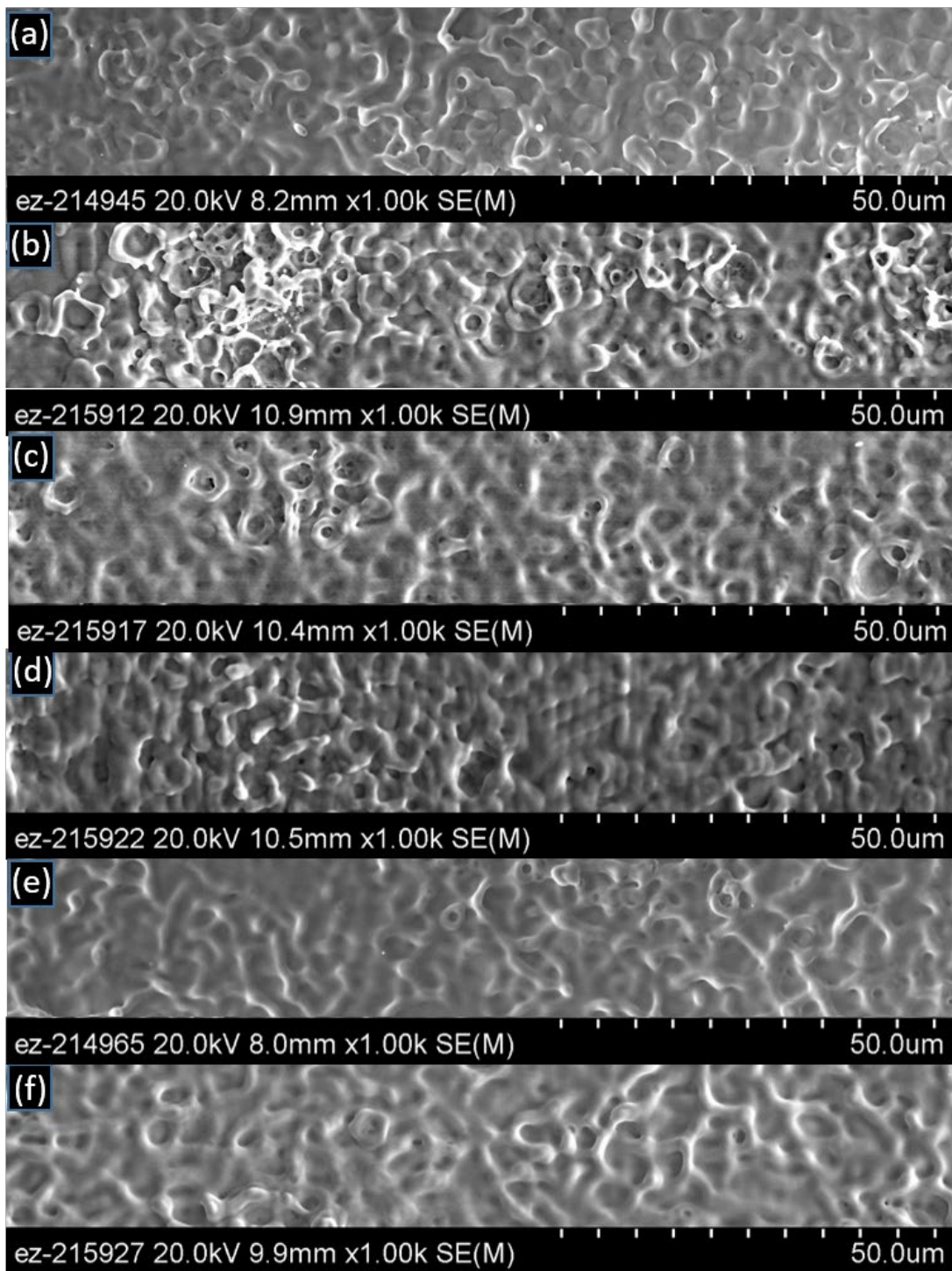


Figure 3.5. SEM micrographs (2000 \times) of the laser-interference-processed area using the spot-by-spot method with a 5 mm spot size on copper. Each frame shows a different number of pulses per spot: (a) 2, (b) 4, (c) 6, (d) 8, (e) 10, (f) 12.

Table 3.5. Topology variation for spot-by-spot laser-interference processing with 5 mm spot size.

Case No.	N_p	Topology description	Protrusion size [μm]	Feature density	Feature height
1	2	Network protrusions	2	Medium	High
2	4	Network protrusions & Melt rings	1.2-1.7	High	High
3	6	Flatter, network protrusions & Melt rings	1.5	Medium	Small
4	8	Network protrusions	1.5	Medium	Medium to Small
5	10	Flatter, thin protrusions	1.5	Medium	Small
6	12	Flatter, thin protrusions	1.7	Medium	Small

Since the expected periodicity was not attained, it is important to investigate what type of surface topology would be attained without laser interference, i.e., using only the main laser beam only without splitting it. The surface topology for specimens processed without laser interference, is presented next section for similar laser parameters to those for which the surface topology is discussed in this Section. The data shows that the laser-interference yields surface topologies with finer protrusions and more uniform surface topologies than processing without laser-interference (Section 3.2.6).

For the sake of completion, a montage with SEM micrographs taken at similar magnifications as those for the as-received specimen (Figure 3.3) was assembled for one laser-processed specimen with 4 mm spot size and 2 pulses per spot in Figure 3.6. At higher magnification as shown in Figure 3.6d and 6e, the filament web diameter size was measured to be $\sim 2 \mu\text{m}$.

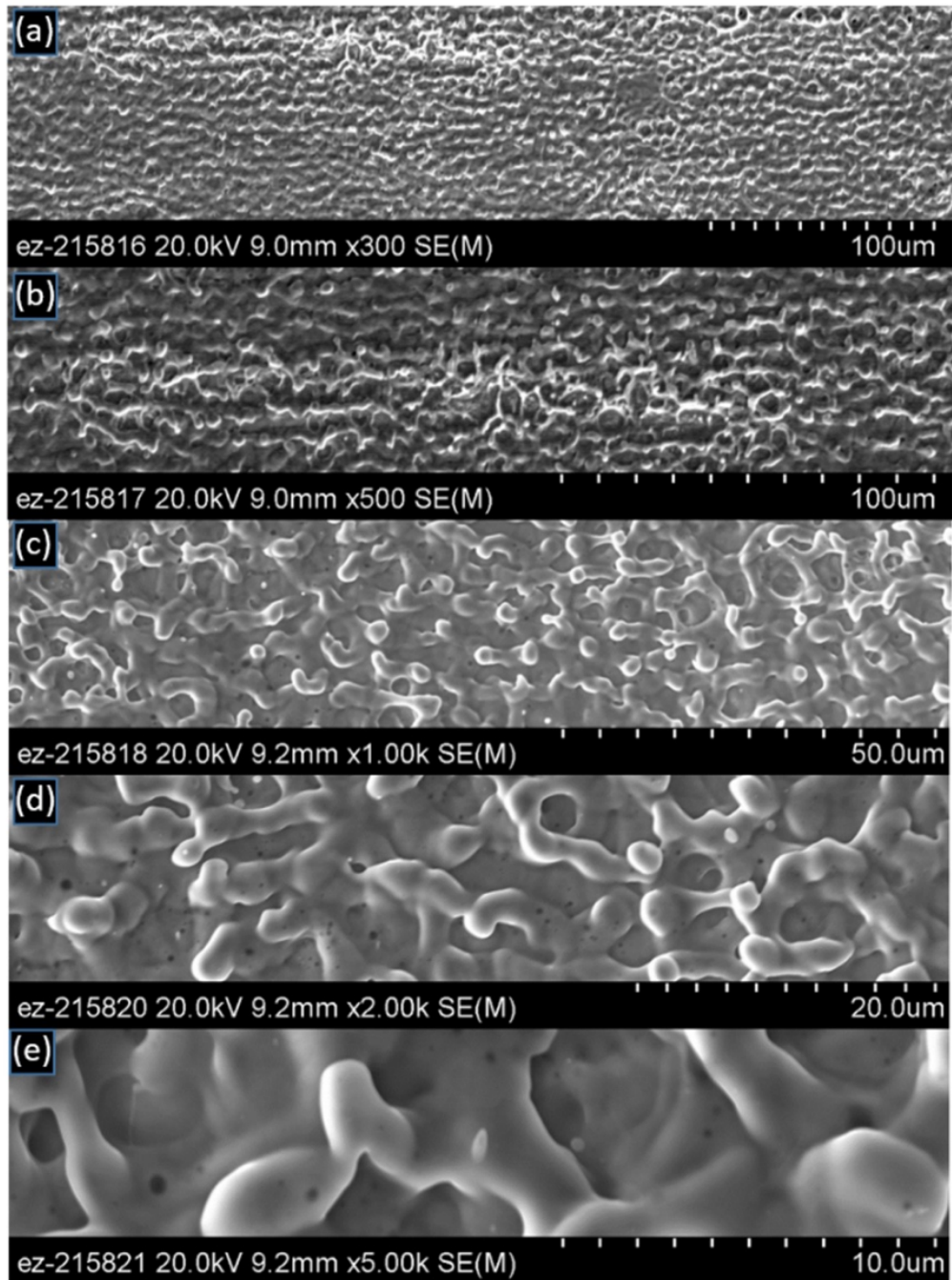


Figure 3.6. SEM micrographs of the laser interference processed Cu surface (spot-by-spot method) with a 4 mm spot size and 2 pulses per spot at different magnifications: (a) 300 \times , (b) 500 \times , (c) 1000 \times , (d) 2000 \times , (e) 5000 \times .

3.2.6 SEM Characterization of Surface Topology for Spot-by-Spot Specimens Without Interference

The surface topology for specimens processed without laser interference, i.e., using only the main laser beam only without splitting it, is presented in this section. The surface topology is shown in Figure 3.7 and Figure 3.8 for specimens processed with the same 5 mm spot size as for those processed with laser interference as shown in Figure 3.5. The surface topology features are summarized in Table 3.6. For 2, 4, and 6 pulses per spot (Figure 3.7a, b, and c), the surface topologies are quite different than those with the laser interference (Figure 3.5 a, b, and c), exhibiting large flat areas without protrusions. The rolling direction is evident through vertical striations in Figure 3.7a and b. Consequently, the feature height and protrusion size exhibit a wide range of variation for each specimen. Overall, these 2, 4, and 6 pulses per spot specimens were found to exhibit thicker protrusions than the corresponding laser interference cases.

Concerning the appearance of the ‘less-affected’ flat areas, the following considerations can be made. First, the SEM images were taken from the laser spot center, which is a similar location to those for the laser interference specimens. Second, as mentioned in Sabau et al. (2016) for Al, the (non)uniformity of the lubrication films from prior rolling operations would affect the overall energy available locally for the laser surface treatment, the local temperature evolution during laser surface treatment, and ensuing melting. Third, the magnitude of the local laser heat flux in the interference maxima is exactly *twice* than that of the one-beam setup, providing more energy for the local melting than that for the one-beam interference-less processing. Thus, more melting is expected for the laser interference processing than for the traditional one-beam laser processing.

For 8, 10, and 12 pulses per spot (Figure 3.8a, b, and c), surface topologies for one-beam processing seem different than those with the laser interference processing (Figure 3.5 d, e, and f), exhibiting areas with small protrusion sizes (e.g., 1.2 to 1.7 μm) and areas with large protrusion sizes (e.g., 2.5 to 3 μm). The less-affected areas seen for processing with lower number of pulses are not present for the processing with a larger number of pulses. However, for 8 and 10 pulses per spot, the feature density exhibits a variation between regions with medium feature density and flatter, less dense regions. The variation in the surface topology is minimum for the 12 pulses per spot condition among all the one-beam laser specimens, making the result of this processing condition the closest to the laser-interference conditions. However, the surface topologies for the 12 pulses per spot, with and without laser interference, still remain quite different. Based on the

data presented in this Appendix for one-beam (without laser interference) processing and corresponding data presented in Section 3.2.5 for the laser interference processing at a periodicity of $1.7\ \mu\text{m}$, which is close that estimated based the thermal diffusion lengthscales, it can be concluded that although the laser interference at this small periodicity does not realize the expected periodic structuring, it yields surface topologies with finer protrusions and more uniform surface topologies.

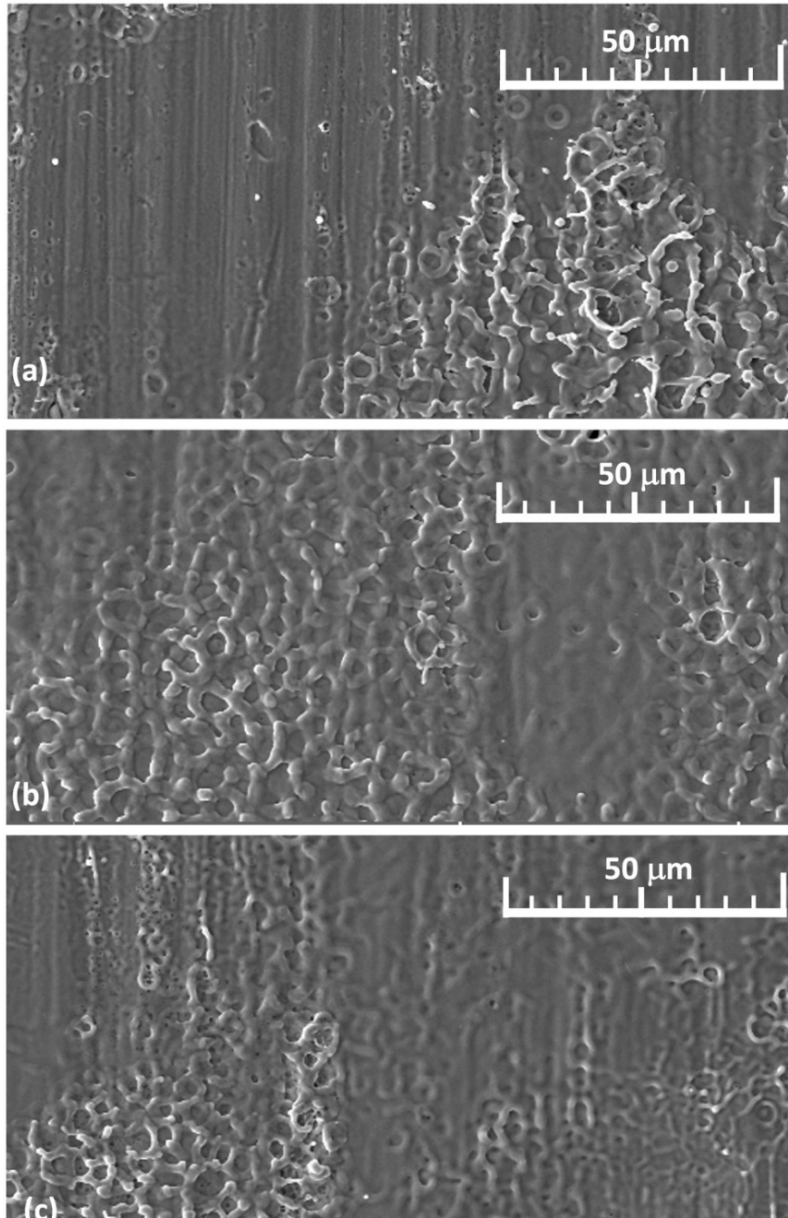


Figure 3.7. SEM micrographs for one-beam laser processed Cu specimens using the spot-by-spot method with a 5 mm spot size for number of pulses per spot of: (a) 2, (b) 4, and (c) 6.

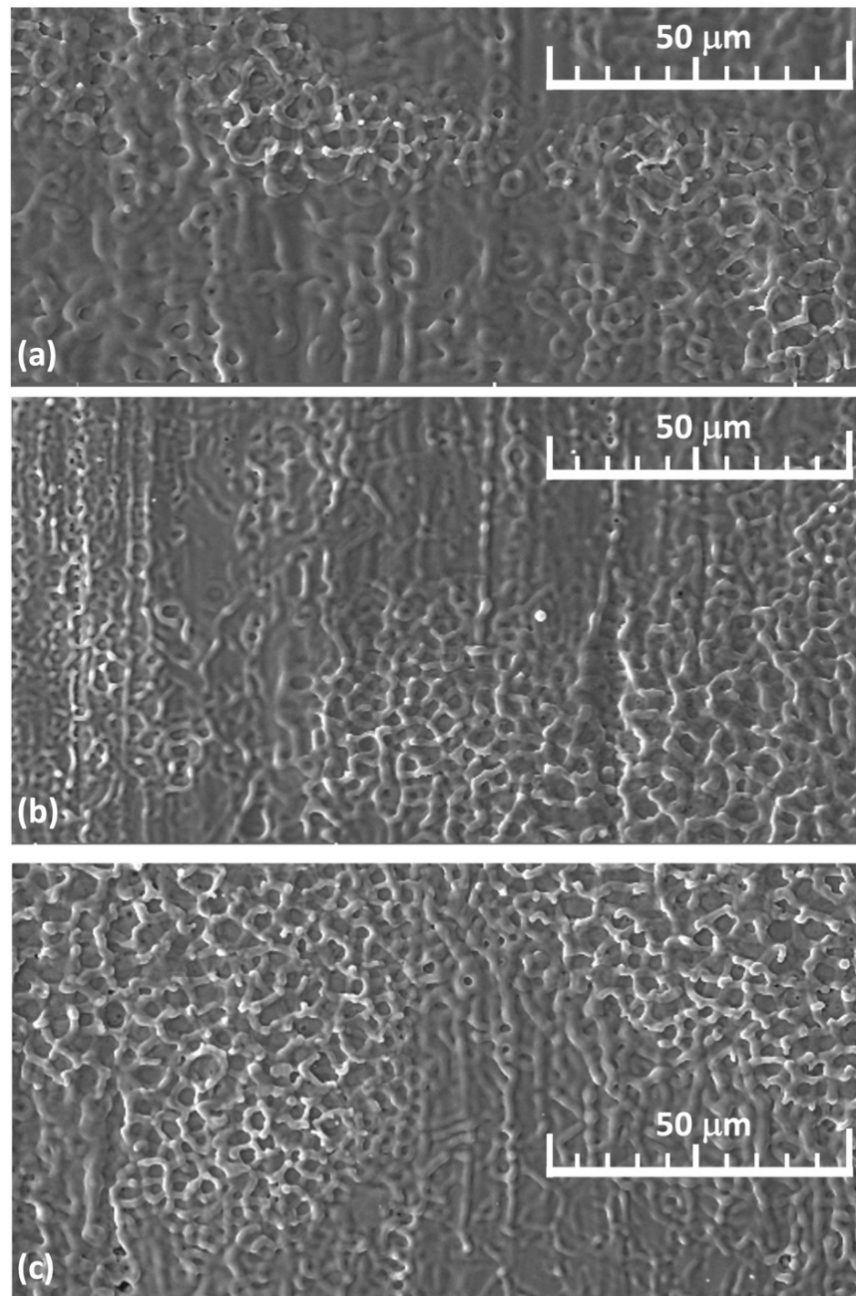


Figure 3.8. SEM micrographs for one-beam laser processed Cu specimens using the spot-by-spot method with a 5 mm spot size for number of pulses per spot of: (a) 8, (b) 10, and (c) 12.

Table 3.6. Topology variation for one-beam laser processed Cu specimens with 5 mm spot size.

Case No.	N_p	Topology description	Protrusion size [μm]	Feature density	Feature height
1	2	Incomplete melting; Network protrusions	0-1.9	None to Medium	None to High
2	4	Incomplete melting; Thick Network protrusions	0-2.3	None to Medium	Very small to Medium
3	6	Flatter, network protrusions & Melt rings	0-2	None to Medium	Very Small to High
4	8	Flatter, medium & thick protrusions	1.3-3	Small to Medium	Medium to Small
5	10	Flatter, thin & thick protrusions	1.2-2.5	Small to Medium	Small
6	12	Flatter, thin protrusions	1.7-2.5	Medium	High

3.2.7 SEM Characterization of Surface Topology for Raster Technique

After spot-by-spot processing, the laser raster processing was conducted for only the 5 mm laser spot size. Six different raster speeds were used: 2, 4, 6, 8, 10, and 12 mm/s. In the raster method, a higher speed decreases the overall input energy. The resulting surface topologies are shown in Figure 3.9 at a SEM magnification of 2000 \times . At lower raster speeds of 2 and 4 mm/s (Figure 3.9a, Figure 3.9b) the raster method was found to yield similar surface topologies to those from the spot-by-spot method. In Figure 3.9a, for the lowest speed, the net-like structure can be found in the left side of the SEM with a flatter uniform right side. Crater-like features are evidenced for the 4 mm/s case (Figure 3.9b), similar to those for the 4/6 pulses per spot for the spot-by-spot processing (Figure 3.6b, Figure 3.6c). As the raster speed is increased from 6 mm/s to 12 mm/s (Figure 3.9c through Figure 3.9f), the surface topology becomes less regular. A summary of surface topologies for the raster technique is presented in Table 3.7. In general, the surface topology appears to be flatter than that for spot-by-spot method with thinner net-like protrusions sticking out of the surface.

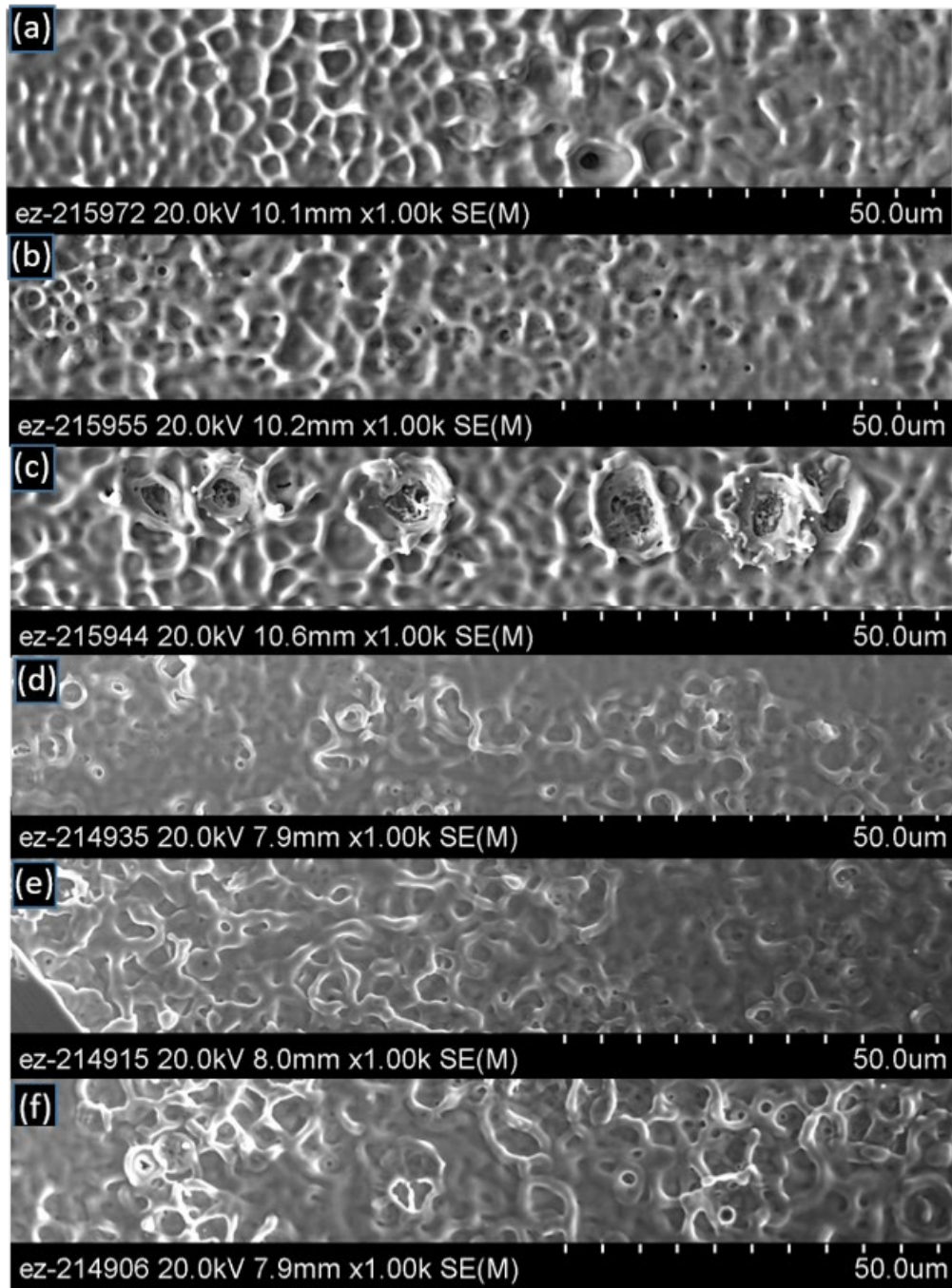


Figure 3.9. SEM images (2000 \times magnification) of the laser-interference-processed area using the laser raster method with a 5 mm spot size on copper. Each frame shows a different raster speed (mm/s): (a) 2, (b) 4, (c) 6, (d) 8, (e) 10, (f) 12.

Table 3.7. Topology variation for the raster laser processing with 5 mm spot size.

Case No.	U [mm/s]	Topology description	Protrusion size [μm]	Feature density	Feature height
1	2	Network protrusions	1.2	Medium	Medium
2	4	Network protrusions & Small melt rings	2	Medium	Small
3	6	Flatter, network protrusions & large melt rings	1.5	Medium	Small/Medium
4	8	Flatter, Network protrusions	1.2-1.5	Low	Small/Medium
5	10	Flatter, thicker protrusions	1.5-2	Low	Small/Medium
6	12	Deeper, thin protrusions	1.5	Medium	High

3.2.8 Surface Profile

A Wyko NT 9100 optical profiling system was used to acquire the surface profile data at a magnification of $50\times$. The area chosen for surface profiling was located near the spot center for spot-by-spot processing and near the centerline of a laser scan for the raster processing. The average roughness, or arithmetical mean deviation of the roughness profile, R_a , was calculated from the profile measurements. R_a was calculated by averaging the absolute height variation within the sampling area by excluding a few outlying points so that the extreme points have no significant impact on the final results. Figure 3.10a shows one surface profile for the original surface, in the as-received, unprocessed condition. In the surface profile, grooves from the prior rolling operation are present without any other patterns. The surface profile for the spot-by-spot laser-processed specimen, for which the SEM micrographs were shown at different magnifications in Figure 3.4, is shown in Figure 3.10b. The surface profile appears to be much rougher than that for the as-received condition. The surface profile for two raster processed specimens were shown in Figure 3.10c and 8d. The R_a was estimated to be 183, 394, 340, and 364 nm, respectively. Basically, R_a was doubled by laser processing. A chemical analysis to assess the surface contamination was not conducted in this study as this effect is very well documented in the literature for a single laser beam (Hernandez, Alfano and Lubineau, 2016) as well as laser-interference (Meyer and Sabau, 2007; Sabau and Meyer 2020).

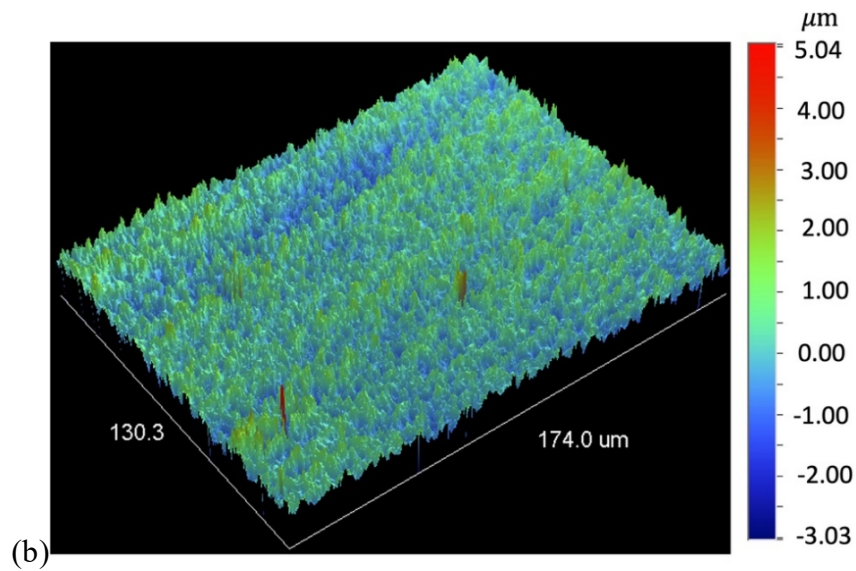
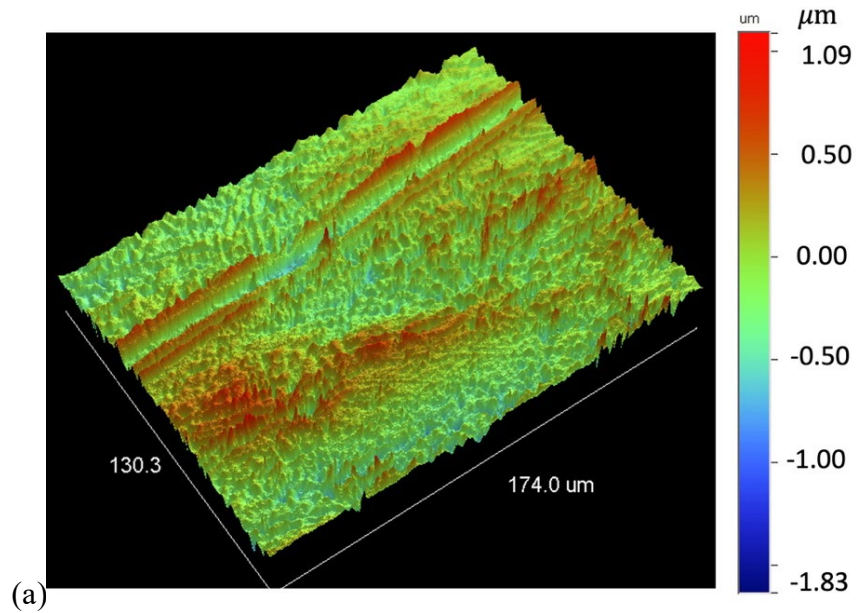
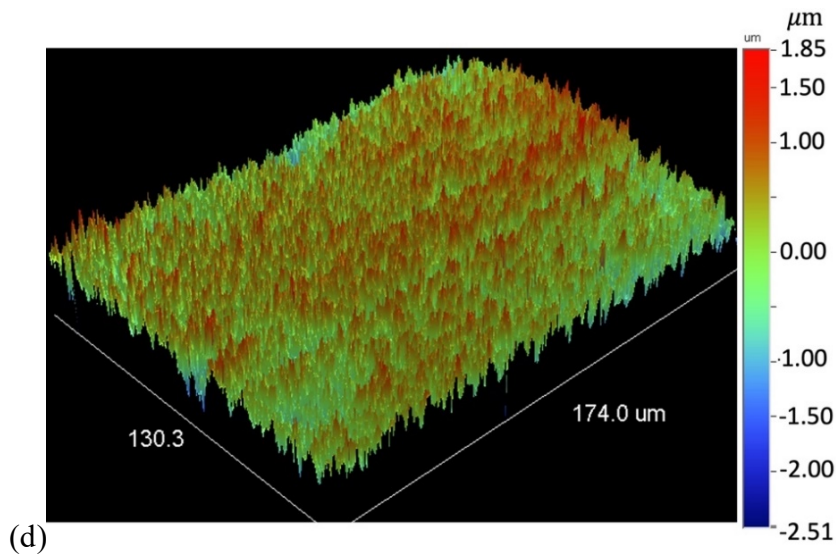
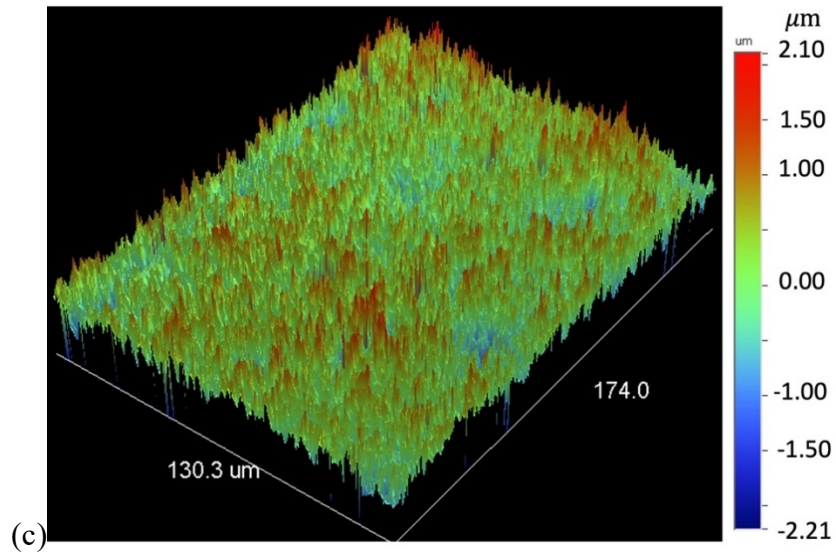


Figure 3.10. 3D surface profile at $50\times$ magnification for: (a) as-received, unprocessed specimen and (b, c, d) laser interference processed Cu with 4 mm spot size: (b) spot-by-spot, 2 pulses, (c) raster, 2 mm/s and (d) raster, 4 mm/s.

Figure 3.10 continued



3.3 Joint Strength Evaluation

In this section, single lap shear joints were made and tested using both a traditional mechanical/chemical surface preparation method and laser interference structuring, to study the bonding strength. The raster processing method was selected to prepare surfaces for joining. The raster method was selected based on several considerations. First, compared with the spot-by-spot method as shown in Figure 3.5 and Figure 3.6, the laser raster method resulted in net-shape structures that had a smaller height and finer length scale. Second, the laser raster method is faster

than the spot-by-spot method. For an industrial application, the two techniques would be actually merged by using: (a) a laser fluence (i.e., laser spot size) that would ensure appropriate texturing in one pulse and (b) a raster speed that would move the beam adjacent the prior spot for the next pulse.

3.3.1 Experimental Setup

In this section, single lap shear joints were made and tested using both a traditional mechanical/chemical surface preparation method and laser interference structuring, to study the bonding strength. The raster processing method was selected to prepare surfaces for joining. The raster method was selected based on several considerations. First, compared with the spot-by-spot method as shown in Figure 3.5 and Figure 3.6, the laser raster method resulted in net-shape structures that had a smaller height and finer length scale. Second, the laser raster method is faster than the spot-by-spot method. For an industrial application, the two techniques would be actually merged by using: (a) a laser fluence (i.e., laser spot size) that would ensure appropriate texturing in one pulse and (b) a raster speed that would move the beam adjacent the prior spot for the next pulse.

For baseline joints, a traditional mechanical/chemical surface preparation method recommended by the adhesive manufacture was applied. The Cu surfaces were first wiped clean with by IPA, followed by sanding using 220 grit sandpaper. After sanding, the surfaces were cleaned using IPA again. For the laser structured joints, the Cu surfaces were processed using the interference technique in as-received condition, i.e., without any solvent wiping. After the surface preparation, specimens were stored in plastic cases (under ambient conditions) and bonded within 48 hours of the structuring. The laser-structured surfaces were not in direct contact with any other surfaces at any time to minimize airborne contamination.

As analyzed in Section 3.2.7, the laser raster method using a 5 mm spot size beam was selected. Considering the range of surface profiles attained the 6 mm/s and 12 mm/s raster speeds were selected to ensure distinct characteristic between each sample. All of the other laser parameters were kept the same as those in the surface characterization study. Three specimens were prepared for the mechanical/chemical surface preparation baseline and four specimens were prepared for each laser raster condition.

The single lap shear joints were bonded with specially designed fixture according to the ASTM D1002-10 standard. The Cu specimens were all cut into 25.4 mm (1 in.) × 95.25 mm (3.75 in.) sizes from the same 110 copper sheet having 1.65 mm (0.065 in.) thickness. The bonding overlap length was controlled to 12.7 mm (0.5 in.) as shown in Figure 3.11. Two specimens were bonded using a toughened, two-part epoxy structural adhesive (3M™ Scotch-Weld™ Epoxy Adhesive DP420). The adhesive bond line thickness was controlled to 0.12 mm, as recommended by the manufacturer, by laying down two fishing lines with a given diameter. The specimen alignment and overlap length were assured by the bonding fixture. The fixture has the capacity to bond eight joint samples at the same time. The first specimen was put in one side of the fixture as shown in Figure 3.12a. Adhesive was evenly distributed on the bonding surface with the dispenser specified by the adhesive manufacturer. A picture of the specimens with adhesive on top is shown in Figure 3.12b. Extra spacers were used to keep the two bonding surfaces parallel to each other. With the spacers in place, specimens were put into the other side of the fixture as shown in Figure 3.12c. These second specimens were then compressed firmly onto the adhesive using the aluminum bars on top of each sample with tightening bolts. The whole fixture with samples in place, as shown in Figure 3.12d, was then left at room temperature for 24 hours for curing. The overlap area was approximately 25.4 mm (1 in.) by 12.7 mm (0.5 in.), following the ASTM D1002-10 standard, to ensure the specimens can be pulled apart without breaking the Cu adherents.

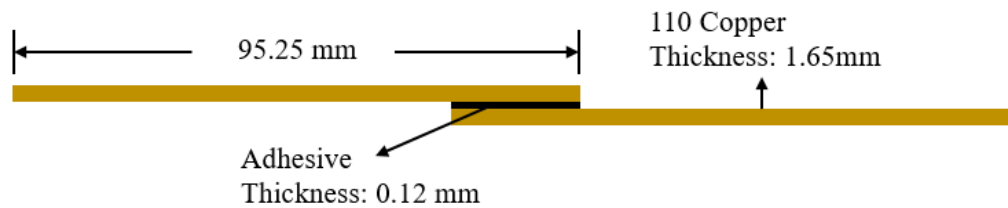


Figure 3.11. Schematic figure for the single lap shear joints.

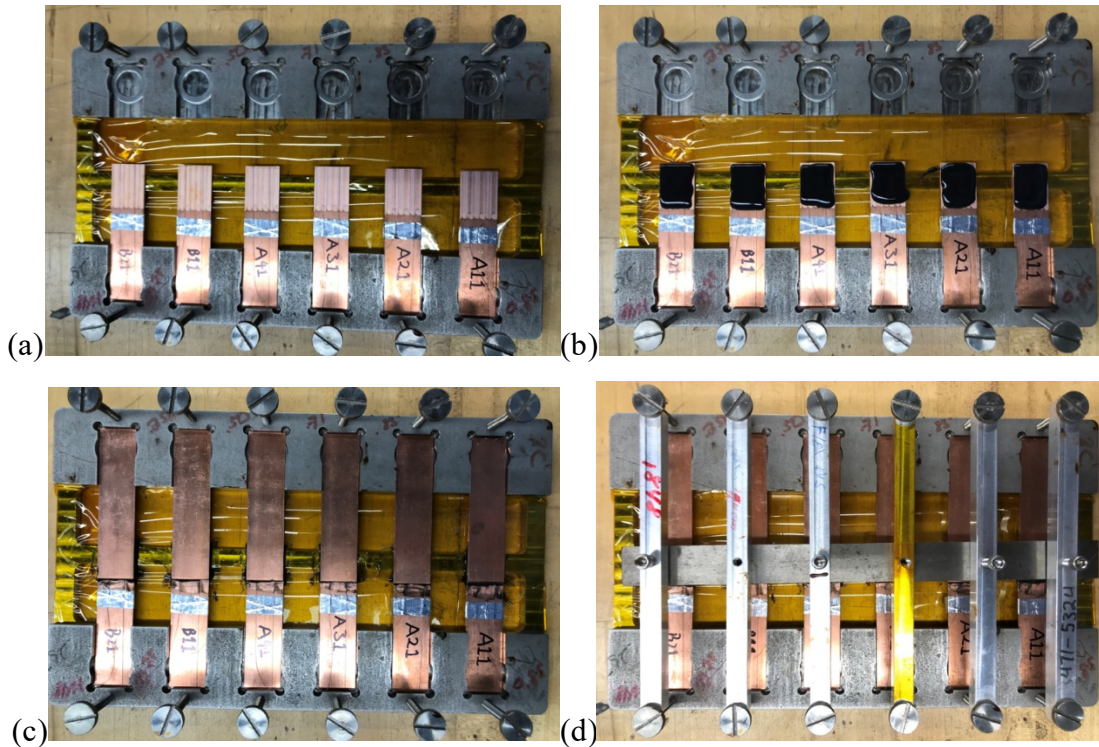


Figure 3.12. Photographs showing the single lap shear joint bonding process and fixture: (a) specimens place on one side of the fixture; (b) adhesive applied on the bonding area; (c) specimens placed on the other side of the fixture; (d) tightened bolts press the two specimens firmly onto each other.

3.3.2 Single-Lap Shear Strength Results

In this section, the results of the adhesive joint shear strength are analyzed and discussed. The failure mechanism can be identified by inspecting the adhesive and adherent surfaces in the overlapping region. Selected photographs of these interfaces are shown in Figure 3.13. For the cases shown in Figure 3.13a, most of the adhesive was found attached to one of adherent, while the other adherent had little trace of the adhesive. This indicates that an *adhesive* failure occurred at the interface between the adherent and adhesive, as opposed to a *cohesive* failure inside the adhesive material itself. In Figure 3.13b, adhesive remnants can be found on both adherents; however, if matched back together, it is clear that the adhesive left on both surfaces have a small overlapping region. The overlapping fracture layer can be seen as the lighter gray regions outlined in red in the bottom image. This indicates a *mixed* failure of the adhesive, with peeling of the adherents during the test. These adhesive and mixed failure mechanisms are not common for toughened epoxy adhesive and are attributed to the nature of the single lap joint test. Although the

specimens were cut from the same material lot and carefully aligned along the tester axis to reduce the eccentricity of the load path, the high shear force needed to pull apart the specimens still caused out-of-plane bending moments.

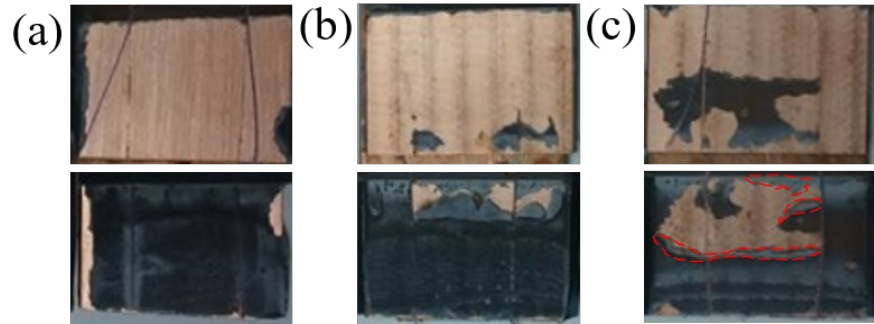


Figure 3.13. Selected photographs of the overlapping bonding area after single lap shear testing. Each top and bottom pair of images correspond to the same bonded specimen: (a) A2 baseline specimen; mixed failure, (b) C3 (12 mm/s) adhesive failure; and (c) C4 (12 mm/s) adhesive failure.

The maximum loading force for single lap shear joints is affected by several factors including the surface preparation method, adhesive thickness, and joints geometry. In the experiments, the adhesive thickness was precisely controlled to be the same for all samples (0.12 mm). In order to isolate the effect of different surface preparation methods, the influence of the bonded area of the joint is reduced by comparing the joint shear lap strength, which is estimated by dividing the maximum load by the overlap bonding area (overlap length times the specimen width). The specimen width was uniform at 25.4 mm (1 in.), but due to slight variation in the cutting operation, the overlap length varied.

The load-displacement curves are shown for several specimens in Figure 3.14. For the baseline specimen, the variation of the load versus displacement curve near the failure point is characteristic of a brittle fracture at failure; for the laser-structured specimens, a ductile fracture is observed, i.e., failure point after a slow decrease in the load rate. These data indicate that the laser-structured joints are more ductile than those without laser-structuring. The increased ductility of the laser-structured joints indicates an enhanced bonding of the adhesive to the Cu adherents. The energy absorbed by the joint during the deformation testing, which is proportional to the area under the load versus displacement curve, is another parameter that can be used to quantify the joint

performance. The energy absorbed during the tensile pull was calculated for the data shown in Figure 3.14 to be 2.02, 3.71, and 3.89 Joules for the baseline joint and laser-structured joints with 6 mm/s and 12 mm/s, respectively. Thus, the absorbed energy during shear-lap testing of laser-structured joints was approximately 1.8 to 1.9 \times than that for the baseline specimen, i.e., an increase by approximately 80-90% over those measured for baseline joints.

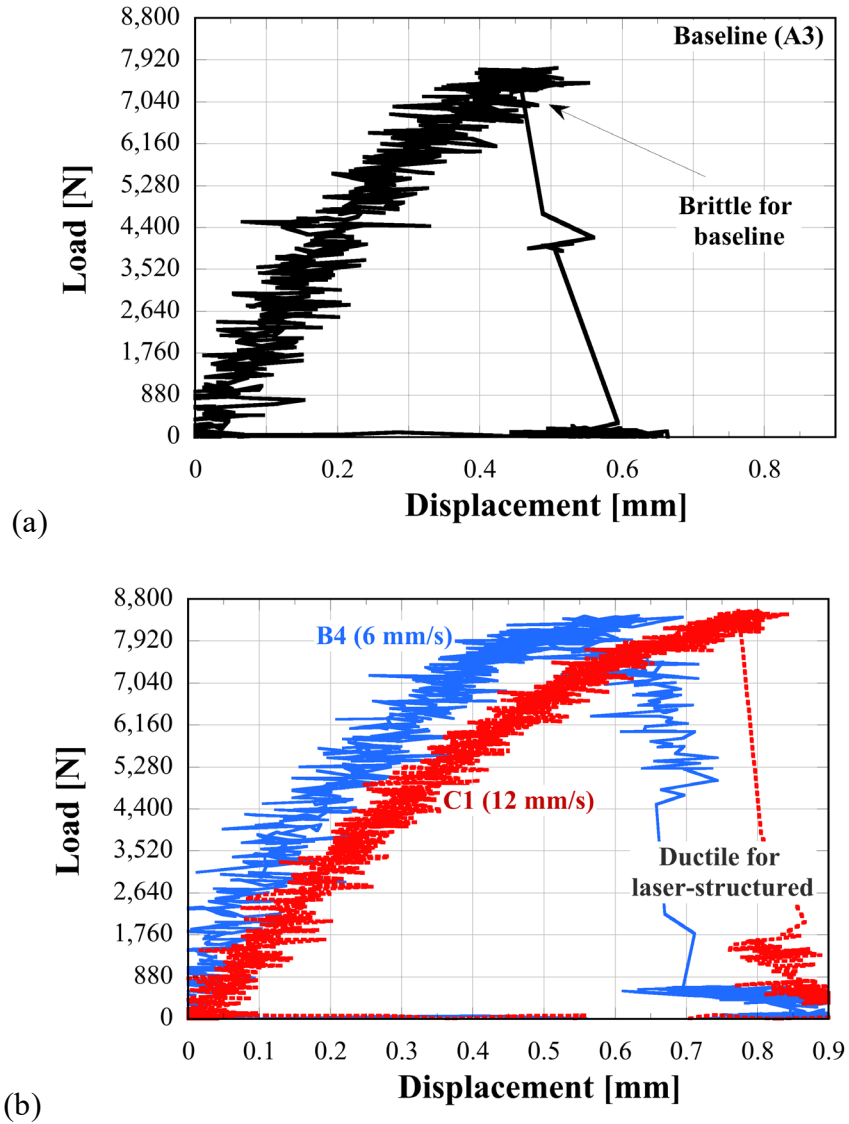


Figure 3.14. Load versus displacement variation during single-lap shear testing for (a): baseline specimen A3 and (b) laser-structured specimens B4 and C1 (6 and 12 mm/s raster speed, respectively).

The results of the tensile shear testing are shown in Table 3.8. The results for specimen C4 exhibit a significant lower maximum loading, shear stress, and maximum displacement than the other samples.

Table 3.8. Geometry, maximum loading, maximum shear stress, and displacement at maximum loading for the laser-structured (raster method) and baseline specimens (A: Baseline: B: 6 mm/s; C: 12 mm/s; D: 2 mm/s;).

Specimen label (condition)	Overlap Length [mm]	Overlap Area [mm²]	Max Load [N]	Shear-lap Stress [MPa]	Disp. at Max Load [mm]	*Surface topology
A1 (base)	13.7	347.5	4981	14.34	0.26	Flatter, typical to rolling operations
A2 (base)	14.9	379.5	6629	17.47	0.39	
A3 (base)	16.0	407.4	7751	19.02	0.50	
B1 (6 mm/s)	16.0	406.2	7969	19.62	0.53	Network, medium density, large melt rings
B2 (6 mm/s)	16.0	400.1	8194	20.49	0.51	
B3 (6 mm/s)	16.1	409.2	8263	20.19	0.51	
B4 (6 mm/s)	15.9	403.6	8453	20.94	0.63	
C1 (12 mm/s)	16.1	401.1	8563	21.34	0.80	Thin protrusions with medium density
C2 (12 mm/s)	17.1	435.1	9262	21.29	0.63	
C3 (12 mm/s)	17.0	431.6	9201	21.32	0.65	
C4 (12 mm/s)	16.1	409.7	4852	11.84	0.36	

*Topology characterization from Table 3.7.

The shear strength and displacement at maximum loading for the rest of the specimens have a clear trend that can be seen in Figure 3.15. The strength and displacement at maximum load are both increased for the laser-structured samples compared to those surfaces prepared by traditional methods.

The statistics metrics were evaluated using the shear-lap testing data for all the specimens, which is shown in Table 3.8, and shown in Table 3.9. As shown in Table 3.9, compared with the traditional method, surface preparation with a laser raster at 6 mm/s was found to increase the shear strength and displacement at maximum loading by 11% and 25%, respectively. At 12 mm/s, the increases in the shear strength and displacement at maximum loading were 17% and 44%,

respectively. These shear-lap testing results indicate that the laser structuring with 12 mm/s yields better shear-lap joints than the laser structuring with 6 mm/s. As shown in the remainder of this paragraph, this finding is in good agreement with the mechanical interlocking and adhesion expected for the surface morphology that was for these conditions. Basically, the 12 mm/s laser processing was shown to yield increased protrusion heights than those with the 6 mm/s, at similar protrusion feature density (Figure 3.9c, Figure 3.9f, and Table 3.7). Thus, a larger surface area is expected for the 12 mm/s processing than for the 6 mm/s processing. In turn, increased surface areas would enhance the mechanical interlocking and adhesion, yielding higher shear strengths. However, detailed explanation for the higher raster speed causing a larger enhancement shown in Table 3.9 needs further testing and surface characterization, such as XPS and wettability tests, to understand and quantify these factors.

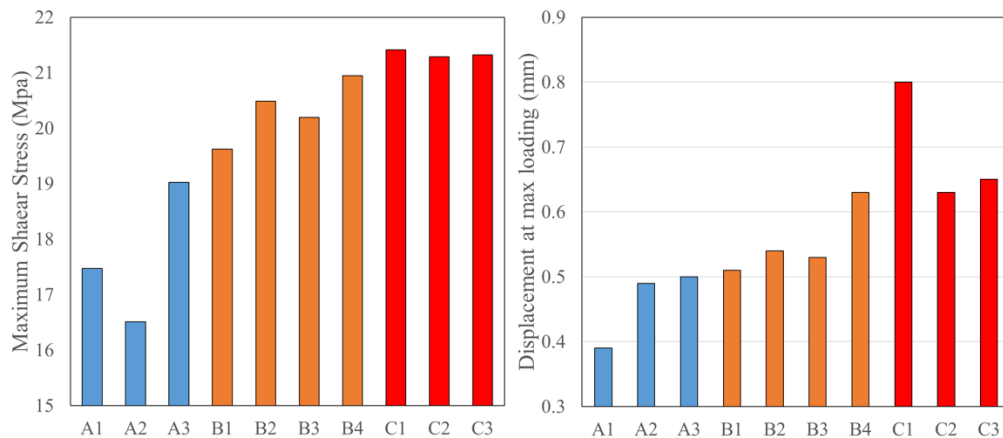


Figure 3.15. Shear strength (left) and displacement at maximum loading (right) for the laser-structured specimens and baseline (A: Baseline; B: 6 mm/s; C: 12 mm/s).

Table 3.9. Statistics and percentage increase in the maximum shear stress and maximum displacement for the laser-structured specimens with respect to the baseline.

Methods	Maximum Shear Stress [MPa]	Std. Deviation [MPa]	Increase [%]	Disp. at Max Loading [mm]	Std. Deviation [mm]	Increase [%]
Baseline	18.25	1.10	N/A	0.45	0.078	N/A
Laser: 6 mm/s	20.25	0.66	11.0	0.56	0.064	25.1
Laser: 12 mm/s	21.30	0.02	16.8	0.64	0.014	43.8

3.4 Conclusions and Discussions

In this study, laser-interference structuring near the interference limit imposed by the localized energy transport is evaluated as a surface preparation technique for adhesive bonding of copper. A nanosecond pulsed Nd:YAG laser was operated at 355 nm wavelength and laser fluences of $F_l = 1.782$ and 2.785 J/cm^2 per pulse. The optical setup considered would enable a structuring periodicity of $1.7 \text{ }\mu\text{m}$, which is near the $1.6\text{-}2 \text{ }\mu\text{m}$ structuring limit that was estimated based on thermal diffusion lengthscale for an 8 ns laser pulse.

The surface topology of Cu formed using spot-by-spot and laser raster methods were characterized using SEM and profilometry. The SEM micrographs showed that the surface topology of laser-processed specimens is characterized by finger-like protrusions, and filament/network-like patterns that evidence widespread melting. The characteristic size of the melt patterning, namely its height and feature density, varies with the laser conditions. These types of filament/network-like topologies are a result of melting not only at the interference maxima but also at the interference minima. Although the expected periodic interference structuring was not attained, SEM micrographs for specimens processed without laser interference indicate that the melt-induced texturing was affected by the interference processing.

Larger surface areas are considered to be more beneficial for bonding. Large surface areas would result from taller features and higher density of features per unit surface area. The height and density of these melt-induced features appear to be maximized for 2 and 6 pulses per spot. For these cases, the accumulated fluences on specimen surfaces were 3.56 J/cm^2 and 7.13 J/cm^2 , respectively. In general, the surface topology appears to be flatter than that for spot-by-spot method with thinner net-like protrusions sticking out of the surface. The height and density of these melt-induced features were maximized for the 12 mm/s raster processing (accumulated fluence of and 7.42 J/cm^2). This finding for the raster method is consistent with fact that the surface topology features were maximized for a similar accumulated fluence (7.42 J/cm^2) to that for the spot-by-spot condition (7.13 J/cm^2).

Joints were adhesively bonded using laser-structured specimens. Baseline joints were prepared by abrading joining specimens. Single lap shear tests were performed for the laser-structured specimens for two raster conditions and abraded specimens. The shear-lap testing indicated significant bonding enhancement compared with a baseline preparation method. The highest raster speed yielded the best bonding performance within the test conditions investigated.

The shear stress and displacement at maximum loading, at a raster speed of 12 mm/s, were increased by 16.8% and 43.8%, respectively over those measured for the specimens prepared by the baseline method. The load-displacement curves indicate that the laser-structured joints are more ductile than those without laser-structuring. The energy absorbed by the joint during the deformation testing, which is proportional to the area under the load versus displacement curve, was found to increase by approximately 80-90% over those measured for baseline joints. The increase ductility for the laser-structured joints is another indicator of enhanced adhesive bonding. Future efforts should be focused on investigating the joining performance with laser interference-induced surface topology, at a target periodicity larger than 2 μm .

4. FATIGUE AND RELIABILITY ANALYSIS

This chapter focuses on experimental investigation of the potential fatigue failure that may happen over the long term. The adhesive joints will go through various pressure and temperature conditions within the usage life. Vibration will also play an important role in fatigue failure. Experimental designs for both temperature/pressure fatigue and vibration fatigue will be introduced in detail. Two test stands are designed and built to study the fatigue resistance for adhesive joints.

4.1 Introduction

Fatigue in engineering is a loss of structural integrity over long-term operation under the influence of repeated or continuous application of stress. The stress can be caused by various factors like thermal stress, external loading, or vibration. Static loading and safety are often the focus; however, failure is frequently observed under repetitive loading at far smaller loads than those required to cause the static failure. Failure may occur suddenly after a long time in service, at which point many parts may simultaneously need an expensive remedy service. Studies in material behavior show that fatigue failure is common to most types of materials and it has been estimated that 80% of all engineering failures can be contributed to fatigue (Dowling, 1998). For adhesive joints in HVAC&R systems, the static stress in most of the tube-to-tube joints is not very high due to the nature of the structure (these joints serve a sealing function instead of a load-bearing function). However, the temperature and pressure change along with the vibration of the system apply a continuously changing stress in the bonding area, which may cause fatigue failure even if the stress is much less than the critical static stress.

4.2 Literature Review

The earliest study of fatigue was in the 1850s with wide usage of steel on railway and steel ships and aluminum alloy aircraft. However, most of the studies were focused on metals and adhesive has more complicated analysis due to the heterogeneous system of adhesive itself. It is worth considering the source of the fatigue loading. As explained by Adams (2005), the stresses in an adhesive joint can be attributed to mechanical loads or to residual effects. The mechanical

loads are the forces that the joints need to withstand and usually are easy to calculate. Mechanical loads can be further divided into static loads, working load, vibratory loads, and accidental loads. The residual effects have more complicated sources including the different thermal expansion of adhesive and adherends (which is called thermal stresses) and the expansion of the adhesive as moisture is absorbed (which is called hygroscopic stresses).

4.2.1 Mechanical Loads and Fatigue

Experimental studies on adhesive joints focus on the fatigue strength and lifetime prediction based on several factors including geometric parameters, material parameters, loading conditions and manufacturing procedures.

Different geometries can strongly influence the fatigue performance. Jen (2012) studied fatigue lifetime of adhesively bonded scarf joints with various different angles and indicated that the fatigue strength increases with scarf angle increasing. de Cista Mattos et al. (2012) performed experimental static and fatigue tests of epoxy adhesively bonded single lap joints (SLJ) for different bonding areas and found that fatigue lifetime of two joints with different adhesive areas can be correlated by a shape factor. Jen and Ko (2010) studied the adhesive dimensions using adhesively bonded aluminum SLJs and found that the fatigue resistance decreased as the overlap length increased with only one exemption of a 0.5 mm adhesive thickness. Melander et al. (1999) concluded that stiffness and fatigue strength are substantially affected by bond defects, based on testing a number of fatigue specimens with artificial bond defects.

Bond-line thickness plays an important role in determining static and fatigue behavior of adhesively bonded joints. Studies show that for a specific joint type and application, it should be optimized to extend the lifetime. Azari et al. (2011a, 2011b) tested the fatigue and quasi-static fracture behavior of aluminum adhesively bonded joints with different bond-line thicknesses from 0.13 mm to 0.79 mm. Double cantilever beam (DCB) samples with toughened epoxy adhesive showed that the fatigue threshold strain energy release rate decreased for very thin bond lines under mode I loading and hardly changed under mixed mode loading. Blanchard et al. (1996) tested a joint with small overlap area but thick substrate with different adhesive thickness and found the fatigue strength was strongly dependent on the strain rate and joint thickness.

Material properties, especially for the modern adhesives with a large amount of plasticity, affect the fatigue behavior of adhesive joints significantly. The studies on material properties

usually involve simulation and modeling work. Kumar and Pandey (2011) computationally simulated the fatigue fracture by considering both geometrical and material nonlinearities and using elastoplastic material models. Markolefas and Papathanassiou (2009) evaluated stress redistribution under fatigue loading using a shear-lag model assuming a linear elastic behavior for substrate but an elastic-perfectly plastic adhesive model. Kumar and Pandey (2006) applied nonlinear finite element analysis to model the fatigue behavior of an SLJ with aluminum substrates. They took into account both material and geometric nonlinearities and using kinematic hardening modeling for adhesive, which accounts for cyclic plasticity. They found that the peel stress in the adhesive layer edge zone grew significantly with failure initiation.

Loading conditions, including type, level, and frequency is another critical factor for determining the fatigue behavior of adhesive joints. Nolting et al. (2008) measured the fatigue failure and lifetime of aluminum double strap joint (DSJ) and found that higher stress could cause adhesive bonding failure while lower stress resulted in substrate failure. Ishii et al. (1998, 1999) investigated butt, scarf, and thick substrate SLJs in order to determine the fatigue failure criterion of adhesively bonded joints under multiaxial stress conditions. They found a similar conclusion as static loading failures, namely, that the fatigue limits were governed by the maximum principal stress except when negative hydrostatic pressure acts in the adhesive layer.

Ursinus (2007) presented a study on cyclic fatigue of adhesively bonded glass fiber reinforced polymer (GFRP) tubes and found that the applied biaxial pipe stress ratio and the type of loading. Knox et al. (2000) carried out experimental tests on adhesively bonded composite pipe joints, inducing fatigue failure by subjecting the joints to an external mechanical loading. They compared the effect of pure axial fatigue loading and cyclic loading and concluded that the former one was more detrimental to fatigue life due to the existence of internal pressure. Takiguchi and Yoshida (2007) conducted a large number of tensile experiments on an aluminum SLJ using a highly ductile acrylic adhesive to understand the effect of pre-strain and loading speed. Experimental results show that the pre-strain did not affect the fatigue life and increasing loading speed can increase the fatigue strength.

Only a few studies can be found with respect to curing conditions, but it should also be considered as part of the manufacturing process. Yang et al. (2011) studied the effect of curing conditions including pressure, temperature, and time on the fatigue performance on carbon fiber

reinforced polymer composites (CFRP) and aluminum bonded joints and optimized the fatigue lifetime within the test range.

4.2.2 Thermal Stress and Fatigue

Thermal stress is created by changes in the temperature of a material. Temperature gradients, thermal expansion, or contraction and thermal shock can lead to thermal stresses. In adhesive joints, the different thermal expansion of adhesive and adherends is the main reason for the thermal stress. Thermal stress also contributes to the fatigue failure, especially when the joints undergo a temperature change. A review on fatigue in adhesively bonded joints by Wahab (2012) revealed that this topic has received limited attention in the literature, as very few studies can be found on thermal fatigue of adhesives.

Banea and da Silva (2010) reported that adhesively bonded steel joints exposed to high temperature (tested at 80 °C) have a decrease in strength by as much as ~30%. Gao et al. (2011) tested and simulated the fatigue lifetime of adhesive films in both hydrothermal aging and thermal cycling, and they found a decrease in fatigue life after longer aging times. As for the thermal cycling, they found that the fatigue life had an initial increase when going through increased thermal cycling, but this eventually decreased. Wu et al. (2016) investigated the effect of thermal exposure on the fatigue characteristics of the adhesive bonded aluminum joints. They found that the fatigue resistance decreased slightly in a high-cycle regime loaded at 40% of the maximum quasi-static strength ($>10^6$ cycles) and significantly degraded in a low-cycle regime loaded at 80% of the maximum quasi-static strength ($\sim 10^3$ - 10^4 cycles); they argued that the reason for degradation was due to adhesive oxidation.

4.2.3 Fatigue Testing in HVAC&R Systems

In order to understand and evaluate the fatigue performance of adhesive joints, a test stand must simulate the joint working conditions of an HVAC&R system. In a review of the available standards, it is found that the specific requirement for adhesive joints in HVAC&R application is given by the ISO standard 14903 (ISO, 2017). Adhesive joints need to go through pressure, temperature, and vibration cycling tests to be qualified for use. As shown in Figure 4.1, the joint under test needs to be subjected to temperature/pressure swings for a certain number of cycles.

The pressure and temperature ranges are to be determined by the manufacturer or application requirements. In the cycling test, a 2-min dwell period should be maintained after reaching the designated maximum or minimum temperature. One complete cycle contains one heating and one cooling process and the complete test should contain 50 cycles.

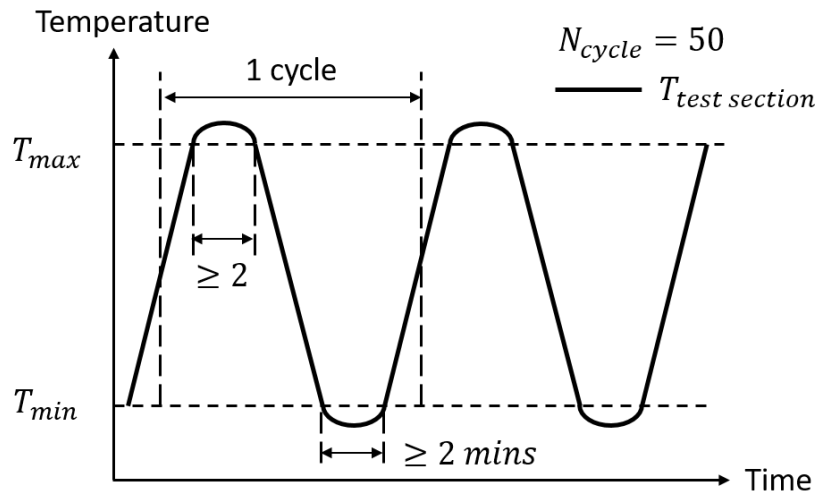


Figure 4.1. Pressure and temperature cycling (PTC) test example adapted from ISO 14903 (2017).

There have been a few pressure and temperature cycling test stands designed in the literature to evaluate refrigerant joints and fittings. Hourahan (1998) described separate test methods to evaluate the pressure and temperature cycling fatigue for refrigerant lines and fittings. The method for achieving thermal fatigue was to heat the pressurized sample to 132 °C and then quench to 4 °C in a water bath. It was observed that a total number of 62,000 cycles without failure could prove that the thermal fatigue failure was not an issue. Separate pressure fatigue cycling tests for rapid pressurization and depressurization of the test samples until failure under multiple stress levels were also described. Wilson and Bowers (2014) designed a test stand for accelerated fatigue testing that was used to evaluate the fatigue performance of flame-free refrigeration fittings. Two separate test stands were designed and built. The thermal shock test stand used a standard vapor compression cycle with a set of solenoid valves to split either hot high-pressure refrigerant or cold low-pressure refrigerant to the test section. The standard four-component vapor compression cycle contained a compressor, condenser, evaporator, and expansion device to provide the hot and cold

refrigerant flow. In both the heating and cooling modes, the vapor compression cycle runs consistently without switching the condenser or evaporator. In order to control the temperature of the test section in the designed range, an additional heat exchanger was installed between the test section and the vapor compression cycle to provide extra heat transfer capacity for condensing the hot gas through the test section without using the condenser in the supporting vapor compression cycle. However, the additional heat exchanger brings challenges in system control and extra cost. The operating range of pressure and temperature are also limited by the hot and cold reservoirs.

The same study by Wilson and Bowers (2014) also proposed a vibration test stand design shown in Figure 4.2. It had two tube supports with one support fixed and the other support oscillating vertically at an amplitude of ± 3.0 mm. The oscillations are the result of a four bar mechanism coupled to a rotating motor with an eccentric shaft.

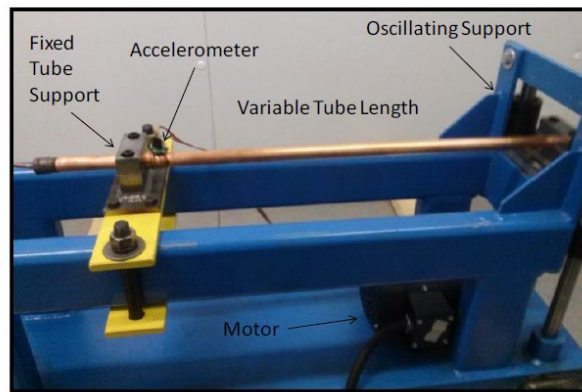


Figure 4.2. Vibration test facility from Wilson and Bowers (2014)

4.3 Proposed Adhesive U-joints for Testing

This section introduces the U-joint geometry that is selected for the fatigue testing. The aim of the selection is to validate the usage of adhesive joints in the assembled state, in this case, U-tube joints in the tube-and-fin heat exchanger, as shown in Figure 4.3. During the tube-and-fin heat exchanger manufacturing process, the copper tubes will be inserted into the pre-made fin plates with openings at both ends. The U-shape joints will then be used to connect the tube ends to form a closed flow path for the refrigerants. There is usually a lot of U-joints needed for tube-and-fin heat exchangers and two tube-to-tube joints are required for a single U-joint, which makes this the most number of joints existing in HVAC&R systems (if using tube-and-fin heat exchangers).



Figure 4.3. Copper and aluminum U-joints used in the tube-and-fin heat exchangers

Due to the large number of U-joints in the tube-and-fin heat exchangers and the interest from the industrial partners, a U-joint geometry is selected as the joint type to be tested. The U-joint has a tube diameter of 3/8 inch based on industry recommendation, with a geometric size shown in Figure 4.4. Certain adhesive formulas will be selected based on the recommendation of the industry partner for the assembly process. The U-joints test sections will be built based on a culmination of all knowledge and experience gathered throughout the project. The following test stands that will be introduced in this chapter are all designed to test the given U-joints.

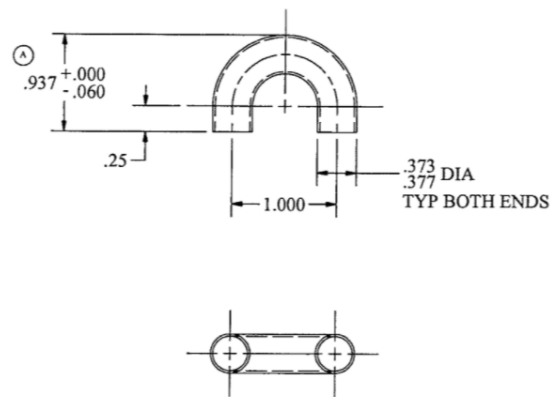


Figure 4.4. Geometric size of the U-joint for testing

4.4 Pressure and Temperature Cyclic Testing for Thermal Fatigue

As reviewed, the fatigue failure of adhesive joints is highly determined by the joint shape, geometry, materials, and operating conditions. For the purpose of this study, a pressure and temperature cycling (PTC) test stand is developed to investigate the thermal fatigue of adhesive (or other) joints in HVAC&R systems. The test stand generally follows the guidance of the ISO 14903 standard, with some interpretation and modifications to better simulate and investigate the joint performance in real HVAC&R systems.

Joints in a standard vapor compression system will experience both steady state operation and stop/start cycles, as most systems are designed to cycle on and off based on the load. For example, air conditioners, heat pumps, and refrigerators in domestic applications can all easily cycle on and off several times a day. In these systems, there are several common refrigerants including R22, R134a, R410A, etc. In this study, R410A is selected as the working fluid for the test stand because, of these common refrigerants, it has the most extreme operating temperature and pressure ranges. An R410A vapor compression cycle running at room temperature can experience severe conditions with large variation and high absolute values for pressure, where the high side pressure is approximately 4 times the pressure of R22 or 8 times the pressure of R134a, operating at similar temperature conditions. Compared to past literature having the same objective, instead of using a vapor compression cycle with both an evaporator and condenser to perform the pressure and temperature cycling, a new type of PTC test stand is introduced that leverages a hot-gas bypass vapor-compression cycle to induce the cycling, which simplifies the system architecture and enhances the controllability and operating range.

4.4.1 Test Stand Design

The test stand was designed to provide combined pressure and temperature cycling. To evaluate the reliability of joints at different temperature and pressure typical in HVAC&R systems, a test stand must control both the evaporating and condensing temperatures as desired. A standard vapor compression cycle as described previously can be used for this testing, but with extra difficulty in changing between the hot and cold source temperature due to the unbalanced condensing and evaporating load in different modes. Splitting of flow between the test section and vapor compression cycle is critical to the safe operation of the test stand, with an additional heat

exchanger required. It also needs two heat exchangers connected to two different constant-temperature sources for the condenser and evaporator. In order to provide the hot and cold gas for the cyclic testing, an alternative hot-gas bypass (HGB) method is used. The HGB method removes the evaporator from the standard vapor compression cycle by adding a hot-gas bypass line with three sets of valves used to control the high-side pressure, low-side pressure, and mass flow rate in the system. It is a well-studied technology and widespread for compressor development and R&D activities in both subcritical refrigerants such as R134a (Zhang 2018), R410A (Schmidt 2018) and supercritical refrigerant CO₂ (Kurtulus et al., 2014). Its comparability with various refrigerants and easy-to-control feature fits the PTC test purpose perfectly. The hot and cold gas can then be simply redirected to a test section containing the joints using two sets of solenoid valves in the discharge and suction lines, without flow splits between the test section and the vapor compression cycle. The full heating or cooling load are used in the test section without additional heat exchanger. There are three operating modes for the system: a non-testing mode where the test section is sealed off from the normally operating hot-gas bypass loop; a heating mode in which the solenoid valves direct the hot gas through the test section; and a cooling mode in which cold gas is directed through the test section. The corresponding schematic figures for each of these operating modes are shown in Figure 4.5. Note that not all the supporting in-line parts are shown in the schematic figures. Non-critical valves and sight glasses used for practical start-up, control, and operation of the facility are omitted for simplicity.

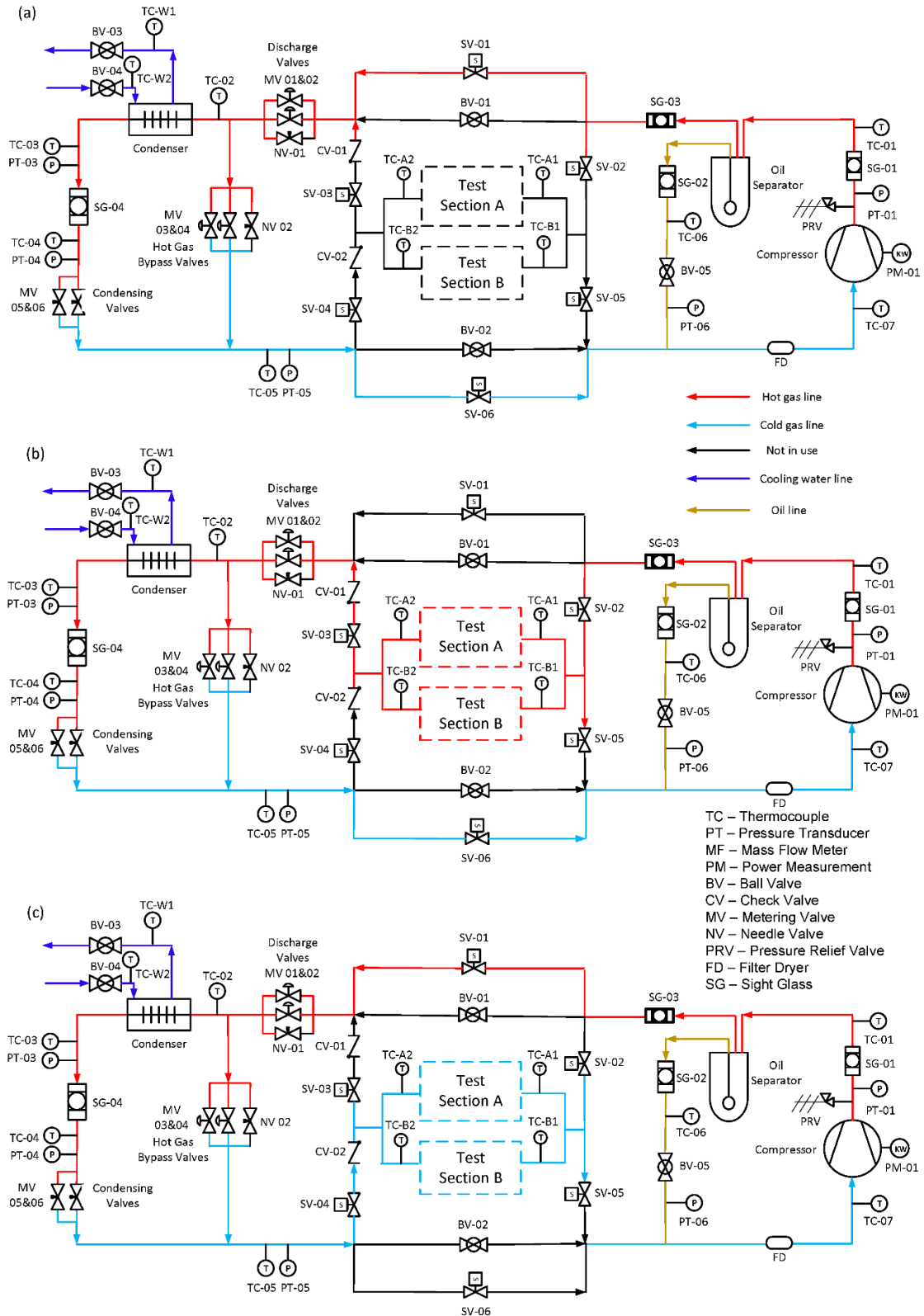


Figure 4.5. Schematic diagram of the developed pressure and temperature cycling test stand with hot-gas bypass control under (a) non-testing, (b) heating, and (c) cooling modes.

Regardless of the operating mode, the HGB loop itself works in the same way outside the test section, which is best illustrated by the red (high temperature/pressure) and blue (low temperature/pressure) flow lines in the schematic diagram in the non-testing mode (Figure 4.5a) where all flow is diverted around the test section. High pressure and temperature gas comes out of the compressor into the oil separator. At the oil separator outlet, the first set of solenoid valves (SV01 and SV02) controls the hot gas into the test section. After the test section, there is a set of discharge valves (MV 01&02 and NV 01) to control the discharge pressure and temperature. After the discharge control valves, the hot gas is split into two streams: one to the condenser liquid line and one to the hot-gas bypass line. A set of hot-gas bypass valves (MV 03&04 and NV 02) are placed after the discharge valves and in front of the suction line, and a set of condensing valves (MV 05&06) are placed after the condenser outlet. Refrigerant from these two lines mixes downstream of these control valves and becomes the single suction gas line to the compressor with low pressure and temperature.

These sets of valves are used to control and maintain three different pressure levels within the HGB loop: the discharge pressure, intermediate (condensing) pressure, and suction pressure. The condenser is cooled by a constant-temperature cold-water loop, which fixes the condensing pressure based on the temperature. With this relatively constant intermediate pressure, the discharge pressure and suction pressure can be changed freely over a relatively large range. For example, if a higher discharge pressure and temperature is needed, reducing the opening of the discharge metering valve will raise the pressure (increase the pressure difference between the condensing and discharge pressure). Similarly, reducing the opening of the suction valves can decrease the suction pressure as well as the suction temperature.

Another important feature of this test stand design is that the mass flow rate can also be controlled by adjusting the three sets of the valves. Changing the metering influences not only the pressure drop across the valve but also the mass flow rate. This is utilized to control the superheat at the inlet of the compressor and the mass flow rate in the system. When the refrigerant vapor is compressed, work input by the compressor also increases the temperature of the refrigerant. If the refrigerant were to be expanded back to the inlet pressure of the compressor without a commensurate amount of heat rejection out of the cycle, the refrigerant would continue to become hotter. To account for this heat input to the refrigerant, and to achieve the appropriate superheat at the inlet to the compressor, the ratio of mass flow of the refrigerant through the condensing line

and through the hot-gas bypass line is adjusted by actuating the respective valves. Because refrigerant in the bypass line is higher temperature vapor, opening the hot-gas bypass valves will increase the refrigerant temperature into the compressor. Conversely, when more refrigerant is routed through the liquid (condenser) line, the compressor inlet temperature is decreased. The relative ratio of these two mass flows of different enthalpies determines refrigerant enthalpy at the compressor inlet. This balance is used to achieve the desired superheat at the compressor inlet and also determines the total mass flow rate of the system.

After the HGB loop reaches the desired operating condition, the solenoid valves within the test section are used to switch between the heating and cooling modes to perform a cycling test. The heating condition is achieved by connecting the test sections with compressor discharge tube to flow the hot gas into the section before going into the condenser by opening SV-01, SV-02 and SV-03, as shown in Figure 4.5b. After finishing the heating condition, SV-02 and SV-03 close and disconnect the test sections from the compressor discharge. The cooling condition starts by turning SV-04 and SV-05 on to flow the mixed cold gas into the test section, as shown in Figure 4.5c. The mixed cold flow will then go back to the compressor to close the loop. The next heating condition follows the cooling condition. The cycle is repeated by switching the valves alternately. In both heating and cooling modes, the HGB loop can operate stably and continuously due to the relatively small thermal capacity from the test sections.

4.4.2 Test Sections and Conditions

There are two identical test sections installed in the test stand. At the inlet and outlet of each test section, connectors are installed to ease the connection of new samples into and out of the test stand. In the current study, in order to have a reference sample for evaluation of the fatigue resistance of the adhesive joints, brazed joints are tested in one of the test sections. The adhesive joints in the other test section are manufactured and assembled by 3M with a pre-machined fixture using a toughened, two-part epoxy structural adhesive. The brazed joints are made at Purdue University by a qualified technician. U-tube joints are selected as our testing samples due to the large number of them in the tube-and-fin heat exchangers. The U-joint has a tube diameter of 0.375 mm (3/8 inch) based on industry recommendation. The center-to-center distance between the two tubes is 25.40 mm (1 inch).

A 3D model for a test section is shown in Figure 4.6. Each test section has a 10 U-bends in series (20 total joints) that are connected by straight tubes that are clamped down in a fixture plate. The lengths of the tubes are kept as short as possible (50.8 mm) to minimize the heating/cooling time (i.e., thermal capacity) of the test section, and also to decrease the amount of hot/cold gas trapped in the test section when switching between the heating and cooling condition. All the test sections are leak-checked using water-immersion method with nitrogen charged to ~ 1700 kPa (250 psi) before testing to ensure that they were leak-free.

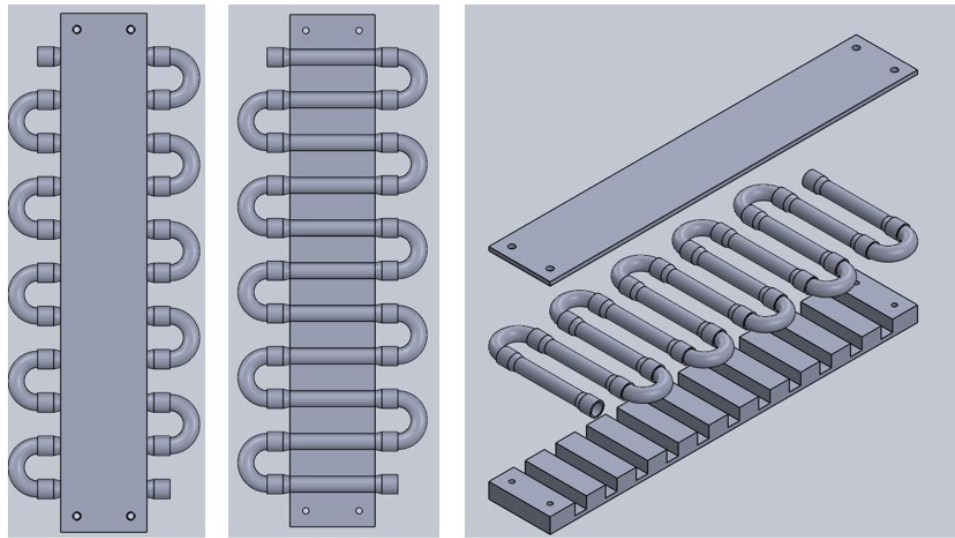


Figure 4.6. 3D model for the fixture plate with adhesively bonded U-joints

The pressure and temperature test conditions for the test section of the hot-gas bypass test stand is mainly determined by the selected compressor and valve openings. Based on the test stand size and capacity, a 2.5-ton single stage reciprocating compressor designed for R410A is used. Based on the data and compressor map provided by the manufacturer, the possible test conditions are calculated using Engineering Equation Solver (EES) assuming no pressure drop. The results are summarized in Table 4.1. These calculations assume operation with a 20 K superheat at the compressor inlet.

Table 4.1. Simulation results for the typical operating conditions of the Hot Gas Bypass Test stand with selected compressor

$T_{suction}$ (°F/°C)	$T_{discharge}$ (°F/°C)	$P_{suction}$ (kPa)	P_{cond} (kPa)
10/-12.2	263/128.3	351.6	2297.3
30/-1.1	238.1/114.5	529.9	2798.6
50/10	229.7/109.8	770.1	3388.8
60/15.6	234.9/112.7	917.7	3834.9
60/15.6	246.7/117.9	917.7	4074.8

The specific set points during testing are decided from this possible range of operation of the system so as to understand the fatigue caused by temperature and pressure variations. The discharge temperature and suction temperature are the most extreme possible temperatures that the test section can experience. The lowest temperature should be above the freezing point of water to avoid freeze/thaw cycles that can potentially have other unintended influences on the fatigue failure. Also, the highest temperature is limited by the compressor discharge overheat protection, which shuts down the compressor when the temperature is too high. Based on this limit, system temperatures typically do not exceed 100 °C in vapor compression cycles with common refrigerants. Thus, the operating condition in the third row of Table 4.1 can be an potential test condition for the given test stand, which thereby will cycle the test section (at maximum) between 10 °C and 109 °C. However, note that the actual temperature swing will be smaller than this due to the heat transfer between the environment and tubes leading to the test section. Ultimately, the test condition temperatureswings should be decided by the application. During the test, the condensing temperature, suction temperature, subcooling, and superheat are adjusted to achieve this desired testing condition.

4.4.3 Cycling Procedure and Instrumentation

In order to achieve the designed cyclic function described in Section 4.2.3, the control algorithm for one single cycle is described below and summarized in Table 4.2. The following steps are repeated to carry out the pressure and temperature cycling test:

- Step 1: Power off all valves and open BV 01&02; start the HGB loop and allow it to reach steady state
- Step 2: Open SV 01&06 and then close BV 01&02 to run the test stand in the non-testing mode
- Step 3: Open SV 02&03 and then close SV 01 to switch to heating mode; allow test section to reach set temperature
- Step 4: Open SV 01 and then close SV 02&03 to reset back to non-testing mode with hot gas in the test section
- Step 5: Open SV 05 to let the high temperature and pressure gas flow out of the test section
- Step 6: Open SV 04 and then close SV 06 to switch to cooling mode; allow test section to reach set temperature
- Step 7: Open SV-06 and then close SV 04&05 to resets back to non-testing mode with cold gas in the test section
- Step 8: Repeat steps 3-7 to achieve the required cycle numbers or until a failure

Because the solenoid valves in the test sections are operating directly between the high-side and low-side pressures, there is a high pressure difference across the valves. Solenoid valves designed for R410A are selected (SPORLAN E series) due to their high maximum operating pressure difference, selecting the appropriate valves to be compatible with the suction and discharge tube sizes (ME9S240-HP and ME14S250-HP). These solenoid valves have a pilot-operated disc construction intended for use in refrigeration and air conditioning applications and can operate manually with a lift stem. The coils are selected (MKC-2; 24 VAC) to give the largest maximum operating pressure difference of 31 bar (450 psi), which satisfies the test stand requirements. Preliminary testing found that the solenoid valves would not always fully close fully in the presence of a high pressure opposite to the flow direction. In order to ensure consistent full closure of the solenoid valves and to avoid backflow when switching between the test modes, two additional check valves are installed in the test section lines (CV 01&02).

The refrigerant temperature and pressure in the test sections are monitored and recorded. Pressure transducers (PT 01 & 06) are installed at the inlet of the test section. The temperatures are measured with two thermocouples (TC A1 & A2 and TC B1 & B2), one placed at the test section inlet and the other one at the outlet. The HGB test stand is equipped with several additional

T-type thermocouples to measure the temperature at various locations, gauge pressure transducers to measure the pressures, and a power meter to measure the compressor power consumption. A Coriolis mass flow meter is used to measure the refrigerant vapor mass flow rate after the oil separator. The sensor specifications are listed in Table 4.3.

Table 4.2. On/off status of solenoid valves under different test conditions

	Non-Testing Mode	Heating Mode	Cooling Mode
SV-01	ON	OFF	ON
SV-02	ON	ON	OFF
SV-03	OFF	ON	OFF
SV-04	OFF	ON	OFF
SV-05	OFF	OFF	ON
SV-06	OFF	OFF	ON

Table 4.3. Sensor specification for the hot-gas bypass test stand

Sensor	Model	Range	Accuracy
Thermocouple	Omega TMQSS-125T-6	0 – 350 °C	1.0 °C OR 0.75% Full Scale
Pressure Transducer	Honeywell PX2AF1XX500PAAAX	0 – 500 psia	0.25 %
Pressure Transducer	Omega PX176-1KS5V	0 – 1000 psig	1.0 % Full Scale
Power Meter	Ohio Semitronics GW059-EG	0-20kW	0.04% Full Scale
Mass Flow Meter	MicroMotion CMF050	0-0.6055 kg/s	0.5%

4.4.4 PTC Test Stand Performance

After test stand construction and leakage testing, multiple tests with different operating conditions were carried out to confirm the operational capabilities of the test stand. The first testing operated the HGB flow loop at steady state, without engaging the test section, to confirm that it could achieve the designed range of testing conditions. At steady state, the temperature can be controlled to achieve as low as ~0 °C at the compressor inlet and as high as 110 °C at the

compressor outlet, with respective inlet and outlet pressures of ~ 350 kPa and ~ 4600 kPa. Note that in the HGB test stand, these pressures are intrinsically coupled to the temperature ranges based on the choice of the refrigerant. After confirmation of this functionality, the cyclic testing capability of the facility is evaluated following the procedure described in Section 4.4.3. Figure 4.7 shows the representative transient temperature profiles during several cycles. The figure shows the temperature cycles at the inlet and outlet of the test section (T_{in}, T_{out}), along with the discharge (T_{dis}) and suction (T_{suc}) temperature of the compressor that are intended to be kept steady. In this figure, the compressor discharge state is controlled at ~ 70 °C and ~ 3750 kPa, while the suction state is at ~ 3 °C 700 kPa. In this testing, the compressor discharge and suction temperature stays stable except during mode switching. The temperature of the test section oscillates when mode switching happens approximately at 800 s, 1000 s, and 1300 s, as indicated by the vertical dashed lines in Figure 4.7. The heating process raises the test section from ~ 10 °C to ~ 50 °C in ~ 120 s, while the following cooling process takes ~ 80 s. The hot-gas bypass test stand ensures that the duration of the heating and cooling parts of the cycle are determined only by the thermal mass of the test section itself. Following the standards introduced in Figure 1, these lengths of time satisfy the minimum two-minute dwell period at the desired temperature. One full cycle period is ~ 7 min, with a 10 - 50 °C temperature swing; the 50-cycle test as required by the standard then takes ~ 6 hr to finish.

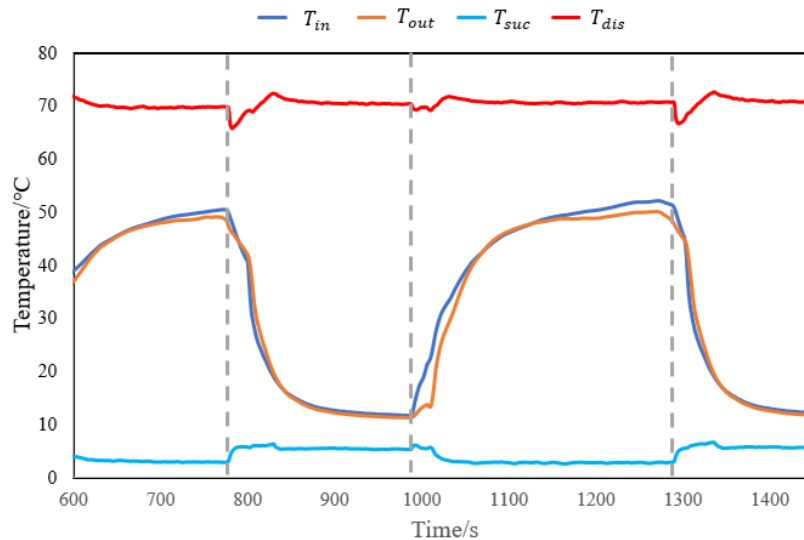


Figure 4.7. Temperature of the compressor inlet and outlet as well as the temperature of the inlet and outlet of the test section for one complete cycle

There is a slight difference between the test section inlet and outlet temperatures when the test section is at a relatively high temperature, which is due to heat losses to the environment from the test section. Also, there are temperature fluctuations in the suction and discharge lines each time the test stand switches between modes, which is caused by the release of hot/cold refrigerant from the test section into the system. It is noteworthy to point out the temperature difference between the hot/cold gas lines in the system and the test section temperatures. For example, in Figure 4.7, the refrigerant temperature at the compressor discharge is ~ 20 °C higher than the maximum test section reached at the end of the heating mode. Likewise, in the cooling mode, the refrigerant at suction of the compressor is ~ 10 °C lower than that at the test section. The major reason for this temperature difference is the heat transfer to the environment along the refrigerant lines. Although all the tubes and components are well-insulated, there are still heat transfer due to the large temperature difference with respect to ambient, especially from the compressor discharge to the test section, where the refrigerant must travel through the oil separator and addition tube lengths. The highest test section temperature that can be achieved in the current facility is 80 °C with a compressor discharge temperature at 105 °C; the lowest temperature achieved is -5 °C in the test section but it can go much lower with decreasing the suction pressure. However, as discussed previously, the low temperature is maintained above 0 °C to avoid freezing and thawing of the joints.

After demonstrating temperature cycling of the test section and determining the cycle time, a full 50-cycle test was performed following the test standard. The test stand performs as designed, as indicated by the results in Figure 4.8, which shows the temperature and pressure of the compressor inlet and outlet as well as the temperature of the inlet and outlet of the test section. The total testing time required for all cycles is only 5 hrs. The average discharge temperature of the compressor is 56.2 °C at a pressure of 3364 kPa. The average suction temperature and pressure are 3.6 °C and 771 kPa, respectively. In the test section, the highest temperature measured during the cycling is 43.4 °C and the lowest temperature is 9.2 °C. During the testing, a time-periodic fluctuation in the suction/discharge temperatures and pressures can be observed due to the switching of the solenoid valves.

Before and after the 50-cycle PTC test, both the brazed joints and adhesive joints in the test sections are leaked checked using the water-immersion bubble test method as suggested by ISO 14903 without any leakage detected.

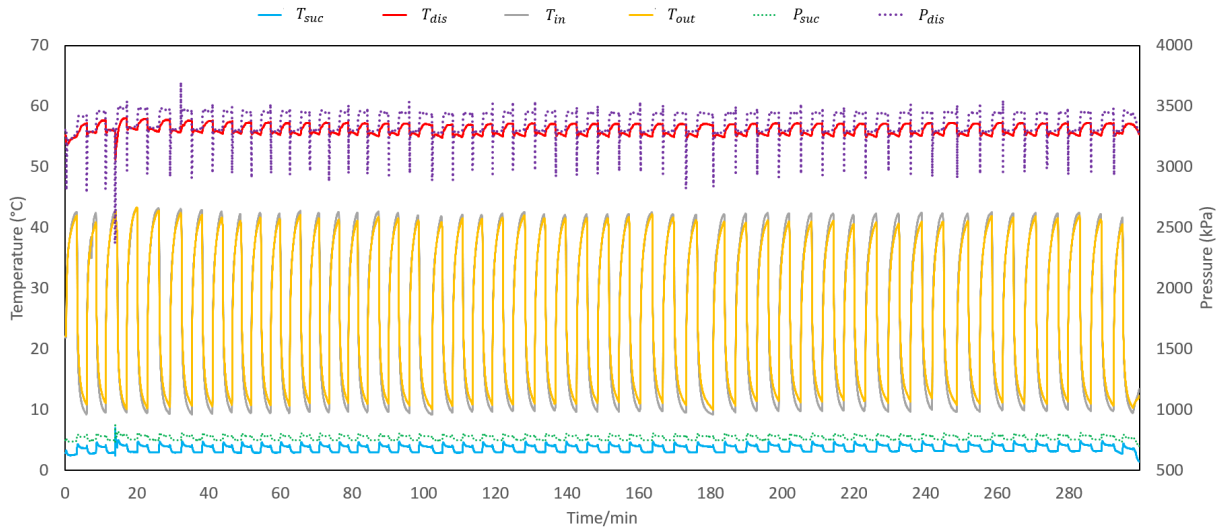


Figure 4.8. Temperature and pressure of the compressor inlet and outlet as well as the temperature of the inlet and outlet of the test section

4.4.5 PTC Test Conclusion

In order to design and evaluate new joining technologies that meet the requirements for the HVAC&R industry, it is important to developing testing methods to evaluate the influence of pressure and temperature cycling on fatigue of the joints. An innovative test stand is designed, built, and demonstrated to simulate the pressure and temperature cycling of joints in an HVAC&R system in an accelerated manner. The test stand applies hot-gas bypass control to reduce the cost and time of cycling operation. The test stand is shown to successfully perform the pressure and temperature cycling test as designed for the assessment and evaluation of adhesive joints, while satisfying the ISO standard 14903. Testing confirms that a full cycle of heating and cooling the test sections can be finished in a period 7 min with controlled temperature and pressure oscillations. In a demonstration of the technique, a 50-cycle PTC test was performed with temperature cycles from ~10 °C to 40 °C and finished in 5 hr. Both the brazed joints and adhesive joints installed in the test sections were confirmed to be leak-free after the testing, which indicates that adhesive joints have thermal fatigue resistance under the given testing condition. A suggested future modification based on the current results is to reduce the heat loss from the test stand lines by using better insulation and reducing the tube length, which would allow evaluation of the joints up to higher maximum temperature. Solid state relays can be easily used to control the solenoid valves in the test stand for long-term testing of joints using this facility. The test stand developed in this

work serves as new research infrastructure for the pressure and temperature fatigue testing of joints and allows for research and development of new joining technologies and other components for HVAC&R applications.

4.5 Vibration Testing for Vibrating Fatigue

Failure in HVAC&R joints caused by vibration is a major concern. Although the PTC testing design test the joints in a real operating system with vibration from the compressor motor and cooling loop flow, the PTC test cannot give accurate measurement on vibration data. Table 4.4 shows vibration test parameter for the joints as requested by ISO Standard 14903 (ISO, 2017). The needed vibration displacement and number of excitations are given based on the different tube sizes and requires precise control. To better study vibration induced fatigue, a separate vibration test is proposed to simulate the field vibration in HVAC&R systems using a shaker test stand available at Ray W. Herrick Laboratories, Purdue University.

Table 4.4. Vibration test parameters for joints from ISO Standard 14903

Pipe Diameter (mm)	Length (mm)	Displacement (mm)	Frequency (Hz)	Number of excitation
< 10		0.30		
≥ 10 and < 20	200	0.25	≤ 200	2 000 000
≥ 20 and < 30		0.20		
≥ 30 and ≤ 50		0.15		

4.5.1 Experimental Setup

The separate vibration test is performed using a shaker test stand. The test system produces controlled vibrations to evaluate the reliability of components used in various applications.

It is a vibration test system TV 59335/*-440 from TIRA Schwingtechnik. The test system reproduces vibration environment under laboratory conditions for testing the reliability in all fields of applications of vibration testing technology. The test system is ideal for performing the 2,000,000 vibration cycles needed since it is designed for long-time operation with a built-in automatic, pneumatic operated load compensation system that allows the nominal vibration

displacement. The shaker is cooled by an air-cooling fan, which sucks the air via a filter to make sure no external heat influence the testing parts. The TIRA “AIT” system is a vibration unit integrated in the frame for guiding the shaker horizontally and vertically. It guarantees the optimum vibration isolation and guides the shaker body in the direction of the excitation at low frequencies. The system is also equipped with an amplifier and vibration control system to establish proof of the reliability. The technical specification for the vibration generator is shown in Figure 4.10 and the technical specification for amplifier is shown in Table 4.5.



Figure 4.9 Pictures of the shaker test stand (left) and its base plate (right)

Rated peak force Sine _{pk} /Random _{RMS} /Shock _{pk} ¹	35000/32000/105000 N
Frequency range	5 - 3000 Hz
Main resonance frequency	> 2400 Hz
Max. displacement Peak-Peak ²	50.8 mm
Max. velocity Sine/Random/Shock	2.0/1.8/2.5 m/s
Max. acceleration Sine/Random/Shock ¹	100/67/207 g
Suspension stiffness	150 N/mm
Effective moving mass	38.0 kg
Max. weight tested	610 kg
Weight with trunnion RIT/AIT/LB*	2350/2700/2250 kg
Magn. stray field std./low degaussing	<1.5/<0.8 mT
Armature diameter	440 mm
Required compressed air supply (load-dependent)	600-1000 kPa
Interlocks	Temperature, displacement, cooling air, overcurrent, compressed air

Figure 4.10. Technical parameters for vibration exciter S 59935/*-440

Table 4.5. Technical specification for amplifier A 3 08 3 057

Parameters:	Value:
KVA ratings	57000VA
Frequency range	DC – 4 kHz
Max. current and voltage	150 V and 375 A
Load resistance	1 Ohm
Input voltage	2.5/5/10 V
Distortion	< 0.7 %
Signal to noise ratio	> 90 dB
Max/ field current and voltage	150 V and 75 A
Dimensions	600 × 2200 × 800 mm

Due to the large number of U-joints that are present in tube-and-fin heat exchangers, this joint geometry is selected for vibration testing. For this geometry, a U-bend tube is joined at both ends to straight tubes, as shown in Figure 4.11. These two tube-to-tube joints are formed by flaring the straight tube for insertion of the U-bend with adhesive, rather than using a coupling. The outer tube diameters are 9.525 mm (3/8 inch) and the straight tube lengths are 152.4 mm (6 inches). A custom adhesive formulation from an industry collaborator (with characteristics similar to the previous one) is used for the joining process, which was performed by the industry partner. Two different sets of U-joints were tested: one set of 8 samples with adhesive joints and another set of 8 samples having brazed joints. Two types of joints are tested simultaneously for comparison.

The vibration exciter generates the vibrations of a specified frequency and displacement to drive the base plate. It is important to firmly clamp the U-joints to the base plate for both safety and accuracy of the testing. For this purpose, aluminum fixtures are custom-designed and fabricated to clamp the extended straight tubes while leaving the U-joints to hang freely at the end, similar to their configuration in tube-and-fin heat exchangers. The 3D drawings of the fixtures are shown in Figure 4.12. The bottom plate of the fixture is affixed to the shaker base plate using bolted connections through two large clearance holes. The bottom and top fixture plates are attached using bolted connections; eight bolts pass through clearance holes in the top plate and thread into the bottom plate. At the interfacing surfaces between these two plates, there are 16 half

cylinder cavities designed to clamp the extended tubes of the samples. Black rubber sheets taped on the extended tubes between the plates and samples provide cushioning and fix the samples in place. The diameter of the cavity is sized to be slightly smaller than the outer tube diameter plus the thickness of the rubber sheet, such that the copper tubes are pushed firmly into place with compression of the black rubber sheets. Figure 4.11 shows a photograph of the two sets of U-joints with fixtures installed on the shaker test stand.



Figure 4.11. Photographs of the U-shape joints with adhesive (left) and the fixtures containing a set of 8 samples each installed on the vibration shaker test stand.

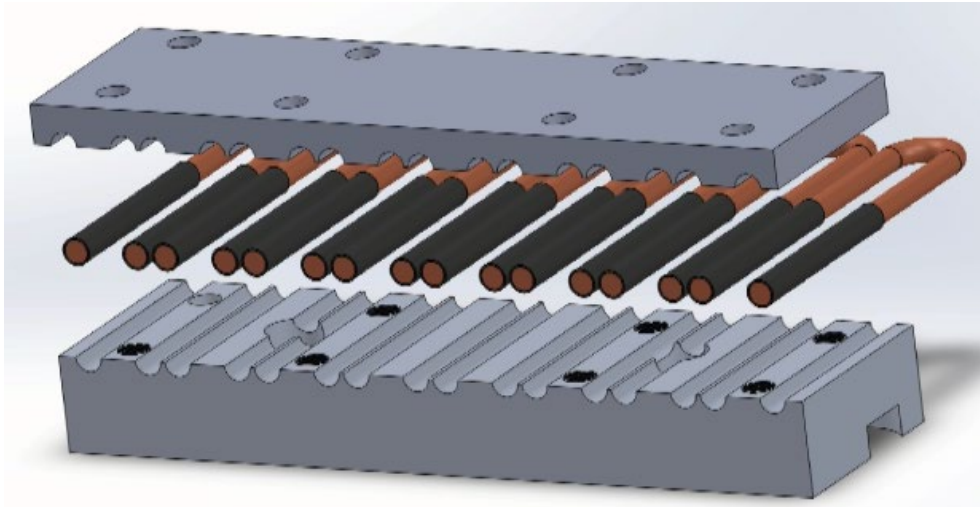


Figure 4.12. 3D Drawing of the fixture assembly with U-shaped joints wrapped with black rubber sheet.

4.5.2 Testing Procedure

Following Table 4.4, the fixtured joints are subjected to vibrations with 0.3 mm displacement at a frequency of 125 Hz. The total number of the excitations is 2,000,000. The displacement and frequency of the test section are monitored and measured throughout the test. The joints are not pressurized with any fluid during the vibration testing in case of failure.

Before and after the vibration testing, the U-joint samples are each visually inspected and checked for leakage. Before vibration testing, fittings are soldered to the open end of the extended tubes to allow charge the samples with high-pressure nitrogen. During the soldering process, the U-joints were cooled using wet cloths to keep the temperature near room temperature. The samples with fittings are charged to 1700 kPa (approximately 250 psi) and immersed in water to observe if there are any air bubbles. The fittings are unsoldered and removed before placing the sample into the fixtures. The same process is repeated after the vibration testing.

4.5.3 Results and Discussion

Before vibration testing, there were no cracks or imperfections in the adhesive or brazed joints, and all the samples were leak-free. The in-situ test stand measurements confirmed that the samples were subjected to 0.3 mm displacement vibrations at 125 Hz; the acceleration for the shaker was 21.2 g. The test stand ran continuously for 4.5 hours, which resulted in a total of 2,025,000 excitations. After testing, the rubber sheets used for fixing the samples into place were worn as expected, but the copper surface and the joints appeared the same as before testing for both brazed joints and adhesive joints as shown in Figure 4.13. All the samples were confirmed to be leak free after testing. The results demonstrate that the adhesive joints are able to survive these extreme vibration conditions just as the brazed joints without any failures.



Figure 4.13. Photographs of the U-shape joints after the vibration test for adhesive joints(left) and vibration joints compared with brazed joints (right).

4.6 Summary and Discussion

In this chapter, the thermal fatigue and vibration fatigue of adhesive joints were investigated by two separately designed qualification tests. The tests refer to the ISO standard and previously reported tests in the literature. In both tests, adhesive joints were tested in parallel with brazed joints to go through extreme thermal or vibration loading conditions. All the samples were leakage checked before and after the testing, and all of them were leak-free after the testing, which indicates the pass of the qualification test according to the standard. It is confirmed that adhesive joints can be a potential alternative when dealing with thermal and vibration fatigue in the common working conditions of HVAC&R systems. However, due to the nature of this study, the long-term (~10 years) reliability test for adhesive joints is not performed at the current stage. It will be beneficial to develop prediction model on tube-to-tube joints to further understand the fatigue failure and the possible effect of each parameters. The detailed model development and results are reported in the next chapter.

5. ANALYTICAL MODEL OF STRESS AND STRAIN IN ADHESIVE TUBE-TO-TUBE JOINTS

This chapter discusses the modeling approach for the prediction of stress and strain distribution in tube-to-tube adhesive joints under static loading with thermal strain. The chapter first reviews the existing modeling techniques including theoretical and numerical methods for tube-to-tube joints and adhesives. The detailed model setup and boundary conditions, including the underlying assumptions, and details of the governing equations and solution techniques are reported next. Lastly, the accuracy assessment and modeling results are reported and discussed. The influences of the thermal expansion and inner tube pressure are further analysed to provide insights about the possible failure. The purpose of the modeling is to better understand influence of joint geometry, adhesive properties, and loading conditions to accurately predict the potential adhesive failure and optimize the performance. This modeling effort builds a framework to provide criteria and instructions on designing adhesive joints across different HVAC&R applications.

5.1 Introduction

Considering the diversity of fields and applications that HVAC&R systems present, it is challenging to build test stands to physically test all possible adhesive joints geometries and boundary conditions. A simulation model is necessary to virtually evaluate the performance and failure of different geometric sizes under various operating conditions.

The simulation model will be built combining the known properties for the adhesive that are provided by the manufacturer. Due to the wide application of adhesive joints in many mechanical structures, investigation of adhesive joint strength and stress distribution and failure prediction has drawn significant attention over the decades. Different modeling and solution method have been provided in the literature. In order to satisfy the safety and reliability analysis, stress and deformation analyses are usually the key targets. The analysis starts with examining the equilibrium of the joints with stress-strain and compatibility equations. Solving the set of governing equations thereby developed can be done either analytically or numerically. Both techniques are reviewed in detail in the following section.

The ultimate goal of this study is to build a comprehensive tube-to-tube joint model where not only the static loading but also the effect of thermal expansion under temperature change will be considered. The model can provide the basis for the design of the new adhesive joints, formulating equivalent strength limits, and predicting the failure for the joints. The model can also be used to design new adhesive joints and new fittings as well as optimize the geometry for different size fittings.

5.2 Literature Review

A literature review of the adhesive properties and general fracture criteria used in the modeling effort has already been described in Chapter 2. In this section, only the detailed adhesively bonded tube-to-tube joint modeling work is reviewed.

5.2.1 Analytical Models

Adhesively bonded tube-to-tube joints are commonly encountered in engineering applications and have been investigated by the pioneers in structural analysis. Different loading conditions, assumptions, and geometries have been studied. One of the earliest models for tube-to-tube joints can be traced back to Lubkin and Reissner (1956). However, over the past several decades, although the use of the adhesives is widespread, the research work on tube-to-tube joints in the technical literature is considerably less compared to planar geometries such as single or double lap joints (Dragoni and Goglio, 2013).

Lubkin and Reissner (1956) developed an approach for predicting normal and shear stress distributions in adhesive layer of tube-to-tube joints under axial loading. They considered the tube-to-tube joints in an axisymmetric configuration and applied several assumptions used for flat single lap joints. The tubes used in the joints are assumed to be thin shells subjected to tension forces, shear forces, and bending moments, but the adhesive is treated as an elastic medium with shear and peel stress. The solid tubes are assumed to not shear while the adhesive is assumed to not sustain normal stress. The stresses are assumed to be constant over the adhesive thickness. The model then used equilibrium equations and stress-strain relations to construct the set of governing differential equations. Results are reported in terms of normalized shear and peel stresses for 48

cases with different data. The authors also pointed out the solution was possible using standard method but no explicit form was provided.

Terekhova and Skoryi (1972) examined the stress field in bonded tube-to-tube joint under external loads and internal pressure, with axial forces uniformly distributed on the faces of the shell. The authors assume both the tubes and adhesive are elastic thin-walled structures such that the bending rigidity is negligibly low. The adhesive thickness is also assumed to be small such that the shear and rupture stress are constant across the thickness. The set of governing equations and their solution procedure are then introduced in detail. The authors report the distribution of stresses from the axial force loading and the internal pressure.

Shi and Cheng (1993) proposed a different model that included the case of thick tubes, providing a wider range of application. The loading condition is only axial loading. In their work, the axisymmetric assumption is also applied to simplify the stress states in the tubes. The axial normal stress in the adhesive is negligible. The model is built in cylindrical coordinates using the equilibrium equation and compatibility equations. The authors report in detail the manipulation of the equation set and eventually use the minimization of the complementary energy to solve the set of equations. Although the authors claim that their method yields a closed-form solution, it is not reported explicitly. Two examples (one for thin tubes and one for thick tubes) with numerical results are given.

Nayeb-Hashemi et al. (1997) investigated the behavior of tube-to-tube joints under axial and torsional loadings. The paper also discusses the fatigue life evaluation for the joints and concludes that the failure of the tubular joints not only depends on the applied loads, but also on the tube geometry, material properties of adhesive / tubes, and the defects in the joint. The shear distribution in this model is calculated using the shear lag model. It is assumed that the adhesive is only subject to shear loading and the adherend only subject to axial loading. However, the model considers the variation of the shear stress across the adhesive thickness. It is worth noting that the effect of a void on the maximum shear stress is also obtained. Under the torsional loading, the assumption is made that the adhesive is to shear only in the circumferential direction, neglecting its other deformation. The variation of the shear stress across the adhesive thickness is solved. Eventually, the failure of adhesively bonded tubular specimens under axial, torsional, and combined axial and torsional loadings is obtained. The model can predict the fatigue life of the tubular joints under cyclic loading reasonably well.

Pugno and Carpinteri (2003) develop a solution for the tube-to-tube joints using shear lap model and optimize the joint geometry by variation of the tube cross section. They also investigate the crack propagation and crack detection by vibration frequency measurement. In their work, the adherends are assumed to only experience tension, causing constant axial stress over their thickness. The adhesive is assumed to be a thin elastic medium as in Lubkin and Reissner (1956) and the stress state is considered constant over its thickness. After solving the shear and normal stress fields, the stress concentration factor and energy balance are investigated to understand the crack propagation. The stress analysis confirms that the maximum shear stresses are attained at the ends of the adhesive and that the peak of maximum shear stress is reached at the end of the stiffer tube and does not tend to zero as the adhesive length approaches infinity. Lastly, an optimization is performed using the model and the optimized shape is predicted to permit both reduced weight and increased strength.

Nemeş et al. (2006) and Nemeş and Lachaud (2009) propose a model considering a complex stress state with non-isotropic behavior of the tubes. The shear and hoop stress in the tubes are both variables over the thickness for both tubes and adhesives. The equilibrium analysis as well as the minimization of potential energy are applied to construct the set of equations. The complete analytical solution and its process are not given in the paper. The authors conduct parametric studies and report the stresses changing with overlap length, thickness, and material properties. Furthermore, Kumar (2009), Kumar and Scanlan (2010), and Martinez et al. (2008) developed models on the same basis to study different formulations and geometries.

There are some other researchers that have contributed to the modeling of tube-to-tube joints that deal with either similar loading condition or used similar approaches to those reported above (Hart-Smith, 1981, Chon, 1982; Thomsen and Kildegaard, 1990; Lee et al., 1991; Lee and Lee, 1992). Although significant progress has been made in the model development of adhesively bonded tube-to-tube joints, a detailed model that focus on the joints with the geometry and operating conditions of common HVAC&R systems is still lacking. Most of the previous work focused on studying the axial or torsional loading; a few of them consider internal pressure, but none have considered this practical application with static loading and thermal expansion.

5.2.2 Finite Element Analysis

Another powerful and common tool in predicting the stress field are finite element methods (FEM). FEM has been developed to study various adhesive-bonded joints (Kinloch and Guild, 1996a; Adams, Comyn et al., 1997). FEM is a numerical method for solving problems of engineering and mathematical physics such as structural analysis. They are usually applied in situations that involve boundary value problems for partial differential equations that are very hard to solve analytically.

Alwar and Nagaraja (1976) used the finite element method to analyze the stresses in the tube-to-tube single lap joints subjected to torsion. The time-dependent properties of the adhesive are taken into account by assuming that the adhesive is viscoelastic. A Prony series fitting is used for the modulus of the adhesive. The long-term redistribution of the stresses in the adhesive is evaluated using the finite element method. As large a reduction as 57% is noticed in the normal stress and an even larger reduction of 62% is noticed in the shear stress over three decades of time. Yadagiri et al. (1987) also studied the viscoelastic analysis of adhesively bonded joints using the finite element method.

Adams and Peppiatt (1977) used the finite element method to calculate the stresses in an adhesive-bonded tube-to-tube single lap joint subjected to both axial and torsional loads using axisymmetric quadratic isoparametric finite elements. The axial loading results are compared with a published closed form solution from Lubkin and Reissner (1956). The torsional loading case is compared with their own analytical model presented in the same paper, with the adherends as an orthotropic composite material subjected to torsion. The comparison is performed and discussed in detail and the trends are consistent. The influences on the stress distributions of an adhesive fillet and of partial tapering of the adherends are also reported.

Goglio and Paolino (2013) perform a critical review and finite element assessment of the published models for stress distributions of adhesive tube-to-tube joints under axial loading. The author firstly reviews the underlying assumptions of the selected theoretical models for adhesively bonded tube-to-tube joints under axial loading. Then, the author compares the model results with the outcome of ad-hoc finite element analysis of five different joint configurations. The authors conclude that all the models predict the shear stress but only the Lubkin and Reissner (1956) method predicts the correct peel stress distribution. In the joints, the axial and the hoop stresses are close to each other and are about one half of the peel stresses.

5.2.3 Summary and Discussions

The modeling of stress and strain in adhesively bonded tube-to-tube joints has been investigated by both analytical approaches and numerical methods. Analytical approach requires simplifying assumptions to reduce the complexity such that the formulated sets of differential equation can be solved. In the literature, many of the approaches do not result in closed-form solutions (or they are not provided). However, analytical solutions are valuable in providing insights into the stress and strain fields. By examining the terms in the solution, the relation between the stresses and inputs such as geometric sizes, material properties and loading conditions can be easily identified. With the stresses and strains available, fatigue evaluation can be subsequently processed as well. Also, compared to numerical approach, analytical approaches are time efficient, allowing exploration of the design space with different inputs, which can be easily used to provide optimization and guidance with a short turn-around time.

Numerical methods using FEM provide an approximate estimate of the exact solution. The element type and mesh size need to be selected carefully, as indicated in Adams and Peppiatt (1977). In the literature, it is pointed out that inconsistency in finite element results is observed due to overly coarse meshes, driven by the computational cost. Also, if the fatigue analysis is desired, the cohesive zone model requires accurate measurements to define the traction separation behavior. It is extremely difficult to measure some of the parameters such as the initial displacement δ_0 , failure displacement δ_f , and fracture toughness G , which are not readily available for the current adhesive.

Comparing these two approaches, because the goal of this model is to better understand the behavior of the tube-to-tube joints and provide guidance on design, optimization, and reliability analysis, an analytical approach is selected as the path forward. As pointed out by Goglio and Paolino (2013), the Lubkin and Reissner (1956) model predicts both peel stress and shear stress accurately under the axial loading condition compared with the FEM results. Thus, the Lubkin and Reissner (1956) model is adapted to adjust for more complicated boundary conditions and loading conditions as experienced in HVAC&R systems.

5.3 Model Formulation

5.3.1 Geometry, Material, and Boundary Conditions

The tube-to-tube joint geometry is shown in Figure 5.1. In HVAC&R applications, the joint connecting two tubes uses either a coupling or an expanded female tube end. The female tube diameter with the gap distance for adhesive determines the outer tube diameter.

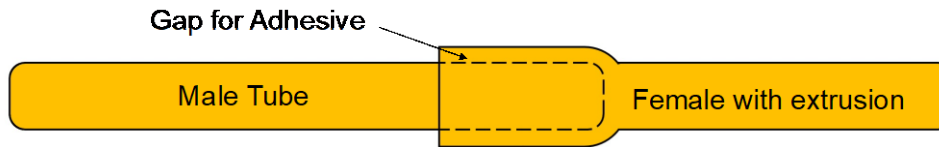


Figure 5.1 Schematic diagram of a typical tube-to-tube joint with adhesive bonding

Figure 5.2 shows a detailed schematic of the tube-to-tube joint region with the main geometric parameters and material properties labelled. In order to keep the model setup more general, here two adherents are assumed to have two different materials with subscripts 1, 2 (e.g., r_1 , r_2 are the radii of the two tubes at the midpoint; E_1 , E_2 are the Young's moduli; ν_1 , ν_2 are the Poisson's ratios). The adhesive is represented by the shaded area in between the tubes where r is the radius at the mid-point of the adhesive, E_a is the Young's modulus, and G_a is the shear modulus of the adhesive. The overlap area as well as the adhesive length is $2l$. The axial coordinate x is set to start at the center of the adhesive overlap region. A normalized coordinate z is defined later in the solution section to start at the left end.

The possible loading conditions are also given as the most general setup. The axial force loading the joint is F and no torsion loading is applied. The tube has internal pressure of P_{in} and outside pressure (usually atmospheric pressure) P_{out} . The temperature swing for purposes of thermal expansion is indicated as ΔT .

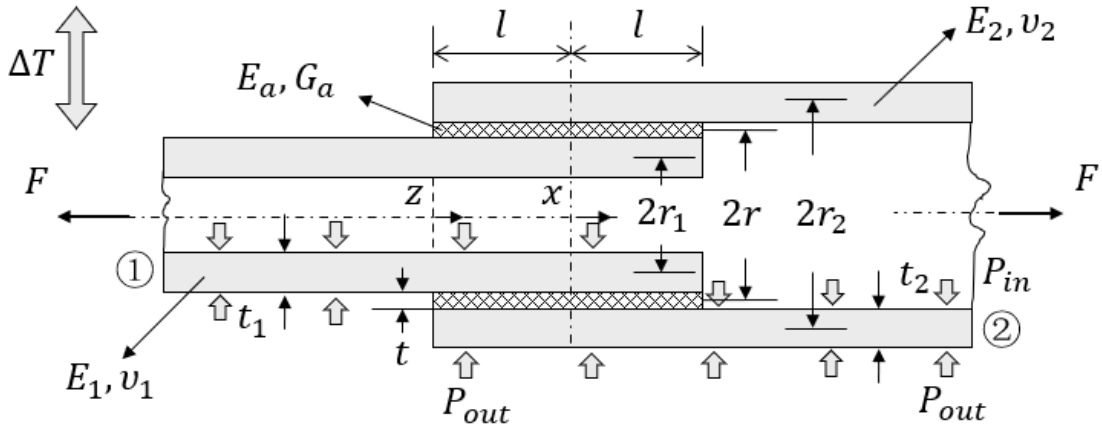


Figure 5.2 Schematic figure of the tube-to-tube joint with the main geometric sizes and material properties labelled.

Before introducing the forces and stresses, several important assumptions are discussed first. The tubes are modeled as thin shells subjected to axial tension, shear force, and bending moments. Both tubes have axial displacement, radial displacement, and rotation. The adhesive is treated as an elastic medium as a spring layer with shear stresses and peel stresses; the axial stress σ_x is assumed negligible. The adhesive layer is thin such that the stresses are constant over the adhesive thickness and varying along the axial direction only. There is no circumferential shear stress because no torsion is applied to the joints. At the end of the adhesive, there is no remaining excessive adhesive. The forces, stresses and strains are assumed to be axisymmetric due to the axisymmetric geometry.

A 3D view of a section of a single tube with detailed forces and stresses is shown in Figure 5.3 and the elementary free body diagrams of the joints are shown in Figure 5.4. In the tubes, the forces per unit length can be grouped into axial direction (T_1, T_2), transverse direction (V_1, V_2), hoop direction (N_1, N_2), and bending moments per unit length (M_1, M_2). In the adhesive layer, there are two stresses considered: peel stresses σ_y and shear stresses τ_{xy} . Also note that due to the axisymmetric geometry, any derivative in the circumferential direction will be zero.

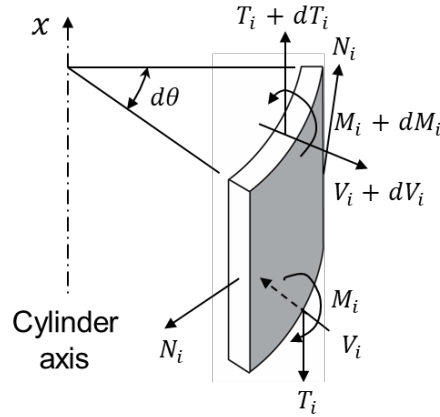


Figure 5.3 3D view of a section of the tube with forces and stresses

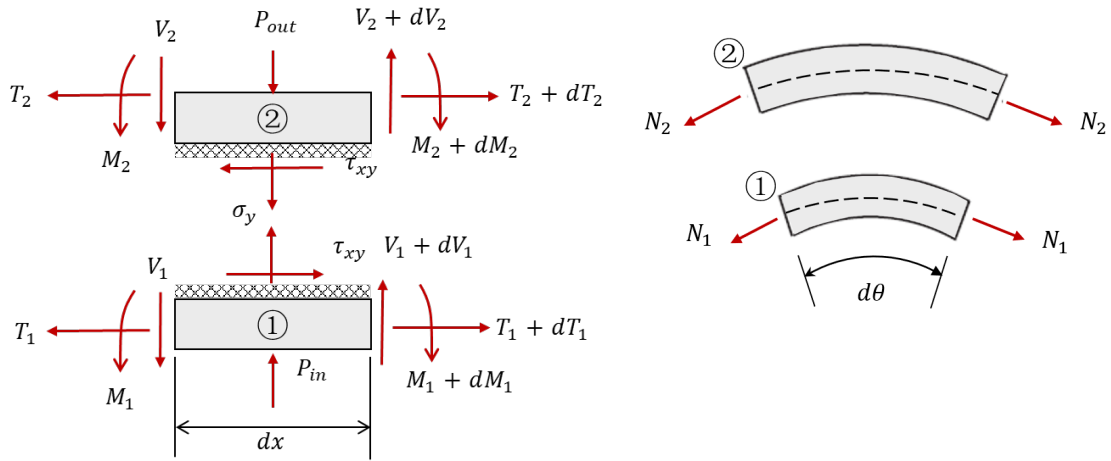


Figure 5.4 Elementary free body diagrams of the joint with forces and stresses

5.3.2 Governing Equations

The equilibrium stress-strain relations are examined in this section to form the set of governing equations to model the joint.

The axial equilibrium in adherent 1 can be written as:

$$r_1 d\theta T_1 = r_1 d\theta (T_1 + dT_1) + r d\theta dx \tau_{xy} \quad (5.1)$$

which simplifies to

$$r_1 \frac{dT_1}{dx} + r \tau_{xy} = 0 \quad (5.2)$$

Similarly, for adherent 2 the axial equilibrium simplifies, noting that the shear stress has opposite signs compared to adherent 1:

$$r_2 \frac{dT_2}{dx} - r\tau_{xy} = 0 \quad (5.3)$$

The transverse equilibrium for adherent 1:

$$2N_1 \sin \frac{d\theta}{2} dx + r_1 d\theta V_1 = P_{in} r_1 dx d\theta + r_1 d\theta (V_1 + dV_1) + \sigma_y r dx d\theta \quad (5.4)$$

which simplifies to

$$r_1 \frac{dV_1}{dx} + r\sigma_y + P_{in} r_1 - N_1 = 0 \quad (5.5)$$

Similarly, for adherent 2 the transverse equilibrium simplifies, noting that the pressure and the peel stresses in the adhesive have opposite signs compared to adherent 1:

$$r_2 \frac{dV_2}{dx} - r\sigma_y - P_{out} r_2 - N_2 = 0 \quad (5.6)$$

The moment balances for both tubes can be written in a similar fashion. The moments are summed at the center point of the element with negligible infinitesimal of higher order:

$$(M_1 + dM_1)r_1 d\theta + \tau_{xy} r dx d\theta \frac{t_1}{2} = M_1 r_1 d\theta + V_1 r_1 dx d\theta \quad (5.7)$$

$$r_1 \frac{dM_1}{dx} - r_1 V_1 + r \frac{t_1}{2} \tau_{xy} = 0 \quad (5.8)$$

$$r_2 \frac{dM_2}{dx} - r_2 V_2 + r \frac{t_2}{2} \tau_{xy} = 0 \quad (5.9)$$

The strain and displacement relations of each adherend can be calculated:

$$\varepsilon_x = \frac{(du + dx) - dx}{dx} = \frac{du}{dx} \quad (5.10)$$

$$\varepsilon_\theta = \frac{(r + v)d\theta - rd\theta}{rd\theta} = \frac{v}{r} \quad (5.11)$$

where u is the axial displacement and v is the radial displacement. (Note that Greek letter v is used for the Poisson ratio).

As mentioned earlier, due to the axisymmetric geometry, the circumferential displacement and strain is zero. The stress-strain relation is given here to consider the axial, hoop, bending deformations. The longitudinal displacement (u_1, u_2) and transverse displacement (v_1, v_2) can be written in terms of the forces and thermal strain. These equations assume that there is no Poisson effect due to radial stress because of thin shell assumptions. The radial stress does not stretch the tubes in axial direction.

$$\varepsilon_{x1} = \frac{du_1}{dx} = \frac{T_1 - \nu_1 N_1}{E_1 t_1} + \alpha_1 \Delta T \quad (5.12)$$

$$\varepsilon_{x2} = \frac{du_2}{dx} = \frac{T_2 - \nu_2 N_2}{E_2 t_2} + \alpha_2 \Delta T \quad (5.13)$$

$$\varepsilon_{\theta 1} = \frac{v_1}{r_1} = \frac{N_1 - \nu_1 T_1}{E_1 t_1} + \alpha_1 \Delta T \quad (5.14)$$

$$\varepsilon_{\theta 2} = \frac{v_2}{r_2} = \frac{N_2 - \nu_2 T_2}{E_2 t_2} + \alpha_2 \Delta T \quad (5.15)$$

where α_1 and α_2 are the thermal expansion coefficients of the adherent 1 and 2. Note that in this modeling, the temperature change ΔT is considered uniform for the entire assembly. The transient process of heat transfer from the fluid to the joints to the environment is not considered due to the high thermal conductivity and small thermal mass.

The bending deformation can be written as:

$$\frac{d^2 v_1}{dx^2} = -\frac{M_1}{D_1} \quad \text{and} \quad \frac{d^2 v_2}{dx^2} = -\frac{M_2}{D_2} \quad (5.16)$$

where D_i is the flexural rigidity for the corresponding adherent:

$$D_i = \frac{E_i t_i^3}{12(1 - \nu_i^2)}, i = 1, 2 \quad (5.17)$$

The adhesive layer is assumed to have both normal stress σ_y and shear stress τ_{xy} . It is usually a very thin layer, and thus, the bending of the adhesive is not considered. It also assumed that the adhesive is linear elastic in behavior.

$$\sigma_y = \frac{E_a}{t} (v_2 - v_1) \quad (5.18)$$

$$\tau_{xy} = \frac{G}{t} (u_{2,in} - u_{1,out}) \quad (5.19)$$

Also, the surface displacements must coincide with those at the mid point to ensure the continuity of the solid for the displacement at the outer diameter of tube 1 and at the inner diameter of tube 2:

$$u_{1,out} = u_1 - \left(\frac{dv_1}{dx}\right)\left(\frac{t_1}{2}\right) \quad (5.20)$$

$$u_{2,in} = u_2 + \left(\frac{dv_2}{dx}\right)\left(\frac{t_2}{2}\right) \quad (5.21)$$

A summary of all the known variables and 16 unknown parameters are listed:

- Knowns:
 - Geometric parameters: r_1, r_2, r, t_1, t_2, t
 - Boundary forces and pressures: P_{in}, P_{out}, F
 - Material properties: $E_1, E_2, \nu_1, \nu_2, \alpha_1, \alpha_2$
 - Temperature change: ΔT
- Unknowns:
 - Stresses: τ_{xy}, σ_y
 - Force terms: $T_1, T_2, V_1, V_2, N_1, N_2, M_1, M_2,$
 - Displacement / strain terms: $u_1, u_2, v_1, v_2, u_{1,out}, u_{2,in}$
- Equations: total of 16 independent equations: (5.2), (5.3), (5.5), (5.6), (5.8), (5.9), (5.12), (5.13), (5.14), (5.15), (5.16), (5.18), (5.19), (5.20), and (5.21)

There are equal number of equations and unknown variables and all the variables are a function of coordinate x .; hence, the problem then can be solved with proper boundary conditions. Moreover, the global axial equilibrium for the joints under the axial force F can be written as:

$$2\pi(r_1T_1 + r_2T_2) = F \quad (5.22)$$

For solving purposes, an auxiliary unknown T_0 , is introduced to satisfy:

$$rT_0 = r_2T_2 - r_1T_1 \quad (5.23)$$

Combined with Eqns. (5.2) and (5.3):

$$\frac{dT_0}{dx} = 2\tau_{xy} \quad (5.24)$$

In the simplification, τ_{xy} will be replaced with $\frac{dT_0}{dx}$ to reduce the order of the differential equation. The mathematical manipulations and variable elimination procedure are discussed briefly below.

With the definition of T_0 , an integration of Eqns. (5.2) and (5.3) yields:

$$r_1 T_1 + \frac{r}{2} T_0 + C_1 = 0; \text{ and } r_1 T_2 - \frac{r}{2} T_0 + C_2 = 0; \quad (5.25)$$

which can be rearranged as

$$r_1 T_1 + r_2 T_2 + C_1 + C_2 = 0; \text{ and } r_1 T_1 - r_2 T_2 + r T_0 + C_1 - C_2 = 0; \quad (5.26)$$

Combined with the global axial equilibrium (5.22) and the definition of T_0 , T_1 and T_2 can be expressed as functions of T_0 :

$$T_1 = \frac{F}{4\pi r_1} - \frac{r}{2} \frac{T_0}{r_1}; \quad T_2 = \frac{F}{4\pi r_2} + \frac{r}{2} \frac{T_0}{r_2}; \quad (5.27)$$

Substituting T_1 and T_2 into Eqns. (5.12 - 5.15), N_1 , N_2 and $\frac{du_1}{dx}$, $\frac{du_2}{dx}$ can be written as functions of T_0 , v_1 , v_2 :

$$N_1 = \frac{v_1}{r_1} E_1 t_1 + \left(\frac{F}{4\pi r_1} - \frac{r}{2} \frac{T_0}{r_1} \right) v_1 + E_1 t_1 \alpha_1 \Delta T \quad (5.28)$$

$$N_2 = \frac{v_2}{r_2} E_2 t_2 + \left(\frac{F}{4\pi r_2} + \frac{r}{2} \frac{T_0}{r_2} \right) v_2 + E_2 t_2 \alpha_2 \Delta T \quad (5.29)$$

$$\frac{du_1}{dx} = \frac{\left(\frac{F}{4\pi r_1} - \frac{r}{2} \frac{T_0}{r_1} \right) (1 - v_1^2)}{E_1 t_1} - \frac{v_1 v_1}{r_1} + (1 - v_1) \alpha_1 \Delta T \quad (5.30)$$

$$\frac{du_2}{dx} = \frac{\left(\frac{F}{4\pi r_2} + \frac{r}{2} \frac{T_0}{r_2} \right) (1 - v_2^2)}{E_2 t_2} - \frac{v_2 v_2}{r_2} + (1 - v_2) \alpha_2 \Delta T \quad (5.31)$$

Combining the derivatives of Eqns. (5.8) and (5.9) with Eqn. (5.18) and substituting $\frac{dV_1}{dx}$, $\frac{dV_2}{dx}$ in Eqns. (5.5) and (5.6):

$$\frac{d^2 M_1}{dx^2} = \frac{N_1}{r_1} - P_{in} - \frac{r}{r_1} \frac{E_a}{t} (v_2 - v_1) - \frac{rt_1}{2r_1} \frac{d\tau_{xy}}{dx} \quad (5.32)$$

$$\frac{d^2 M_2}{dx^2} = \frac{N_2}{r_2} + P_{out} - \frac{r}{r_2} \frac{E_a}{t} (v_2 - v_1) - \frac{rt_2}{2r_2} \frac{d\tau_{xy}}{dx} \quad (5.33)$$

In Eqns. (5.32) and (5.33), substituting in M_1 and M_2 using Eqns. (5.16) and (5.17), N_1 and N_2 using Eqns. (5.28) and (5.29), and τ_{xy} using Eqn. (5.24), all the terms become a function of T_0 , v_1 , v_2 :

$$\begin{aligned} & \frac{d^4 v_1}{dx^4} + 12(1-\nu_1^2) \left(\frac{1}{r_1^2 t_1^2} + \frac{rE_a}{E_1 t_1^3 r_1 t} \right) v_1 - 12(1-\nu_1^2) \frac{rE_a}{E_1 t_1^3 r_1 t} v_2 - 3 \frac{(1-\nu_1^2)r}{E_1 t_1^2 r_1} \frac{d^2 T_0}{dx^2} \\ & - 6 \frac{(1-\nu_1^2)r v_1}{E_1 t_1^3 r_1^2} T_0 = - \left(\frac{F v_1}{4\pi r_1^2} + \frac{E_1 t_1 \alpha_1}{r_1} \Delta T - P_{in} \right) \left(\frac{12(1-\nu_1^2)}{E_1 t_1^3} \right) \end{aligned} \quad (5.34)$$

$$\begin{aligned} & \frac{d^4 v_2}{dx^4} + 12(1-\nu_2^2) \left(\frac{1}{r_2^2 t_2^2} + \frac{rE_a}{E_2 t_2^3 r_2 t} \right) v_2 - 12(1-\nu_2^2) \frac{rE_a}{E_2 t_2^3 r_2 t} v_1 - 3 \frac{(1-\nu_2^2)r}{E_2 t_2^2 r_2} \frac{d^2 T_0}{dx^2} \\ & + 6 \frac{(1-\nu_2^2)r v_1}{E_2 t_2^3 r_2^2} T_0 = - \left(\frac{F v_2}{4\pi r_2^2} + \frac{E_2 t_2 \alpha_2}{r_2} \Delta T + P_{out} \right) \left(\frac{12(1-\nu_2^2)}{E_2 t_2^3} \right) \end{aligned} \quad (5.35)$$

The last differential equation can be obtained by substituting Eqns. (5.20) and (5.21) into Eqn. (5.19) and further combining with Eqns. (5.24), (5.30) and (5.31). All the remaining terms are as function of T_0 , v_1 , v_2 .

$$\begin{aligned} & \frac{d^2 T_0}{dx^2} - \frac{G_a r}{t} \left(\frac{(1-\nu_1^2)}{E_1 r_1 t_1} + \frac{(1-\nu_2^2)}{E_2 r_2 t_2} \right) T_0 - \frac{G_a}{t} \left(t_1 \frac{d^2 v_1}{dx^2} + t_2 \frac{d^2 v_2}{dx^2} \right) - \frac{2G_a \nu_1}{t r_1} v_1 + \frac{2G_a \nu_2}{t r_2} v_2 \\ & = \frac{2G_a}{t} \left(- \frac{F(1-\nu^2)}{4\pi r_1 E_1 t_1} + \frac{F(1-\nu^2)}{4\pi r_2 E_2 t_2} - (1-\nu_1) \alpha_1 \Delta T + (1-\nu_2) \alpha_2 \Delta T \right) \end{aligned} \quad (5.36)$$

Thus, a set of three coupled differential equations (5.34), (5.35) and (5.36) is obtained with three unknowns v_1 , v_2 and T_0 . With appropriate boundary conditions, this set can be solved to further solve for the stress and strain field in the joint.

The solution procedure presented by Goglio and Paolino (2013) is adopted. The set of equations can be further simplified by introducing the following dimensionless functions $f(z)$, $g(z)$, and $h(z)$ where $z = \frac{x+l}{2l}$ is a dimensionless variable such that $z = 0$ ($x = -l$) at the

left end of the adhesive and $z = 1$ ($x = l$) at the right end of the adhesive. The dimensionless functions are given by:

$$v_1 = \frac{F}{2\pi r} \frac{(1-\nu_1^2)}{E_1} \left(\frac{2l}{t_1}\right)^2 f(z) \quad (5.37)$$

$$v_2 = \frac{F}{2\pi r} \frac{(1-\nu_2^2)}{E_2} \left(\frac{2l}{t_2}\right)^2 g(z) \quad (5.38)$$

$$T_0 = \frac{F}{2\pi r} h(z) \quad (5.39)$$

The set of differential equations then becomes:

$$\begin{aligned} f^{IV} + (K_1^4 + \gamma_{11}^4)f - \gamma_{12}^4 g - \frac{3r}{r_1} h'' - \frac{3\Lambda_1 r}{r_1} h &= -\frac{3\Lambda_1 r}{r_1} + C_1 \\ g^{IV} + (K_2^4 + \gamma_{22}^4)g - \gamma_{21}^4 f - \frac{3r}{r_2} h'' + \frac{3\Lambda_2 r}{r_2} h &= -\frac{3\Lambda_2 r}{r_2} + C_2 \\ h'' - \left(\frac{B_2^2}{r_2} + \frac{B_1^2}{r_1}\right) rh - (B_2^2 g'' + B_1^2 f'') + \Lambda_2 B_2^2 g - \Lambda_1 B_1^2 f &= \frac{B_2^2 r}{r_2} - \frac{B_1^2 r}{r_1} + C_3 \end{aligned} \quad (5.40)$$

The primes in the previous set of equations set indicating the differentiation order and the coefficients and constants are defined as follows:

$$B_i^2 = (1-\nu_i^2) \left(\frac{2l}{t_i}\right)^2 \frac{t_i G_a}{t E_i} \quad (5.41)$$

$$\Lambda_i = 2\nu_i \left(\frac{2l}{t_i}\right)^2 \frac{t_i}{r_i} \quad (5.42)$$

$$K_i^4 = 12(1-\nu_i^2) \left(\frac{2l}{t_i}\right)^4 \left(\frac{t_i}{a_i}\right)^2 \quad (5.43)$$

$$\gamma_{ij}^4 = 12(1-\nu_i^2) \left(\frac{2l}{t_j}\right)^3 \frac{2l}{t_i} \frac{r E_a t_j}{r_j E_j t} \quad (5.44)$$

Note that the constants C_1 , C_2 and C_3 are the contribution of adding the pressure forces and thermal strain on the joint.

$$C_1 = \frac{-12 \left(\frac{E_1 t_1 \alpha_1}{r_1} \Delta T \right) \left(\frac{2l}{t_1} \right)^2 t_1 + 12 P_{in} \left(\frac{2l}{t_1} \right)^2 t_1}{\frac{F}{2\pi r}} = 24\pi r \left(\frac{2l}{t_1} \right)^2 t_1 \frac{P_{in} - \frac{E_1 t_1 \alpha_1}{r_1} \Delta T}{F} \quad (5.45)$$

$$C_2 = \frac{-12 \left(\frac{E_2 t_2 \alpha_2}{r_2} \Delta T \right) \left(\frac{2l}{t_2} \right)^2 t_2 - 12 P_{out} \left(\frac{2l}{t_2} \right)^2 t_2}{\frac{F}{2\pi r}} = 24\pi r \left(\frac{2l}{t_2} \right)^2 t_2 \frac{-P_{out} - \frac{E_2 t_2 \alpha_2}{r_2} \Delta T}{F} \quad (5.46)$$

$$C_3 = \frac{2G_a [(1-\nu_2)\alpha_2 - (1-\nu_1)\alpha_1] \Delta T}{\frac{F}{2\pi r}} \left(\frac{2l}{t} \right)^2 t = 4\pi r G_a \left(\frac{2l}{t} \right)^2 t \frac{(1-\nu_2)\alpha_2 - (1-\nu_1)\alpha_1}{F} \Delta T \quad (5.47)$$

5.3.3 Boundary Conditions

The differential equations can only be solved with appropriate boundary conditions. In HVAC&R systems, the joints at different locations may have different boundary conditions. The common scenario for joints is to seal and connect two tubes without large axial forces and torsion. The following boundary conditions are therefore considered. As shown in Figure 5.2, for the part where the tube and adhesive layer both ends, it is evident that in the end sections of the tubes, the forces and moments must disappear:

$$\begin{aligned} \text{at } x = -l, \quad T_2 = V_2 = M_2 &= 0 \\ \text{at } x = l, \quad T_1 = V_1 = M_1 &= 0 \end{aligned} \quad (5.48)$$

In contrast, in the section where adhesive layer ends but the tube continues, the tubes are subjected to bending and shear. The boundary conditions for tubes at the transition between the overlap and non-overlap are not of simple axial loading and must be found by ensuring the continuity of force, moment, displacement, and rotation. As discussed in Goglio and Paolino (2014), the results can be derived by deleting the terms related to the adhesive layers or by referring to the theory for thin cylinder shells with bending (Coates, 1930):

$$v_{1,tube} = e^{\lambda_1 x} (A_{v1} \cos \lambda_1 x + B_{v1} \sin \lambda_1 x) - \frac{\nu_1 F}{2\pi E_1 t_1} \quad (5.49)$$

$$v_{2,tube} = e^{-\lambda_2 x} (A_{v_2} \cos \lambda_2 x + B_{v_2} \sin \lambda_2 x) - \frac{\nu_2 F}{2\pi E_2 t_2} \quad (5.50)$$

where $\lambda_i^4 = \frac{3(1-\nu_i^2)}{r_i^2 t_i^2}$; A_{v_i}, B_{v_i} are constants to be determined.

The continuity of force, moment, displacement, and rotation at both ends of the joints can be written as:

$$\begin{aligned} \text{Force:} \quad & V_{1,tube} \Big|_{x=-l} = V_1 \Big|_{x=-l} ; & V_{2,tube} \Big|_{x=l} = V_2 \Big|_{x=l} ; \\ \text{Moment:} \quad & M_{1,tube} \Big|_{x=-l} = M_1 \Big|_{x=-l} ; & M_{2,tube} \Big|_{x=l} = M_2 \Big|_{x=l} ; \\ \text{Displacement:} \quad & v_{1,tube} \Big|_{x=-l} = v_1 \Big|_{x=-l} ; & v_{2,tube} \Big|_{x=l} = v_2 \Big|_{x=l} ; \\ \text{Rotation:} \quad & \frac{dv_{1,tube}}{dx} \Big|_{x=-l} = \frac{dv_1}{dx} \Big|_{x=-l} ; & \frac{dv_{2,tube}}{dx} \Big|_{x=l} = \frac{dv_2}{dx} \Big|_{x=l} ; \end{aligned} \quad (5.51)$$

where $V_{i,tube} = -D_i \frac{d^3 v_1}{dx^3}$, $M_{i,tube} = -D_i \frac{d^2 v_1}{dx^2}$, and $D_i = \frac{E_i t_i^3}{12(1-\nu_i^2)}$ ($i=1,2$).

Using the earlier defined dimensionless variable z and functions $f(z), g(z), h(z)$ and substituting the boundary conditions. At the region where adhesive and tube both ends as indicated in (5.48):

$$\begin{aligned} T_2(0) = 0 &\Rightarrow h_0 = -1; \\ M_2(0) = 0 &\Rightarrow g_0'' = 0; \\ V_2(0) = 0 &\Rightarrow g_0''' - \frac{3r}{r_2} h_0' = 0; \\ T_1(1) = 0 &\Rightarrow h_1 = 1; \\ M_1(1) = 0 &\Rightarrow f_1'' = 0; \\ V_1(1) = 0 &\Rightarrow f_1''' - \frac{3r}{r_1} h_1' = 0; \end{aligned} \quad (5.52)$$

At the transition region as indicated in (5.51):

$$\begin{aligned}
f_0''' - \sqrt{2}K_1 f_0'' + K_1^2 f_0' - \frac{3r}{r_1} h_0' &= 0; \\
f_0'' - \sqrt{2}K_1 f_0' + K_1^2 f_0 &= -2\sqrt{3}\nu_1 \frac{r}{r_1(\sqrt{1-\nu_1^2})}; \\
g_1''' + \sqrt{2}K_2 g_1'' + K_2^2 g_1' - \frac{3r}{r_2} h_1' &= 0; \\
g_1'' + \sqrt{2}K_2 g_1' + K_2^2 g_1 &= -2\sqrt{3}\nu_2 \frac{r}{r_2(\sqrt{1-\nu_2^2})};
\end{aligned} \tag{5.53}$$

5.4 Solution Method

The study by Lubkin and Reissner (1956) provides no details on the solution procedure. It is remarked that the equation set is linear with constant coefficients thus it can be solved with standard method. The results are given as normalized stress values at 11 points of the overlap area with a collection of 48 cases with respect to different configurations, including variations in overlap length, stiffness, and curvature. In the search for an explicit closed-form solution, there are several challenges. The high order of the set of differential equations is a major practical difficulty. It is possible to achieve approximate solutions without particular difficulties by numerical integration, but if an analytical solution is possible, it can provide insights of the stresses and strains to study the properties of the solution. Goglio and Paolino (2014) revisit the Lubkin and Reissner (1956) model and provide a solution method using Laplace transforms. A similar solution approach using Laplace transforms is applied in this study, but the procedure of finding the partial fractions decomposition is modified to simplify the calculation. The solution process is evaluated using Mathematica due to the complicated symbolic manipulations involved.

The algorithm used to solve the set of governing equations is shown in Figure 5.5. The major steps are reported in this section and the complete details of the solution process (namely, the complete Mathematica notebook) are reported in Appendix A.

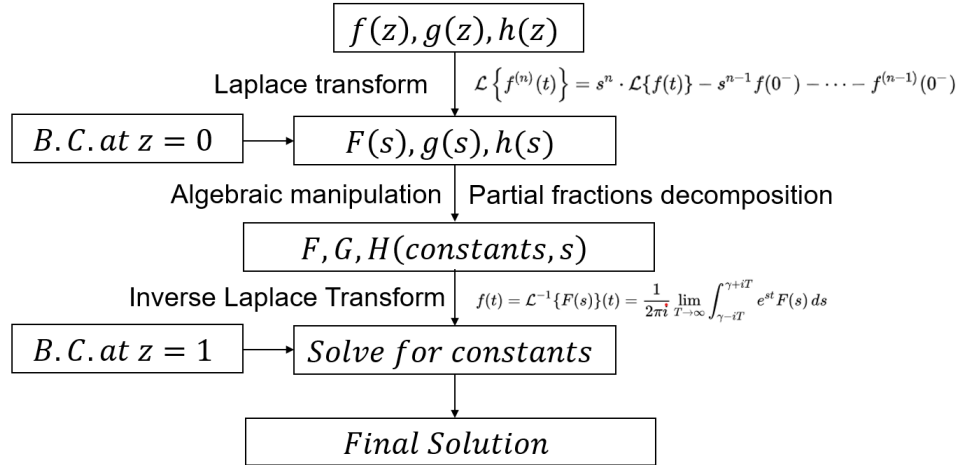


Figure 5.5 Solution algorithm using Laplace transform with boundary conditions.

By applying the Laplace transform to Eqn. (5.40) and substituting the boundary conditions at $z=0$ from Eqns. (5.52) and (5.53), the transferred Laplace functions can be written in the following format:

$$\begin{bmatrix} S(3 \times 3) \end{bmatrix} \begin{Bmatrix} F(s) \\ G(s) \\ H(s) \end{Bmatrix} = \begin{Bmatrix} f(s, f_0, f_0', g_0, g_0', h_0') \\ g(s, f_0, f_0', g_0, g_0', h_0') \\ h(s, f_0, f_0', g_0, g_0', h_0') \end{Bmatrix} \quad (5.54)$$

where s is the complex variable and $F(s), G(s), H(s)$ are the Laplace transforms of the functions $f(z), g(z), h(z)$. The 3×3 matrix S is fully determined by the previously defined variables: $K_i, \gamma_{ij}, \Lambda_i, B_i (i, j = 1, 2)$. Note that these can be calculated by the known geometric parameters and material properties. For matrix S , assuming the inverse matrix exists, then $F(s), G(s), H(s)$ can be found by multiply S^{-1} on both sides. This is a reasonable assumption considering the actual values of the properties. Nevertheless, the existence should be checked once the values are substituted into the matrix.

$$\begin{Bmatrix} F(s) \\ G(s) \\ H(s) \end{Bmatrix} = \begin{bmatrix} S^{-1}(3 \times 3) \end{bmatrix} \begin{Bmatrix} f(s, f_0, f_0', g_0, g_0', h_0') \\ g(s, f_0, f_0', g_0, g_0', h_0') \\ h(s, f_0, f_0', g_0, g_0', h_0') \end{Bmatrix} \quad (5.55)$$

By calculating the inverse matrix and multiplying, the three Laplace transforms can be written as:

$$\begin{cases} F(s) \\ G(s) \\ H(s) \end{cases} = \frac{1}{p(s)} \begin{cases} q_1(s, f_0, f_0', g_0, g_0', h_0') \\ q_2(s, f_0, f_0', g_0, g_0', h_0') \\ q_3(s, f_0, f_0', g_0, g_0', h_0') \end{cases}$$

$$p(s) = \det|S| = \sum_{i=0}^5 d_i \times s^{2i+1} \quad (5.56)$$

$$q_i(s) = \sum_{j=0}^{10} n_{i,j}(s, f_0, f_0', g_0, g_0', h_0') \times s^j \quad (i = 1, 2, 3)$$

The coefficients in $q_i(s)$ are known and the coefficients in $p(s)$ ($i = 1, 2, 3$) are unknown as functions of the initial conditions. Note that $\frac{p(s)}{q_j(s)}$ is a proper rational function with 11th order polynomials on the numerator and 10th order polynomials on the denominator. The method of partial fraction decomposition can be applied to express the fraction as a sum of a polynomial (possibly zero) and one or several fractions with a simpler denominator. Note that in the numerous cases studied in this work and in the literatures, with the material properties and geometric parameters in its reasonable range, the 11th degree polynomials $p(s)$ always had distinct roots $\lambda_k, k = 1, 2, \dots, 11$. Without loss of generality, it can be assumed that the coefficient of s^{11} in $p(s)$ is 1; otherwise, both $p(s)$ and $q_i(s)$ ($i = 1, 2, 3$) can be divided by that coefficient. Then it can be written as:

$$p(s) = \sum_{k=1}^{11} (s - \lambda_k)$$

$$r_i(s) = \frac{q_i(s)}{p(s)} = \sum_{k=1}^{11} \frac{c_{i,k}}{s - \lambda_k} \quad (i = 1, 2, 3) \quad (5.57)$$

Recombining $r_i(s)$ into a single fraction whose denominator is the least common denominator $p(s)$:

$$r_i(s) = \sum_{k=1}^{11} \frac{c_{i,k}}{s - \lambda_{i,k}} = \frac{\sum_{k=1}^{11} c_k \left(\prod_{j=1(j \neq k)}^{11} (s - \lambda_k) \right)}{p(s)} = \frac{q_i(s)}{p(s)} \quad (i = 1, 2, 3)$$

$$q_i(s) = \sum_{k=1}^{11} c_k \left(\prod_{j=1(j \neq k)}^{11} (s - \lambda_k) \right) \quad (i = 1, 2, 3) \quad (5.58)$$

If both sides of Eqn. (5.58) are evaluated at $s = \lambda_m$, ($1 \leq m \leq 11$) then all the terms on the right-hand side become zero except the one corresponding to $k = m$, therefore:

$$q_i(\lambda_m) = c_{i,m} \prod_{j=1(j \neq m)}^{11} (\lambda_m - \lambda_k) \quad (i = 1, 2, 3) \quad (5.59)$$

It can be noticed that $\prod_{j=1(j \neq m)}^{11} (\lambda_m - \lambda_k)$ in right side of Eqn. (5.59) following from differentiation of $p(s)$ in its product form and the condition that $p(s)$ has distinct roots implies that $p(\lambda_m) \neq 0$. Dividing Eqn. (5.59) by the differentiation of $p(s)$ yields:

$$c_{i,m} = \frac{q_i(\lambda_m)}{p'(\lambda_m)} \quad (i = 1, 2, 3) \quad (5.60)$$

If $p(s)$ and $q_i(s)$ ($i = 1, 2, 3$) have real coefficients and $\lambda_{i,m} = \overline{\lambda_{i,l}}$, it can be derived that:

$$c_{i,l} = \frac{q(\lambda_{i,l})}{p'(\lambda_{i,l})} = \frac{\overline{q(\lambda_{i,m})}}{\overline{p'(\lambda_{i,m})}} = \overline{c_{i,m}} \quad (i = 1, 2, 3) \quad (5.61)$$

With the following basic inverse Laplace transform:

$$\mathcal{L}^{-1}\left(\frac{1}{s}\right) = 1 \quad \& \quad \mathcal{L}^{-1}\left(\frac{1}{s-a}\right) = e^{at} \quad (5.62)$$

The inverse Laplace transform can be performed on the decomposed functions:

$$\mathcal{L}^{-1}\left\{\frac{p(s)}{q_i(s)}\right\} = \sum_{j=1}^{11} c_{i,j} e^{\lambda_j z} \quad (5.63)$$

Note that $\lambda = 0$ is also one root for $p(s)$, Eqn. (5.63) can be further written as:

$$\begin{aligned} \mathcal{L}^{-1}\left\{\frac{p(s)}{q_i(s)}\right\} &= \frac{n_{i,0}}{d_0} + \sum_{j=1}^{10} c_{i,j} e^{\lambda_j z} \quad (i = 1, 2, 3) \\ f(z) &= \mathcal{L}^{-1}\left\{\frac{p(s)}{q_1(s)}\right\}; \quad g(z) = \mathcal{L}^{-1}\left\{\frac{p(s)}{q_2(s)}\right\}; \quad h(z) = \mathcal{L}^{-1}\left\{\frac{p(s)}{q_3(s)}\right\}; \end{aligned} \quad (5.64)$$

where λ_j is the non-zero root for $p(s)$, which can be expressed as follows:

$$\begin{aligned} \lambda_1 &= -\lambda_6 = r_1; \quad \lambda_2 = -\lambda_9 = r_2 + m_2 i; \\ \lambda_3 &= -\lambda_{10} = r_3 + m_3 i; \quad \lambda_4 = \overline{\lambda_2} = -\lambda_7; \quad \lambda_5 = \overline{\lambda_3} = -\lambda_8; \quad \lambda_{11} = 0 \end{aligned} \quad (5.65)$$

This can be simplified by using the Euler formula and considering the conjugate relation of the roots and coefficients. The final solutions can be given:

$$\begin{aligned} \mathcal{L}^{-1}\left\{\frac{p(s)}{q_i(s)}\right\} &= \frac{n_{i,0}}{d_0} + \sum_{j=1}^{10} e^{\lambda_j z} = \frac{n_{i,0}}{d_0} + \sum_{j=1}^3 (\cosh(r_j z) \times (c_{i,j,1} \cos(m_j z) + c_{i,j,2} \sin(m_j z)) \\ &+ \sinh(r_j z) \times (c_{i,j,3} \cos(m_j z) + c_{i,j,3} \sin(m_j z))) \quad (i = 1, 2, 3) \end{aligned} \quad (5.66)$$

$$f(z) = \mathcal{L}^{-1}\left\{\frac{p(s)}{q_1(s)}\right\}; g(z) = \mathcal{L}^{-1}\left\{\frac{p(s)}{q_2(s)}\right\}; h(z) = \mathcal{L}^{-1}\left\{\frac{p(s)}{q_3(s)}\right\};$$

where the new coefficients are all real and depend on the initial conditions. The relation of the new coefficients $c_{i,j,k}$ and previous coefficients $c_{i,m}$ can be given as:

$$\begin{aligned} c_{1,1,i} &= \text{Re}[c_{i,1}] + \text{Re}[c_{i,6}]; \quad c_{1,2,i} = \text{Im}[c_{i,1}] + \text{Im}[c_{i,6}]; \\ c_{1,3,i} &= \text{Re}[c_{i,1}] - \text{Re}[c_{i,6}]; \quad c_{1,4,i} = \text{Im}[c_{i,1}] - \text{Im}[c_{i,6}]; \\ c_{2,1,i} &= 2(\text{Re}[c_{i,2}] + \text{Re}[c_{i,7}]); \quad c_{2,2,i} = -2(\text{Im}[c_{i,2}] + \text{Im}[c_{i,7}]); \\ c_{3,3,i} &= 2(\text{Re}[c_{i,2}] - \text{Re}[c_{i,7}]); \quad c_{2,4,i} = -2(\text{Im}[c_{i,2}] + \text{Im}[c_{i,7}]); \\ c_{3,1,i} &= 2(\text{Re}[c_{i,3}] + \text{Re}[c_{i,8}]); \quad c_{3,2,i} = -2(\text{Im}[c_{i,3}] + \text{Im}[c_{i,8}]); \\ c_{3,3,i} &= 2(\text{Re}[c_{i,3}] - \text{Re}[c_{i,8}]); \quad c_{3,4,i} = -2(\text{Im}[c_{i,3}] + \text{Im}[c_{i,8}]); \\ i &= 1, 2, 3; \quad f(z) \rightarrow i = 1; \quad g(z) \rightarrow i = 2; \quad h(z) \rightarrow i = 3; \end{aligned} \quad (5.67)$$

where $Re[\]$ and $Im[\]$ indicate respectively the real and imaginary part of the complex number.

Eqns. (5.66) and (5.67) defined the coefficients and equations for the final solution. However, there are still five unknown constants as the initial conditions at $z = 0$. In order to solve these unknown constants, the other set of boundary conditions must be applied. Substituting in Eqn. (5.66) to the given boundary conditions in Eqns. (5.52) and (5.53) evaluating at $z=1$, a set of linear algebraic equations can be achieved and solved as shown below.

$$\begin{Bmatrix} f_0 \\ f_0' \\ g_0 \\ g_0' \\ h_0' \end{Bmatrix} = \begin{bmatrix} & & & & \\ & & & & \\ & & & & \\ & & & & \\ & & & & \end{bmatrix} \begin{Bmatrix} b_1 \\ b_2 \\ b_3 \\ b_4 \\ b_5 \end{Bmatrix} \quad (5.68)$$

Once the five unknowns are solved, the solution process for the three dimensionless functions are completed. Then the peel and shear stress can be related with the dimensionless function.

$$\begin{aligned}\sigma_y &= \frac{E_a}{t}(v_2 - v_1) = \frac{F}{2\pi r} \frac{E_a}{G_a} \left(\frac{B_2^2}{t_2} g(z) - \frac{B_1^2}{t_1} f(z) \right) \\ \tau_{xy} &= \frac{G_a}{t}(u_{2,in} - u_{1,out}) = \frac{1}{2} \frac{dT_0}{dx} = \frac{F}{4\pi r l} \frac{E_a}{G_a}\end{aligned}\quad (5.69)$$

Substituting the expression into the peel and shear stress, with suitable mathematical manipulation and reorganization, the final solution of the stresses are:

$$\begin{aligned}\sigma_y(z) &= \frac{F}{2\pi r} \frac{E_a}{G_a} \left(\frac{B_2^2}{t_2} \frac{n_{2,0}}{d_0} - \frac{B_1^2}{t_1} \frac{n_{1,0}}{d_0} \right) + \frac{F}{4\pi r l} \frac{E_a}{G_a} \sum_{i=1}^3 (\cosh(r_j z) \times (c_{\sigma,i,1} \cos(m_i z) \\ &\quad + c_{\sigma,i,2} \sin(m_i z)) + \sinh(r_i z) \times (c_{\sigma,i,3} \cos(m_i z) + c_{\sigma,i,4} \sin(m_j z))) \\ \tau_{xy}(z) &= \frac{F}{8\pi r l} \sum_{i=1}^3 (\cosh(r_j z) \times (c_{\tau,i,1} \cos(m_i z) + c_{\tau,i,2} \sin(m_i z)) + \sinh(r_i z) \\ &\quad \times (c_{\tau,i,3} \cos(m_i z) + c_{\tau,i,4} \sin(m_j z)))\end{aligned}\quad (5.70)$$

where the new coefficients can be expressed as:

$$\begin{aligned}c_{\sigma,i,j} &= B_2^2 \frac{2l}{t_2} c_{i,j,2} - B_1^2 \frac{2l}{t_2} c_{i,j,2} & i = 1, 2, 3 \\ c_{\tau,2k-1,j} &= r_i c_{i,2k-1,3} + m_i c_{i,2k,3} & j = 1, 2, 3, 4 \\ c_{\tau,2k,j} &= r_i c_{i,2k+1,3} - m_i c_{i,2k-1,3} & k = 1, 2\end{aligned}\quad (5.71)$$

5.5 Results and Discussion

5.5.1 Model Validation

The model developed here is based on the previous model by Lubkin and Reissner (1956), but with the additional consideration of the effects of pressure and thermal expansion. Goglio and Paolino (2014) revisited the model of Lubkin and Reissner (1956) to develop an explicit closed-form solution and analyzed the same loading condition with finite element analysis. They compared the original solution of Lubkin and Reissner, their explicit closed-form analytical solution, and the finite element analysis solution and concluded that all three solutions are consistent.

In this study, the solution method also uses Laplace transforms, as suggested by Goglio and Paolino (2014). In order to validate the current model and its solution method, a validation case is simulated using the same loading condition as reported in the literature. Note that in the validation

case, an external axial force is given without considering the effect of pressure and thermal expansion. The geometric parameters, material properties, and axial loading for the validation cases are reported in Table 5.1 and Table 5.2, which were first studied by Lubkin and Reissner (1956) and then reproduced by Goglio and Paolino (2014) with numerical values reported for the solution.

Table 5.1. Geometric size of the validation case in the literature (Dragoni and Goglio, 2013)

Parameters	$r_1(mm)$	$r_2(mm)$	$r(mm)$	$t(mm)$	$t_1=t_2(mm)$	$l(mm)$
Values	48.625	51.375	50	0.25	2.5	12.5

*The actual numerical data used in the calculation example in the paper is $r_1 = 48.75$, $r_2 = 51.25$

Table 5.2. Material properties and loading condition of the validation case in the literature (Dragoni and Goglio, 2013)

Parameters	E_1	E_2	ν_1	ν_2	E_a	G_a	F
Unit	GPa	GPa	–	–	MPa	MPa	N
Values	200	200	0.3	0.3	1000	375	7854

The validation is done by comparing the key numerical values as shown in Table 5.3 and also overlaying the normalized stress predictions in the same plot. The same values for the initial boundary conditions, as well as the coefficients for the final solution, are achieved with minimal error only, which we attribute to the number of significant figures used in the calculation process.

Table 5.3. Comparison of the numerical values of the initial conditions at $z = 0$ of the reported data in the literature with the solved model in this study

Parameters	f_0	f_0^I	g_0	g_0^I	h_0^I
Dragoni and Goglio, 2013	0.00459	0.02978	0.02384	-0.17159	2.70675
Solution in this Study	0.0045952	0.0297451	0.0238371	-0.171582	2.7068

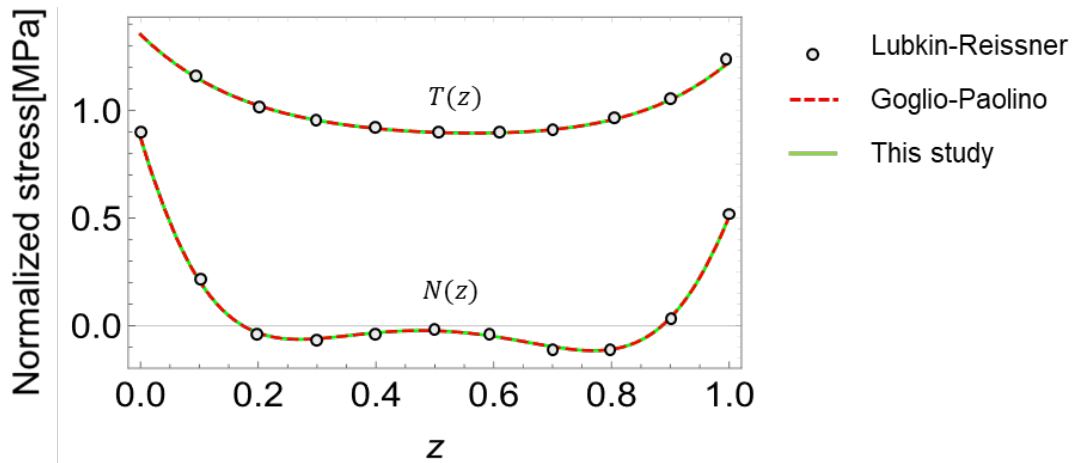


Figure 5.6. Comparison of the normalized stress field with the Lubkin-Reissner solution and Goglio-Paolino solution using the data given in Table 5.1 and Table 5.2. (Note that the lines are exactly overlapping)

As shown in Figure 5.6, the graphs of the corresponding normalized normal and shear stress are all identically matching with the reported data in the literature. This demonstrates that the current solution approach can successfully solve the equation set. Although in this study, the effects of pressure and thermal expansion are added into the model, they just make changes to the constants in the differential equation set. The order and coefficients of each unknown variables are kept the same with identical solution approaches. It is fully expected that the model will be accurate with the addition of these new effects.

5.5.2 Parametric Studies Setup

With modeling and solution method validated, the stresses in tube-to-tube adhesive joints are studied for practical operating parameters occurring in HVAC systems. There are various possible combinations of material and geometries in different such applications. A representative example joint is selected matching the geometry of the joints tested in Chapter 4 to carry out parametric studies and understand the influence on the key parameters. The first study focuses on the adhesive geometric design, namely, the overlap bonding length and adhesive layer thickness, which are important parameters to determine before manufacturing. Note that the pressure and temperature effect are not considered during this initial variation of the geometric sizing. Then, after the geometric variations, the second study investigates the effect of thermal expansion on the stress and strain fields.

The baseline case is given in Table 5.4 and Table 5.5 below, where the geometric parameters are measured from the actual joints and the material properties are collected from the corresponding manufacturers. Note that E_a and G_a of the adhesive DP420 used in Chapter 4 are not available. As suggested and provided by the manufacturer, the property data of DP460 available from experiment measurements are instead used in the following tables, which will provide similar trends and guidance on the application of adhesives for joining in HVAC&R systems.

Table 5.4. Geometric size of the tested adhesive joints in this study

Parameters	$r_1(mm)$	$r_2(mm)$	$r(mm)$	$t(mm)$	$t_1=t_2(mm)$	$l(mm)$
Values	9.1186	9.9514	9.545	0.1	0.8128	4

Table 5.5. Material properties and loading conditions of the tube and adhesive used in this study

Parameters	$E_1 = E_2$	$\nu_1 = \nu_2$	α	E_a	G_a	F_{ext}	P_{in}	P_{out}
Unit	<i>GPa</i>	–	<i>1/K</i>	<i>MPa</i>	<i>MPa</i>	<i>N</i>	<i>bar</i>	<i>bar</i>
Values	117.2	0.33	1.7×10^{-5}	2135	375	0	30	1

The internal pressure of 30 bar is selected based on the operating pressure of the typical HVAC&R systems based on the common refrigerants. Among the common refrigerants, R410A has a relatively high operating pressure compared to the rest. At the compressor discharge, a 30 bar (~435 kPa) is usually expected, which is at the higher end of common system operating pressures. There are other refrigerants operate at a much higher pressure (e.g., CO₂), but they need a corresponding tube material with higher strength (e.g., stainless steel).

The loading condition re-defined for the studied joints in HVAC&R systems as these joints usually are not structural parts with large external force. As discussed in Chapter 1, the main purpose of these joints is to connect the components together without leakage under the operating pressure. Thus, in the parametric studies, the axial force is not given arbitrarily, but instead evaluated based on the pressure difference acting on the tubes in the axial direction. Nevertheless, in some applications there may be a different external force on these joints (e.g., if they are load-

bearing) in the system. In any case, the following analysis is valid as long as the force is along the axial direction.

As indicated in Figure 5.7, the tube axial force balance can be calculated as following assuming no external axial force exists. In the case where external force needs to be considered, it can be trivially added into (5.73).

$$F_{out} = P_{out} \times \pi \left(\left(r_2 + \frac{t_2}{2} \right)^2 - \left(r - \frac{t}{2} \right)^2 \right)$$

$$F_{in} = P_{in} \times \pi \left(\left(r + \frac{t}{2} \right)^2 - \left(r_1 - \frac{t_1}{2} \right)^2 \right) \quad (5.72)$$

$$F = F_{in} - F_{out} \quad (5.73)$$

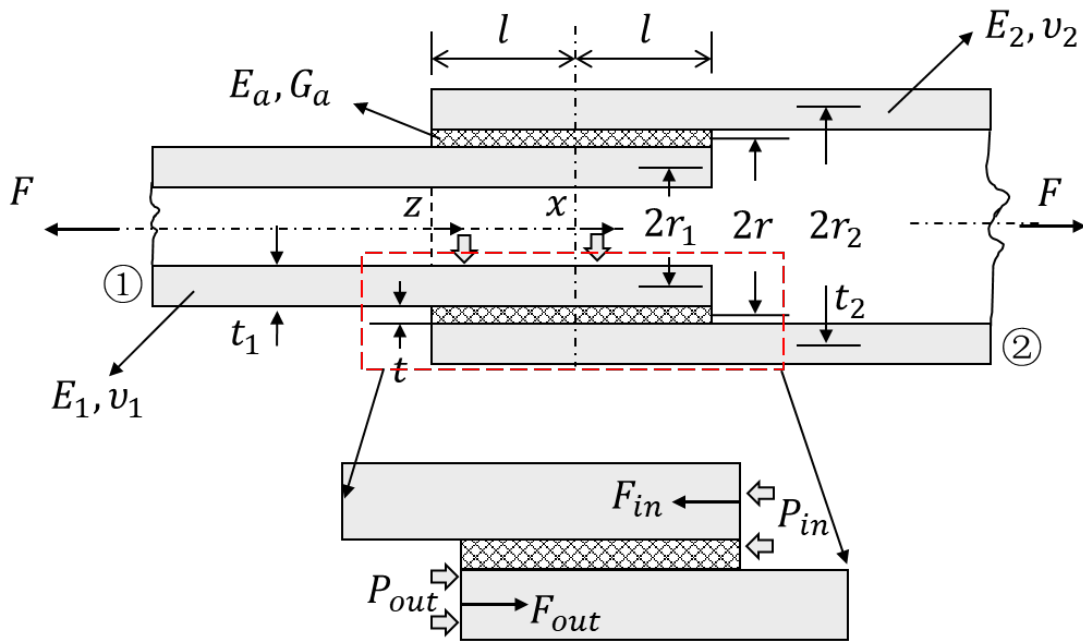


Figure 5.7. Axial force balance with pressure different across the tubes

5.5.3 Influence of Geometric Sizes

The geometric sizes are firstly investigated due to the importance in deciding these parameters during the manufacturing process. It is critical to provide guidance to HVAC&R manufacturers such that the sizes are properly decided for the specific application.

For tube-to-tube joints, there are two critical sizes that need to be determined for a given tube size and materials, the bonding length ($2l$) and adhesive thickness (t). The bonding overlap length $2l$ is first varied from 2 mm to 16 mm while the rest of the parameters are kept the same. The length selected in Chapter 4 is 8 mm, which is selected based on the typical brazed joint at same tube diameter. The variation range is determined such that it can provide a clear trend near this current practical value. The results are shown in Figure 5.8 as the stress distribution in the adhesive layer plotted along the previously defined dimensionless axial coordinate variable z .

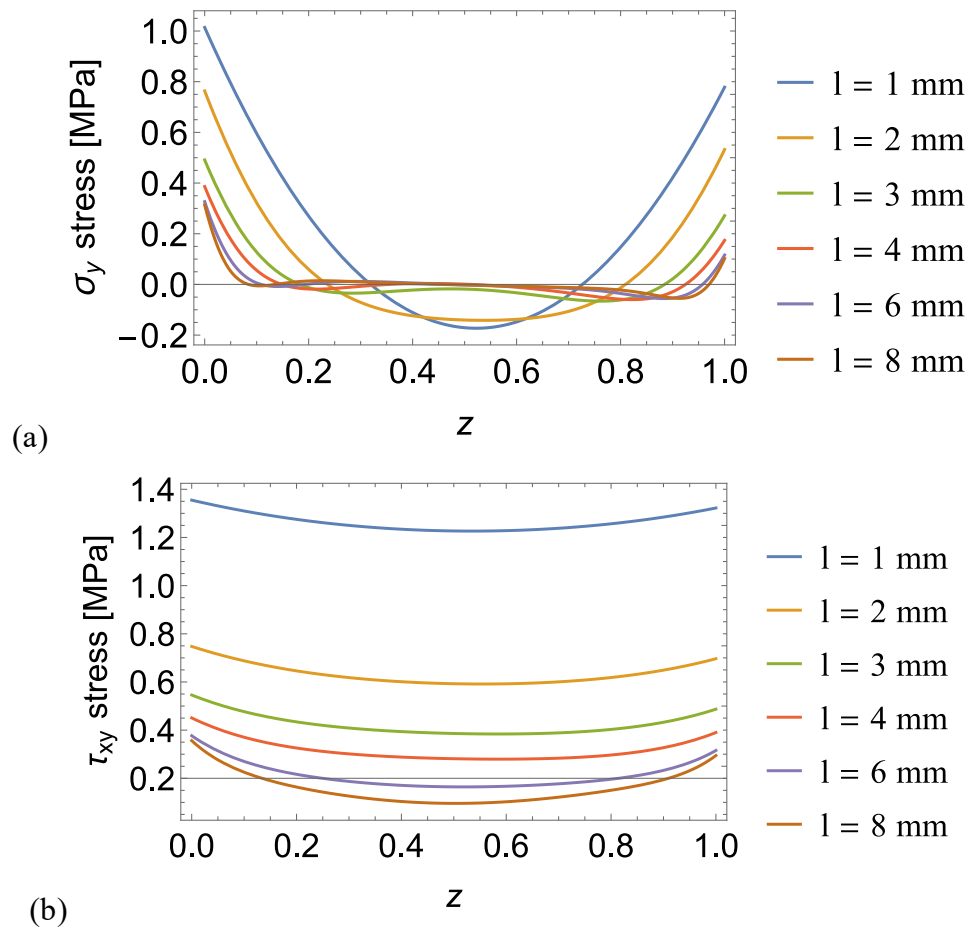


Figure 5.8. Variation of stress distributions with the change of bonding length ($2l$) plotted against the dimensionless variable z : (a) normal stress; (b) shear stress.

Several observations and conclusions can be made from the modeling results:

- For both of the stresses, the two peak stresses appear at end of the adhesive, with the maximum stress at location $z = 0$. This is consistent with the results from literature.

- The normal stress profile shape changes with the bonding length while the shear stress profile stays relative consistent in shape (but with very different values).
- Decreasing the bonding length will significantly increase the maximum stress for both the shear and normal stress in the adhesive layer.
- In the situation where the joints are not load-bearing components, with relatively high internal pressure (30 bar), the stresses are very low compared to the adhesive strength. Therefore static loading failure is not a concern for normal operating pressures.
- In the case of external loading existing where static failure might be a concern, the length should be selected such that the maximum stress is smaller than the allowed material strength for both normal and shear stress.

A finer change in bonding length is investigated to observe the shape change in normal stress as shown in Figure 5.9. In this particular case, the profile change can be observed clearly. With $l > 2.5 \text{ mm}$, there are two local minimums in the stress profile. With decreasing the length, two minimums move to the center point and merge as one global minimum when $l < 2.5 \text{ mm}$ and the compressive stress becomes largest at the center point.

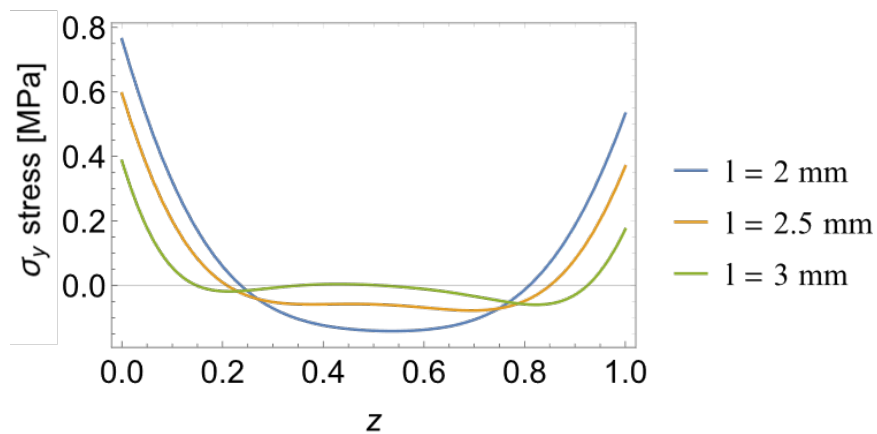


Figure 5.9. Variation of the normal stress distributions with the change of bonding length ($2l$) plotted against the dimensionless variable z .

Adhesive thickness (t) is varied next while the keeping the rest of the geometric parameters constant. Note that the model assumes the adhesive is a thin layer without considering bending,

which limits the applicability for thick adhesive layers. In general, for epoxy-type adhesives, a thin layer is always recommended by the manufacturer due to the fact that epoxies have been shown to have higher shear strength in standardized testing with relative thin layers. Also, thicker bondline thickness may have more cavity and pre-cracking in the manufacturing process. For example, for DP420 the manufacturer-recommend bondline thickness is in a small range from $\sim 0.1 - 0.2$ mm. Thus, the thickness t is varied from $0.06 - 0.2$ mm.

Note that if only the thickness is varied, there will be a change in axial force due to the change of cross section of the adhesive area used in the pressure-force calculation. Compared to the baseline, the axial force decreases by 5% at $t = 0.06$ mm and increased 12% at $t = 0.2$ mm. In order to isolate the changing parameter, the axial force is kept constant using the baseline value. The results are shown in Figure 5.10 as the stress distribution in the adhesive layer plotted along the previously defined dimensionless axial coordinate variable z . The studies that allow the change of axial forces were also performed and showed same conclusions and trends (plots not shown).

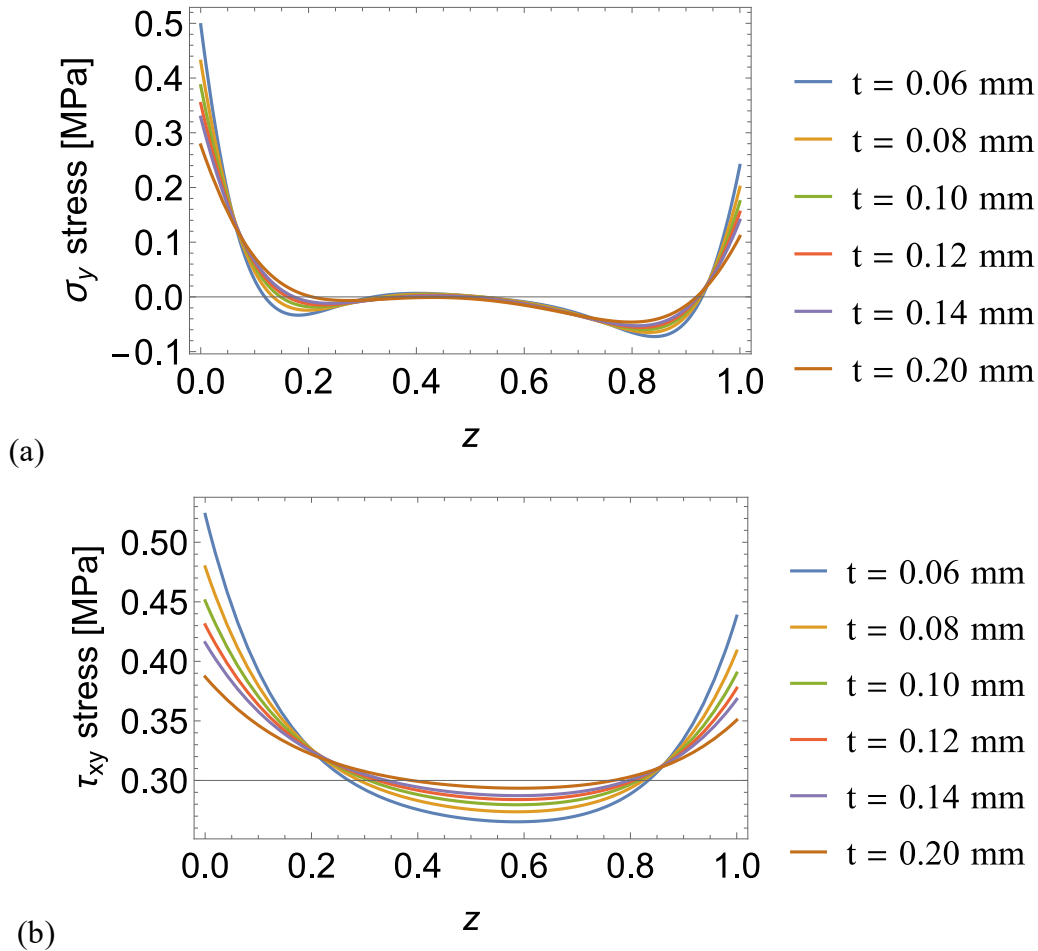


Figure 5.10. Variation of stress distributions with the change of adhesive thickness (t) while keeping the axial force constant. The results are plotted against the dimensionless variable z : (a) normal stress; (b) shear stress.

Several observations and conclusions can be made from the modeling results:

- For both stresses, the two peak stresses appear at end of the adhesive, with the maximum stress at location $z = 0$. This is consistent with the results from literature.
- For normal stress, the adhesive thickness has relatively small impact on the stress distribution; increasing the thickness decreases the maximum stress. Unlike the bonding length case, the stress profile is not affected by the bonding thickness over the range investigated.
- For shear stress, increasing the thickness also decreases the maximum stress but increases the minimum stress. The shear stress profile is more flattened with higher stress in the center part and lower stress at both ends.

- Under heavy loading condition where maximum stress values are a concern for static loading failure, the thickness should be selected properly to limit the maximum stresses. However, the effect of thickness on stress is less significant compared to the bonding length. In practice, following the manufacturer recommendation within a narrow range will usually result in satisfactory performance.

5.5.4 Influence of Thermal Expansion

The thermal expansion is key to the joint reliability in HVAC&R applications. Large temperature changes are expected to occur periodically throughout the life of the system. The modified model adds thermal strain due to the thermal expansion such that it can capture the influence of temperature change on the stress fields in adhesive layer.

As already discussed in Section 4.4.2, based on the common operating conditions in HVAC&R systems, the change in temperature is varied from $\Delta T = 10\text{ K} \sim 100\text{ K}$. A temperature change of 100 K is considered as an extreme case. A positive temperature change stands for increase in the temperature compared to the original temperature while negative stands for decrease from original temperature. It is important to consider this when dealing with joints in different locations of the systems. For example, considering a unit working at room temperature, the joints on the condensing side will usually experience a positive temperature change while the joints on the evaporating side will see a negative temperature change. The effect on positive temperature change is discussed first and the effect of negative temperature change is discussed separately later. The results of positive temperature change on the stress distributions are shown in Figure 5.11 as the stress distribution in the adhesive layer plotted along the previously defined dimensionless axial coordinate variable z .

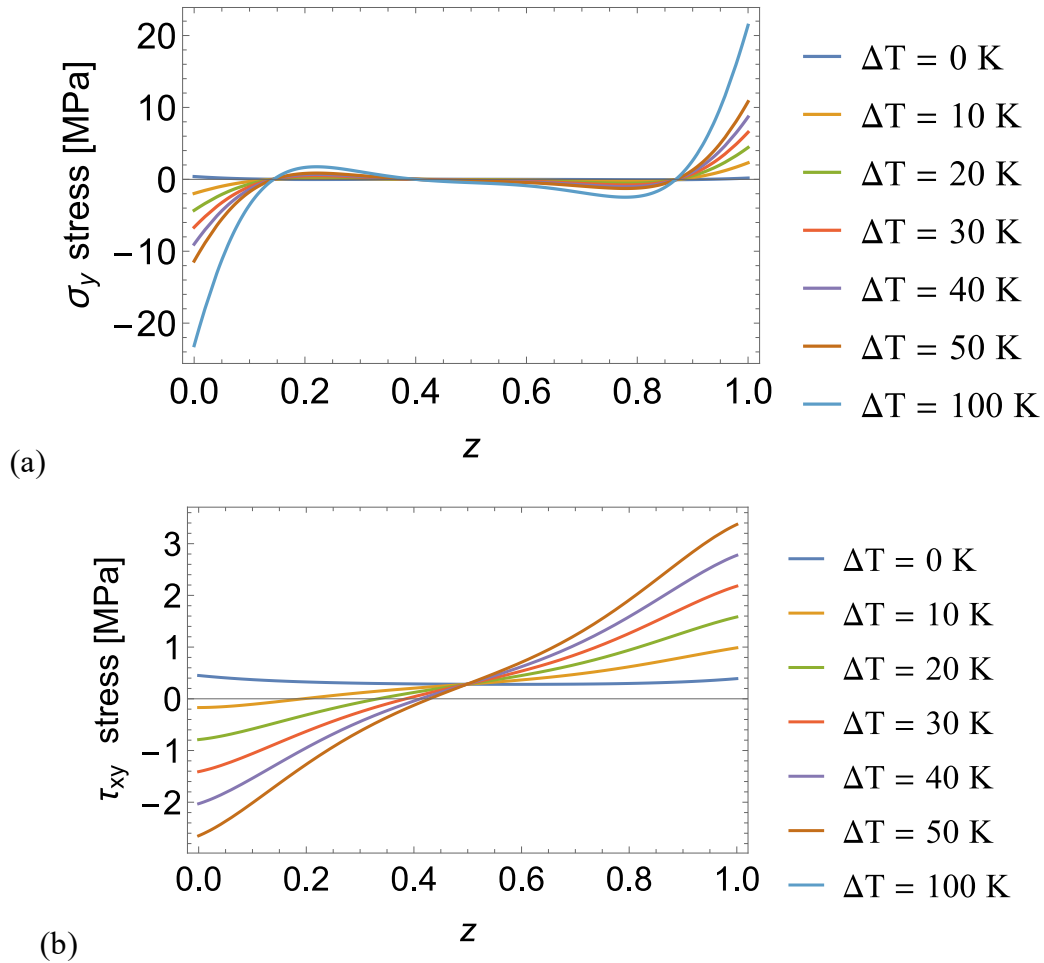


Figure 5.11. Variation of stress distributions with the change of temperature ($\Delta T = 10K \sim 100K$) plotted against the dimensionless variable z : (a) normal stress; (b) shear stress.

Comparing Figure 5.11 with Figure 5.8 and Figure 5.10, and noticing the different scales for vertical axes, it can be concluded that the thermal-expansion-induced stresses are dominant compared to the contribution of the internal pressure to the stress field. Due to the symmetries in the of the joint, the thermal-expansion-induced stress fields are centrosymmetric around $z = 0.5$ with both normal and shear stress values at the $z = 0.5$ do not change with temperature. Moving from $z = 0.5$ towards both ends ($z = 0$ and $z = 1$), thermal expansion has higher impact on the stress distributions. The peak stresses appear at both ends of the adhesive for normal and shear stress. The maximum stresses increase as the change in temperature increase. It is worth noting that in a positive temperature change, positive values for both stresses appear at location $z = 1$ and negative values appear at $z = 0$.

In order to further understand the thermal-expansion-induced stresses, a finer temperature range $\Delta T = -5 K \sim 5 K$ with both positive and negative temperature change is used for the model and the results are shown in Figure 5.12.

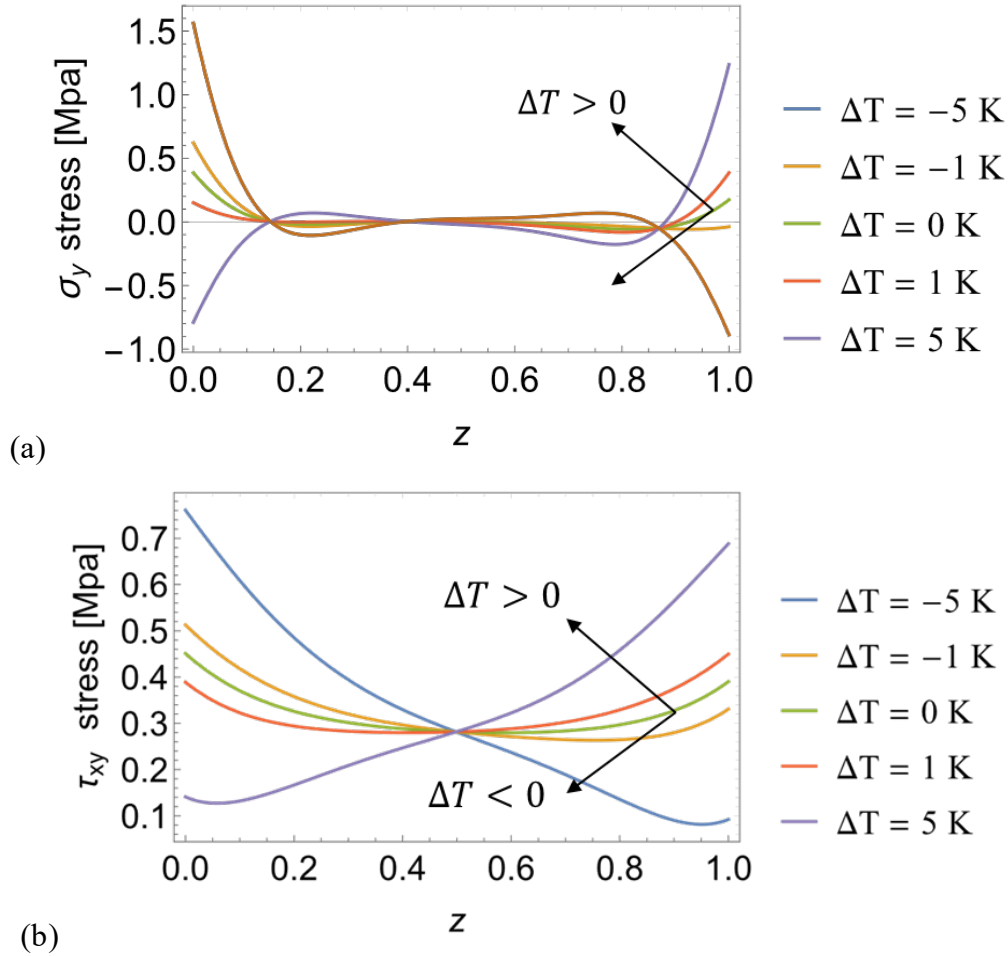


Figure 5.12. Variation of stress distributions with the small and negative change of temperature (ΔT) plotted against the dimensionless variable z : (a) normal stress; (b) shear stress.

It can be clearly observed that the negative temperature change has the opposite influence on the stress fields compared to the positive temperature change as labeled in Figure 5.12. The difference when comparing positive and negative temperature change (e.g., the maximum and minimum stress are not the same) is due to the pre-existing stress due to the axial loading. This is expected as the expansion or contraction has opposite impact on the thermal strain. With only a small temperature change, the stress profiles have changed significantly. Note that this will be different if the joints are used as load-bearing structures. In the previous results shown in Figure

5.11 and Figure 5.12, the axial force is calculated using Eqn. (5.72) and Eqn. (5.73) with the parameters given in Table 5.4 and Table 5.5. The axial force is only ~ 152 N. A heavily loaded case with axial force of 5,000 N is presented to further illustrate the major influence of the thermal stresses at an intermediate temperature change of $\Delta T = 50$ K, which is realistic and common in HVAC&R systems such as in ice makers or frozen storage applications. The values here are picked for demonstration purpose within the reasonable range but the general conclusion is valid for other conditions. Figure 5.13 and Figure 5.14 show the normal stress and shear stress distributions comparison respectively with loading condition under $\Delta T = 0$ K and $\Delta T = 50$ K with small axial loading $F = 152$ N and large axial force $F = 5000$ N. In both figures, the stress distributions in the adhesive layer are plotted along the previously defined dimensionless axial coordinate variable z .

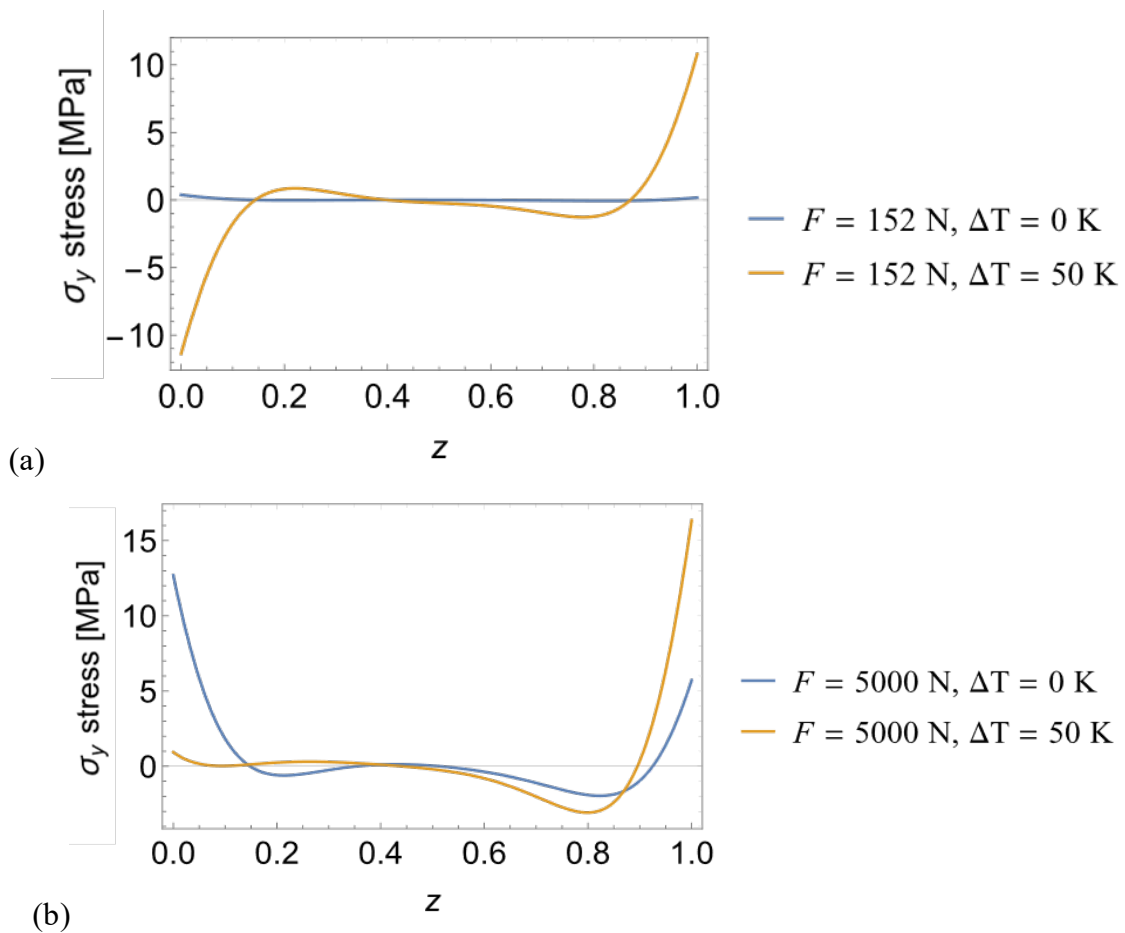


Figure 5.13. Comparison of normal stress distributions with low and high axial loading force experience the same temperature change ($\Delta T = 50$ K) plotted against the dimensionless variable z : (a) low axial force $F = 152$ N; (b) high axial force $F = 5000$ N.

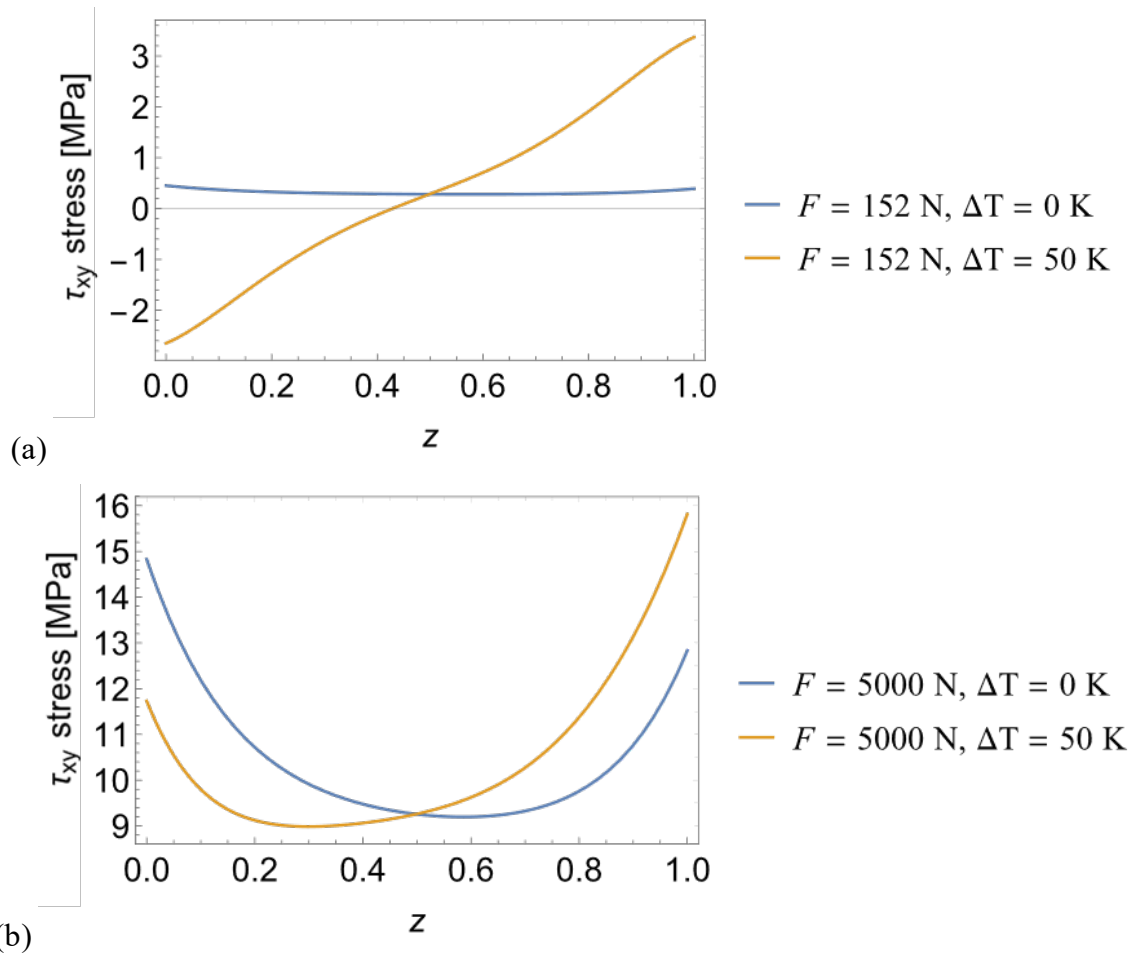


Figure 5.14. Comparison of shear stress distributions with low and high axial loading force experience the same temperature change ($\Delta T = 50$ K) plotted against the dimensionless variable z : (a) low axial force $F = 152$ N; (b) high axial force $F = 5000$ N.

The presented stresses have two sources: axial-force-induced stress and thermal-expansion-induced stress. As shown in Figure 5.13 and Figure 5.14, with low axial force, the thermal stresses dominate the stress profile with respect to the baseline. The axial stresses induced by pressure along are close to zero. However, with the very high axial force, both the axial force and thermal stress play important roles. It can be noticed the maximum normal and shear stresses have different values and locations after experiencing temperature change. A summary of the stresses at both ends of the adhesive for low and high axial loading with temperature is shown in Table 5.6.

Table 5.6. Geometric size of the tested adhesive joints in this study

Cases	$F = 152N$			$F = 5000N$		
	$\Delta T = 0 K$	$\Delta T = 50 K$	$\Delta T = -50 K$	$\Delta T = 0 K$	$\Delta T = 50 K$	$\Delta T = -50 K$
$\sigma_{z=0}(Mpa)$	0.39	-11.4	12.1	12.7	0.94	24.5
$\sigma_{z=1}(Mpa)$	0.17	10.8	-10.5	5.7	16.3	-4.9
$\tau_{z=0}(Mpa)$	0.45	-2.6	3.5	14.8	11.7	17.9
$\tau_{z=1}(Mpa)$	0.39	3.4	-2.6	12.8	15.8	9.8

The thermal stresses together with axial force loading can create complicated stress distributions. It can be noticed the maximum normal and shear stresses have different values and locations after experiencing temperature change. Depending on the loading condition and location, the thermal stress can significantly increase the maximum stress, which is especially critical with pre-existing loading as shown in the last two columns of Table 5.6. Both positive and negative temperature change as well as the external loading conditions should be considered in the system design phase.

5.5.5 Discussion on Thermal Stress

The above analyses thoroughly discussed the thermally induced stresses from a static loading perspective to check the maximum stress. It is clearly observed that in adhesive tube-to-tube joints, thermal-expansion-induced stresses plays a critical role in determining the stress distribution. Variation in joints temperature can significantly change the stress distribution. In HVAC&R systems, these large temperature swings will happen frequently with typical system operations. Thermal stress and strain must be included in the stress analysis.

As discussed in Chapter 4, fatigue failure can happen with stress cycling at values much lower than the static strength limit. If the system experiences temperature cycling, the thermally induced stresses will appear cyclically. In fact, the effect of the thermally induced stresses on the total stress distributions can be treated as a superposition independent of the axial-loading induced stresses. Comparing the difference between the stresses for low and high axial forces, the thermal induced normal and shear stresses in both loading conditions are identical to each other. It can be

concluded that the thermal induced stresses are independent of the axial force loading. This is consistent with the model setup. In the simplified system equations showed in Eqns.(5.40), the thermal expansion coefficients only appear in the constants. From a mathematical perspective, the superposition of solution for system of differential equations also yields the same conclusion.

The most accurate method to predict the failure of adhesive is evaluation of crack initiation and crack propagation. However, material behavior of adhesive, especially the fatigue crack growth must be obtained using costly and time-consuming experiments. In order to properly calculate the crack propagation, it is critical to check that no pre-existing defect below the detectable size will grow during the lifetime of the joints, which is another extremely challenging task.

From a design perspective, the developed stress distribution model can be further applied considering the maximum stress change with given temperature change or loading change. As shown in Table 5.6, assuming the system operates with a 50 K temperature swing, $\Delta\sigma_{y,max}$ and $\Delta\tau_{xy,max}$ can be retrieved from the model, as inputs parameter to a damage parameter method with Paris' Law to provide guidance for reliability design for thermal fatigue without exhaustive testing.

5.6 Summary and Conclusions

In this chapter, an analytical model predicting normal and shear stress distributions in adhesive layer of tube-to-tube adhesive joint is developed, validated and applied for parametric studies. The model reconsidered the classical model for this situation but added the influence of thermal expansion and contraction, which is necessary for consideration due to the constantly changing temperatures in HVAC&R systems. A solution process using Laplace transforms is implemented in Mathematica to provide an explicit closed-form solution. The solution is validated against published data from the literature and an exact match is achieved.

Applying the developed model of tube-to-tube joints, the relation between the joint stress and strain distributions and determining parameters can be clearly probed. The validated model is used in parametric studies to investigate the influence of adhesive overlapping length, adhesive bondline thickness, and temperature change experienced by the joints. Several conclusions are made about the trend of stress changes as well as the maximum stress:

For geometric parameters: the peak stresses usually appear at both ends of the adhesive; decreasing the bonding length will largely increase the maximum stress appeared for both the shear

and normal stress in the adhesive layer; increasing the thickness slightly decreases the maximum normal stress with relatively small impact on the shear stress field; and increasing the thickness decreases the maximum shear stress but increase the minimum stress resulting in a more flattened shear stress profile.

For thermally induced stress, they can be treated as a superposition over the original solution. Higher temperature differences cause higher stresses distribution changes. The negative and positive temperature changes will have opposite influence on the stress fields. The stresses are determined by both axial force induced stress and thermal induced stress. The relative values of the external force and temperature change determines the stress profiles. The possible further fatigue analysis is introduced but no detailed work is given due to the goal of current study.

More importantly, it is concluded that thermally induced stress plays a critical role in determination of the stress distributions of adhesive joints, especially in HVAC&R systems that will have large temperature swings. From both static and fatigue perspectives, thermal expansion must be included in the joint stress analysis.

From a design guidance perspective, the trend and understanding discovered in this model can help determine the geometry sizes. Adhesive bonding length should be selected such that the maximum stress is smaller than the allowed material strength for both normal and shear stress. Adhesive thickness has less impact and usually limited by the manufacturer recommendation from practical consideration. If temperature change is present, all the possible combination of loading and temperature change should be analyzed to find the most extreme loading condition. The thermally induced stresses must be always considered since even a small temperature change ($|\Delta T| < 5 K$) can cause significant stress changes.

This work reports the first detailed tube-to-tube joint model of stress and strain distributions aiming to simulate the working conditions of HVAC&R applications. All of these results provide a detailed guidance for use of adhesive joints across different application or locations in HVAC&R systems. The model can be also used as a framework to evaluate and compare the performance of different adhesives, as long as the adhesive properties can be determined as inputs.

6. PROOF OF CONCEPT TEST

In this chapter, a proof-of-concept test is conducted to evaluate the performance of adhesive joints in an HVAC&R system under normal working condition. The aim is to directly apply the adhesive into system joining or manufacturing process to prove the concept. At the same time, the tests can help to detect any unexpected issues in the assembly process and failures that are not captured by the traditional testing methods.

The proof-of-concept test uses tube-to-tube joints in a commercial heat pump dryer test stand. The test covers both tube-to-tube assembly as may happen in installation or repair in the field. The heat pump dryer test stand has been finished with experimental data and preliminary results.

6.1 Experimental Design

A heat pump system taken from a commercial clothes dryer is selected as the test system. The system components are summarized in Table 6.1. Figure 6.1 shows an image of the test stand alongside a schematic diagram of the flow loop with the primary components labelled. The system is a vapour compression cycle: the refrigerant vapour comes out of compressor and is condensed to liquid against ambient air through the subcooler and condenser. A separate fan is used to provide the airflow for the subcooler and to cool down the compressor. The liquid out of the condenser expands through a capillary tube and evaporates in the evaporator which then goes back to the compressor and closes the cycle. There is a blower that provides airflow for both the condenser and evaporator through the same air duct.

Table 6.1. Components and material applied in the heat pump dryer system

Compressor	HIGHLY (Shanghai Hitachi) BSD122DN-H3BDA
Condenser	Tube-and-fin type (Material: Aluminum)
Subcooler	Tube-and-fin type (Material: Aluminum)
Capillary Tube	Material: Copper)
Evaporator	Tube-and-fin type (Material: Aluminum)
Filter Dryer	Material: Copper)
Tubing	1/4-inch for discharge and 3/8-inch for suction (material: Copper)

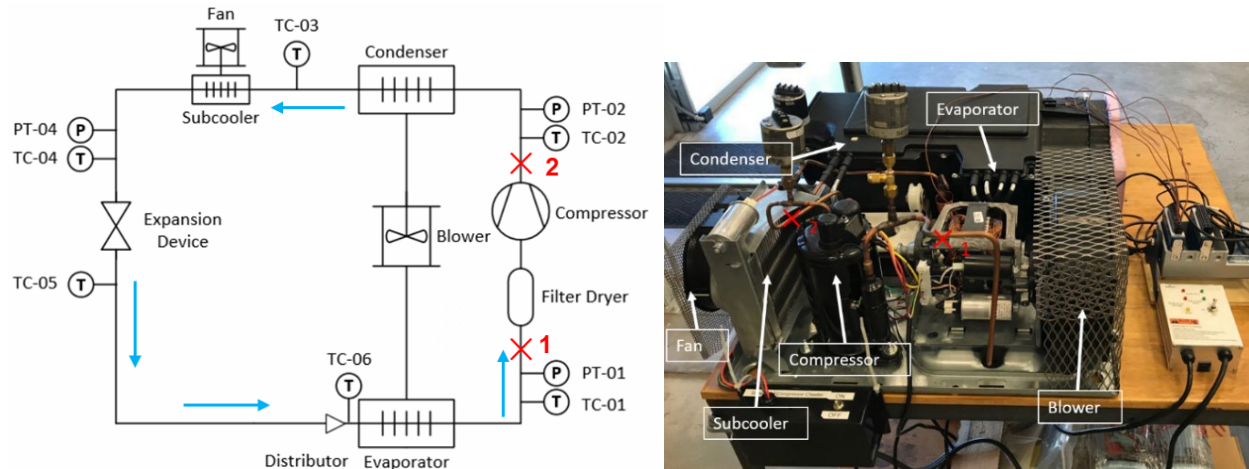


Figure 6.1. Schematic drawing (left) and photograph (right) of the custom-instrumented heat pump dryer test stand with the locations of the pressure transducers (P) and thermocouple measurements (T) indicated. The adhesive joints are placed at the locations labelled “1” and “2”.

The commercial system introduces various factors that may influence the adhesive joint performance. The system has a relatively high pressure of up to 15 bar at 55 °C with R134a as the refrigerant. The tubing is exposed to sudden pressure changes and random vibrations when the compressor and blower are running. It is an oil-lubricated system with oil passing through the tubing along with the refrigerant. There is tension and torque on the joints caused by thermal expansion and contraction as the system heats and cools as it is cycled on and off. All of these factors simultaneously act on the adhesive joints in a manner that is hard to simulate through standardized testing.

The system was also selected due to its simplicity in system control. The system consists of a single speed compressor, blower and fan with a capillary tube. There is no active control, and hence, the system operating conditions are only determined by the refrigerant charge amount and environmental temperature. Within a lab-testing environment, the temperature stays relatively constant. The operating conditions can thereby be used as an indicator for the system refrigerant charge amount.

The system is custom-instrumented with sensors to monitor the operating conditions. Three pressure transducers and five thermocouples are installed to measure the pressure at several selected locations and the temperatures at the inlet/outlet of each component, as labelled in Figure 6.1. The pressure transducers measure from 0 – 500 psig with an accuracy of ± 0.65 psig. The

thermocouples are copper-constantan (T) type with ± 1 °C uncertainty. Two different locations are selected for insertion of the adhesive joint based on the operating conditions of the system, as marked by red crosses in Figure 6.1. Location “1” is at the compressor outlet where there is the highest temperature and pressure in the system; location “2” is at the compressor inlet, with the lowest temperature and pressure. At each location, the original tubing is cut with a chip-free tube cutter in the middle, leaving two open ends. A copper coupling is used to form a new tube-to-tube connection using the adhesive, as will be described in the subsequent section.

6.2 Heat Pump Dryer System Modeling

In order to better describe the system operating condition and compare the testing results in a consistent manner, a simulation model of the heat pump dryer system was built in Engineering Equation Solver (EES, introduced in Chapter 3). As described in Figure 6.1, there are only three measured pressure values: compressor inlet, compressor outlet, and subcooler outlet before the expansion valve. All the temperature values at the component inlets and outlets are measured and can be considered known. The simulation model should be able to calculate the properties at each state point with reasonable assumptions and simplifications to represent the system in T-s diagram and p-h diagram.

Compressor inlet and outlet pressures and temperatures are measured; the state points are fully determined to look up the enthalpy and entropy:

$$h_{comp, in / out} = \text{enthalpy}(R134a, P_{comp, in / out}, T_{comp, in / out}) \quad (6.1)$$

$$s_{comp, in / out} = \text{entropy}(R134a, P_{comp, in / out}, T_{comp, in / out}) \quad (6.2)$$

For the condenser, it is assumed that there is no pressure drop in the tubing, so the inlet is fully decided by the pressure and temperature, similar to the compressor. The condensing temperature is determined by:

$$P_{cond} = P_{saturation, in}, T(R134a, T_{cond, in}) \quad (6.3)$$

Because the size of subcooler is much smaller than the condenser, assuming there is no pressure drop across the subcooler, the pressure at condenser outlet can be determined by:

$$P_{cond, out} = P_{subcooler, out} \quad (6.4)$$

The condenser outlet (subcooler inlet) state properties are then fully decided by this pressure and measured temperature. The subcooler outlet temperature and pressure are both measured, which is also the inlet of the expansion device (capillary tube in this system). Assuming constant enthalpy, the outlet state can be determined with the measured temperature:

$$h_{capli, out} = h_{capli, in} = h_{subcoller, out} \quad (6.5)$$

$$P_{capli, out} = Pressure(R134a, T_{capli, out}, h_{capli, out}) \quad (6.6)$$

Note that this is where the refrigerant just leaving the expansion device. There is extra pressure drop in the distribution tube before flowing into evaporator. It can be treated as a second expansion device with same assumption of constant enthalpy:

$$h_{tube, out} = h_{tube, in} = h_{capli, out} \quad (6.7)$$

$$P_{tube, out} = Pressure(R134a, T_{tube, out}, h_{tube, out}) \quad (6.8)$$

The evaporating pressure is determined by the inlet temperature:

$$P_{evap} = P_{saturation, in, T}(R134a, T_{evap, in} = T_{tube, out}) \quad (6.9)$$

The evaporator outlet temperature and pressure are both measured, which closes the loop. The subcooling of the condenser the superheat of evaporator then can be calculated by:

$$\Delta sub = T_{cond} - T_{cond, out} \quad (6.10)$$

$$\Delta sup = T_{evap, out} - T_{evap} \quad (6.11)$$

6.3 Adhesive Joining Procedure

A structural adhesive two-part epoxy was used as the bonding material for the application process. As suggested by the manufacturer, a manual applicator with a static mixing nozzle were used to evenly mix and apply the adhesive to the surface.

The outer tube surfaces were prepared by a traditional method of acetone cleaning, followed by sanding, and lastly a second acetone cleaning. The coupling is only acetone-cleaned because the inner surface of the small-diameter tube is inaccessible for sanding. Note that the coupling is a standard size for brazing purposes and is not specifically designed for adhesive joining. The gap size between the tube outer diameter and coupling inner diameter at both locations is measured to be 0.85 mm; this is within the recommended working range for the adhesive, which will guarantee

a strong adhesive bond. Figure 6.2 shows the location “1” tube cut, with the two open ends aligned after preparing the bonding surface; the coupling is shown slid onto the left-side tube end. The difference in color of the copper tube near the coupling indicates that the surface preparation removed the oxide layer and other contaminants. Before applying the adhesive, the two tube ends are aligned coaxially and pressed against each other to decrease the possibility of adhesive leaking into the inner surface of the copper tubing. The adhesive is circumferentially applied on the cleaned tube area to cover a region the same length as the coupling. The coupling is slowly slid along the tube until the cut is at the center of the coupling. It is ensured that the adhesive fills the gap between the tube and the coupling, with no visible openings; the assembled joint is shown in Figure 6.2. Because the tube is in a horizontal orientation, the adhesive accumulates at the bottom of the tube due to the effect of gravity. The adhesive is left to cure at room temperature for 24 hours. After curing, an aluminum safety shield is placed around the joints in case of a catastrophic failure. The other adhesive joint in location “2” is manufactured following the same procedure.

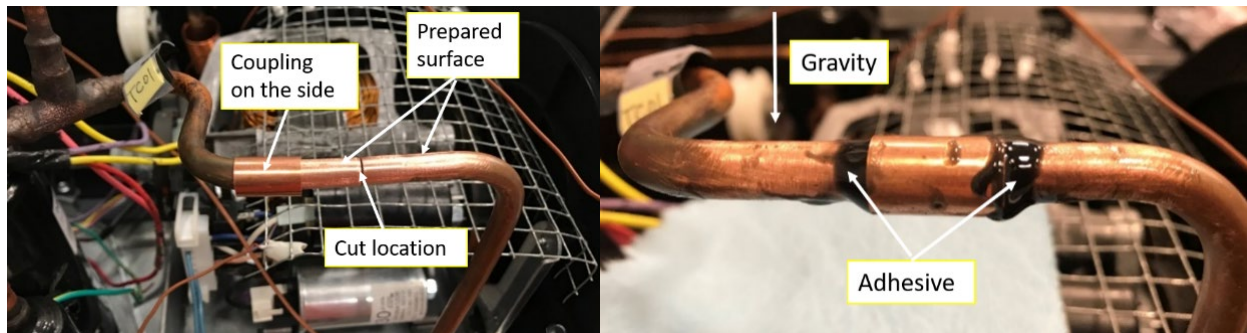


Figure 6.2. Photographs of the cut location “1” for the tube-to-tube joint after preparing bonding surface (left) and within the coupling in place over the cut after application of the adhesive (right).

6.4 Testing Procedure

Before cutting the tubes, a baseline test was performed to measure the system operating conditions. The system was charged with 428 g of refrigerant R134a, which is recommended by the manufacturer. All of the system components (e.g., the compressor, fan, and blower) were run at a fixed speed that was maintained constant for the duration of the test until steady-state operating conditions were achieved.

After recording the standard operating condition benchmark, the tubes were cut and re-assembled with adhesive joints as described in the previous section. Before recharging the system with refrigerant, a leakage check was performed by charging the lines with high-pressure nitrogen and pulling a vacuum on the system. The system high-side operating pressure is approximately 960 kPa and it was charged with nitrogen to 1900 kPa. After 72 hours, the pressure dropped by ~1% to 1880 kPa and then held steady. When a vacuum was pulled on the system, no pressure increase was observed after 6 hours. These tests confirm that the system was leak-free after the initial adhesive joining and ready for testing.

The system was charged with the same amount of refrigerant as during the baseline testing. After charging, a long-term test plan was followed for the adhesive joints: the system was run for several hours every one or two weeks, similar to the anticipated operation of the device, with the pressure and temperature recorded after reaching a steady operating point. The procedure evaluates whether the prototype adhesive joints can hold the pressure over a long time while being subjected to normal running cycles. The system pressures and temperatures are compared with baseline results, which would differ if there was a significant loss of charge.

6.5 Results and Discussion

The operating conditions for the baseline and the case with adhesive joints case are compared in Figure 6.3. The baseline condition is defined as the standard operating condition, achieved by the initial charge without any modification with adhesive joints. Several assumptions were made to calculate all state points where there is not a direct measurement, namely: no pressure drop in the condenser, constant enthalpy across the expansion devices, and two-phase operation the condenser and evaporator. Due to the long tubing and distributor before evaporator, there is an additional pressure drop between the capillary tube (point 5) and evaporator (point 6). This was treated as a second expansion device to accurately capture the pressure and temperature at the evaporator inlet.

The data presented in Figure 6.3. indicates that there is a consistent operation before and after installation of the adhesive joints. In both cases, between state points 5 and 6, there is additional pressure drop with the according temperature decrease. Also, note that the there is pressure drop across the evaporator, which explains the temperature decrease from state point 6 to 1. A small variation in the pressure and temperature, comparing the baseline and adhesive data,

are attributed to slightly different charge amounts due to the refrigerant scale uncertainty and difference in the room temperature (21.9 °C for the baseline versus 22.4 °C in the adhesive case).

In order to further evaluate the feasibility of this concept, the system was operated periodically over the next 6 months per the testing procedure described in the previous section. The corresponding temperature-entropy (T-s) and pressure-enthalpy (P-h) diagrams are shown in Figure 6.4, with the adhesive test operating points overlaid on a plot of the baseline condition. As shown in Figure 6.4, the system performed consistently with each subsequent test after sealing the joints with adhesive. The consistent pressure level and system performance indicates that there was no leakage over the testing period and that the adhesive joints operate successfully under the temperature changes and vibrations associated with operation of the system using refrigerant R134a. Despite the limitations of testing only two adhesive joints over a moderate temperature/pressure range for a period shorter than the typical lifetime, as a proof-of-concept test, this suggests that adhesives may be feasible and practical to replace brazed joints in HVAC&R systems. Further testing is recommended to evaluate the performance of adhesive joints in HVAC&R systems to the point of failure or leakage.

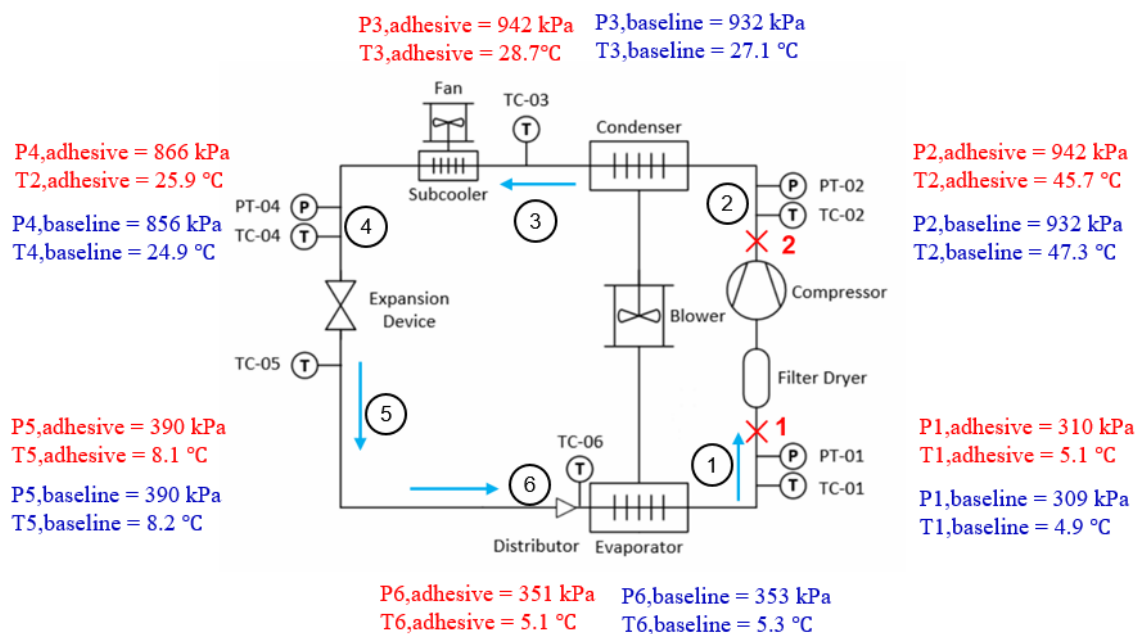


Figure 6.3. Schematic diagram of the heat pump system showing the pressure and temperature values measured or calculated at each state point. The baseline data are shown in blue and the data for the tests with the adhesive joints are shown in red.

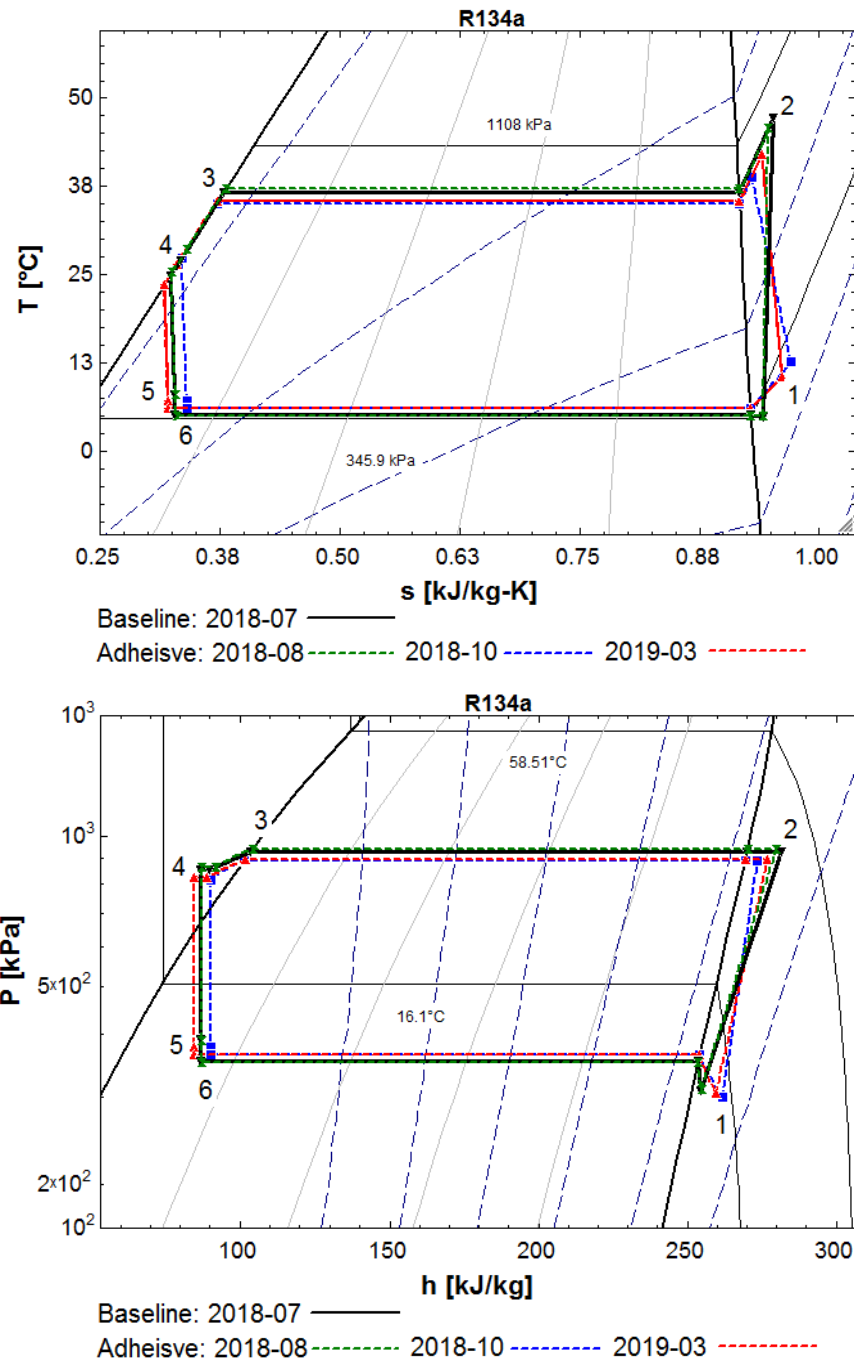


Figure 6.4. T-s (top) and P-h (bottom) diagrams of heat pump system operation conditions at the baseline condition and for three selected tests over a 6-month period after installing the adhesive joints.

6.6 Summary

Adhesive joints have the potential to replace brazed joints and improve system efficiencies in the HVAC&R industry. After various testing and modeling, to demonstrate the application procedure and explore the feasibility of an adhesive joint, a proof-of-concept tests were performed using a heat pump dryer system. An adhesive joining procedure is presented including surface preparation, adhesive preparation, adhesive application, and curing. For the heat pump dryer system, tube-to-tube adhesive joints were installed at the inlet and outlet of the compressor. The system was first pressurized to check for initial leaks and then charged with refrigerant for performance testing over a 6-month period. Results showed that the adhesive joints hold the refrigerant pressure without leaks and the system performs consistently before and after the installation of adhesive joints. The proof-of-concept tests indicate that it is practical to use of adhesive joints to replace brazed joints in HVAC&R applications, which warrants further investigation.

7. SUMMARY AND RECOMMENDATIONS

In this chapter an overall conclusion is given of the main investigations of the current work. While the research performed achieved the objectives and addressed the questions posed in the introduction, the current works also opens several new doors to future extensions and improvements. These potential future research investigations are outlined in the final section of this chapter.

7.1 Overall Conclusion

Adhesive joints have the potential to replace brazed joints and improve system efficiencies in the HVAC&R industry. Compared to existing brazed and mechanical joints, the use of adhesives offers lowers cost, eases manufacturing without an open flame, and provides the flexibility to be applied to various materials and geometries. However, the adhesive joints' performance and reliability in the long-term needs further evaluation. The research and applications employing adhesive joints for HVAC&R systems is still at early stage and limited results are available on fatigue failure and real system testing conditions. In order to contribute to the research area, both experimental and analytical modeling work have been performed in the present work. Firstly, laser-interference structuring is evaluated as a surface preparation technique for adhesive joints, which enhances the bonding performance compared with those joints made with the traditional preparation method. Next, the fatigue failure of adhesive joints in HVAC&R systems are investigated since it is the major concern for long-term reliability. Two separate tests are designed and performed to evaluate the vibration fatigue resistance and pressure and temperature cyclic fatigue resistance. The tested adhesive joints showed good fatigue resistance and passed both tests. The pressure and temperature cyclic test stand serves as new research infrastructure for the pressure and temperature fatigue testing of joints and allows for research and development of new joining technologies and other components for HVAC&R applications. Furthermore, an analytical model on stress and strain for adhesively bonded tube-to-tube joints under thermal stresses is built and solved to establish a framework for failure prediction under thermal loading. Lastly, to demonstrate the application procedure and explore the feasibility of an adhesive joint, two separate proof-of-concept tests were performed using a heat pump dryer system. An adhesive joining

procedure is presented including surface preparation, adhesive preparation, adhesive application, and curing. The installed adhesive joints hold the refrigerant pressure without leaks. The system performs consistently before and after the installation of adhesive joints, which indicate the potential or use of adhesive joints to replace brazed joints in HVAC&R applications.

7.2 Recommendations for Future Research

7.2.1 Extended Reliability Testing

The experiments designed and performed in the current work, including the pressure temperature cyclic (PTC) test stand, vibration testing and proof-of-concept testing, constructed a platform to perform reliability testing on the adhesive joints. However, only a limited number of tests were performed to demonstrate the functions of these test stands. In the PTC testing and vibration testing, only U-shape joints with one geometry were selected and passed the qualification testing with test conditions recommended by the ISO standard.

Using the current infrastructure, extended PTC and vibration tests can be performed under various testing conditions with different joint type, size, and material. Here are some potential studies in the future:

- PTC tests with low temperature below 0 °C. This can be steadily achieved with the current stands. The effect freezing of condensed water and moisture in the adhesive can be studied for those applications involving low-temperature operation.
- Reliability testing on different joint sizes for all possible HVAC&R applications. Much larger tube diameters are used in large-scale systems. In practice, the tests should be performed based on the targeting application. Both PTC and vibration tests are capable of testing joints in different sizes.
- Conducting the same sets of testing with different metals for adherents can be beneficial, such as Cu-Al joint and Al-to-Al joints. This can extend the usage of adhesive joints which may also enables the possibility to use adhesive joints in other industries.
- The current work shows adhesive joints can pass the standard required testing and work in heat pump dryer system. Long-term (in timescale of years) reliability testing in both fatigue test stands and real systems can better prove the reliability and identify potential issues.

7.2.2 Improvements to the Analytical Structural Model

A number of possible improvements to the analytical structural model are reported here.

- The model only considered elastic material properties for both adherents and adhesive. While it is a good assumption for the studied case, plasticity can be also considered, especially for adhesives.
- The adhesive is assumed to be a thin layer due to the manufacture-recommended bondline thickness. Further investigation without thin layer assumption can improve the applicable range of this model, even for different geometries and applications.
- The model only considered axial loading force as external forces based on the working conditions of these joints in HVAC&R systems. Further loading scenarios can be added into the model, including radial force, torsion, or bending to extend the capability of the model.
- For thermal effects, a linear thermal expansion coefficient is used. A more complicated and accurate thermal expansion model can be applied with detailed measurement data to capture the thermal strain at different temperature levels. This can further improve the accuracy of the model.
- The model does not consider the thermal expansion and contraction of the adhesive. This can be another improvement to increase the application range and accuracy.
- The current work concluded thermal stress is significant in adhesive joints in HVAC&R systems with parametric studies on static loading conditions. The failure under fatigue can be further developed. Based on the approaches available, fracture energies or stress intensity factor under different loading conditions and testing environment are needed to develop the failure model. This requires a complete set of characterization testing for the given adhesive. The results of the current model can be used as inputs to the failure prediction model.

7.2.3 Other Possible Research

Some other related future research inspired by the current work is summarized, which require multidisciplinary engineering and collaboration, but can be very beneficial to the industry.

- In Chapter 3, the conclusion indicates that the laser interference technique can increase the joint strength, which has great potential to replace the traditional surface preparation methods. However, these tests were completed in a laboratory setup that cannot be directly used in manufacturing environment. Compared with sanding and chemical cleaning, laser processing can be integrated with automatic manufacturing, for example robotic arms. Efforts are needed to design small-scale devices for laser interference structuring with either hand processing or automatic production lines.
- Adhesive has great flexibility as discussed in the introduction part. Adhesive co-development with joint testing for HVAC&R systems can ensure the final success in using adhesive joint in HVAC&R systems. Adhesive formula can be modified based on the requirements. Once issues and needs are identified in the joint evaluation tests, adhesive manufacturers can correspondingly modify the formulation to satisfy the newly identified needs for HVAC&R system.
- HVAC&R manufacturing process optimization can be another great opportunity enabled by the current work. Once adhesive is ready to be used in HVAC&R systems, the current assembly lines using brazing / soldering must be modified to adapt the different technology. With potentially fully automatic manufacture process with surface preparation, adhesive applying and curing without open flame, the assembly cost can be decreased with increasing efficiency.
- Comparing to conventional joints in the HVAC&R industry, application of adhesive provides design freedom to remove the geometrics limitation for components in the system that are governed by the need for brazing. Heat exchangers may be redesigned to potentially leads to more compact systems using less mass and refrigerant charge; for example, flat tube heat exchangers can be joined by an adhesive without additional challenge. Reduced refrigerant charging is also critical for systems with flammable refrigerants.
- Thermal and heat transfer studies of adhesive layers. There is a widespread interest to use high strength bonding material (adhesives) with high thermally conductivities (e.g., micro-channel heat exchanger assembly, cylinder-to-cylinder heat exchangers). Most of the adhesives in current markets have very low thermal conductivities. To overcome this problem, filler particles can be added to the adhesive to enhance the heat transfer

performance. This has limited increase on heat transfer with adverse effect on the strength and fatigue resistance. The tests and model developed in this work can be readily used to evaluate the newly developed adhesives. It is also possible to further develop co-optimization model for both structural and thermal performance.

APPENDIX. WOLFRAM MATHEMATICA PRINTOUT

Symbolic calculation for adhesive tube-to-tube model

Left side Matrix S

```

In[ ]:= (S = {{s^4 + K1^4 + γ11^4, -γ12^4, -3 r / r1 * (s^2 + A1)},
             {-γ21^4, s^4 + K2^4 + γ22^4, -3 r / r2 * (s^2 - A2)},
             {-B1^2 (s^2 + A1), -B2^2 (s^2 - A2), s^2 - (B1^2 / r1 + B2^2 / r2) * r}}) //
MatrixForm

```

Out[]/MatrixForm=

$$\begin{pmatrix} s^4 + K_1^4 + \gamma_{11}^4 & -\gamma_{12}^4 & -\frac{3r(s^2 + A_1)}{r_1} \\ -\gamma_{21}^4 & s^4 + K_2^4 + \gamma_{22}^4 & -\frac{3r(s^2 - A_2)}{r_2} \\ -B_1^2(s^2 + A_1) & -B_2^2(s^2 - A_2) & s^2 - r\left(\frac{B_1^2}{r_1} + \frac{B_2^2}{r_2}\right) \end{pmatrix}$$

```

In[ ]:= det = Det[S]

```

```

In[ ]:= MatrixForm[

```

mat2o =

$$\frac{1}{s} \left\{ \left\{ s^4 f_\theta + s^3 f_{\theta,dev1} + s^2 \left(f_{\theta,dev2} - \frac{3r h_\theta}{r_1} \right) + s \left(f_{\theta,dev3} - \frac{3r h_{\theta,dev1}}{r_1} \right) - \frac{3A_1 r}{r_1} + C_1 \right\}, \right. \\ \left. \left\{ s^4 g_\theta + s^3 g_{\theta,dev1} + s^2 \left(g_{\theta,dev2} - \frac{3r h_\theta}{r_2} \right) + s \left(g_{\theta,dev3} - \frac{3r h_{\theta,dev1}}{r_2} \right) - \frac{3A_2 r}{r_2} + C_2 \right\}, \right. \\ \left. \left\{ s^2 (h_\theta - B_1^2 f_\theta - B_2^2 g_\theta) + s (h_{\theta,dev1} - B_1^2 f_{\theta,dev1} - B_2^2 g_{\theta,dev1}) - \left(\frac{B_1^2 r}{r_1} - \frac{B_2^2 r}{r_2} \right) + C_3 \right\} \right\}$$

Out[]/MatrixForm=

$$\begin{pmatrix} \frac{C_1 + s^4 f_\theta - \frac{3r A_1}{r_1} + s^3 f_{\theta,dev1} + s^2 \left(-\frac{3r h_\theta}{r_1} + f_{\theta,dev2} \right) + s \left(f_{\theta,dev3} - \frac{3r h_{\theta,dev1}}{r_1} \right)}{s} \\ \frac{C_2 + s^4 g_\theta - \frac{3r A_2}{r_2} + s^3 g_{\theta,dev1} + s^2 \left(-\frac{3r h_\theta}{r_2} + g_{\theta,dev2} \right) + s \left(g_{\theta,dev3} - \frac{3r h_{\theta,dev1}}{r_2} \right)}{s} \\ \frac{C_3 + s^2 \left(-B_1^2 f_\theta - B_2^2 g_\theta + h_\theta \right) - \frac{r B_1^2}{r_1} + \frac{r B_2^2}{r_2} + s \left(-B_1^2 f_{\theta,dev1} - B_2^2 g_{\theta,dev1} + h_{\theta,dev1} \right)}{s} \end{pmatrix}$$

Boundary Conditions

$${}^{in[-]} \mathbf{f}_{\theta,dev2} = \sqrt{2} K_1 \mathbf{f}_{\theta,dev1} - K_1^2 \mathbf{f}_{\theta} - \frac{2\sqrt{3} \nu_1 r}{r_1 \sqrt{1-\nu_1^2}}$$

$$\mathbf{f}_{\theta,dev3} = \sqrt{2} K_1 \left(\sqrt{2} K_1 \mathbf{f}_{\theta,dev1} - K_1^2 \mathbf{f}_{\theta} - \frac{2\sqrt{3} \nu_1 r}{r_1 \sqrt{1-\nu_1^2}} \right) - K_1^2 \mathbf{f}_{\theta,dev1} + \frac{3 r h_{\theta,dev1}}{r_1}$$

$$\mathbf{g}_{\theta,dev2} = -\sqrt{2} K_2 \mathbf{g}_{\theta,dev1} - K_2^2 \mathbf{g}_{\theta} - \frac{2\sqrt{3} \nu_2 r}{r_2 \sqrt{1-\nu_2^2}}$$

$$\mathbf{g}_{\theta,dev3} = -\sqrt{2} K_2 \left(-\sqrt{2} K_2 \mathbf{g}_{\theta,dev1} - K_2^2 \mathbf{g}_{\theta} - \frac{2\sqrt{3} \nu_2 r}{r_2 \sqrt{1-\nu_2^2}} \right) - K_2^2 \mathbf{g}_{\theta,dev1} + \frac{3 r h_{\theta,dev1}}{r_2}$$

$$-\mathbf{f}_{\theta} K_1^2 - \frac{2\sqrt{3} r \nu_1}{r_1 \sqrt{1-\nu_1^2}} + \sqrt{2} K_1 \mathbf{f}_{\theta,dev1}$$

$$-K_1^2 \mathbf{f}_{\theta,dev1} + \sqrt{2} K_1 \left(-\mathbf{f}_{\theta} K_1^2 - \frac{2\sqrt{3} r \nu_1}{r_1 \sqrt{1-\nu_1^2}} + \sqrt{2} K_1 \mathbf{f}_{\theta,dev1} \right) + \frac{3 r h_{\theta,dev1}}{r_1}$$

$$-\mathbf{g}_{\theta} K_2^2 - \frac{2\sqrt{3} r \nu_2}{r_2 \sqrt{1-\nu_2^2}} - \sqrt{2} K_2 \mathbf{g}_{\theta,dev1}$$

$$-K_2^2 \mathbf{g}_{\theta,dev1} - \sqrt{2} K_2 \left(-\mathbf{g}_{\theta} K_2^2 - \frac{2\sqrt{3} r \nu_2}{r_2 \sqrt{1-\nu_2^2}} - \sqrt{2} K_2 \mathbf{g}_{\theta,dev1} \right) + \frac{3 r h_{\theta,dev1}}{r_2}$$

Right side matrix formed by f(s),g(s),h(s)

In[]:= MatrixForm[

mat2 =

$\frac{1}{s}$

$$\left\{ \left\{ s^4 f_0 + s^3 f_{0,dev1} + s^2 \left(\left(\sqrt{2} K_1 f_{0,dev1} - K_1^2 f_0 - \frac{2\sqrt{3} u_1 r}{r_1 \sqrt{1-u_1^2}} \right) - \frac{3 r h_0}{r_1} \right) + \right. \right.$$

$$s \left(\left(\sqrt{2} K_1 \left(\sqrt{2} K_1 f_{0,dev1} - K_1^2 f_0 - \frac{2\sqrt{3} u_1 r}{r_1 \sqrt{1-u_1^2}} \right) - K_1^2 f_{0,dev1} + \frac{3 r h_{0,dev1}}{r_1} \right) - \right.$$

$$\left. \left. \frac{3 r h_{0,dev1}}{r_1} \right) - \frac{3 A_1 r}{r_1} + C_1 \right\},$$

$$\left\{ s^4 g_0 + s^3 g_{0,dev1} + s^2 \left(\left(-\sqrt{2} K_2 g_{0,dev1} - K_2^2 g_0 - \frac{2\sqrt{3} u_2 r}{r_2 \sqrt{1-u_2^2}} \right) - \frac{3 r h_0}{r_2} \right) + \right.$$

$$s \left(\left(-\sqrt{2} K_2 \left(-\sqrt{2} K_2 g_{0,dev1} - K_2^2 g_0 - \frac{2\sqrt{3} u_2 r}{r_2 \sqrt{1-u_2^2}} \right) - K_2^2 g_{0,dev1} + \frac{3 r h_{0,dev1}}{r_2} \right) - \right.$$

$$\left. \left. \frac{3 r h_{0,dev1}}{r_2} \right) - \frac{3 A_2 r}{r_2} + C_2 \right\},$$

$$\left\{ s^2 (h_0 - B_1^2 f_0 - B_2^2 g_0) + s (h_{0,dev1} - B_1^2 f_{0,dev1} - B_2^2 g_{0,dev1}) - \left(\frac{B_1^2 r}{r_1} - \frac{B_2^2 r}{r_2} \right) + C_3 \right\} \Bigg]$$

Out[]:=MatrixForm

$$\begin{pmatrix} \frac{C_1 + s^4 f_0 - \frac{3 r A_1}{r_1} + s^3 f_{0,dev1} + s^2 \left(-f_0 K_1^2 - \frac{3 r h_0}{r_1} - \frac{2\sqrt{3} r u_1}{r_1 \sqrt{1-u_1^2}} + \sqrt{2} K_1 f_{0,dev1} \right) + s \left(-K_1^2 f_{0,dev1} + \sqrt{2} K_1 \left(-f_0 K_1^2 - \frac{2\sqrt{3} r u_1}{r_1 \sqrt{1-u_1^2}} + \sqrt{2} K_1 f_{0,dev1} \right) \right)}{s} \\ \frac{C_2 + s^4 g_0 - \frac{3 r A_2}{r_2} + s^3 g_{0,dev1} + s^2 \left(-g_0 K_2^2 - \frac{3 r h_0}{r_2} - \frac{2\sqrt{3} r u_2}{r_2 \sqrt{1-u_2^2}} - \sqrt{2} K_2 g_{0,dev1} \right) + s \left(-K_2^2 g_{0,dev1} - \sqrt{2} K_2 \left(-g_0 K_2^2 - \frac{2\sqrt{3} r u_2}{r_2 \sqrt{1-u_2^2}} - \sqrt{2} K_2 g_{0,dev1} \right) \right)}{s} \\ \frac{C_3 + s^2 \left(-B_1^2 f_0 - B_2^2 g_0 + h_0 \right) - \frac{r B_1^2}{r_1} + \frac{r B_2^2}{r_2} + s \left(-B_1^2 f_{0,dev1} - B_2^2 g_{0,dev1} + h_{0,dev1} \right)}{s} \end{pmatrix}$$

Solve the Laplace function F(s),G(s),H(s)

In[]:= `MatrixForm[gmat = Inverse[S].mat2]`

In[]:= `fs = Simplify[Part[gmat, 1]]`

$$\begin{aligned} \text{Out[]:= } & \left\{ - \left(r_1 r_2 \left(\left(s^2 - r \left(\frac{B_1^2}{r_1} + \frac{B_2^2}{r_2} \right) \right) (s^4 + K_2^4 + \gamma_{22}^4) - \frac{1}{r_2} 3 r B_2^2 (s^2 - A_2)^2 \right) \right. \\ & \left(f_0 s^4 + f_{0,\text{dev1}} s^3 - f_0 K_1^2 s^2 + \sqrt{2} K_1 f_{0,\text{dev1}} s^2 - \frac{3 r h_0 s^2}{r_1} - \sqrt{2} f_0 K_1^3 s + \right. \\ & \left. K_1^2 f_{0,\text{dev1}} s - (2 \sqrt{3} r (s + \sqrt{2} K_1) v_1 s) / (r_1 \sqrt{1 - v_1^2}) + C_1 - \frac{3 r A_1}{r_1} \right) + \\ & \left(1 / (r_1 r_2^2 \sqrt{1 - v_2^2}) \right) \left((s^2 r_1 - r B_1^2) r_2 \gamma_{12}^4 + r B_2^2 (3 r_2 (s^2 + A_1) (s^2 - A_2) - r_1 \gamma_{12}^4) \right) \\ & \left(\sqrt{1 - v_2^2} (g_0 r_2 s^4 + r_2 g_{0,\text{dev1}} s^3 - 3 r h_0 s^2 - g_0 K_2^2 r_2 s^2 - \sqrt{2} K_2 r_2 g_{0,\text{dev1}} s^2 + \sqrt{2} \right. \\ & \left. g_0 K_2^3 r_2 s + K_2^2 r_2 g_{0,\text{dev1}} s + C_2 r_2 - 3 r A_2) - 2 \sqrt{3} r s (s - \sqrt{2} K_2) v_2 \right) + \\ & 3 r \left(\frac{(s^2 - A_2) \gamma_{12}^4}{r_2} + \frac{1}{r_1} (s^2 + A_1) (s^4 + K_2^4 + \gamma_{22}^4) \right) \left(-B_2^2 g_0 s^2 + h_0 s^2 - B_2^2 g_{0,\text{dev1}} s + \right. \\ & \left. h_{0,\text{dev1}} s + C_3 + B_1^2 \left(-f_{0,\text{dev1}} s - s^2 f_0 - \frac{r}{r_1} \right) + \frac{r B_2^2}{r_2} \right) \Bigg) / \\ & \left(s (3 r (s^2 + A_1) (r_1 (s^2 - A_2) \gamma_{12}^4 + r_2 (s^2 + A_1) (s^4 + K_2^4 + \gamma_{22}^4)) B_1^2 + \right. \\ & \left. 3 r B_2^2 (s^2 - A_2) (r_2 (s^2 + A_1) \gamma_{21}^4 + r_1 (s^2 - A_2) (s^4 + K_1^4 + \gamma_{11}^4)) + \right. \\ & \left. \left((s^2 r_1 - r B_1^2) r_2 - r B_2^2 r_1 \right) (\gamma_{12}^4 \gamma_{21}^4 - (s^4 + K_1^4 + \gamma_{11}^4) (s^4 + K_2^4 + \gamma_{22}^4)) \right) \Bigg) \Bigg\} \end{aligned}$$

In[]:= `gs = Simplify[Part[gmat, 2]]`

$$\begin{aligned} \text{Out[]:= } & \left\{ - \left(r_1 r_2 \left(\left(1 / (r_1^2 r_2 \sqrt{1 - v_1^2}) \right) (r_1 (s^2 r_2 - r B_2^2) \gamma_{21}^4 + r B_1^2 (3 r_1 (s^2 + A_1) (s^2 - A_2) - r_2 \gamma_{21}^4) \right) \right. \right. \\ & \left(\sqrt{1 - v_1^2} (f_0 r_1 s^4 + r_1 f_{0,\text{dev1}} s^3 - 3 r h_0 s^2 - f_0 K_1^2 r_1 s^2 + \sqrt{2} K_1 r_1 f_{0,\text{dev1}} s^2 - \sqrt{2} \right. \\ & \left. f_0 K_1^3 r_1 s + K_1^2 r_1 f_{0,\text{dev1}} s + C_1 r_1 - 3 r A_1) - 2 \sqrt{3} r s (s + \sqrt{2} K_1) v_1 \right) + \\ & \left(\left(s^2 - r \left(\frac{B_1^2}{r_1} + \frac{B_2^2}{r_2} \right) \right) (s^4 + K_1^4 + \gamma_{11}^4) - \frac{1}{r_1} 3 r B_1^2 (s^2 + A_1)^2 \right) \left(g_0 s^4 + g_{0,\text{dev1}} s^3 - g_0 K_2^2 s^2 - \right. \\ & \left. \sqrt{2} K_2 g_{0,\text{dev1}} s^2 - \frac{3 r h_0 s^2}{r_2} + \sqrt{2} g_0 K_2^3 s + K_2^2 g_{0,\text{dev1}} s - (2 \sqrt{3} r (s - \sqrt{2} K_2) v_2 s) / \right. \\ & \left. \left(r_2 \sqrt{1 - v_2^2} \right) + C_2 - \frac{3 r A_2}{r_2} \right) + 3 r \left(\frac{(s^2 + A_1) \gamma_{21}^4}{r_1} + \frac{1}{r_2} (s^2 - A_2) (s^4 + K_1^4 + \gamma_{11}^4) \right) \\ & \left(-B_2^2 g_0 s^2 + h_0 s^2 - B_2^2 g_{0,\text{dev1}} s + h_{0,\text{dev1}} s + C_3 + B_1^2 \left(-f_{0,\text{dev1}} s - s^2 f_0 - \frac{r}{r_1} \right) + \frac{r B_2^2}{r_2} \right) \Bigg) / \\ & \left(s (3 r (s^2 + A_1) (r_1 (s^2 - A_2) \gamma_{12}^4 + r_2 (s^2 + A_1) (s^4 + K_2^4 + \gamma_{22}^4)) B_1^2 + \right. \\ & \left. 3 r B_2^2 (s^2 - A_2) (r_2 (s^2 + A_1) \gamma_{21}^4 + r_1 (s^2 - A_2) (s^4 + K_1^4 + \gamma_{11}^4)) + \right. \\ & \left. \left((s^2 r_1 - r B_1^2) r_2 - r B_2^2 r_1 \right) (\gamma_{12}^4 \gamma_{21}^4 - (s^4 + K_1^4 + \gamma_{11}^4) (s^4 + K_2^4 + \gamma_{22}^4)) \right) \Bigg) \Bigg\} \end{aligned}$$

In[]:= **hs = Simplify[Part[gmat, 3]]**

$$\begin{aligned}
 \text{Out[]:= } & \left\{ - \left(\left(r_1 r_2 \left((\gamma_{11}^4 + K_1^4 + s^4) (\gamma_{22}^4 + K_2^4 + s^4) - \gamma_{12}^4 \gamma_{21}^4 \right) \right. \right. \\
 & \left. \left(B_1^2 \left(s (-f_{0,\text{dev1}}) - f_0 s^2 - \frac{r}{r_1} \right) - B_2^2 s g_{0,\text{dev1}} + s h_{0,\text{dev1}} - B_2^2 g_0 s^2 + \frac{B_2^2 r}{r_2} + C_3 + h_0 s^2 \right) + \frac{1}{r_1 \sqrt{1 - v_1^2}} \right. \\
 & \left. \left(B_1^2 (A_1 + s^2) (\gamma_{22}^4 + K_2^4 + s^4) + B_2^2 \gamma_{21}^4 (s^2 - A_2) \right) \left(\sqrt{1 - v_1^2} (\sqrt{2} K_1 r_1 s^2 f_{0,\text{dev1}} + K_1^2 r_1 s f_{0,\text{dev1}} + r_1 \right. \right. \\
 & \quad \left. \left. s^3 f_{0,\text{dev1}} + C_1 r_1 - f_0 K_1^2 r_1 s^2 - \sqrt{2} f_0 K_1^3 r_1 s + f_0 r_1 s^4 - 3 h_0 r s^2 - 3 A_1 r \right) - \right. \\
 & \quad \left. 2 \sqrt{3} r s v_1 (\sqrt{2} K_1 + s) \right) + \frac{1}{r_2 \sqrt{1 - v_2^2}} \left(B_2^2 (s^2 - A_2) (\gamma_{11}^4 + K_1^4 + s^4) + B_1^2 \gamma_{12}^4 (A_1 + s^2) \right) \\
 & \left(\sqrt{1 - v_2^2} (-\sqrt{2} K_2 r_2 s^2 g_{0,\text{dev1}} + K_2^2 r_2 s g_{0,\text{dev1}} + r_2 s^3 g_{0,\text{dev1}} + C_2 r_2 - g_0 K_2^2 r_2 \right. \\
 & \quad \left. s^2 + \sqrt{2} g_0 K_2^3 r_2 s + g_0 r_2 s^4 - 3 h_0 r s^2 - 3 A_2 r) - 2 \sqrt{3} r s v_2 (s - \sqrt{2} K_2) \right) \left. \right) \Bigg/ \\
 & \left(s \left(3 B_1^2 r (A_1 + s^2) (r_2 (A_1 + s^2) (\gamma_{22}^4 + K_2^4 + s^4) + \gamma_{12}^4 r_1 (s^2 - A_2)) + 3 B_2^2 r (s^2 - A_2) \right. \right. \\
 & \quad \left. \left(r_1 (s^2 - A_2) (\gamma_{11}^4 + K_1^4 + s^4) + \gamma_{21}^4 r_2 (A_1 + s^2) \right) + \right. \\
 & \quad \left. \left. \left(r_2 (r_1 s^2 - B_1^2 r) - B_2^2 r r_1 \right) (\gamma_{12}^4 \gamma_{21}^4 - (\gamma_{11}^4 + K_1^4 + s^4) (\gamma_{22}^4 + K_2^4 + s^4)) \right) \right) \Bigg\}
 \end{aligned}$$

Substitute the inputs: geometry, loading and material properties.

The rest of the solution is case dependent and should be evaluate numerically.

$$B_1 = \sqrt{\frac{(1 - \nu_1^2) \left(\frac{2l}{t_1}\right)^2 t_1 G_a}{t * E l_1}} ;$$

$$B_2 = \sqrt{\frac{(1 - \nu_2^2) \left(\frac{2l}{t_2}\right)^2 t_2 G_a}{t * E l_2}} ;$$

$$K_1 = \left(12 (1 - \nu_1^2) \left(\frac{2l}{t_1}\right)^4 \left(\frac{t_1}{r_1}\right)^2\right)^{1/4} ;$$

$$K_2 = \left(12 (1 - \nu_2^2) \left(\frac{2l}{t_2}\right)^4 \left(\frac{t_2}{r_2}\right)^2\right)^{1/4} ;$$

$$A_1 = \frac{2 \nu_1 \left(\frac{2l}{t_1}\right)^2 t_1}{r_1} ;$$

$$A_2 = \frac{2 \nu_2 \left(\frac{2l}{t_2}\right)^2 t_2}{r_2} ;$$

$$\gamma_{11} = \left(\left(12 (1 - \nu_1^2) \left(\frac{2l}{t_1}\right)^3 (2l) r * E l_a * t_1\right) / (t_1 (r_1 E l_1 t)) \right)^{1/4} ;$$

$$\gamma_{12} = \left(\left(12 (1 - \nu_2^2) \left(\frac{2l}{t_2}\right)^3 (2l) r * E l_a * t_2\right) / (t_1 (r_1 E l_2 t)) \right)^{1/4} ;$$

$$\gamma_{21} = \left(\left(12 (1 - \nu_1^2) \left(\frac{2l}{t_1}\right)^3 (2l) r * E l_a * t_1\right) / (t_2 (r_2 E l_1 t)) \right)^{1/4} ;$$

$$\gamma_{22} = \left(\left(12 (1 - \nu_2^2) \left(\frac{2l}{t_2}\right)^3 (2l) r * E l_a * t_2\right) / (t_2 (r_2 E l_2 t)) \right)^{1/4} ;$$

Tube-to-Tube Joints Modeling

Case with copper and copper considering the thermal effect

Material properties of the adherents and adhesive

$$\begin{aligned} \ln[1]= & \mathbf{E11 = 117\ 210.874;} \\ & \mathbf{E12 = 117\ 210.874;} \\ & \mathbf{\nu2 = \nu1 = 0.33;} \\ & \mathbf{E1a = 2135.03;} \\ & \mathbf{Ga = 375;} \\ & \mathbf{\alpha1 = \frac{17}{10^6};} \\ & \mathbf{\alpha2 = \frac{17}{10^6};} \end{aligned}$$

Geometric information

$$\begin{aligned} \ln[0]= & \mathbf{t1 = \frac{0.8128}{10^3};} \\ & \mathbf{t2 = \frac{0.8128}{10^3};} \\ & \mathbf{t = \frac{0.1}{10^3};} \\ \ln[11]= & \mathbf{rad = \frac{9.525}{10^3} + t * 0.5;} \\ & \mathbf{rad1 = \frac{9.525}{10^3} - \frac{0.8128}{10^3} * 0.5;} \\ & \mathbf{rad2 = \frac{9.525}{10^3} + t + \frac{0.8128}{10^3} * 0.5;} \\ & \mathbf{l = \frac{4}{10^3};} \end{aligned}$$

Thermal and pressure loading conditions

$$\begin{aligned} \ln[15]= & \mathbf{\Delta T = 50;} \\ & \mathbf{pin = 3;} \\ & \mathbf{pout = 0.1;} \end{aligned}$$

Axial force balance based on the pressure:

In[18]= $F = \text{pin} * \pi * (-(\text{rad1} - \text{t1} / 2)^2 + (\text{rad} + \text{t} / 2)^2) - \text{pout} * \pi * ((\text{rad2} + \text{t2} / 2)^2 - (\text{rad} - \text{t} / 2)^2)$
 Out[18]= 0.000152029

Calculation of the constant coefficients and S matrix as defined in the paper:

In[19]= $B1 = \sqrt{\left(\frac{1}{t \text{El1}} (1 - \nu1^2) \left(\frac{21}{t1}\right)^2 t1 \text{Ga}\right)}$;
 $B2 = \sqrt{\left(\frac{1}{t \text{El2}} (1 - \nu2^2) \left(\frac{21}{t2}\right)^2 t2 \text{Ga}\right)}$;
 $K1 = \left(12 (1 - \nu1^2) \left(\frac{21}{t1}\right)^4 \left(\frac{t1}{\text{rad1}}\right)^2\right)^{1/4}$;
 $K2 = \left(12 (1 - \nu2^2) \left(\frac{21}{t2}\right)^4 \left(\frac{t2}{\text{rad2}}\right)^2\right)^{1/4}$;
 $A1 = \frac{2 \nu1 \left(\frac{21}{t1}\right)^2 t1}{\text{rad1}}$;
 $A2 = \frac{2 \nu2 \left(\frac{21}{t2}\right)^2 t2}{\text{rad2}}$;
 $\gamma11 = \left(\left(12 (1 - \nu1^2) \left(\frac{21}{t1}\right)^3 (21) \text{radEl1} t1\right) / (t1 (\text{rad1El1} t))\right)^{1/4}$;
 $\gamma12 = \left(\left(12 (1 - \nu2^2) \left(\frac{21}{t2}\right)^3 (21) \text{radEl1} t2\right) / (t1 (\text{rad1El2} t))\right)^{1/4}$;
 $\gamma21 = \left(\left(12 (1 - \nu1^2) \left(\frac{21}{t1}\right)^3 (21) \text{radEl1} t1\right) / (t2 (\text{rad2El1} t))\right)^{1/4}$;
 $\gamma22 = \left(\left(12 (1 - \nu2^2) \left(\frac{21}{t2}\right)^3 (21) \text{radEl1} t2\right) / (t2 (\text{rad2El2} t))\right)^{1/4}$;
 MatrixForm[mat1 = $\left\{\left\{s^4 + K1^4 + \gamma11^4, -\gamma12^4, -\frac{3 \text{rad} (s^2 + A1)}{\text{rad1}}\right\}, \left\{-\gamma21^4, s^4 + K2^4 + \gamma22^4, -\frac{3 \text{rad} (s^2 - A2)}{\text{rad2}}\right\}, \left\{-B1^2 (s^2 + A1), -B2^2 (s^2 - A2), s^2 - \left(\frac{B1^2}{\text{rad1}} + \frac{B2^2}{\text{rad2}}\right) \text{rad}\right\}\right\}$]

Out[29]//MatrixForm=

$$\begin{pmatrix} 16398.7 + s^4 & -15601.4 & -3.15015 (5.69918 + s^2) \\ -14181.8 & 14840.6 + s^4 & -2.86351 (-5.18058 + s^2) \\ -2.24484 (5.69918 + s^2) & -2.24484 (-5.18058 + s^2) & -4.49991 + s^2 \end{pmatrix}$$

Extra constants added to the system due to the pressure and thermal loading

```
In[30]= thermal1 = - (12 * E11 * t1 * α1 * ΔT / rad1 * (2 l / t1) ^ 2 * t1) / (F / (2 π * rad));
pres1 = (12 * pin * (2 l / t1) ^ 2 * t1) / (F / (2 π * rad)) * θ;
thermal2 = (-12 * E12 * t2 * α2 * ΔT / rad2 * (2 l / t2) ^ 2 * t2) / (F / (2 π * rad));
pres2 = (12 * pout * (2 l / t2) ^ 2 * t2) / (F / (2 π * rad)) * θ;
thermal3 = (2 Ga ((1 - ν2) α2 * ΔT - (1 - ν1) α1 * ΔT) * (2 l / t) ^ 2 * t) / (F / (2 π * rad));
pres3 = 0;
```

```
In[36]= con1 = thermal1 + pres1;
con2 = thermal2 + pres2;
con3 = thermal3 + pres3;
```

Polynomials on the right side with initial boundary conditions:

```
In[39]= mat2o = 1/s { {s^4 fθ + s^3 fθd1 + s^2 (fθd2 - 3 rad hθ / rad1) + s (fθd3 - 3 rad hθd1 / rad1) - 3 A1 rad / rad1 + con1},
{s^4 gθ + s^3 gθd1 + s^2 (gθd2 - 3 rad hθ / rad2) + s (gθd3 - 3 rad hθd1 / rad2) - 3 A2 rad / rad2 + con2},
{s^2 (hθ - B1^2 fθ - B2^2 gθ) +
s (hθd1 - B1^2 fθd1 - B2^2 gθd1) - (B1^2 rad / rad1 - B2^2 rad / rad2) + con3} }
```

```
hθ = -1;
gθd2 = 0;
```

$$f\theta d2 = \sqrt{2} K1 f\theta d1 - K1^2 f\theta - \frac{2\sqrt{3} \nu1 \text{ rad}}{\text{rad1} \sqrt{1 - \nu1^2}};$$

$$f\theta d3 = \sqrt{2} K1 \left(\sqrt{2} K1 f\theta d1 - K1^2 f\theta - \frac{2\sqrt{3} \nu1 \text{ rad}}{\text{rad1} \sqrt{1 - \nu1^2}} \right) - K1^2 f\theta d1 + \frac{3 \text{ rad } h\theta d1}{\text{rad1}};$$

$$g\theta d3 = \frac{3 \text{ rad } h\theta d1}{\text{rad2}};$$

```
MatrixForm[mat2o]
```

```
Out[39]= { { 1/s (-3338.52 + (fθd3 - 3.15015 hθd1) s + (fθd2 - 3.15015 hθ) s^2 + fθd1 s^3 + fθ s^4) },
{ 1/s (-3033.24 + (gθd3 - 2.86351 hθd1) s + (gθd2 - 2.86351 hθ) s^2 + gθd1 s^3 + gθ s^4) },
{ 1/s (-0.214492 + (-2.24484 fθd1 - 2.24484 gθd1 + hθd1) s + (-2.24484 fθ - 2.24484 gθ + hθ) s^2) } }
```

```
Out[45]//MatrixForm=
```

$$\begin{pmatrix} \frac{-3338.52 - (0. - 28.2372 f\theta d1 + 7.51495 (-1.2716 - 28.2372 f\theta + 7.51495 f\theta d1)) s + (1.87855 - 28.2372 f\theta + 7.51495 f\theta d1) s^2 - f\theta d1 s^3 + f\theta s^4}{s} \\ \frac{-3033.24 - 2.86351 s^2 - g\theta d1 s^3 + g\theta s^4}{s} \\ \frac{0.214492 + (-2.24484 f\theta d1 - 2.24484 g\theta d1 + h\theta d1) s + (-2.24484 f\theta - 2.24484 g\theta) s^2}{s} \end{pmatrix}$$

Calculate the Laplace functions with matrix calculation:

In[46]= **MatrixForm**[**gmat** = **Inverse**[**mat1**].**mat2o**]

Out[46]//MatrixForm=

$$\begin{pmatrix} \frac{(-70413.7-15605.1s^2+7.0716s^4)(-3033.24-2.86351s^2-g0d1s^3+g0s^4)}{s(-9.98168 \times 10^7-2.19037 \times 10^7s^2-551912. s^4-31225.3s^6-17.9996s^8+s^{10})} + \frac{(-3338.52-(0.-28.2372f0d1+7.51495(-1.2716-28.2372f0-7.51495f0d1))s+(1.87855-28.2372f0+7.51495f0d1)s^2-64006.4+14185.1s^2+6.42813s^4)(-3338.52-(0.-28.2372f0d1+7.51495(-1.2716-28.2372f0-7.51495f0d1))s+(1.87855-28.2372f0+7.51495f0d1)s^2-64006.4+14185.1s^2+6.42813s^4)}{s(-9.98168 \times 10^7-2.19037 \times 10^7s^2-551912. s^4-31225.3s^6-17.9996s^8+s^{10})} \\ \frac{(-3033.24+2.86351s^2+g0d1s^3+g0s^4)(8889.74+71835.3s^2-11.6296s^4+2.24484s^6)}{s(-9.98168 \times 10^7+2.19037 \times 10^7s^2-551912. s^4-31225.3s^6-17.9996s^8+s^{10})} + \frac{(-3338.52+(0.-28.2372f0d1+7.51495(-1.2716-28.2372f0-7.51495f0d1))s+(1.87855-28.2372f0+7.51495f0d1)s^2-64006.4+14185.1s^2+6.42813s^4)(-3338.52+(0.-28.2372f0d1+7.51495(-1.2716-28.2372f0-7.51495f0d1))s+(1.87855-28.2372f0+7.51495f0d1)s^2-64006.4+14185.1s^2+6.42813s^4)}{s(-9.98168 \times 10^7+2.19037 \times 10^7s^2-551912. s^4-31225.3s^6-17.9996s^8+s^{10})} \end{pmatrix}$$

Extract the three Laplace functions from the matrix:

In[47]= **fs** = **Simplify**[**Part**[**gmat**, 1]]

gs = **Simplify**[**Part**[**gmat**, 2]]

hs = **Simplify**[**Part**[**gmat**, 3]]

Out[47]= $\left\{ \left(4.37101 \times 10^8 + (639814. + 1.42077 \times 10^7 f0 - 1.96915 \times 10^6 f0d1 - 78561.1 g0d1 + 34996.2 h0d1) s + (-9.74839 \times 10^7 + 1.81203 \times 10^6 f0 - 503155. f0d1 - 78561.1 g0) s^2 + (-142454. - 3.16332 \times 10^6 f0 + 148749. f0d1 - 275648. g0d1 + 91424.9 h0d1) s^3 + (-3706.06 - 693126. f0 + 112027. f0d1 - 275648. g0) s^4 + (104.429 + 2318.94 f0 + 14558.3 f0d1 + 15564.8 g0d1 + 17.9533 h0d1) s^5 + (-3357.42 + 15175.5 f0 - 82.1237 f0d1 + 15564.8 g0) s^6 + (-9.55604 - 212.201 f0 + 10.2376 f0d1 + 3.15015 h0d1) s^7 + (-1.2716 - 46.2369 f0 + 7.51495 f0d1) s^8 + f0d1 s^9 + f0 s^{10} \right) / (s(-9.98168 \times 10^7 + 2.19037 \times 10^7 s^2 - 551912. s^4 + 31225.3 s^6 - 17.9996 s^8 + s^{10})) \right\}$

Out[48]= $\left\{ \left(4.38212 \times 10^8 + (611648. + 1.35822 \times 10^7 f0 - 1.83282 \times 10^6 f0d1 - 25455.8 g0d1 + 11339.7 h0d1) s + (-9.72172 \times 10^7 + 1.78191 \times 10^6 f0 - 481005. f0d1 - 25455.8 g0) s^2 + (-135553. - 3.01009 \times 10^6 f0 + 130840. f0d1 - 279723. g0d1 + 91632.6 h0d1) s^3 + (-4616.11 - 670255. f0 + 106600. f0d1 - 279723. g0) s^4 + (-61.4275 - 1364.06 f0 + 14399.9 f0d1 + 16351.4 g0d1 - 14.8346 h0d1) s^5 + (-3040.08 + 14036.9 f0 + 48.3071 f0d1 + 16351.4 g0) s^6 + (-17.9996 g0d1 + 2.86351 h0d1) s^7 - 17.9996 g0 s^8 + g0d1 s^9 + g0 s^{10} \right) / (s(-9.98168 \times 10^7 + 2.19037 \times 10^7 s^2 - 551912. s^4 + 31225.3 s^6 - 17.9996 s^8 + s^{10})) \right\}$

Out[49]= $\left\{ \left(-1.14966 \times 10^8 + (-238316. - 5.29204 \times 10^6 f0 - 4.89332 \times 10^7 f0d1 - 4.96374 \times 10^7 g0d1 + 2.21118 \times 10^7 h0d1) s + (-4.5744 \times 10^8 - 5.03416 \times 10^7 f0 + 187414. f0d1 - 4.96374 \times 10^7 g0) s^2 + (-622582. - 1.3825 \times 10^7 f0 + 1.86461 \times 10^6 f0d1 + 8889.74 g0d1) s^3 + (313952. - 1.81473 \times 10^6 f0 + 489603. f0d1 + 8889.74 g0) s^4 + (-122.258 - 2714.85 f0 - 4615.51 f0d1 + 1707.88 g0d1 + 31239.3 h0d1) s^5 + (-45552.2 - 5338.03 f0 + 96.1444 f0d1 + 1707.88 g0) s^6 + (-21.4518 - 476.359 f0 + 76.1819 f0d1 - 11.6296 g0d1) s^7 + (10.4307 - 50.5944 f0 + 16.8699 f0d1 - 11.6296 g0) s^8 + h0d1 s^9 - 1. s^{10} \right) / (s(-9.98168 \times 10^7 + 2.19037 \times 10^7 s^2 - 551912. s^4 + 31225.3 s^6 - 17.9996 s^8 + s^{10})) \right\}$

Extract the three Laplace functions numerator and denominator, get ready for partial fraction:

```
In[50]= ftop[s_] = Numerator[fs]
gtop[s_] = Numerator[gs]
htop[s_] = Numerator[hs]
q[s_] = Denominator[fs]
qred[s_] = q[s] / s;
```

$$\text{Out[50]}= \left\{ 4.37101 \times 10^8 + (639814. + 1.42077 \times 10^7 f_0 - 1.96915 \times 10^6 f_{0d1} - 78561.1 g_{0d1} + 34996.2 h_{0d1}) s + \right. \\ \left. (-9.74839 \times 10^7 + 1.81203 \times 10^6 f_0 - 503155. f_{0d1} - 78561.1 g_0) s^2 + \right. \\ \left. (-142454. - 3.16332 \times 10^6 f_0 + 148749. f_{0d1} - 275648. g_{0d1} + 91424.9 h_{0d1}) s^3 + \right. \\ \left. (-3706.06 - 693126. f_0 + 112027. f_{0d1} - 275648. g_0) s^4 + \right. \\ \left. (104.429 + 2318.94 f_0 + 14558.3 f_{0d1} + 15564.8 g_{0d1} + 17.9533 h_{0d1}) s^5 + \right. \\ \left. (-3357.42 + 15175.5 f_0 - 82.1237 f_{0d1} + 15564.8 g_0) s^6 + \right. \\ \left. (-9.55604 - 212.201 f_0 + 10.2376 f_{0d1} + 3.15015 h_{0d1}) s^7 + \right. \\ \left. (-1.2716 - 46.2369 f_0 + 7.51495 f_{0d1}) s^8 + f_{0d1} s^9 + f_0 s^{10} \right\}$$

$$\text{Out[51]}= \left\{ 4.38212 \times 10^8 + (611648. + 1.35822 \times 10^7 f_0 - 1.83282 \times 10^6 f_{0d1} - 25455.8 g_{0d1} + 11339.7 h_{0d1}) s + \right. \\ \left. (-9.72172 \times 10^7 + 1.78191 \times 10^6 f_0 - 481005. f_{0d1} - 25455.8 g_0) s^2 + \right. \\ \left. (-135553. - 3.01009 \times 10^6 f_0 + 130840. f_{0d1} - 279723. g_{0d1} + 91632.6 h_{0d1}) s^3 + \right. \\ \left. (-4616.11 - 670255. f_0 + 106600. f_{0d1} - 279723. g_0) s^4 + \right. \\ \left. (-61.4275 - 1364.06 f_0 + 14399.9 f_{0d1} + 16351.4 g_{0d1} - 14.8346 h_{0d1}) s^5 + \right. \\ \left. (-3040.08 + 14036.9 f_0 + 48.3071 f_{0d1} + 16351.4 g_0) s^6 + \right. \\ \left. (-17.9996 g_{0d1} + 2.86351 h_{0d1}) s^7 - 17.9996 g_0 s^8 + g_{0d1} s^9 + g_0 s^{10} \right\}$$

$$\text{Out[52]}= \left\{ -1.14966 \times 10^8 + \right. \\ \left. (-238316. - 5.29204 \times 10^6 f_0 - 4.89332 \times 10^7 f_{0d1} - 4.96374 \times 10^7 g_{0d1} + 2.21118 \times 10^7 h_{0d1}) s + \right. \\ \left. (-4.5744 \times 10^8 - 5.03416 \times 10^7 f_0 + 187414. f_{0d1} - 4.96374 \times 10^7 g_0) s^2 + \right. \\ \left. (-622582. - 1.3825 \times 10^7 f_0 + 1.86461 \times 10^6 f_{0d1} + 8889.74 g_{0d1}) s^3 + \right. \\ \left. (313952. - 1.81473 \times 10^6 f_0 + 489603. f_{0d1} + 8889.74 g_0) s^4 + \right. \\ \left. (-122.258 - 2714.85 f_0 - 4615.51 f_{0d1} + 1707.88 g_{0d1} + 31239.3 h_{0d1}) s^5 + \right. \\ \left. (-45552.2 - 5338.03 f_0 + 96.1444 f_{0d1} + 1707.88 g_0) s^6 + \right. \\ \left. (-21.4518 - 476.359 f_0 + 76.1819 f_{0d1} - 11.6296 g_{0d1}) s^7 + \right. \\ \left. (10.4307 - 50.5944 f_0 + 16.8699 f_{0d1} - 11.6296 g_0) s^8 + h_{0d1} s^9 - 1. s^{10} \right\}$$

$$\text{Out[53]}= \left\{ s (-9.98168 \times 10^7 + 2.19037 \times 10^7 s^2 - 551912. s^4 + 31225.3 s^6 - 17.9996 s^8 + s^{10}) \right\}$$

Calculate the coefficients for each fraction:

```
In[55]= c1[s_] = ftop[s] / D[q[s], s]
```

```
c2[s_] = gtop[s] / D[q[s], s]
```

```
c3[s_] = htop[s] / D[q[s], s]
```

```
Out[55]= { (4.37101 × 108 + (639814. + 1.42077 × 107 f0 - 1.96915 × 106 f0d1 - 78561.1 g0d1 + 34996.2 h0d1) s +
(-9.74839 × 107 + 1.81203 × 106 f0 - 503155. f0d1 - 78561.1 g0) s2 +
(-142454. - 3.16332 × 106 f0 + 148749. f0d1 - 275648. g0d1 + 91424.9 h0d1) s3 +
(-3706.06 - 693126. f0 + 112027. f0d1 - 275648. g0) s4 +
(104.429 + 2318.94 f0 + 14558.3 f0d1 + 15564.8 g0d1 + 17.9533 h0d1) s5 +
(-3357.42 + 15175.5 f0 - 82.1237 f0d1 + 15564.8 g0) s6 +
(-9.55604 - 212.201 f0 + 10.2376 f0d1 + 3.15015 h0d1) s7 +
(-1.2716 - 46.2369 f0 + 7.51495 f0d1) s8 + f0d1 s9 + f0 s10) /
(-9.98168 × 107 + 2.19037 × 107 s2 - 551912. s4 + 31225.3 s6 - 17.9996 s8 + s10 +
s (4.38074 × 107 s - 2.20765 × 106 s3 + 187352. s5 - 143.997 s7 + 10 s9)) }
```

```
Out[56]= { (4.38212 × 108 + (611648. + 1.35822 × 107 f0 - 1.83282 × 106 f0d1 - 25455.8 g0d1 + 11339.7 h0d1) s +
(-9.72172 × 107 + 1.78191 × 106 f0 - 481005. f0d1 - 25455.8 g0) s2 +
(-135553. - 3.01009 × 106 f0 + 130840. f0d1 - 279723. g0d1 + 91632.6 h0d1) s3 +
(-4616.11 - 670255. f0 + 106600. f0d1 - 279723. g0) s4 +
(-61.4275 - 1364.06 f0 + 14399.9 f0d1 + 16351.4 g0d1 - 14.8346 h0d1) s5 +
(-3040.08 + 14036.9 f0 + 48.3071 f0d1 + 16351.4 g0) s6 +
(-17.9996 g0d1 + 2.86351 h0d1) s7 - 17.9996 g0 s8 + g0d1 s9 + g0 s10) /
(-9.98168 × 107 + 2.19037 × 107 s2 - 551912. s4 + 31225.3 s6 - 17.9996 s8 + s10 +
s (4.38074 × 107 s - 2.20765 × 106 s3 + 187352. s5 - 143.997 s7 + 10 s9)) }
```

```
Out[57]= { (-1.14966 × 108 +
(-238316. - 5.29204 × 106 f0 - 4.89332 × 107 f0d1 - 4.96374 × 107 g0d1 + 2.21118 × 107 h0d1) s +
(-4.5744 × 108 - 5.03416 × 107 f0 + 187414. f0d1 - 4.96374 × 107 g0) s2 +
(-622582. - 1.3825 × 107 f0 + 1.86461 × 106 f0d1 + 8889.74 g0d1) s3 +
(313952. - 1.81473 × 106 f0 + 489603. f0d1 + 8889.74 g0) s4 +
(-122.258 - 2714.85 f0 - 4615.51 f0d1 + 1707.88 g0d1 + 31239.3 h0d1) s5 +
(-45552.2 - 5338.03 f0 + 96.1444 f0d1 + 1707.88 g0) s6 +
(-21.4518 - 476.359 f0 + 76.1819 f0d1 - 11.6296 g0d1) s7 +
(10.4307 - 50.5944 f0 + 16.8699 f0d1 - 11.6296 g0) s8 + h0d1 s9 - 1. s10) /
(-9.98168 × 107 + 2.19037 × 107 s2 - 551912. s4 + 31225.3 s6 - 17.9996 s8 + s10 +
s (4.38074 × 107 s - 2.20765 × 106 s3 + 187352. s5 - 143.997 s7 + 10 s9)) }
```

```
In[58]= roots = Solve[qred[s] == 0, s]
```

```
Out[58]= {{s → -9.34534 - 9.34491 i}, {s → -9.34534 + 9.34491 i}, {s → -4.0025 - 3.08764 i},
{s → -4.0025 + 3.08764 i}, {s → -2.23847}, {s → 2.23847}, {s → 4.0025 - 3.08764 i},
{s → 4.0025 + 3.08764 i}, {s → 9.34534 - 9.34491 i}, {s → 9.34534 + 9.34491 i}}
```

```
In[59]:= values = roots[[All, 1, 2]];
p1 = values[[6]];
p6 = -p1;
p2 = values[[8]];
p9 = -p2;
p3 = values[[10]];
p10 = -p3;
p4 = Conjugate[p2];
p7 = -p4;
p5 = Conjugate[p3];
p8 = -p5;
r1 = Re[p1];
m1 = Im[p1];
r2 = Re[p2];
m2 = Im[p2];
r3 = Re[p3];
m3 = Im[p3];
```

```
In[76]= C11 = c1[p1] // Simplify;  
C12 = c1[p2] // Simplify;  
C13 = c1[p3] // Simplify;  
C14 = c1[p4] // Simplify;  
C15 = c1[p5] // Simplify;  
C16 = c1[p6] // Simplify;  
C17 = c1[p7] // Simplify;  
C18 = c1[p8] // Simplify;  
C19 = c1[p9] // Simplify;  
C10 = c1[p10] // Simplify;  
C21 = c2[p1] // Simplify;  
C22 = c2[p2] // Simplify;  
C23 = c2[p3] // Simplify;  
C24 = c2[p4] // Simplify;  
C25 = c2[p5] // Simplify;  
C26 = c2[p6] // Simplify;  
C27 = c2[p7] // Simplify;  
C28 = c2[p8] // Simplify;  
C29 = c2[p9] // Simplify;  
C20 = c2[p10] // Simplify;  
C31 = c3[p1] // Simplify;  
C32 = c3[p2] // Simplify;  
C33 = c3[p3] // Simplify;  
C34 = c3[p4] // Simplify;  
C35 = c3[p5] // Simplify;  
C36 = c3[p6] // Simplify;  
C37 = c3[p7] // Simplify;  
C38 = c3[p8] // Simplify;  
C39 = c3[p9] // Simplify;  
C30 = c3[p10] // Simplify;
```

```

In[106]:= c11f = C11 + C16;
          c12f = 0;
          c13f = C11 - C16;
          c14f = 0;
          c21f = 2 (ComplexExpand [Re [C12] ] + ComplexExpand [Re [C17] ] ) ;
          c22f = -2 (ComplexExpand [Im [C12] ] + ComplexExpand [Im [C17] ] ) ;
          c23f = 2 (ComplexExpand [Re [C12] ] - ComplexExpand [Re [C17] ] ) ;
          c24f = -2 (ComplexExpand [Im [C12] ] - ComplexExpand [Im [C17] ] ) ;
          c31f = 2 (ComplexExpand [Re [C13] ] + ComplexExpand [Re [C18] ] ) ;
          c32f = -2 (ComplexExpand [Im [C13] ] + ComplexExpand [Im [C18] ] ) ;
          c33f = 2 (ComplexExpand [Re [C13] ] - ComplexExpand [Re [C18] ] ) ;
          c34f = -2 (ComplexExpand [Im [C13] ] - ComplexExpand [Im [C18] ] ) ;
          c11g = C21 + C26;
          c12g = 0;
          c13g = C21 - C26;
          c14g = 0;
          c21g = 2 (ComplexExpand [Re [C22] ] + ComplexExpand [Re [C27] ] ) ;
          c22g = -2 (ComplexExpand [Im [C22] ] + ComplexExpand [Im [C27] ] ) ;
          c23g = 2 (ComplexExpand [Re [C22] ] - ComplexExpand [Re [C27] ] ) ;
          c24g = -2 (ComplexExpand [Im [C22] ] - ComplexExpand [Im [C27] ] ) ;
          c31g = 2 (ComplexExpand [Re [C23] ] + ComplexExpand [Re [C28] ] ) ;
          c32g = -2 (ComplexExpand [Im [C23] ] + ComplexExpand [Im [C28] ] ) ;
          c33g = 2 (ComplexExpand [Re [C23] ] - ComplexExpand [Re [C28] ] ) ;
          c34g = -2 (ComplexExpand [Im [C23] ] - ComplexExpand [Im [C28] ] ) ;
          c11h = C31 + C36;
          c12h = 0;
          c13h = C31 - C36;
          c14h = 0;
          c21h = 2 (ComplexExpand [Re [C32] ] + ComplexExpand [Re [C37] ] ) ;
          c22h = -2 (ComplexExpand [Im [C32] ] + ComplexExpand [Im [C37] ] ) ;
          c23h = 2 (ComplexExpand [Re [C32] ] - ComplexExpand [Re [C37] ] ) ;
          c24h = -2 (ComplexExpand [Im [C32] ] - ComplexExpand [Im [C37] ] ) ;
          c31h = 2 (ComplexExpand [Re [C33] ] + ComplexExpand [Re [C38] ] ) ;
          c32h = -2 (ComplexExpand [Im [C33] ] + ComplexExpand [Im [C38] ] ) ;
          c33h = 2 (ComplexExpand [Re [C33] ] - ComplexExpand [Re [C38] ] ) ;
          c34h = -2 (ComplexExpand [Im [C33] ] - ComplexExpand [Im [C38] ] ) ;

In[142]:= n10 = ftop [0] ;
          n20 = gtop [0] ;
          n30 = htop [0] ;
          d0 = qred [0] ;

```

Calculate the inverse Laplace transform results:

$$\begin{aligned}
\text{In[146]}= & \mathbf{f[z_]} = \mathbf{n10 / d0 + Cosh[r1 * z] * (c11f * Cos[m1 * z] + c12f * Sin[m1 * z]) +} \\
& \mathbf{Sinh[r1 * z] * (c13f * Cos[m1 * z] + c14f * Sin[m1 * z]) +} \\
& \mathbf{Cosh[r2 * z] * (c21f * Cos[m2 * z] + c22f * Sin[m2 * z]) +} \\
& \mathbf{Sinh[r2 * z] * (c23f * Cos[m2 * z] + c24f * Sin[m2 * z]) +} \\
& \mathbf{Cosh[r3 * z] * (c31f * Cos[m3 * z] + c32f * Sin[m3 * z]) +} \\
& \mathbf{Sinh[r3 * z] * (c33f * Cos[m3 * z] + c34f * Sin[m3 * z])} \\
& \mathbf{g[z_]} = \mathbf{n20 / d0 + Cosh[r1 * z] * (c11g * Cos[m1 * z] + c12g * Sin[m1 * z]) +} \\
& \mathbf{Sinh[r1 * z] * (c13g * Cos[m1 * z] + c14g * Sin[m1 * z]) +} \\
& \mathbf{Cosh[r2 * z] * (c21g * Cos[m2 * z] + c22g * Sin[m2 * z]) +} \\
& \mathbf{Sinh[r2 * z] * (c23g * Cos[m2 * z] + c24g * Sin[m2 * z]) +} \\
& \mathbf{Cosh[r3 * z] * (c31g * Cos[m3 * z] + c32g * Sin[m3 * z]) +} \\
& \mathbf{Sinh[r3 * z] * (c33g * Cos[m3 * z] + c34g * Sin[m3 * z])} \\
& \mathbf{h[z_]} = \mathbf{n30 / d0 + Cosh[r1 * z] * (c11h * Cos[m1 * z] + c12h * Sin[m1 * z]) +} \\
& \mathbf{Sinh[r1 * z] * (c13h * Cos[m1 * z] + c14h * Sin[m1 * z]) +} \\
& \mathbf{Cosh[r2 * z] * (c21h * Cos[m2 * z] + c22h * Sin[m2 * z]) +} \\
& \mathbf{Sinh[r2 * z] * (c23h * Cos[m2 * z] + c24h * Sin[m2 * z]) +} \\
& \mathbf{Cosh[r3 * z] * (c31h * Cos[m3 * z] + c32h * Sin[m3 * z]) +} \\
& \mathbf{Sinh[r3 * z] * (c33h * Cos[m3 * z] + c34h * Sin[m3 * z])} \\
\text{Out[146]}= & \left\{ -4.37903 + (-0.553133 - 0.0686587 f_0 + 0.00304854 f_{0d1} - 0.0571067 g_0 - 8.67362 \times 10^{-19} h_{0d1}) \right. \\
& \text{Cosh}[2.23847 z] + \\
& \text{Cosh}[4.0025 z] \left(2 (2.46319 + 0.271653 f_0 - 0.00144495 f_{0d1} + 0.289753 g_0 - 3.46945 \times 10^{-18} g_{0d1}) \right. \\
& \left. \text{Cos}[3.08764 z] - 2 (0.0142262 + 0.315906 f_0 - 0.0631344 f_{0d1} - \right. \\
& \left. 4.16334 \times 10^{-17} g_0 - 0.02499 g_{0d1} - 0.00807703 h_{0d1}) \text{Sin}[3.08764 z] \right) + \\
& \text{Cosh}[9.34534 z] \left(2 (0.00289568 + 0.262677 f_0 - 0.0000793222 f_{0d1} - 0.2612 g_0 + \right. \\
& \left. 8.67362 \times 10^{-19} g_{0d1} - 1.01644 \times 10^{-20} h_{0d1}) \text{Cos}[9.34491 z] - \right. \\
& \left. 2 (0.00076053 + 0.0168883 f_0 - 0.0163347 f_{0d1} + 8.67362 \times 10^{-18} g_0 + \right. \\
& \left. 0.0140217 g_{0d1} - 4.75411 \times 10^{-6} h_{0d1}) \text{Sin}[9.34491 z] \right) + \\
& (-0.00173178 - 0.038456 f_0 - 0.0204377 f_{0d1} - 0.0255115 g_{0d1} + 0.0117883 h_{0d1}) \\
& \text{Sinh}[2.23847 z] + \\
& \left(2 (0.0114335 + 0.253893 f_0 + 0.016454 f_{0d1} - 8.32667 \times 10^{-17} g_0 + \right. \\
& \left. 0.053115 g_{0d1} - 0.00944572 h_{0d1}) \text{Cos}[3.08764 z] - \right. \\
& \left. 2 (0.604162 + 0.343247 f_0 - 0.0725405 f_{0d1} + 0.0639779 g_0 - 1.73472 \times 10^{-18} g_{0d1}) \right. \\
& \left. \text{Sin}[3.08764 z] \right) \text{Sinh}[4.0025 z] + \\
& \left(2 (0.000771288 + 0.0171272 f_0 + 0.0117101 f_{0d1} + 2.77556 \times 10^{-17} g_0 - \right. \\
& \left. 0.0139286 g_{0d1} - 0.000039682 h_{0d1}) \text{Cos}[9.34491 z] - \right. \\
& \left. 2 (0.00168661 + 0.0413762 f_0 - 0.0112575 f_{0d1} + 0.000875971 g_0 - 8.67362 \times 10^{-19} g_{0d1} - \right. \\
& \left. 8.47033 \times 10^{-22} h_{0d1}) \text{Sin}[9.34491 z] \right) \text{Sinh}[9.34534 z] \left. \right\}
\end{aligned}$$

$$\begin{aligned}
\text{Out[147]} = & \left\{ -4.39017 + (-0.526845 - 0.0653957 f_0 + 0.00290366 f_{0d1} - 0.0543927 g_0 + 1.73472 \times 10^{-18} g_{0d1}) \right. \\
& \text{Cosh}[2.23847 z] + \\
& \text{Cosh}[4.0025 z] \left\{ 2 (2.46113 + 0.271447 f_0 - 0.00144916 f_{0d1} + 0.289511 g_0 + 1.73472 \times 10^{-18} h_{0d1}) \right. \\
& \quad \text{Cos}[3.08764 z] - 2 (0.0142132 + 0.315617 f_0 - 0.0630818 f_{0d1} - 2.77556 \times 10^{-17} g_0 - \\
& \quad \quad 0.0249727 g_{0d1} - 0.00806943 h_{0d1}) \text{Sin}[3.08764 z] \left. \right\} + \text{Cosh}[9.34534 z] \\
& \left(2 (-0.00262373 - 0.238749 f_0 - 2.66698 \times 10^{-6} f_{0d1} + 0.237686 g_0 + 6.77626 \times 10^{-21} h_{0d1}) \right. \\
& \quad \text{Cos}[9.34491 z] - 2 (-0.000697175 - 0.0154815 f_0 + 0.0147859 f_{0d1} + \\
& \quad \quad 3.46945 \times 10^{-18} g_0 - 0.0126665 g_{0d1} + 4.58985 \times 10^{-6} h_{0d1}) \text{Sin}[9.34491 z] \left. \right\} + \\
& (-0.00164948 - 0.0366284 f_0 - 0.0194664 f_{0d1} - 3.46945 \times 10^{-18} g_0 - \\
& \quad 0.0242991 g_{0d1} + 0.0112281 h_{0d1}) \text{Sinh}[2.23847 z] + \\
& \left(2 (0.0114248 + 0.2537 f_0 + 0.0164353 f_{0d1} + 0.0530679 g_{0d1} - 0.00943826 h_{0d1}) \text{Cos}[3.08764 z] - \right. \\
& \quad 2 (0.603461 + 0.342933 f_0 - 0.0724785 f_{0d1} + 0.0639015 g_0 - 5.20417 \times 10^{-18} g_{0d1}) \\
& \quad \left. \text{Sin}[3.08764 z] \right\} \text{Sinh}[4.0025 z] + \\
& \left(2 (-0.00069678 - 0.0154727 f_0 - 0.0107643 f_{0d1} + 1.38778 \times 10^{-17} g_0 + \right. \\
& \quad \quad 0.0127677 g_{0d1} + 0.0000360772 h_{0d1}) \text{Cos}[9.34491 z] - \\
& \quad 2 (-0.00155399 - 0.0393969 f_0 + 0.0102443 f_{0d1} + 0.000939525 g_0 - \\
& \quad \quad 8.67362 \times 10^{-19} g_{0d1} + 4.23516 \times 10^{-22} h_{0d1}) \text{Sin}[9.34491 z] \left. \right\} \text{Sinh}[9.34534 z] \left. \right\}
\end{aligned}$$

$$\begin{aligned}
\text{Out[148]} = & \left\{ 1.15177 + \right. \\
& (-25.6402 - 3.18264 f_0 + 0.141314 f_{0d1} - 2.64715 g_0 - 1.11022 \times 10^{-16} g_{0d1}) \text{Cosh}[2.23847 z] + \\
& \text{Cosh}[4.0025 z] \left\{ 2 (11.7434 + 1.53278 f_0 - 0.0689088 f_{0d1} + 1.37532 g_0 + 1.38778 \times 10^{-17} g_{0d1} - \right. \\
& \quad 3.46945 \times 10^{-18} h_{0d1}) \text{Cos}[3.08764 z] - 2 (0.0550027 + 1.22139 f_0 - 0.301829 f_{0d1} + \\
& \quad \quad 5.55112 \times 10^{-17} g_0 - 0.159509 g_{0d1} - 0.0286901 h_{0d1}) \text{Sin}[3.08764 z] \left. \right\} + \\
& \text{Cosh}[9.34534 z] \left\{ 2 (0.000834684 + 0.0585407 f_0 - 0.00174804 f_{0d1} - 0.0517456 g_0 + \right. \\
& \quad 3.25261 \times 10^{-19} g_{0d1} + 1.69407 \times 10^{-21} h_{0d1}) \text{Cos}[9.34491 z] - \\
& \quad 2 (0.0000323744 + 0.000718905 f_0 - 0.00504638 f_{0d1} - 3.46945 \times 10^{-18} g_0 + \\
& \quad \quad 0.00492837 g_{0d1} + 5.16193 \times 10^{-6} h_{0d1}) \text{Sin}[9.34491 z] \left. \right\} + \\
& (-0.0802759 - 1.78261 f_0 - 0.947377 f_{0d1} - 1.18257 g_{0d1} + 0.546442 h_{0d1}) \\
& \text{Sinh}[2.23847 z] + \\
& \left(2 (0.0643231 + 1.42836 f_0 + 0.020735 f_{0d1} + 0.220565 g_{0d1} - 0.0499819 h_{0d1}) \text{Cos}[3.08764 z] - \right. \\
& \quad 2 (0.636766 + 1.33072 f_0 - 0.329312 f_{0d1} + 0.0425892 g_0 + \\
& \quad \quad 4.16334 \times 10^{-17} g_{0d1} - 3.46945 \times 10^{-18} h_{0d1}) \text{Sin}[3.08764 z] \left. \right\} \text{Sinh}[4.0025 z] + \\
& \left(2 (0.000270225 + 0.00600062 f_0 - 0.000187651 f_{0d1} - 0.000608911 g_{0d1} - 8.61334 \times 10^{-6} h_{0d1}) \right. \\
& \quad \text{Cos}[9.34491 z] - 2 (-0.000110584 - 0.032202 f_0 - 0.00222379 f_{0d1} + \\
& \quad \quad 0.040367 g_0 - 8.67362 \times 10^{-19} g_{0d1}) \text{Sin}[9.34491 z] \left. \right\} \text{Sinh}[9.34534 z] \left. \right\}
\end{aligned}$$

```

In[149]:= fd1[z_] = D[f[z], {z, 1}];
          fd2[z_] = D[f[z], {z, 2}];
          fd3[z_] = D[f[z], {z, 3}];
          gd1[z_] = D[g[z], {z, 1}];
          gd2[z_] = D[g[z], {z, 2}];
          gd3[z_] = D[g[z], {z, 3}];
          hd1[z_] = D[h[z], {z, 1}];
          hd2[z_] = D[h[z], {z, 2}];
          hd3[z_] = D[h[z], {z, 3}];

```

Solve for the initial conditions at $z = 0$ using the boundary condition at $z = 1$:

```

In[158]:= solution = Solve[{h[1] == 1, fd2[1] == 0, fd3[1] - 3 * rad / rad1 * hd1[1] == 0,
          gd3[1] + (sqrt[2]) * K2 * gd2[1] + K2^2 * gd1[1] - 3 * rad / rad2 * hd1[1] == 0,
          gd2[1] + (sqrt[2]) * K2 * gd1[1] + K2^2 * g[1] + 2 * (sqrt[3]) * v2 * rad / (rad2 * sqrt[1 - v2^2]) == 0},
          {f0, f0d1, g0, g0d1, h0d1}]

```

```

Out[158]= {{f0 -> -2.70766, f0d1 -> -8.11876, g0 -> -2.99388, g0d1 -> -4.71842, h0d1 -> -16.7704}}

```

Substitute the values and calculate the final expressions:

```

In[159]:= {f0, f0d1, g0, g0d1, h0d1} = solution // Values // Flatten;

In[160]:= c0sig = n20 / d0 * B2^2 * 2 l / t2 - n10 / d0 * B1^2 * 2 l / t1;
          c11sig = c11g * B2^2 * 2 l / t2 - c11f * B1^2 * 2 l / t1;
          c12sig = c12g * B2^2 * 2 l / t2 - c12f * B1^2 * 2 l / t1;
          c13sig = c13g * B2^2 * 2 l / t2 - c13f * B1^2 * 2 l / t1;
          c14sig = c14g * B2^2 * 2 l / t2 - c14f * B1^2 * 2 l / t1;
          c21sig = c21g * B2^2 * 2 l / t2 - c21f * B1^2 * 2 l / t1;
          c22sig = c22g * B2^2 * 2 l / t2 - c22f * B1^2 * 2 l / t1;
          c23sig = c23g * B2^2 * 2 l / t2 - c23f * B1^2 * 2 l / t1;
          c24sig = c24g * B2^2 * 2 l / t2 - c24f * B1^2 * 2 l / t1;
          c31sig = c31g * B2^2 * 2 l / t2 - c31f * B1^2 * 2 l / t1;
          c32sig = c32g * B2^2 * 2 l / t2 - c32f * B1^2 * 2 l / t1;
          c33sig = c33g * B2^2 * 2 l / t2 - c33f * B1^2 * 2 l / t1;
          c34sig = c34g * B2^2 * 2 l / t2 - c34f * B1^2 * 2 l / t1;
          c11tau = r1 * c13h + m1 * c12h;
          c21tau = r2 * c23h + m2 * c22h;
          c31tau = r3 * c33h + m3 * c32h;
          c12tau = -(m1 * c11h - r1 * c14h);
          c22tau = -(m2 * c21h - r2 * c24h);
          c32tau = -(m3 * c31h - r3 * c34h);
          c13tau = r1 * c11h + m1 * c14h;
          c23tau = r2 * c21h + m2 * c24h;
          c33tau = r3 * c31h + m3 * c34h;
          c14tau = -(m1 * c13h - r1 * c12h);
          c24tau = -(m2 * c23h - r2 * c22h);
          c34tau = -(m3 * c33h - r3 * c32h);

```

```

In[185]= sigma[z_] = F / (4 * pi * rad * l) * Ela / Ga * c0sig +
  F / (4 * pi * rad * l) * Ela / Ga * (Cosh[r1 * z] * (c11sig * Cos[m1 * z] + c12sig * Sin[m1 * z]) +
  Sinh[r1 * z] * (c13sig * Cos[m1 * z] + c14sig * Sin[m1 * z]) +
  Cosh[r2 * z] * (c21sig * Cos[m2 * z] + c22sig * Sin[m2 * z]) +
  Sinh[r2 * z] * (c23sig * Cos[m2 * z] + c24sig * Sin[m2 * z]) +
  Cosh[r3 * z] * (c31sig * Cos[m3 * z] + c32sig * Sin[m3 * z]) +
  Sinh[r3 * z] * (c33sig * Cos[m3 * z] + c34sig * Sin[m3 * z]))
tau[z_] = F / (8 * pi * rad * l) * (Cosh[r1 * z] * (c11tau * Cos[m1 * z] + c12tau * Sin[m1 * z]) +
  Sinh[r1 * z] * (c13tau * Cos[m1 * z] + c14tau * Sin[m1 * z]) +
  Cosh[r2 * z] * (c21tau * Cos[m2 * z] + c22tau * Sin[m2 * z]) +
  Sinh[r2 * z] * (c23tau * Cos[m2 * z] + c24tau * Sin[m2 * z]) +
  Cosh[r3 * z] * (c31tau * Cos[m3 * z] + c32tau * Sin[m3 * z]) +
  Sinh[r3 * z] * (c33tau * Cos[m3 * z] + c34tau * Sin[m3 * z]))

Out[185]= {-0.442511 + 1.79842 (0.232071 Cosh[2.23847 z] +
  Cosh[4.0025 z] (-0.0326327 Cos[3.08764 z] - 0.00582773 Sin[3.08764 z]) +
  Cosh[9.34534 z] (-6.2774 Cos[9.34491 z] + 1.79862 Sin[9.34491 z]) -
  0.200562 Sinh[2.23847 z] + (0.0337511 Cos[3.08764 z] + 0.00561399 Sin[3.08764 z])
  Sinh[4.0025 z] + (6.27631 Cos[9.34491 z] - 1.79886 Sin[9.34491 z]) Sinh[9.34534 z]) }

Out[186]= {0.157939 (19.8188 Cosh[2.23847 z] +
  Cosh[4.0025 z] (-36.0818 Cos[3.08764 z] - 21.5533 Sin[3.08764 z]) +
  Cosh[9.34534 z] (-0.507473 Cos[9.34491 z] + 0.0799981 Sin[9.34491 z]) - 22.9325
  Sinh[2.23847 z] + (34.8957 Cos[3.08764 z] + 22.3165 Sin[3.08764 z]) Sinh[4.0025 z] +
  (0.507561 Cos[9.34491 z] - 0.0799898 Sin[9.34491 z]) Sinh[9.34534 z]) }

```

REFERENCES

- Abdel Wahab, M.M. (2012). Fatigue in Adhesively Bonded Joints: A Review, *ISRN Materials Science*, vol. 2012, Article ID 746308, 25 pages.
- Adams, R., and Peppiatt, N. (1977). Stress Analysis of Adhesive Bonded Tubular Lap Joints. *Journal of Adhesion*, vol. 9, pp. 1-18.
- Adams, R.D. (1986). The Mechanics of Bonded Joint. International Conference on Structural Adhesives in Engineering, IMechE Conference publications, C180/86, University of Bristol/London, pp. 17 - 24.
- Adams, R.D. (2005). Adhesive bonding, NW Boca Raton, FL: Woodhead Publishing Limited.
- Adams, R.D., Comyn, J., and Wake, W.C. (1997). Structural adhesive joints in engineering Chapman & Hall.
- Alwar, R.S., and Nagaraja, Y. R. (1976). Elastic Analysis of Adhesive Butt Joints. *Journal of Adhesion*, vol. 7:4, pp. 279-287,
- Andersen, T., and Stigh, U. (2004). The stress-elongation relation for an adhesive layer loaded in peel using equilibrium of energetic forces. *International journal for solids and structures*, vol. 41, pp. 413-434.
- Arment, B., Duggan, M.J., Nixon, F., Wilson, M. (2012). Refrigeration line set fitting and method of using the same to join refrigeration lines to each other, US Patent Publication No. 20130167357.
- Ashcroft, I.A., Gilmore, R.B., and Shaw, S.J. (1996). Cyclic fatigue and environmental effects with adhesively bonded joints, AGARD 83rd SMP Meeting, Florence.

ASM International. Handbook Committee (1992). ASM Handbook Volume 2: Properties and Selection: Nonferrous Alloys and Special-Purpose Materials. ASM International, Materials Park, OH.

ASTM D 907 (2015). Standard definitions of terms relating to adhesives. American society for testing and materials, Conshohocken, PA.

ASTM, D2651-01 (2008). Standard recommended practice for preparation of metal surfaces for adhesive bonding. Annual Book of ASTM Standards, Philadelphia, PA.

ASTM, D3433 (1975). Standard Test Method For Fracture Strength In Cleavage Of Adhesives In Bonded Metal Joints. Annual Book of ASTM standards, Philadelphia, PA.

ASTM, D3933 (1998) Standard practice for preparation of aluminum surfaces for structural bonding. Annual Book of ASTM Standards, Philadelphia, PA.

ASTM, D7803 (2019). Standard Practice for Preparation of Zinc (Hot-Dip Galvanized) Coated Iron and Steel Product and Hardware Surfaces for Powder Coating, West Conshohocken, PA.

ASTM, E8/E8M (2009). Standard test methods for tension testing of metallic materials. Annual Book of ASTM Standards, Philadelphia, PA.

AWS (2007). Brazing Handbook, 5th Edition. American Welding Society, Miami, Florida.

AWS Committee on Definitions (2001). Standard welding terms and definitions, including terms for adhesive bonding, brazing, soldering, and thermal spraying, AWS, Miami, American Welding Society, pp. 5.

Azari, S., Papini, M., and Spelt, J. K. (2011). Effect of adhesive thickness on fatigue and fracture of toughened epoxy joints—part I: experiments, *Engineering Fracture Mechanics*, vol. 78, no.1, pp. 153–162.

- Azari, S., Papini, M., and Spelt, J. K. (2011). Effect of adhesive thickness on fatigue and fracture of toughened epoxy joints - part II: analysis and finite element modeling. *Engineering Fracture Mechanics*, vol. 78, no. 1, pp. 138–152.
- Baburaja, E.G., Starikovb, D., Evansc, J., Shafeevd, G.A., and Bensaoulab, A. (2007). Enhancement of adhesive joint strength by laser surface modification, *International Journal of Adhesion and Adhesives*, 2007, vol. 27, pp. 268-276.
- Bachir Bouiadjra, B., Fekirini, H., Belhouari, M., Boutabout, B., Serier, B. (2007). FE analysis of the behaviour of microcracks in the cement mantle of reconstructed acetabulum in the total hip prosthesis. *Computational Materials Science*, vol. 40, pp. 485-491.
- Bakos, I., Szabó, S. (2008). Corrosion behaviour of aluminium in copper containing environment, *Corrosion Science*, vol. 50, pp. 200-205.
- Banea, M.D., and Da Silva, L.F.M. (2010). The effect of temperature on the mechanical properties of adhesives for the automotive industry. *Proceedings of the Institution of Mechanical Engineers, Part L: Journal of Materials: Design and Applications*, vol. 224, pp. 51–62.
- Barenblatt, G.I. (1959). The formation of equilibrium cracks during brittle fracture. General ideas and hypotheses. Axially-symmetric cracks. *Journal of Applied Mathematics and Mechanics*, vol. 23, pp. 622-636.
- Barenblatt, G.I. (1961/1962). Mathematical theory of equilibrium cracks in brittle fracture. *Journal of Applied Mechanics and Technical Physics*, no. 4, pp. 3-56 (1961) (in Russian); *Advances in Applied Mechanics*, VII, pp. 55-129 (1962) (in English).
- Bauer, C., Treyer, K., Heck, T., Hirschberg, S. (2015). Greenhouse gas emissions from energy systems, comparison, and overview. In: *Reference Module in Earth Systems and Environmental Sciences*.

- Benard, Q., Fois, M., Grisel, M., Laurens, P., Joubert, F. (2009). Influence of the polymer surface layer on the adhesion of polymer matrix composites. *Journal of Thermoplastic Composite Materials*, vol. 22, pp. 51–61.
- Bennett, S.J., Devries, K.L., Williams, M.L. (1974). Adhesive fracture mechanics. *International Journal of Fracture*, vol. 10(1), pp. 33-43.
- Bernasconi, A., Beretta, S., Beretta, Moroni, F., Moroni, Pironi, A. (2010). Local stress analysis of the fatigue behaviour of adhesively bonded thick composite laminates. *Journal of Adhesion*, vol. 86, no. 5 – 6, pp. 480.
- Beshr, M., Aute, V. Sharma, V. Abdelaziz, O. Fricke, B., Radermacher, R. (2015). A comparative study on the environmental impact of supermarket refrigeration systems using low GWP refrigerants. *International Journal of Refrigeration*, 56, pp. 154-64.
- Birnbaum, M. (1965). Semiconductor surface damage produced by ruby lasers. *Journal of Applied Physics*, vol. 36, pp. 3688.
- Blackman, B.R.K., Hadavinia, H., Kinloch, A.J., and Williams, J.G. (2003). The use of a cohesive zone model to study the fracture of fiber composites and adhesively-bonded joints. *International journal of fracture*, vol. 119, pp. 25-46.
- Blackman, B.R.K., Kinloch, A.J. (1997). Determination of the mode I adhesive fracture energy, GIC, of structural adhesives using the double cantilever beam (DCB) and the tapered double cantilever beam (TDCB) specimens. Version 97-04. ESIS TC4 Protocol.
- Blackman, B.R.K., Kinloch, A.J., Paraschi, M. (2005). The determination of the mode II adhesive fracture resistance, GIIC, of structural adhesive joints: an effective crack length approach. *Engineering Fracture Mechanics*, vol. 72, pp. 877-897.

- Blackwood, D. J., and Chong, A.S.L. (1998). Pitting corrosion on aluminum in absence of chloride, *British Corrosion Journal*, vol. 33, pp. 219-224.
- Blanchard, C., Chateauminos, A., and Vincent, L. (1996). A new testing methodology for the assessment of fatigue properties of structural adhesives. *International Journal of Adhesion and Adhesives*, vol. 16, no. 4, pp. 289–299.
- Bowden, P.B., and Dukes, J.A. (1972). The plastic flow of isotropic polymers, *Journal of Materials Science*, vol. 7, pp. 52-63.
- Broek, D. (1978). *Elementary Engineering Fracture Mechanics*, Sijthoff & Noordhoff, Alphen aan den Rijn.
- Broughton, W.R., and Hinopoulos, G. (1999). Evaluation of the Single-Lap Joint Using Finite Element Analysis. NPL Report CMMT (A) 206.
- Callister, W.D. JR. (2007). *Materials Science and Engineering: An Introduction*. 7th edition. John Wiley & Sons, Inc, Hoboken, NJ.
- Camacho, G.T., and Ortiz, M. (1996). Computational modeling of impact damage in brittle materials. *International Journal of Solids and Structures*, vol. 33, pp. 2899-2938.
- Castro Sousa, F., Akhavan-Safar, A., Goyal, R., da Silva, L.F.M. (2021). Fatigue life estimation of single lap adhesive joints using a critical distance criterion: An equivalent notch approach, *Mechanics of Materials*, Volume 153, 103670.
- Chang, Y., Jung, S., Lee, S., Choi, J., Kim, Y., (2007). Fatigue data acquisition, evaluation and optimization of district heating pipes. *Applied Thermal Engineering*, 27, pp. 2524-2535.
- Chen, J.M., Sun, T.S., Venables, J.D., Hopping, R. (1977) Effect of fluorine contamination on the microstructure and bondability of aluminum surfaces. *SAMPE NSS&E* 22, pp. 25-46.

- Chérif, M., Loumena, C., Jumel, J., Kling R., (2016). Performance of Laser Surface Preparation of Ti6Al4 V, *Procedia CIRP*, vol. 45, pp. 311-314.
- Chon, C.T. (1982). Analysis of Tubular Lap Joint in Torsion. *Journal of Composite Materials*, vol. 16(4), pp. 268–284. C.W. Macosko (1994) *Rheology: Principles, Measurements, and Applications*, VCH, New York.
- Copper Development Association Inc. (2019). CDA Publication A4015-14-19: Copper Tube Handbook. McLean, VA.
- Cottis, B., Graham, M., Lindsay, R., Lyon, S., Richardson, T., Scantlebury, D. Stott, H. (2010). Environmental modification for cooling, heating and potable water systems. In *shreir's corrosion*. Elsevier: Amsterdam, The Netherlands, vol. 4, pp. 2930–2970.
- Coulomb, D. (2008) Refrigeration and cold chain serving the global food industry and creating a better future: two key IIR challenges for improved health and environment. *Trends in Food Science & Technology*. 19 (8), pp. 413-417.
- da Costa Mattos, H.S., Monteiro, A.H., and Palazzetti R. (2012). Failure analysis of adhesively bonded joints in composite materials, *Materials & Design*, vol. 33, pp. 242–247.
- Da Silva, L.F.M., èOchsner, A., Adams, R.D. (2011) *Handbook of adhesion Technology*. Springer-Verlag Berlin Heidelberg, Heidelberg.
- Daniel, C., Mücklich, F. (2004), Quantification of periodical surface structures by white light interferometry. *Practical Metallography*, vol. 6, pp. 277-285.
- Daniel, C., Mücklich, F., Liu, Z. (2003). Periodical micro-nano-structuring of metallic surfaces by interfering laser beams. *Applied Surface Science*, vol. 208-209, pp 317-321.

- Datla, N.V., Papini, M., Schroeder, J.A., Spelt, J.K. (2010). Modified DCB and CLS specimens for mixed-mode fatigue testing of adhesively bonded thin sheets. *International Journal of Adhesion and Adhesives*, vol. 30, pp. 439-447.
- De Mol van Otterloo, J.L., Bagnoli, D., De Hosson, J.Th.M. (1995). Enhanced mechanical properties of laser treated Al-Cu alloys: A microstructural analysis. *Acta Metallurgica et Materialia*, vol. 43, pp 2649-2656.
- Dean, G.D., and Crocker, L. (2000). Comparison of the measured and predicted deformation of an adhesively bonded lap-joint specimen, NPL Report CMMT (A) 293.
- Dehmas, M., Valdés, R., Lafont, M.C., Lacaze, J., and Viguier, B. (2006). Identification of intermetallic precipitates formed during re-solidification of brazed aluminum alloys. *Scripta Materialia*, vol. 55, pp. 191–194.
- Dieter, G.E. (1976). *Mechanical Metallurgy*, 2nd ed., McGraw-Hill.
- Dowling, M. (2007). From Husserl to van Manen. A review of different phenomenological approaches. *International Journal of Nursing Studies*, vol. 44, pp. 131-142.
- Dowling, N.E. (1998). *Mechanical behaviour of materials: engineering methods for deformation, fracture and fatigue*, Upper Saddle River, NJ, Prentice Hall.
- Du, B., He, Y., Zheng, Z., Cheng, Z. (2016). Analysis of thermal stress and fatigue fracture for the solar tower molten salt receiver. *Applied Thermal Engineering*, 99, pp. 741-750.
- Ducept, F., Davies, P., Gamby, D. (2000). Mixed mode failure criteria for a glass/epoxy composite and an adhesively bonded composite/composite joint. *International Journal of Adhesion and Adhesives*, vol. 20, pp. 233-244.
- Dugdale, D.S. (1960). Yielding of steel sheets containing slits. *Journal of the Mechanics and Physics of Solids*, vol. 8, pp. 100-104.

- Ebnesajjad, S. (2011). 6 - Surface Preparation of Metals, In Handbook of Adhesives and Surface Preparation, Plastics Design Library, William Andrew Publishing, Oxford, pp. 83-106.
- Eickner, H.W., Schowalter, N.E. (1950). A study of methods for preparing clad 24 s-t3 aluminum alloy sheet surfaces for adhesive bonding, Forest products laboratory report, no. 1813.
- Elbel, S., Duggan, M., LaGrotta, T., Raj, S., and Hrnjak, P. (2016). Accelerated fatigue testing of aluminum refrigeration press fittings for HVAC & R applications. International Refrigeration and Air Conditioning Conference. Paper 1753.
- EPA (2015). Inventory of U.S. greenhouse gas emissions and sinks: 1990-2013. U.S. Environmental Protection Agency. EPA 430-R-15-004. April 15.
- Fernlund, G., and Spelt, J.K. (1991), Failure load prediction: II. experimental results, International Journal of Adhesion and Adhesives, vol. 11, no. 4, pp. 221-227.
- Fernlund, G., and Spelt, J.K. (1991). Failure load prediction: I. analytical method, international journal of adhesion and adhesives, vol. 11, no. 4, 1991, pp. 213-220.
- Fernlund, G., Papini, M., McCammond, D., and Spelt, J.K. (1994), Fracture load predictions for adhesive joints, Composites Science and Technology, vol. 51, pp. 587- 600.
- Fessel, G., Broughton, J.G., Fellows, N.A., Durodola, J.F., Hutchinson, A.R. (2009). Fatigue performance of metallic reverse-bent joints. Fatigue and Fracture of Engineering Materials and Structures, vol. 32 (9), pp. 704-712.
- Francis, C., Maidment, G., Davies, G. (2017). An investigation of refrigerant leakage in commercial refrigeration International Journal of Refrigeration, 74, pp. 12-21.
- Gao, L.-L., Wang, L., Gao, H., Chen, G., and Chen, X. (2011). Fatigue life evaluation of anisotropic conductive adhesive film joints under mechanical and hygrothermal loads. Microelectronics Reliability, vol. 51, no. 8, pp. 1393–1397.

- Garcia, J., Swidersky, H-W., Schwarze, T., and Eicher, J. (2010). Inorganic fluoride materials from solvay fluor and their industrial applications, in functionalized inorganic fluorides: synthesis, Characterization & Properties of Nanostructured Solids (ed. A. Tressaud), Chichester, UK, John Wiley & Sons Ltd.
- Geubelle, P.H., and Baylor, J. (1998). Impact-induced delamination of laminated composites: a 2D simulation. *Composites Part B Engineering*, vol. 29, pp. 589-602.
- Gilbertson, T. (2001), “Enercon industries, atmospheric plasma. What is it? and What’s it good for?”, *ENEWS Surface Treating Technology*, 2nd Quarter.
- Goglio, L., Dragoni, E. (2013). Adhesive stresses in axially-loaded tubular bonded joints—Part I: Critical review and finite element assessment of published models. *International Journal of Adhesion and Adhesives*, vol. 47, pp. 35-45.
- Goglio, L., Paolino, D. (2014). Adhesive stresses in axially-loaded tubular bonded joints—part ii: Development of an explicit closed-form solution for the lubkin and reissner model. *International Journal of Adhesion and Adhesives*, vol. 48, pp. 35-42.
- Gray, A., Flemming, A.J., Evans, J.M. (1999). Optimizing the properties of long- life brazingsheet alloys for vacuum and NOCOLOK brazed components. *VTMS 4 Conference Proceedings*, London.
- Gray, A., Swidersky, H.W., Oman, L. (2006). Reactive Zn flux - an opportunity for controlled Zn diffusion and improved corrosion resistance. *AFC-Holcroft 11th International Invitational Aluminum Brazing Seminar*, Livonia, Michigan.
- Greer, C.M., Chen, J, Warren, C.D., Daniel, C. (2016). Surface characterization of carbon fiber polymer composites and aluminum alloys after laser interference structuring. *Journal of the Minerals, Metals, and Materials Society*, vol. 68, pp. 1882-1889.

- Griffith, A.A. (1921). The Phenomena of Rupture and Flow in Solids, Philosophical Transactions of the Royal Society of London, vol. 221, pp. 163-198.
- Groth, H.L. (1985). A method to predict fracture in an adhesively bonded joint, International Journal of Adhesion and Adhesives, vol. 5, no. 1, pp 19 - 22.
- Groth, H.L. (1988). Stress singularities and fracture at interface corners in bonded, International Journal of Adhesion and Adhesives, vol. 8, no. 2, pp. 107 - 113.
- Gschrey, B., Schwarz, W., Elsner, C., Engelhardt, R. (2011). High increase of global F-gas emissions until 2050. Greenhouse Gas Measurement and Management. 1 (2), pp. 85–92.
- Hart-Smith, L.J. (1973) Adhesive-bonded double-lap joints. NASA Report CR-112238.
- Hart-Smith, L.J. (1973) Adhesive-bonded scarf and stepped-lap joints. NASA Report CR-112237.
- Hart-Smith, L.J. (1973). Adhesive-bonded single-lap joints. NASA Report CR-112236.
- Hart-Smith, L.J. (1981). Further developments in the design and analysis of adhesive-bonded structural joints. In K. Kedward (Ed.), STP749-EB Joining of Composite Materials, pp. 3-31.
- Hatch, J.E. (1984), Aluminum: Properties and Physical Metallurgy. American Society for Metals, Metals Park, OH.
- Haward, R.N. (1973). The Physics of Glassy Polymers. Applied Science Publishers Pty. Ltd., London.
- He, X. (2011). A review of finite element analysis of adhesively bonded joints. International Journal of Adhesion and Adhesives, vol. 31, no. 4, pp. 248–264.
- He, X. (2011). FEA of fatigue behaviour of adhesively bonded joints. Advanced Materials Research, vol. 148-149, pp. 753–757.

- Hernandez, E., Alfano, M., Lubineau, G., and Buttner, U. (2006). Improving adhesion of copper/epoxy joints by pulsed laser ablation, *International Journal of Adhesion and Adhesives*, vol. 61, pp. 23-32.
- Hinopoulos, G., and Broughton, W.R. (1999), Evaluation of the t-peel joint using the finite element method, NPL Report CMMT (A) 207.
- Hirschberg, P., Sindelar, M., Kassar, M., and Haupt, R. (2017) Vibration testing of compression joints. Proceedings of the ASME 2017 Pressure Vessels and Piping Conference. Volume 3A: Design and Analysis. Waikoloa, Hawaii, USA. July 16–20, 2017.
- International Organization for Standardization (2017). ISO 14903: 2017, Refrigerating systems and heat pumps - Qualification of tightness of components and joints, Geneva, Switzerland.
- Irwin, G. (1957). Analysis of stresses and strains near the end of a crack traversing a plate, *Journal of Applied Mechanics*, vol. 24, pp. 361–364.
- Ishii, K., Imanaka, M., Nakayama, H. (2007). Fatigue crack propagation behavior of adhesively-bonded CFRP/aluminum joints. *Journal of Adhesion Science and Technology*, vol. 21, pp. 153-167.
- Ishii, K., Imanaka, M., Nakayama, H., and Kodama, H. (1998). Fatigue failure criterion of adhesively bonded CFRP/metal joints under multiaxial stress conditions, *Composites A*, vol. 29, no. 4, pp. 415–422.
- Ishii, K., Imanaka, M., Nakayama, H., and Kodama, H. (1999). Evaluation of the fatigue strength of adhesively bonded CFRP/metal single and single-step double-lap joints. *Composites Science and Technology*, vol. 59, no. 11, pp. 1675–1683.
- Jen, Y.M. (2012). Fatigue life evaluation of adhesively bonded scarf joints. *International Journal of Fatigue*, vol. 36, no. 1, pp. 30 - 39.

- Jen, Y.M., and Ko, C.W. (2010) Evaluation of fatigue life of adhesively bonded aluminum single-lap joints using interfacial parameters. *International Journal of Fatigue*, vol. 32, no. 2, pp. 330–340.
- Jordan, M.F., Milner D.R., (1956–7). The removal of oxide from aluminum by brazing fluxes. *Journal of the Institute of Metals*, vol. 85, pp. 33–40.
- Kahraman, R., Al-Harthi, M. (2005). Moisture diffusion into aluminum powder-filled epoxy adhesive in sodium chloride solutions. *The International Journal of Adhesion and Adhesives*, vol. 25, pp. 337-341.
- Khedr, M.G.A., Lashien, A.M.S. (1992) The role of metal cations in the corrosion and corrosion inhibition of aluminum in aqueous solutions. *Corrosion Science*, vol. 33, pp. 137-151.
- Kinloch, A.J., Guild, F. (1996a). Predictive modeling of the properties and toughness of rubber-toughened epoxies. In: C.K. Riew CK, A.J. Kinloch, editors. *Toughened plastics II, novel approaches in science and engineering*. USA: *Advances in Chemistry Series Publications*, pp. 1–25.
- Knox, E. M., Cowling, M. J., and Hashim, S. A. (2000), Fatigue performance of adhesively bonded connections in GRE pipes, *International Journal of Fatigue*, vol. 22, no. 6, pp. 513–519.
- Kobayasi, K., Kumada, T. (1968). Measuring thermal diffusivity of a small solid disk by step-wise heating. *Technol Rep Tohoku Univ.* 33(2), 169-186.
- Kumar, S. (2009). Analysis of tubular adhesive joints with a functionally modulus graded bondline subjected to axial loads. *International Journal of Adhesion and Adhesives*, vol. 29, pp. 785-795.
- Kumar, S., and Pandey, P.C. (2006). Cyclic-fatigue performance of adhesively bonded lap joint, in *Computational Methods*, part 1, pp. 541–546.

- Kumar, S., and Pandey, P.C. (2011). Fatigue life prediction of adhesively bonded single lap joints. *International Journal of Adhesion and Adhesives*, vol. 31, no. 1, pp. 43–47.
- Kumar, S., and Scanlan, J.P. (2010). Stress analysis of shaft-tube bonded joints using a variational method. *Journal of Adhesion*, vol. 86, pp. 369-394.
- Kurtulus, O., Yang, B., Lumpkin, D., Groll, E.A., Jestings, L., and Conde, R. (2014). Performance and Operating Characteristics of a Novel Positive-Displacement Oil-Free CO₂ Compressor. *International Compressor Engineering Conference*. Paper 2375.
- Lacaze, J., S. Tierce, M.C. Lafont, Y. Thebault, N. Pébère, et al. (2005). Study of the microstructure resulting from brazed aluminum materials used in heat exchangers', *Materials Science and Engineering A*, vol. 413–414, pp. 317–321.
- Lasagni, A., D'Alessandria, M., Giovanelli, R., Mücklich, F. (2007). Advanced design of periodical architectures in bulk metals by means of Laser Interference Metallurgy. *Applied Surface Science*, vol. 254 (4), pp. 930-936.
- Lee, D.G., Kim, K.S. Lim, Y.T. (1991). An experimental study of fatigue strength for adhesively bonded tubular single lap joints. *Journal of Adhesion*, vol. 35, pp. 39-53.
- Lee, S.J., and Lee, D.G. (1992). Development of a failure model for the adhesively bonded tubular single lap joint. *Journal of Adhesion*, vol. 40, pp. 1-14.
- Lee, S.J., and Lee, D.G. (1995). Optimal-design of the adhesively bonded tubular single lap joint. *Journal of Adhesion*, vol. 50, pp.165-180.
- Lee, S.J., and Lee, D.G. (1996). Development of a fatigue failure model for the adhesively bonded tubular single lap joint under dynamic torsional loading. *Journal of Adhesion*, vol. 56, pp. 157-169.

- Leffler, K., Alfredsson, K.S., Stigh, U. (2007). Shear behaviour of adhesive layers. *International Journal of Solids and Structures*, vol. 44, pp. 530-545.
- Liljedahl, C.D.M., Crocombe, A.D., Wahab, M.A., and Ashcroft, I.A. (2006). Damage modeling of adhesively bonded joints. *International journal of fracture*, vol. 141, pp. 147-161.
- Lokring Company Website, www.lokring.com
- Lubkin, J.L., and Reissner, E. (1956). Stress distribution and design data for adhesive lap joints between circular tubes. *Transactions of the ASME*, vol. 78, pp. 1213-1221.
- Markolefas, S.I., and Papathanassiou, T.K. (2009) Stress redistributions in adhesively bonded double-lap joints, with elastic perfectly plastic adhesive behavior, subjected to axial lap shear cyclic loading, *International Journal of Adhesion and Adhesives*, vol. 29, no. 7, pp. 737–744.
- Martinez, M.A, Velasco, F., Abenojar, J., Pantoja, M., Del Real, J.C. (2008). Analytical solution to calculate the stress distribution in pin-and-collar samples bonded with anaerobic adhesives (following ISO 10123 standard). *International Journal of Adhesion and Adhesives*, vol. 28, pp. 405-410.
- Melander, A., Linder, J., Stensiö, H., Larsson, M., Gustavsson, A., Björkman, G. (1999). How defects in an adhesive layer influence the fatigue strength of bonded steel-sheet specimens. *Fatigue & Fracture of Engineering Materials & Structures*, vol. 22, no.5, pp. 421-426.
- Mostovoy, S., Crosley, P.B., Ripling, E.J. (1967). Use of crack-line loaded specimens for measuring plane-strain fracture toughness. *Journal of Materials Chemistry*, vol. 2, pp. 661-681.

- Nairn, J.A. (2000). Energy release rate analysis for adhesive and laminate double cantilever beam specimens emphasizing the effect of residual stresses. *International Journal of Adhesion and Adhesives*, vol. 20, pp. 59-70.
- Nayeb-Hashemi, H, Rossettos, JN., Melo, AP. (1997). Multiaxial fatigue life evaluation of tubular adhesively bonded joints. *International Journal of Adhesion and Adhesives*, vol. 17, pp. 55-63.
- Neddersen, J., Chumanov, G., and Cotton, T. M. (1993). Laser ablation of metals: a new method for preparing sers active colloids. *Applied Spectroscopy*, vol. 47, pp. 1959-1964.
- Needleman, A. (1987). A continuum model for void nucleation by inclusion debonding. *Journal of Applied Mechanics*, vol. 54, pp 525-531.
- Needleman, A. (1990). An analysis of decohesion along an imperfect interface. *International Journal of Fracture*, vol. 42, pp. 21-40.
- Needleman, A. (1990). An analysis of tensile decohesion along an interface. *Journal of the Mechanics and Physics of Solids*, vol. 38, pp. 289-324.
- Nemeş, O., and Lachaud, F. (2009). Modeling of cylindrical adhesively bonded joints. *Journal of Adhesion Science and Technology*, vol. 23, pp. 1383-1393.
- Nemeş, O., Lachaud, F., Mojtabi, A. (2006). Contribution to the study of cylindrical adhesive joining. *International Journal of Adhesion and Adhesives*, vol. 26, pp. 474-480.
- Nolting, A.E., Underhill, P.R., Dean, S.W. (2009). Fatigue behavior of adhesively bonded aluminum double strap joints. *Journal of ASTM International*, pp. 761-777.
- Nordlien, J.H., Daaland, O., Lian, K.A., and Espedal, A. (2011). Multiport extruded tube alloy development for HVAC&R applications. 2nd International Congress Aluminum Brazing Technologies for HVAC&R Aluminum-Verlag, Düsseldorf, Germany.

- Orowan, E. (1949). Fracture and strength of solids. Reports on Progress in Physics XII, pp. 185–232.
- Paffumi, E., Nilsson, K.F., Szaraz, Z. (2015). Experimental and numerical assessment of thermal fatigue in 346 austenitic steel pipes. *Engineering Failure Analysis*, 47 (Pt B), pp. 312-327.
- Panton, R.L. (2013). *Incompressible Flow* (Fourth ed.). John Wiley & Sons, Hoboken, pp. 114.
- Park, C.Y., and Hrnjak, P. (2002). R-410A air conditioning system with microchannel condenser, Proceedings of the 9th Purdue Refrigeration Conference, University of Purdue.
- Pinto, M. A., Cheung, N., Filippini Ierardi, M.C., Garcia, A. (2003). Microstructural and hardness investigation of an aluminum–copper alloy processed by laser surface melting. *Materials Characterization*, vol. 50, pp. 249-253.
- Poursaeidi, E., Bazvandi, H. (2016). Effects of emergency and fired shut down on transient thermal fatigue life of a gas turbine casing. *Applied Thermal Engineering*, 100, pp. 453-461.
- Pugno, N., Carpinteri, A. (2003). Tubular adhesive joints under axial load. *Journal of Applied Mechanics*, vol. 70, pp. 832-839.
- Ripling, E.J., Mostovoy, S., Patrick R.L. (1964). Measuring fracture toughness of adhesive joints *Mater Res Stand (ASTM Bull)*, vol. 4, pp. 129-134.
- Rogers, N.L. (1966). Surface preparation of metals for adhesive bonding. In: Bodnar MJ, ed. *Applied Polymer Symposia No. 3, Structural Adhesives Bonding*. New York, NY: Interscience Publishers, pp. 327-340.
- Romoli, L. Moroni, F., and Khan, M.M.A. (2017). A study on the influence of surface laser texturing on the adhesive strength of bonded joints in aluminum alloys. *CIRP Annals - Manufacturing Technology*, vol. 66, pp. 237–240.

- Russell, W.J., Garnis, E.A. (1981). A chromate-free low toxicity method of preparing aluminum surfaces for adhesive bonding. *SAMPE Journal*, vol. 17 (3), pp. 19-23.
- Sabau, A.S., Chen, J., Jones, J.F., Hackett, A., Jellison, G.D., Daniel, C., Warren, C.D., and Rehkopf, J.D. (2015). Surface modification of carbon fiber polymer composites after laser structuring. *Advanced Composites for Aerospace, Marine, and Land Applications II*, pp. 297-309.
- Sabau, A.S., Chen, J., Warren, C.D., Erdman, D.L. III, Daniel, C., Skszek, T., and Caruso Dailey M. (2016). A laser interference-based surface treatment of al and carbon fiber polymer composites for enhanced bonding. paper LB15-0070, SAMPE Conference and Exhibition, Long Beach, CA, May 23-26.
- Sabau, A.S., Meyer, H. M. Leonard, D. N. (2020). Laser-interference pulse number dependence of surface chemistry and sub-surface microstructure of AA2024-T3 alloy. *Optics Laser Technology*, 131, 106457.
- Schmidt, D., Singleton, J., Bradshaw, C.R. (2018). Development of a Light-Commercial Compressor Load Stand to Measure Compressor Performance using Low-GWP Refrigerants. In: *International Compressor Engineering Conference at Purdue*. Paper 1455.
- Schuecker, C., Davidson, B.D. (2000). Effect of friction on the perceived mode II delamination toughness from three- and four-point bend end notched flexure tests, *ASTM STP 1383*, pp. 334-344.
- Schwartz, M.M. (2003). *Brazing*, ASM International, Materials Park, OH.
- Shapiro, A.E. (2010). Brazing Q&A. *Welding Journal*, vol. 89, pp. 18–20.

- Shenoy, V., Ashcroft, I.A., Critchlow, G.W., Crocombe, A.D. (2010). Unified methodology for the prediction of the fatigue behaviour of adhesively bonded joints. *International Journal of Fatigue*, vol. 32 (8), pp. 1278-1288.
- Shi, Y.P., Cheng, S. (1993). Analysis of adhesive-bonded cylindrical lap joints subjected to axial load. *Journal of Engineering Mechanics*, vol. 119, pp. 584-602.
- Sih, G.C., and Chen, E.P. (1973). Fracture analysis of unidirectional composites. *Journal of Composite Materials*, vol. 7, pp. 230–244.
- Slámová, M., Sláma, P., Juricek, Z., Karger, A. (2002). Corrosion behaviour of Al fins in heat exchangers. *Materials Science Forum*, vol. 396-402, pp. 1505-1510.
- Söntgerath, J.A.H., Kooij, N.D.A., Vieregge, K., and Haszler, A. (1996). The effect of microstructure on flow behavior of braze clad material. *Materials Science Forum*, vol. 217 - 222, pp. 1721 - 1726.
- Swidersky, H.W. (2001). Aluminum brazing with non-corrosive flux, state of the art and trends in NOCOLOK® flux technology, 6th International Conference on Brazing, High Temperature Brazing and Diffusion Bonding, Aachen, Germany.
- Tadjamoli, M., Tzinmann, M., and Fiaud, C. (1984). Galvanic Corrosion of the Aluminium–Copper Couple in Uninhibited Aqueous Solutions of Glycols. *British Corrosion Journal*, vol. 19, pp. 36-40.
- Tai, R.C.L., Szklarskasmialowska, Z. (1993). Effect of fillers on the degradation of automotive epoxy adhesives in aqueous solutions part I absorption of water by different fillers-incorporated automotive epoxy adhesives. *Journal of Materials Science*, vol. 28, pp. 6199-6204.

- Taib, A.A., Boukhili, R., Achiou, S., Boukehili H. (2006). Bonded joints with composite adherends. Part II. Finite element analysis of joggle lap joints. *International Journal of Adhesion and Adhesives*, vol. 26, pp. 237-248.
- Takiguchi, M., and Yoshida, F. (2007). Effects of loading speed and shear prestrain on adhesive fatigue strength in single-lap joint. *Key Engineering Materials*, vol. 340-341, pp. 1479 – 1484.
- Tanchev, R.T., and Falzon, B.G. (2008). An experimental and numerical study of the static and fatigue performance of a composite adhesive repair. *Key Engineering Materials*, vol. 383, pp. 25–34.
- Terekhova, L.P., Skoryi, I.A (1972) Stresses in bonded joints of thin cylindrical shells. *Strength of Materials* 4, pp. 1271–1274
- Terrill, J.R., Cochran, C.N., Stokes, J.J., and Haupin, W.E. (1971). Understanding the mechanisms of aluminum brazing. *Welding Journal*, vol. 50, pp. 833–839.
- Thomsen, O.T., and Kildegaard, A. (1990). Analysis of adhesive bonded generally orthotropic circular shells. *Developments in the Science and Technology of Composite Materials, Proceedings of the Fourth European Conference of Composite Materials*, pp. 723-729.
- Tvergaard, V., and Hutchinson, J.W. (1992). The relation between crack growth resistance and fracture process parameters in elastic plastic solids. *Journal of the Mechanics and Physics of Solids*, vol. 40(6), pp. 1377-1397.
- UNEP (2015). “Proposed Amendment to the Montreal Protocol Submitted by Canada, Mexico and the United States of America.” Open-Ended Working Group of the Parties to the Montreal Protocol on Substances that Deplete the Ozone Layer, Thirty-Fifth Meeting, March.

- Wang, C.H., and Chalkley (2000), Plastic yielding of a film adhesive under multiaxial stresses, *International Journal of Adhesion and Adhesives*, vol. 20, no. 2, pp. 155-164.
- Wang, J., Rider, A.N., Heller, M., Kaye, R. (2005). Theoretical and experimental research into optimal edge taper of bonded repair patches subject to fatigue loadings, vol 25, no. 5, pp. 410-426.
- Ward, I.M. (1971). *Mechanical Properties of Solid Polymers*. John Wiley & Sons, Ltd, Hoboken.
- Watkins, K.G, McMahon, M.A., Steen, W.M. (1997). Microstructure and corrosion properties of laser surface processed aluminum alloys: a review, *Materials Science and Engineering A*, vol. 231, pp. 55-61.
- Wegman, R.F., and Levi, D.W. (1985). *Structural adhesive processing, Part B, Chapter 22, Section V Materials and Processes*, Marcel Dekker Inc., New York, NY, pp. 1177-1191.
- Wegman, R.F., and Twisk, J.V. (2013) *Aluminum and Aluminum Alloys in Surface preparation techniques for adhesive bonding (Second Edition)*, William Andrew Publishing, Norwich, NY.
- Williams, J.G., and Hadavinia, H. (2002). Analytical solutions of cohesive zone models. *Journal Mechanics Physics Solids*, vol. 50, pp. 809–825.
- Williams, M.L. (1966). *Stress Singularities, Adhesion and Fracture*. Proceedings of the Fifth U.S. National Congress of Applied Mechanics, pp. 451-464.
- Wilson, M., and Bowers, C.D. (2014). Design of accelerated fatigue tests for flame free refrigeration fittings. *International Refrigeration and Air Conditioning Conference*. Paper 1529.
- Wong, D., Swette, L., Cocks, F.H. (1979). Aluminum Corrosion in Uninhibited Ethylene Glycol-Water Solutions. *Journal of the Electrochemical Society*, vol. 126, pp. 11-15.

- Wu, Y.R., Lin, J.P., Wang, P.C., & Zheng, R. (2016). Effect of Thermal Exposure on Static and Fatigue Characteristics of Adhesive-bonded Aluminum Alloys. *Journal of Adhesion*, vol. 92:7-9, pp. 722-738.
- Xu, X.P., Needleman, A. (1994). Numerical simulations of fast crack growth in brittle solids. *Journal of the Mechanics and Physics of Solids*, vol. 42, pp. 1397-1434.
- Yang, Q.D., Thouless, M.D., and Ward, S.M. (2001). Elastic-plastic mode-II fracture of adhesive joints. *International journal for solids and structures*, vol. 38, pp. 3251-3262.
- Yang, Z., Zhang, K., Ma, Y., and Li, Y. (2011). Orthogonal test research on the effect of curing technology on the fatigue life of adhesive bonding of CFRP and aluminum alloy. *Advanced Materials Research*, vol. 181-182, pp. 534–539.
- Yoon, S., Kim, H.J., and Lee, C. (2007). Fabrication of automotive heat exchanger using kinetic spraying process. *Surface & Coatings Technology*, vol. 201, pp. 9524–9532.
- Young, R.J. (1981). *Introduction to Polymers*. Chapman and Hall, London.
- Zhang, Q.Y., and Zhuang, H.S. (2008). *Brazing and Soldering Manual*, 2nd edition, Beijing, China Machine Press, in Chinese.
- Zhang, X., Ziviani, D., Braun, J.E., Groll, E.A. (2018). Experimental Validation and Analysis of a Dynamic Model for Linear Compressors. In: *International Compressor Engineering Conference at Purdue 1671*.
- Zhang, Y., Vassilopoulos, A.P., and Keller, T. (2008). Stiffness degradation and fatigue life prediction of adhesively-bonded joints for fiber-reinforced polymer composites. *International Journal of Fatigue*, vol. 30, no. 10-11, pp. 1813 - 1820.
- Zhao, H., D. Sekulic (2006). Diffusion-controlled melting and re-solidification of metal micro layers on a reactive substrate. *Heat and Mass Transfer*. vol. 42, pp. 464-469.

Zhao, H., Woods, R., Sekulic, D. (Ed.), (2013). Controlled atmosphere brazing of aluminum
Advances in brazing – science, technology and applications, Woodhead Publishing
Cambridge, pp. 280-292.

VITA

Haotian Liu received his Bachelor in Mechanical Engineering (2015) from Shanghai Jiaotong University (SJTU) in China. At SJTU, he was the leader of the ME debate team and was awarded the SJTU academic Excellence Scholarship. He began his study at Purdue in 2014 as a senior exchange student in part of the ‘SJTU-Purdue’ graduate program. He continued his graduate studies at Purdue and received his Master of Science degree (2017) with research focus on energy recovery on power plants. He is expected to be awarded a Ph.D. degree in August 2021 from the School of Mechanical Engineering. His Ph.D. work focused on reliability experiments and structural analysis on adhesive joints applied in HVAC&R systems. He received the Ward A. Lambert Graduate Teaching Fellowship as an instructor. He will continue his research as a postdoctoral researcher at School of Mechanical Engineering at Purdue University upon graduation.

PUBLICATIONS

Journal Articles

H. Liu, J.A. Weibel, A.S. Sabau, P. Geoghegan, J. Chen, and E.A. Groll. Adhesive bonding of copper prepared by laser-interference near the interference structuring limits. Under review.

H. Liu, G. Subbarayan, J.A. Weibel, E.A. Groll. Prediction of stress distribution in adhesive tube-to-tube joints under HVAC&R loading conditions. In preparation.

H. Liu, J.A. Weibel, P.J. Geoghegan, E.A. Groll (2021). A pressure and temperature cycling test stand with hot-gas bypass control for evaluation of adhesive joints in HVAC&R applications. In preparation.

H. Liu; J.A. Weibel; E.A. Groll (2017). Performance analysis of an updraft tower system for dry cooling in large-scale power plants. *Energies*, vol. 10, no. 11: 1812.

Conference Proceedings

H. Liu, P.J. Geoghegan, J.A. Weibel, D. Ziviani, E.A. Groll (2021). Proof-of-concept testing of adhesive joints for HVAC&R applications, 13th IEA Heat Pump Conference, Paper 332, Jeju, Korea, April 26-29, 2021.

H. Liu, A. Dhunput, H. Miyamura, T Young, D. Lafford, E.A. Groll, D. Ziviani (2021). Mechanistic force analysis of single-screw compressor with 6-11 geometry configuration. International Compressor Engineering Conference. Paper No. 1580